JOURNAL OF THE

Electrochemical Society

Vol. 115, No. 5 May 1968

In the long run...

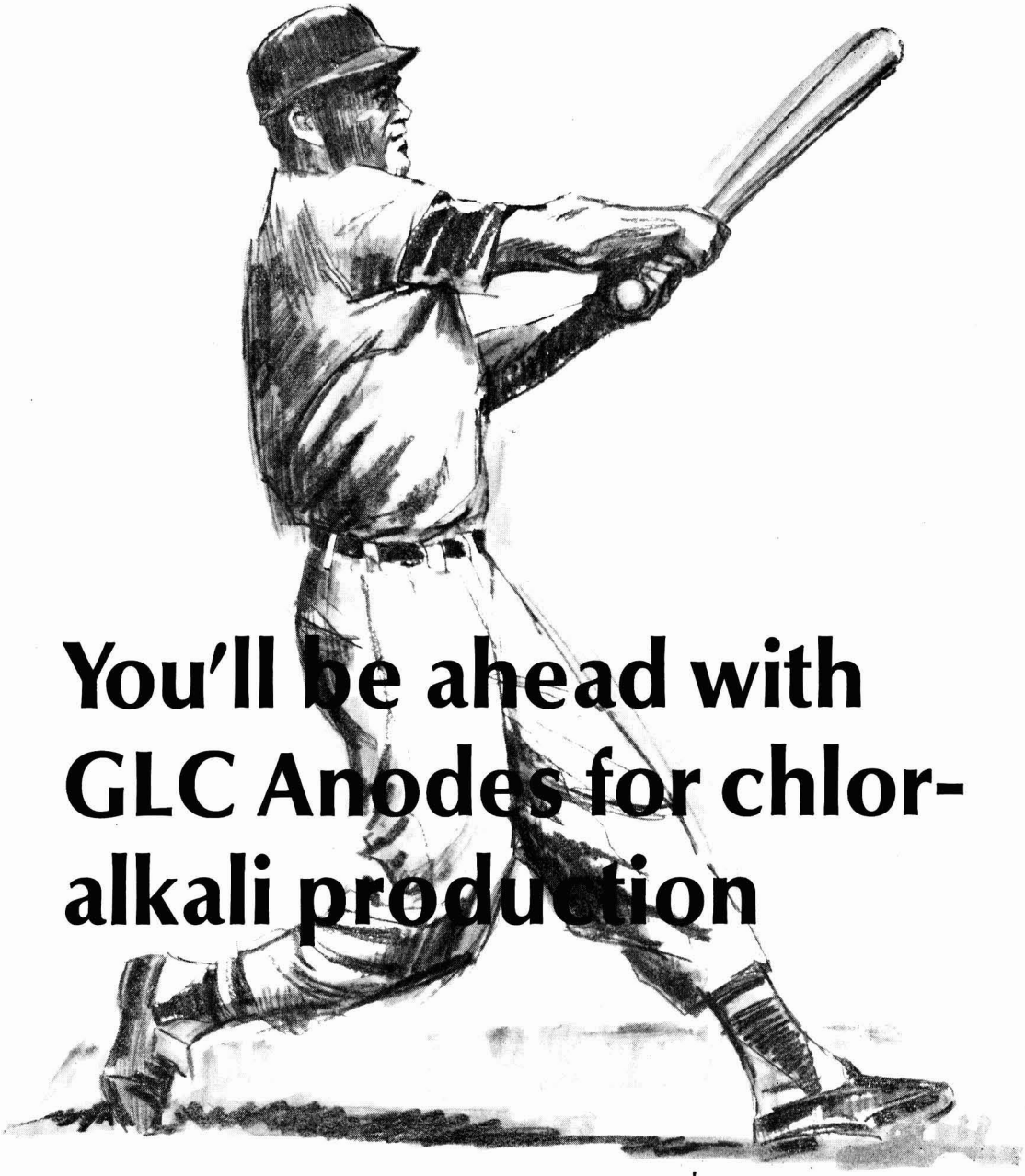

You'll be ahead with GLC Anodes for chlor-alkali production

PRODUCTS YOU CAN TRUST ® GLC

GRAPHITE PRODUCTS DIVISION
GREAT LAKES CARBON CORPORATION
299 Park Avenue • New York, N. Y. 10017
OFFICES AND AGENTS FROM COAST-TO-COAST AND AROUND THE WORLD

Great Lakes Carbon Corporation is one of the world's largest manufacturers of graphite for electrochemical and electrothermic processes—and for aerospace, nuclear, metallurgical and other industrial uses.

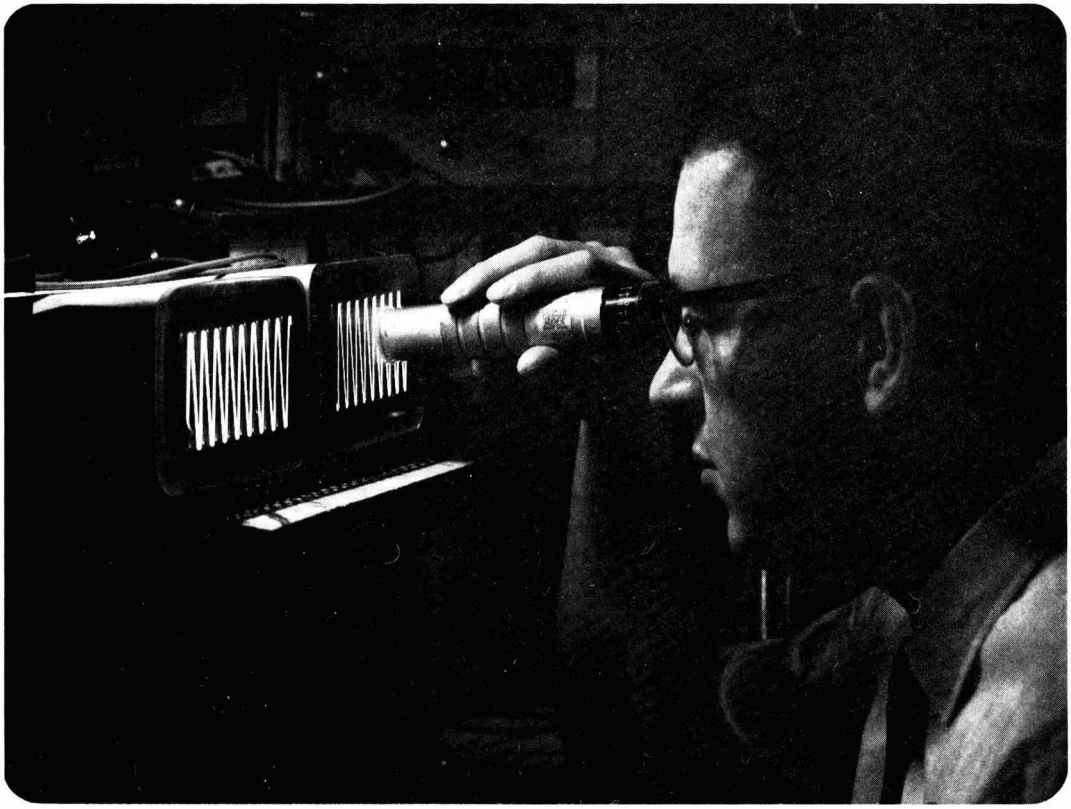

display devices for tomorrow ...

opportunities for Physical Scientists at Tektronix® today

If you have practical experience in Materials and Processes Development, Manufacturing Engineering, Cathode-Ray Tube Design; or if your education is in the disciplines of Physical Chemistry, Chemical Engineering, Physics or Metallurgy, Tektronix is interested in talking with you. Our commitment to progress in waveform measurement has produced significant contributions toward advancing the state-of-the-art in high-performance, storage and special-purpose oscilloscopes.

Tektronix provides an informal atmosphere, encouraging a free exchange of ideas between engineers and scientists of the many disciplines required for electronic instrument development.

While helping advance the state-of-the-measurement art, Tektronix engineers and scientists share in the financial success of the company through a merit-oriented salary plan and a substantial profit-sharing program. For the family, the Portland area offers excellent educational, cultural and recreational facilities. Abundant fishing, hunting and skiing are available nearby, with either the Cascade Mountains or the rugged Oregon beaches only 90 minutes away.

Please send the coupon or your resume to Professional Placement Manager, Tektronix, Inc., P. O. Box 500A, Beaverton, Oregon 97005. If you prefer, please call us at (503) 644-0161, Ext. 7346.

Tektronix, Inc.

Professional Placement Mgr., Tektronix, Inc.
P. O. Box 500A, Beaverton, Oregon 97005

☐ My resume is enclosed. Please send an application.

☐ Please send your booklet, "Tektronix."

NAME: _____

ADDRESS: _____

CITY: _____ STATE: _____ ZIP: _____

An equal opportunity employer

JOURNAL OF THE

MAY 1968

ELECTROCHEMICAL SCIENCE

TECHNICAL PAPERS

BRIEF COMMUNICATIONS

ELECTROCHEMICAL SOCIETY

Vol. 115 • No. 5

Manuscripts submitted to the Journal should be sent, in triplicate, to the Editorial Office at 30 East 42 St., New York, N. Y., 10017. They should conform to the revised Instructions to Authors available from Society Headquarters. Manuscripts so submitted, as well as papers presented before a National technical meeting, become the property of the Society and may not be published elsewhere in whole or in part without written permission of the Society. Address such requests to the Society Director of Publications.

The Electrochemical Society does not maintain a supply of reprints of papers appearing in its Journal. A photoprint copy of any particular paper, however, may be obtained by corresponding direct with the Engineering Societies Library, 345 E. 47 St., New York, N. Y., 10017.

Inquiries re positive microfilm copies of volumes should be addressed to University Microfilms, Inc., 300 N. Zeeb St., Ann Arbor, Mich.

Walter J. Johnson, Inc., 111 Fifth Ave., New York, N. Y., 10003, have reprint rights to out-of-print volumes of the Journal, and also have available for sale back volumes and single issues, with the exception of the current calendar year. Anyone interested in securing back copies should correspond direct with them.

Published monthly by The Electrochemical Society, Inc., at 215 Canal St., Manchester, N. H.; Executive Offices, Editorial Office and Circulation Dept., and Advertising Office at 30 East 42 St., New York, N. Y., 10017, combining the JOURNAL and TRANSACTIONS OF THE ELECTROCHEMICAL SOCIETY. Statements and opinions given in articles and papers in the JOURNAL OF THE ELECTROCHEMICAL SOCIETY are those of the contributors, and The Electrochemical Society assumes no responsibility for them.

Claims for missing numbers will not be allowed if received more than 60 days from date of mailing plus time normally required for postal delivery of JOURNAL and claim. No claims allowed because of failure to notify the Circulation Dept., The Electrochemical Society, 30 East 42 St., New York, N. Y., 10017, of a change of address, or because copy is "missing from files." Subscription to members as part of membership service; subscription to nonmembers $24.00 plus $1.50 for postage outside U.S. and Canada Single copies $1.70 to members, $2.25 to nonmembers.

Entered as second-class matter at the Post Office at Manchester N. H., under the act of August 24, 1912. Postage paid at Manchester, N. H.

An important message from your Board of Directors

Change in Publication Policy and Membership Dues Structure Beginning in 1969

The purpose for which the Society has been formed is the advancement of the theory and practice of electrochemistry, electrometallurgy, electrothermics, electronics, and allied subjects. Among the means to this end shall be the holding of meetings for the presentation and discussion of professional and scientific papers on these subjects, the publication of papers, discussions, and communications on these subjects, and cooperation with chemical, electrical and other scientific and technical societies.

The effectiveness of these functions is dependent on the resources provided not only by its members but by such nonmember sources as subscriptions and advertising.

The charts in Fig. 1 indicate the distribution of income and expense for 1967. These show that income from sources other than dues is over 71% of the total.

For many years all papers were published in the JOURNAL OF THE ELECTROCHEMICAL SOCIETY. In 1963 a second publication, ELECTROCHEMICAL TECHNOLOGY, was introduced to provide a medium for papers covering electroprocesses in the areas of engineering, technology, design, economics, and reviews.

This publication filled the need and has been subscribed to by over 25% of our members and a larger segment of the nonmember subscribers.

Figure 1.

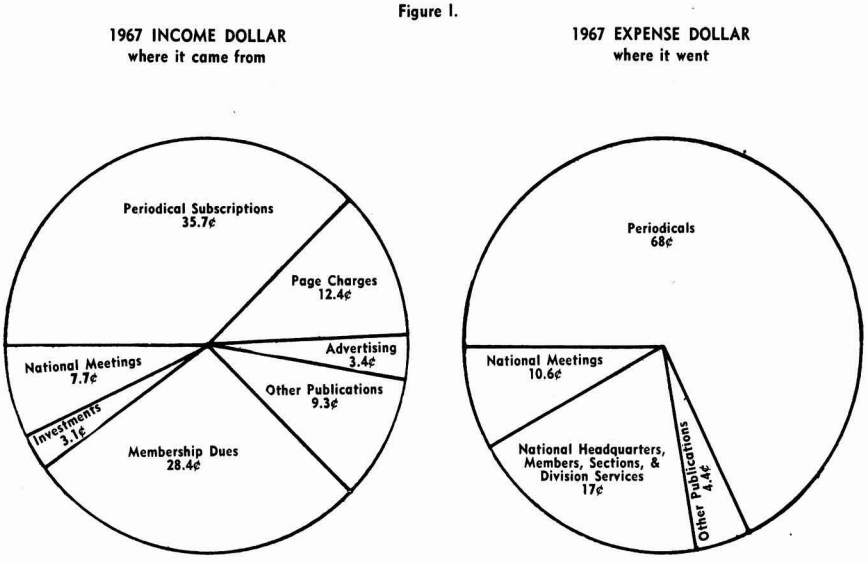

Each member receives a copy of the JOURNAL, and ELECTROCHEMICAL TECHNOLOGY is available at special membership rates. In addition, nonmembers subscribe to both publications.

For more than a year, all aspects of the Society's periodical program have been examined by our Publication and Finance Committees. In addition, an Ad Hoc Committee on Publication Plans conducted a questionnaire survey among our members and nonmember subscribers.

In the January 1968 issue of the JOURNAL OF THE ELECTROCHEMICAL SOCIETY there appeared the report of the Ad Hoc Committee.

The publication study indicated the desire of interdisciplinary flavor in a single publication. Further review of the effectiveness of the publications, reader interest and financial situation revealed the need for some changes.

In addition, because of rising costs and predicted future increases by all vendors, including U.S. Post Office, the Society is faced with an unbalanced budget regardless of future publication plans.

Combining both periodicals into one publication without sacrificing quality of printing and number of papers would result in the broadest technical program with the least economic adjustment.

The Board of Directors considered all of the reports and recommendations and has taken positive actions resulting in significant changes to take effect January 1969.

(1) A single monthly publication, JOURNAL OF THE ELECTROCHEMICAL SOCIETY, with separate sections consisting of:

ELECTROCHEMICAL SCIENCE
SOLID STATE SCIENCE
ELECTROCHEMICAL TECHNOLOGY
ELECTROCHEMICAL SOCIETY NEWS AND REVIEWS

will be published.

Each member will receive the enlarged monthly publication as part of his membership benefits.

(2) Active and Associate membership dues will be increased $5.00 per year.

(3) Nonmember subscription for the enlarged JOURNAL will be $40.00 per year, plus postage for foreign subscribers.

The Board of Directors has given the most careful consideration to the decision to change the publication program and increase dues. The course of action embarked upon will provide, we are firmly convinced, a sound fiscal basis for growth of the Society and will enable it to fulfill its publication obligations to the membership and subscribers. It is the hope of the Board that the members will feel that it has acted responsibly in their behalf.

JOURNAL OF THE ELECTROCHEMICAL SOCIETY

ELECTROCHEMICAL SCIENCE

MAY 1968

Journal of The Electrochemical Society is the fundamental research journal serving the interdisciplinary interests of chemistry, physics, electronics, biology, medicine, and engineering as they pertain to electrochemistry and to electrochemical phenomena. Written for the research scientist in industry, government, the independent laboratory and the university, it publishes contributed Technical Papers, Technical Notes and Brief Communications describing current basic research of original character, and is edited in two sections: 1) ***Electrochemical Science*** including such areas as batteries, fuel cells, corrosion and corrosion mechanisms, electrothermics and metallurgy, electrodeposition, electroorganic reactions and phenomena, and allied work of theoretical electrochemical nature. 2) ***Solid State Science*** including such areas as dielectrics and insulation, electrothermics and metallurgy, semiconductors, luminescence and related solid state investigations.

The Anodic Behavior of Zinc in KOH Solutions

T. P. Dirkse,* David De Wit, and R. Shoemaker

Calvin College, Grand Rapids, Michigan

ABSTRACT

The anodic behavior of zinc in strongly alkaline solutions was studied making special note of the limiting current density and of the overvoltage for the zinc/zincate reaction. The effect of temperature, KOH concentration, presence of zincate, and amalgamation on these values was measured. Under the conditions studied, zincate ion diffusion away from the electrode controls the limiting current density. The overvoltage at amalgamated electrodes is that for the charge transfer reaction, while at nonamalgamated electrodes it is due to adatom diffusion.

In developing and designing alkaline batteries using zinc anodes, there are several modifications that can be made to improve the performance of the system. One such modification is the amalgamation of the zinc electrode. This is done in practically all zinc-alkaline batteries. The purpose is to raise the hydrogen overvoltage and thus reduce the corrosion or open-circuit reaction. This amalgamation, however, may also affect the other zinc electrode processes.

A review of the published literature revealed that few factual data are available to show what effect electrolyte concentration, amalgamation, zincate concentration, and temperature have on the anodic processes of the zinc/zincate electrode. For this reason a program of work was undertaken to obtain such information, and the results are reported here.

It is generally agreed that the anodic zinc processes in an alkaline solution consist of at least: (*a*) the formation of the charge transfer product, probably zinc hydroxide; (*b*) the dissolution of this product in the electrolyte; and (*c*) the formation finally of a passivating layer, either by precipitation from the electrolyte or because of inability of the electrolyte to dissolve the charge transfer product as fast as it is formed. While this model serves to account satisfactorily and qualitatively for most observations made on the zinc electrode, still there is little agreement as to the details of these various steps. Furthermore, it has been difficult to get sufficient experimental information to describe some of these processes in detail.

Experimental

Two methods were used to study the zinc electrode processes.

Interrupter.—An interrupted d.c. was used to study the overvoltage of the zinc electrode processes. The circuit has been described (1). A standard resistor was placed in the circuit, and the voltage drop across this was measured on an oscilloscope to determine the current rate. All traces on the oscilloscope were photographed, and in calculating the overvoltage, correction was made for the internal IR drop. The cell, Fig. 1, held about 20 ml of electrolyte. The working zinc electrode area was the cross-sectional area of a 0.063-in. diameter zinc wire encased in a Teflon tube. This was polished smooth on an emery cloth (3/0) before use in the cell. The reference electrode was a 1-in. length of similar wire which had previously been amalgamated. It was held in a polyethylene tube. The auxiliary electrode was a circular zinc sheet, about 0.75 in. diameter, embedded in the bottom of the Plexiglas cell case. In making a series of measurements the current was first increased in several steps then decreased, and finally increased again. In the anodic direction measurements were discontinued when the electrode became passive or a limiting current density was reached.

* Electrochemical Society Life Member.

Sine wave.—In the second approach to the study of the zinc electrode reactions, the method of Kordesch and Marko (2) was used. A zinc wire served as the reference electrode in some instances, while in others a HgO/Hg reference was used. The latter was connected to the cell by a capillary and contained the same KOH concentration as the cell. The cell case was 8.8 x 5.4 x 2.3 cm. The counter electrodes were two commercial zinc electrodes, 4 x 5 cm, and these were encased in fibrous sausage casing separator. The working electrode, amalgamated where required by dipping it for 30 sec in a solution containing 50 g/l of $HgCl_2$, was inserted between these electrodes. The current was increased manually at prescribed time intervals and the polarization (IR free) of the working zinc electrode was measured. A typical anodic curve is shown on Fig. 2.

Results

In making measurements on the anodic processes, two values were used for comparisons: (*a*) the limiting current density (*a* in Fig. 2); and (*b*) the overvoltage associated with the formation of zincate. For convenience this latter was taken as the overvoltage at a current density of 50 ma/in^2 (*b* in Fig. 2). These values were all obtained by use of the sine wave pulse tester method.

Four variables were considered: (*i*) KOH concentration; (*ii*) zincate concentration; (*iii*) effect of amalgamation; and (*iv*) temperature. A summary of the results at room temperature is given on Fig. 3 and 4.

Limiting current density.—The limiting current density (lcd), Fig. 3, shows a general tendency to decrease markedly with increasing KOH concentration in the range of 30-45%. Below 30% KOH the lcd varies somewhat erratically with KOH concentration. For KOH solutions saturated with ZnO there is no apparent effect of KOH concentration on lcd in solutions of 20-30% KOH. Furthermore, the presence of appre-

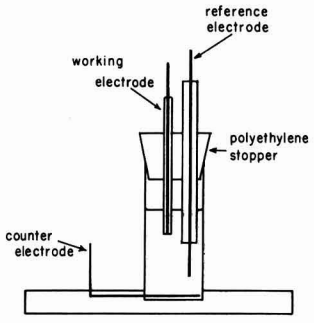

Fig. 1. Cell case used for studying anodic zinc electrode processes.

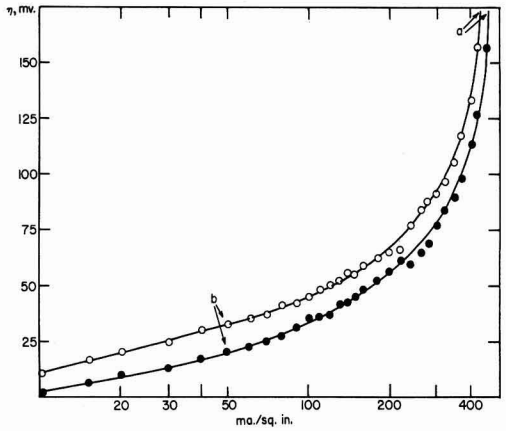

Fig. 2. Anodic overvoltage current curve for a zinc electrode in 35% KOH saturated with ZnO. Open circles, zinc; closed circles, amalgamated zinc.

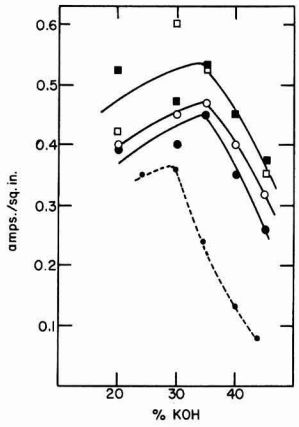

Fig. 3. Limiting anodic current density for zinc electrodes at room temperature. Circles, zinc; squares, amalgamated zinc; open symbols, KOH solutions; closed symbols, KOH saturated with ZnO; dashed line, diffusion coefficients (relative scale) for zincate ions, from ref. (7).

ciable amounts of zincate in the solution results in a slightly lower lcd for plain zinc electrodes but has no significant effect on the lcd of amalgamated zinc electrodes.

Zincate overvoltage.—The overvoltage for the zincate reaction, Fig. 4, shows irregularities with KOH concentration. But in all cases it is lower at the amalgamated electrodes. This is true in the presence as well as in the absence of zincate ions. The overvoltages in KOH solutions containing no zincate originally (open symbols, Fig. 4) are subject to some uncertainty because of the uncertainty in the open circuit voltage in plain KOH solutions. Since no zincate is present, it is possible that no equilibrium potential for the zinc/zincate reaction is obtained. However, a fairly constant potential was obtained at the beginning of each run, and this value was within the experimental uncertainty of that which was obtained by extrapolation of the potentials obtained in solutions containing varying amounts of zincate.

Temperature effect.—These anodic processes were also studied over the temperature range of 0-50°C. The lcd did increase with temperature for both types of

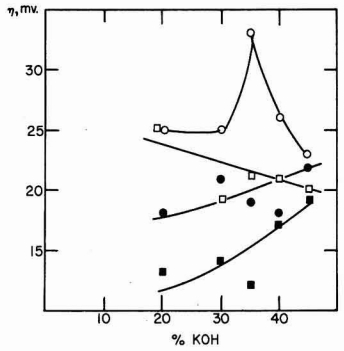

Fig. 4. Overvoltage for zincate formation at zinc electrodes in KOH solutions. Symbols same as for Fig. 3.

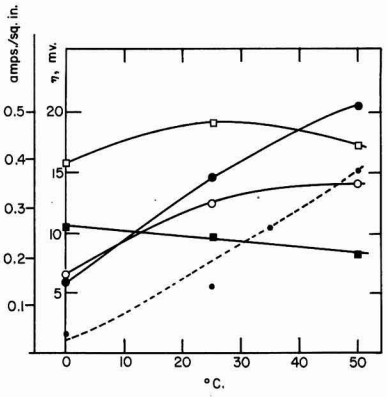

Fig. 5. Variation of lcd and overvoltage at a zinc/zincate electrode with temperature. Circles, lcd; squares, overvoltage; open symbols, zinc; closed symbols, amalgamated zinc. All solutions were 40% KOH + 0.5M ZnO. Dashed line, diffusion coefficients (relative scale) for zincate ion, from ref. (7).

electrodes but the difference between amalgamated and nonamalgamated zinc became less as the temperature was lowered, Fig. 5. The effect of temperature on the overvoltage of the zinc/zincate reaction is very slight.

Discussion

The results obtained in this study for nonamalgamated electrodes can readily be accounted for and explained in terms of the generally accepted outline of the mechanism for the anodic zinc reactions as outlined in the introductory paragraphs. However, the effects of amalgamation on the zinc electrode performance cannot be so readily explained in terms of this scheme. The effects are two:

1. Amalgamation raises the lcd, except at temperatures near 0°C.
2. Amalgamation lowers the overvoltage for the zinc/zincate reaction.

The extensive work of Hampson *et al.* (5) suggests a possible explanation for these phenomena. This explanation assumes that the oxidation of nonamalgamated zinc begins with the movement of zinc atoms from the kink sites (lattice dissolution points, *e.g.*, screw dislocations) to become mobile surface atoms with a low coordination number (adatoms).

$$Zn_{kink} \rightarrow Zn_{ad} \qquad [1]$$

These adatoms readily adsorb OH^- ions and this may stabilize them.

$$Zn_{ad} + 2\,OH^- \rightarrow Zn(OH)_{2\,ad}{}^{=} \qquad [2]$$

Metallic zinc electrodes have a high double layer capacity (5a). This results from the charge transfer reaction, Eq. [3], which may proceed in two one-electron stages.

$$Zn(OH)_{2\ ad}^{=} \rightarrow Zn(OH)_{2\ ads} + 2e \qquad [3]$$

i_o for reaction [3] is of the order of 200 ma/cm^2 (5b).

Reaction [3], which is in agreement with the work of Gerischer (6), is followed by

$$Zn(OH)_{2\ ad} \rightarrow Zn(OH)_{2\ diss} \qquad [4]$$

and

$$Zn(OH)_{2\ diss} + 2\ OH^- \rightarrow Zn(OH)_4^{=} \qquad [5]$$

As the zincate concentration increases, a further reaction occurs (3).

$$Zn(OH)_4^{=} \rightarrow ZnO + 2\ OH^- + H_2O \qquad [6]$$

The rate-controlling processes may be [1], [4], or [5]. Reaction [3] is likely not rate controlling because of the high value for i_o. Reaction [2] probably is also a fast reaction.

The anodic oxidation of amalgamated zinc electrodes proceeds by a somewhat different mechanism because the surface is different. Amalgamation "smooths out" the surface or makes it approach a liquid. Consequently atoms can dissolve at any point on the surface. There are no kink sites and no adatoms. Furthermore, there is no evidence for OH^- adsorption at a zinc amalgam electrode, in contrast to a nonamalgamated electrode (5d). Therefore the first step likely is

$$Zn(Hg) + 2\ OH^- \rightarrow Zn(OH)_2 + 2e \qquad [7]$$

The $Zn(OH)_2$ is not necessarily adsorbed and goes into solution

$$Zn(OH)_2 \rightarrow Zn(OH)_{2\ diss} \qquad [8]$$

This is then followed by reactions [5] and [6].

The fact that the variation of lcd with KOH concentration, Fig. 3, is the same for both types of electrodes suggests that the same process is rate-limiting in each case. This could be reaction [4] or [8]. Reaction [5] is a fast reaction and reaction [6] is too slow to take any part in the results we obtained.

Reactions [4] and [8] are step (*b*) in the anodic process outlined in the introductory paragraphs. The rate of dissolution of the charge transfer product is an important factor especially because of the apparent high solubility of this substance and the slow decomposition of the resulting solute species (3). It is reasonable to expect that this rate of dissolution will decrease with decreasing temperature. This qualitatively accounts for the temperature effect on the lcd. Unfortunately, no quantitative data are available to evaluate this suggestion.

However, the rate of dissolution of the charge transfer product will also depend on the zincate concentration in the layer of electrolyte in contact with the electrode surface. In order for the charge transfer product to continue to dissolve, it is necessary that the zincate ions diffuse away from the electrode. The diffusion of zincate ions from the electrode thus controls the lcd because it affects the rate of dissolution of the charge transfer product. The shape of the curves on Fig. 2 does suggest such a diffusion controlled process.

The diffusion currents and the diffusion coefficients for zincate ions have been measured by a polarographic method over a range of temperatures and KOH concentrations (7). These values for the diffusion coefficients at 25°C are included on Fig. 3 and 5.

There is a marked similarity between the variation of lcd and of diffusion coefficient with KOH concentration at the higher concentrations. There is likewise a similarity between these values as a function of temperature, Fig. 5. Thus it is reasonable to conclude that the lcd's observed in our work can be explained by the diffusion control of the zincate ion (4). In our work, convection as well as diffusion undoubtedly played a role and so the processes cannot be expected to be strictly or only diffusion controlled.

It was noted also that the lcd was higher at the amalgamated electrodes. This is likely a surface area effect. Amalgamation produces more reaction sites on the surface. This larger available area serves to reduce the actual current density at which the electrode is being oxidized. The current densities used in Fig. 2, for example, are calculated on the basis of the gross geometrical area. A lower current density would give rise to a lower overvoltage, Fig. 2. In either event, the result would be to give a higher lcd at the amalgamated electrodes.

It may be argued that if the above explanation is correct, then the presence of zincate ions in the solution should result in a lower lcd. A solution already containing zincate ions can dissolve fewer additional zincate ions (from the electrode reaction) than can a solution which originally contained no zincate ions. There is some evidence for this at the plain zinc electrodes, Fig. 3. The fact that this effect is so slight is explained by the high solubility of the charge transfer product. This substance gives zincate concentrations considerably higher than those obtained by saturating aqueous KOH with ZnO (3).

The difference in overvoltage for the zinc/zincate reaction at the two types of electrodes can be explained by the difference in the mechanism of the reaction at the two electrodes. The overvoltage, or energy barrier, for nonamalgamated zinc electrodes is associated with reaction [1] while for amalgamated electrodes it is associated with reaction [7], the charge transfer reaction.

Acknowledgment

This work was sponsored and supported by the U.S. Air Force Aero Propulsion Laboratories. The authors also wish to thank Dr. N. A. Hampson for his many helpful discussions and suggestions.

Manuscript received Aug. 9, 1967; revised manuscript received Nov. 13, 1967. This paper was presented at the Chicago Meeting, Oct. 15-19, 1967, as Abstract 27.

Any discussion of this paper will appear in a Discussion Section to be published in the December 1968 JOURNAL.

REFERENCES

1. T. P. Dirkse and G. Werkema, *This Journal*, **106**, 88 (1959).
2. K. Kordesch and A. Marko, *ibid.*, **107**, 480 (1960).
3. T. P. Dirkse, *ibid.*, **102**, 497 (1955).
4. R. Landsberg, H. Furtig, and L. Muller, *Wiss. Z. Techn. Hochschule fur Chemie Leuna-Merseburg*, **2**, 453 (1959/60).
5. (*a*) J. P. G. Farr and N. A. Hampson, *Trans. Faraday Soc.*, **62**, 3493 (1966); (b) J. P. G. Farr and N. A. Hampson, *J. Electroanalytical Chem.*, **13**, 433 1967); (*c*) J. P. G. Farr, N. A. Hampson, and M. E. Williamson, *ibid.*, **13**, 462 (1967); (*d*) N. A. Hampson, Ph.D. Thesis, University of London, 1966.
6. H. Gerischer, *Z. physik. Chem.*, **202**, 302 (1953).
7. J. McBreen, "Study to Improve the Zinc Electrode for Spacecraft Electrochemical Cells," 2nd Quarterly Report on Contract NAS 5-10231, June 1967, Yardney Electric Corp, New York, N.Y.

Solubility and Complex Formation of AgCl in Propylene Carbonate-Water Mixtures

James N. Butler,* David R. Cogley,** and Walter Zurosky

Corporate Research Division, Tyco Laboratories, Inc. Waltham, Massachusetts

ABSTRACT

The solubility and complex formation equilibria of silver chloride in propylene carbonate-water mixtures (0.004 to 3.57M H_2O) have been studied potentiometrically in a constant ionic medium of 0.1M tetraethylammonium perchlorate, at 25°C. The complexes are predominately mononuclear, and the principal species in solution is $AgCl_2^-$. The over-all complex formation constants $\beta_n (n = 1,2,3)$ decrease and the solubility product K_{so} increases with increasing water concentration. Approximate empirical expressions describing these changes are: $\log K_{so} = -20.0 + 3.25 \sqrt{C_{H_2O}}$ and $\log \beta_2 = +21.2 - 4.87 \sqrt{C_{H_2O}}$. The intrinsic solubility of AgCl (K_{s1}) is $10^{-4.7}$, essentially independent of the water content of the solvent.

Although the dielectric constant of propylene carbonate [$\epsilon = 64.4$ (1)] is nearly as large as that of water ($\epsilon = 78.54$), the solubility and complex formation equilibria of silver chloride are vastly different in the two solvents. Our studies (2) have established that mononuclear complexes predominate in solutions containing excess chloride and have provided accurate values of the equilibrium constants in anhydrous propylene carbonate. These constants are summarized in Table I and are compared with the corresponding constants for aqueous solutions (3, 4). Although the solubility product (K_{so}) is more than ten orders of magnitude smaller in propylene carbonate than in water, the complex $AgCl_2^-$ is so stable that the solubility equilibrium of AgCl in excess chloride, represented by the reaction

$$AgCl(s) + Cl^- \rightleftharpoons AgCl_2^-$$

(equilibrium constant K_{s2}) is six orders of magnitude greater in propylene carbonate.

These dramatic differences in equilibrium constants reflect large differences in solvation of ions in the two solvents, and their detailed variation is of interest in the general context of solvation theory. In addition, the current interest in silver chloride both as a reference electrode and as a battery cathode material in aprotic electrolytes (5-9), has prompted us to study these equilibria in mixtures of propylene carbonate with water.

Experimental

Propylene carbonate was obtained from Matheson, Coleman, and Bell, and purified by distillation, as described in detail elsewhere (10). Gas chromatographic analysis indicated that the purified solvent contained less than 10 ppm organic impurities and water. Silver perchlorate (Chemical Procurement), tetraethyl ammonium chloride (Eastman), and tetraethyl ammonium perchlorate (Eastman) were dried over anhydrous $CaSO_4$ in a dessicator before solutions were prepared. Solutions were analyzed (± 0.1%) for chloride ion by potentiometric titration with aqueous silver nitrate, and for silver ion (± 0.2%) by potentiometric titration with the propylene carbonate-chloride solutions of known concentration. Mixtures of propylene carbonate with triple-distilled water were prepared by weight, and their density measured with a pycnometer. The density values (Table II) were used in converting to molar concentrations.

The cell consisted of two electrode compartments connected by a salt bridge with coarse glass frits at each end. One of the electrode compartments contained a Teflon-coated magnetic stirrer, and the entire cell was jacketed and maintained at 25.0° ± 0.1°C by means of a Haake circulating thermostat. Solution preparation, storage, and all experiments were carried out in a dry nitrogen atmosphere in a glovebox. Etched silver wires were used for electrodes in both compartments, and a uniform ionic strength of 0.100M was maintained in all three compartments with Et_4NClO_4. The reference compartment contained either Ag^+ at approximately 0.004M concentration or Cl^- saturated with AgCl at the same concentration. The compartment with the stirrer contained various concentrations of Ag^+ and Cl^- which were added from 2 ml RGI micrometer burettes containing 0.1M $AgClO_4$ or 0.1M Et_4NCl in the same solvent mixture as was used for the supporting electrolyte. Potentials were measured with a Fluke high-impedance differential voltmeter, and were usually steady to within 0.1 mv.

Results

The results of nine experiments in different solvent mixtures are summarized in Table III. The values given in the table were selected to give a representative shape of both the saturated and unsaturated portions of the titration curve. Sufficient data have been given to permit future workers to make different statistical curve-fitting calculations, but when measurements were so closely spaced that they provided no additional information, the extra points were elim-

Table I. Solubility and complex formation equilibria for AgCl in water and propylene carbonate (0.1M ionic strength, 25°C)

Solvent	Water (3, 4)	Propylene carbonate (2)
Dielectric constant	78.54	64.4 (1),
$\log K_{so}$ ($AgCl(s) \rightleftharpoons Ag^+ + Cl^-$)	−9.42	−19.86 ± 0.02
$\log \beta_1$ ($Ag^+ + Cl^- \rightleftharpoons AgCl$ (soln))	+2.85	+15.15 ± 0.15
$\log \beta_2$ ($Ag^+ + 2\ Cl^- \rightleftharpoons AgCl_2^-$)	+4.72	+20.86 ± 0.02
$\log \beta_3$ ($Ag^+ + 3\ Cl^- \rightleftharpoons AgCl_3^=$)	+5.04	+23.39 ± 0.06
$\log K_{s2}$ ($AgCl(s) + Cl^- \rightleftharpoons AgCl_2^-$)	−4.70	+1.00 ± 0.03

Table II. Density of propylene carbonate-water mixtures at 25°C

Weight % H_2O	C_{H_2O}, mole/liter	Density, g/ml
0	0	1.206
1.27	0.845	1.199
3.17	2.09	1.192
5.43	3.57	1.187

* Electrochemical Society Active Member.
** Electrochemical Society Associate Member.

Table III. Titration data[a]

Experiment No. 1

$E^0 = 0.1428$, $C_{H_2O} = 0.004M$

C_{Ag}	C_{Cl}	E
0.371	7.511	−1.0468
0.379	5.773	−1.0336
0.388	3.953	−1.0125
0.394	2.819	−0.9877
0.398	2.044	−0.9604
0.399	1.651	−0.9378
0.401	1.254	−0.9033
0.403	1.014	−0.8641
0.403	0.854	−0.7926
(0.404)	(0.834)	(−0.7708)[b]
0.404	0.773	−0.7650
0.404	0.692	−0.7553
0.405	0.611	−0.7437
0.405	0.530	−0.7201
0.405	0.490	−0.6972
0.405	0.457	−0.6803
0.405	0.453	−0.6516

Experiment No. 2

$E^0 = 0.1359$, $C_{H_2O} = 0.0094M$

C_{Ag}	C_{Cl}	E
0.345	6.873	−1.0394
0.352	5.268	−1.0222
0.359	3.595	−0.9944
0.364	2.555	−0.9691
0.367	1.847	−0.9408
0.369	1.488	−0.9169
0.371	1.126	−0.8776
0.372	0.834	−0.7944
(0.372)	(0.814)	(−0.7780)[b]
0.372	0.760	−0.7753
0.373	0.687	−0.7680
0.373	0.613	−0.7590
0.373	0.577	−0.7520
0.373	0.503	−0.7820
0.374	0.466	−0.7175
0.374	0.429	−0.6976
0.374	0.403	−0.6352
0.374	0.399	−0.6159
0.374	0.395	−0.6134

Experiment No. 3

$E^0 = 0.1351$, $C_{H_2O} = 0.0147M$

C_{Ag}	C_{Cl}	E
0.370	5.746	−1.0195
0.379	3.924	−0.9729
0.384	2.790	−0.9466
0.388	2.015	−0.9178
0.390	1.622	−0.8932
0.392	1.225	−0.8535
0.393	0.985	−0.8055
(0.393)	(0.912)	(−0.7800)[b]
0.393	0.904	−0.7797
0.394	0.824	−0.7737
0.394	0.743	−0.7695
0.395	0.663	−0.7653
0.395	0.582	−0.7510
0.395	0.500	−0.7309
0.396	0.460	−0.7246

Experiment No. 4

$E^0 = 0.1333$, $C_{H_2O} = 0.0308M$

C_{Ag}	C_{Cl}	E
0.356	7.504	−1.0406
0.364	5.765	−1.0225
0.372	3.943	−0.9957
0.378	2.808	−0.9702
0.381	2.033	−0.9421
0.383	1.640	−0.9198
0.385	1.243	−0.8810
0.386	1.003	−0.8311
0.387	0.922	−0.7909
(0.387)	(0.912)	(−0.7782)[b]
0.387	0.842	−0.7766
0.387	0.802	−0.7758
0.387	0.761	−0.7734
0.388	0.721	−0.7706
0.388	0.680	−0.7659
0.388	0.640	−0.7610
0.388	0.599	−0.7559
0.388	0.559	−0.7481
0.389	0.518	−0.7397
0.389	0.478	−0.7248
0.389	0.449	−0.7083
0.389	0.445	−0.7033
0.389	0.441	−0.6985
0.389	0.437	−0.6919

Experiment No. 5

$E^0 = 1.066$, $C_{H_2O} = 0.25M$

C_{Ag}	C_{Cl}	E
3.17	47.45	−0.0365
4.66	46.73	−0.0161
6.28	45.95	+0.0011
9.17	44.56	+0.0322
11.04	43.66	+0.0532
12.73	42.84	+0.0742
15.49	41.52	+0.1127
(15.81)	(41.36)	(+0.1180)[b]
17.63	39.47	+0.1226

Experiment No. 5 (Continued)

$E^0 = 1.066$, $C_{H_2O} = 0.25M$

C_{Ag}	C_{Cl}	E
21.11	37.79	+0.1305
25.33	35.76	+0.1436
29.39	33.80	+0.1674
31.47	32.80	+0.2009
31.61	32.73	+0.2047
31.73	32.68	+0.2114
31.96	32.56	+0.2254
32.14	32.48	+0.2413
32.26	32.42	+0.2624

Experiment No. 6

$E^0 = 1.066$, $C_{H_2O} = 0.25M$

C_{Ag}	C_{Cl}	E
1.134	5.733	+0.0945
1.264	5.656	+0.1043
1.405	5.572	+0.1142
1.578	5.469	+0.1275
1.733	5.377	+0.1411
1.843	5.311	+0.1508
1.950	5.248	+0.1619
(2.025)	(5.203)	(+0.1702)[b]
2.181	5.110	+0.1740
2.243	5.073	+0.1742
2.391	4.985	+0.1763
2.742	4.776	+0.1828
3.179	4.516	+0.1959
3.449	4.355	+0.2036
3.495	4.327	+0.2063
3.554	4.293	+0.2103
3.697	4.207	+0.2204
3.794	4.149	+0.2307
3.856	4.113	+0.2400
3.908	4.082	+0.2500
3.960	4.051	+0.2692
3.998	4.028	+0.3030

Experiment No. 7

$E^0 = 0.940$, $C_{H_2O} = 0.845M$

C_{Ag}	C_{Cl}	E
1.43	47.28	−0.0427
2.42	46.57	−0.0277
3.45	45.84	−0.0147
5.53	44.37	+0.0074
6.68	43.55	+0.0170
7.82	42.75	+0.0272
9.02	41.90	+0.0381
(9.75)	(41.38)	(+0.0447)[b]
10.51	40.84	+0.0454
12.37	39.52	+0.0480
13.76	38.53	+0.0497
15.32	37.43	+0.0528
17.16	36.12	+0.0571
19.57	34.41	+0.0636
20.90	33.46	+0.0684
21.74	32.88	+0.0712
22.63	32.24	+0.0757
23.25	31.80	+0.0790
24.09	31.06	+0.0853
24.95	30.60	+0.0901
25.79	30.00	+0.0986
26.58	29.44	+0.1093

Experiment No. 8

$E^0 = 0.868$, $C_{H_2O} = 2.09M$

C_{Ag}	C_{Cl}	E
1.19	47.33	−0.0068
2.40	46.75	+0.0192
3.06	46.43	+0.0294
(4.27)	(45.86)	(+0.0448)[b]
6.34	44.88	+0.0454
7.12	44.50	+0.0463
21.01	37.89	+0.0659
27.91	34.60	+0.0913
30.95	33.15	+0.1196
31.26	33.00	+0.1254
31.66	32.81	+0.1366
31.91	32.69	+0.1483
32.28	32.51	+0.1759

Experiment No. 9

$E^0 = 0.768$, $C_{H_2O} = 3.57M$

C_{Ag}	C_{Cl}	E
0.496	48.21	+0.0274
0.643	48.14	+0.0306
(0.864)	(48.03)	(+0.0335)[b]
1.76	47.59	+0.0334
4.74	46.14	+0.0363
6.86	45.11	+0.0380
9.26	43.95	+0.0413
10.99	43.11	+0.0435
12.35	42.44	+0.0454
16.50	40.30	+0.0523
17.96	39.71	+0.0550
19.34	39.04	+0.0577
24.03	36.76	+0.0695
26.66	35.48	+0.0793
29.04	34.33	+0.0936
30.67	33.53	+0.1095
31.94	32.92	+0.1371
32.30	32.74	+0.1579

[a] C_{Ag}, C_{Cl} in millimoles/liter, E in volts. All data at 25°C in 0.1M Et_4NClO_4.

[b] Interpolated saturation point; data preceding are for unsaturated, data following are for saturated solutions.

inated from the table. The total concentrations of silver and chloride (C_{Ag} and C_{Cl}) were calculated from the known volumes and concentrations of the titrating solutions. The potential E is the value measured after equilibrium had been reached and may be converted to the concentration of free silver ion by means of the equation

$$E = E^0 + \frac{RT}{F} \ln [Ag^+] \qquad [1]$$

using the value of E^0 listed with each experiment. We have previously shown that the Nernst equation holds for silver ion in Et_4NClO_4 supporting electrolyte in anhydrous propylene carbonate (2). This was verified to within 0.5 mv in propylene-carbonate water mixtures as well.

As the concentration of water increases, the saturation point of the titration curve shifts to lower C_{Ag}/C_{Cl} ratios, making it difficult to evaluate the equilibrium constants accurately in unsaturated solutions of high water content. Nevertheless, an attempt was made to evaluate the equilibrium constants for all solvent mixtures both in unsaturated and saturated solutions, using the methods described previously (2).

In unsaturated solutions, the equilibrium species were assumed to be Ag^+, Cl^-, AgCl, $AgCl_2^-$, and $AgCl_3^=$, on the basis of our experiments in anhydrous propylene carbonate (2), and Leden's experiments in aqueous solutions (3, 4). The mass balances and equilibria may be combined to give the two equations

$$C_{Ag} = [Ag^+] \sum_{n=0}^{3} \beta_n [Cl^-]^n \qquad [2]$$

$$C_{Cl} = [Cl^-] + [Ag^+] \sum_{n=1}^{3} n\beta_n [Cl^-]^n \qquad [3]$$

which define the unsaturated portion of the titration curve. A nonlinear least-squares pit-mapping technique (2, 11) was used to fit the data to the theoretical curve. The values of the three constants β_1, β_2, and β_3 were adjusted to minimize the function

$$\left.\begin{aligned} U &= \sum_i (1 - Z'_i/Z_i)^2 \\ \text{where} \\ Z_i &= \frac{(C_{Cl})_i - [Cl^-]_i}{[Ag^+]_i} \\ \text{and} \\ Z'_i &= \sum_{n=1}^{3} n\beta_n [Cl^-]_i^n \end{aligned}\right\} \quad i = 1,2,3 \ldots \text{(points in set)} \qquad [4]$$

For each point Eq. [2] was solved by Newton's approximation method to obtain $[Cl^-]_i$ consistent with the assumed values of β_n. If the equilibrium expressions were exact and the data were exact, we should observe $Z_i = Z'_i$ for each point and hence $U = 0$. Because of experimental errors and theoretical approximations, U was finite, provided the number of points in the set exceeded the number of adjustable parameters. From the shape of the pit U (β_1, β_2, β_3), the standard deviations of the constants were calculated (2, 11).

The best values obtained for the constants, together with their standard deviations, are given in Table IV. Figure 1 shows the deviations of the experimental data from the theoretical equations, expressed as the ratio Z'/Z. The abscissa is the average number of chlo-

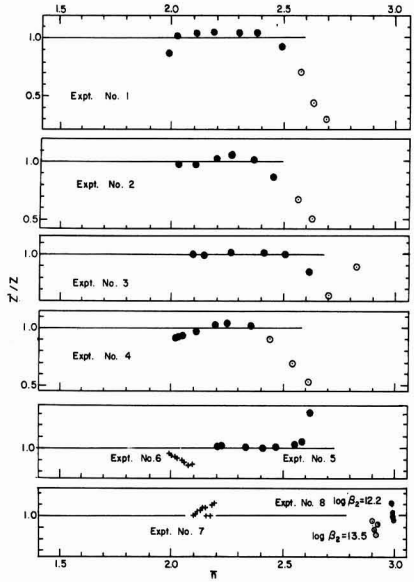

Fig. 1. Variation of experimental measurements from theoretical Eq. [2-4]. The detailed data are given in Table III and the constants used for the theoretical curves are given in Table IV.

rides bound to a silver ion, defined by the equation

$$\bar{n} = \frac{C_{Cl^-} - [Cl^-]}{C_{Ag}} \qquad [5]$$

i.e., $\bar{n} = 2$ corresponds to the predominance of $AgCl_2^-$ and $\bar{n} = 3$ to the predominance of $AgCl_3^=$. For a good fit, the values of Z'/Z should be normally distributed about unity. The constants were obtained with the set of crosses or solid points, the open points being discarded.

Systematic deviations from the theoretical equations were observed at high values of $\bar{n}$ (high C_{Cl}/C_{Ag} ratios). Similar deviations were observed previously (2) and were attributed to the failure of the constant ionic medium assumption. However, the deviations are smaller for experiment 5, even though the total concentrations are nearly ten times larger than in experiment 4. One possible explanation is that complexes of higher $\bar{n}$, possibly polynuclear, may exist in solutions of high chloride-to-silver ratio, but these are of less importance as the water content is increased.

The predominance of mononuclear complexes has been confirmed in experiments 5 and 6. The total concentrations in 5 were approximately ten times those in 6, and the combined sets of data were fitted with the same three constants. The values of Z'/Z agreed (Fig. 1) to within 10%, although a slightly different set of constants would have produced a better fit to experiment 6. The slight difference, which appears to be outside the precision of the individual experiments, may reflect small amounts of polynuclear complexes, but is small enough to be accounted for by systematic errors in the measurements.

The value of β_1 calculated from experiment 7 is uncertain, but is probably less than 10^{14}. Saturation of the solution at low C_{Ag}/C_{Cl} ratios made it difficult to cover a wide range of $\bar{n}$ without doing experiments in very dilute solutions; and since these would be subject to systematic errors from impurities in the solvent and supporting electrolyte, they were not attempted. The constants β_n calculated from experiments 8 and 9 are uncertain for the same reason. The best fit to experiment 3 was obtained with $\log \beta_2 = 12.2$, but an almost equally good fit was obtained with $\log \beta_2 = 13.5$ (see Fig. 1). Thus we have indicated in Table IV that $\log \beta_2$ is between 12 and 14. Since a large excess of chloride is present and $\bar{n}$ is nearly 3, $\log \beta_3$ is more certain. For this set of data β_1 could not be determined, but it is almost certainly less than β_2.

In experiment 9, the shape of the curve was not even close to the theoretical, and no amount of parameter adjustment (within reasonable values) could make Z'/Z close to unity for all three points. Therefore we assumed that $\bar{n} = 3$ and hence that the complex $AgCl_3^=$ predominates. This gave $\log \beta_3 = 14.2 \pm 0.5$, which we have listed in Table IV. β_2 and β_1 are probably less than 10^{12}, but more detailed studies of these solutions with high water concentrations are required before accurate estimates of the constants are possible.

From each point obtained in the saturated region, a value of the solubility product K_{so} can be obtained by solving the equation (2)

$$(C_{Cl} - C_{Ag} + [Ag^+])[Ag^+]^2 = K_{so}(1 + \beta_2 K_{so})[Ag^+] + 2\beta_3 K_{so}^3 \qquad [6]$$

using Newton's approximation method. These values are shown in Fig. 2 and 3. Systematic variations of $-\log K_{so}$ to smaller values as C_{Ag}/C_{Cl} increases are observed in all the experiments, but were greatest for the lowest and highest water content. Similar deviations were observed before (2) but no simple explanation is apparent. The values of the solubility product listed in Table IV were obtained from the region close to the saturation point.

Values of the constant K_{s2} were obtained by combining the experimental values of β_2 and K_{so} according to the relation

Table IV. Equilibrium constants for AgCl in propylene carbonate-water mixtures

Expt. No. (see Table III)	C_{H_2O} mole/liter	Log of equilibrium constant[a] β_1	β_2	β_3	K_{so}	K_{s2}[b]
1	0.004	15.0 ± 0.5	20.95 ± 0.04	23.65 ± 0.13	−19.90 ± 0.05	+1.05 ± 0.07
2	0.0094	14.5 ± 1.0	20.58 ± 0.03	23.07 ± 0.06	−19.72 ± 0.03	+0.86 ± 0.04
3	0.0147	<15	20.04 ± 0.05	23.0 ± 0.1	−19.46 ± 0.02	+0.58 ± 0.06
4	0.0308	13.3 ± 1.7	20.48 ± 0.03	22.89 ± 0.03	−19.64 ± 0.02	+0.84 ± 0.04
5	0.25	14.1 ± 0.3	18.51 ± 0.03	20.10 ± 0.06	−18.17 ± 0.04	+0.34 ± 0.05
6	0.25				−18.15 ± 0.01	+0.36 ± 0.03
7	0.845	<14	16.52 ± 0.02	17.28 ± 0.04	−16.91 ± 0.01	−0.39 ± 0.03
8	2.09	<12	12-14	16.0 ± 0.05	−15.36 ± 0.02	−1 ?
9	3.57	<12	<12	14.2 ± 0.5	−13.79 ± 0.02	<−2

[a] Errors are standard deviations except for β_2 and β_3 in 8 and 9, where the data sets were too small for statistical treatment.
[b] Calculated using the relation $K_{s2} = K_{so}\beta_2$.

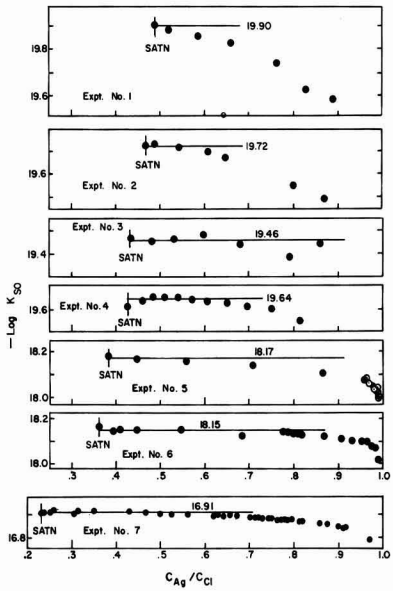

Fig. 2. Variation of experimental solubility product throughout the saturated region of the titration curve. Best values are listed in Table IV.

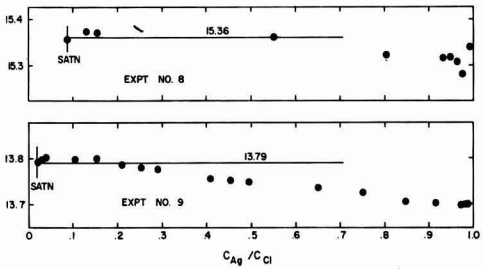

Fig. 3. Variation of experimental solubility product throughout the saturated region of the titration curve. Best values are listed in Table IV.

$$K_{s2} = \beta_2 K_{so}$$

and assuming that the variances were additive.

Discussion

The results of our experiments have shown a smooth variation in all the equilibrium constants as the concentration of water increases. The constants obtained in this study with the lowest water concentration are in agreement with those obtained previously (2); and for water contents below 10^{-2}M, the constants vary by an amount approximately equal to the experimental error.

Although no simple equilibrium or structural model predicts the form of the equations, a convenient empirical expression of the dependence on water concentration is a linear function of the square root of C_{H_2O}. A similar dependence has been observed for the standard potential of the Ag/AgCl electrode in ethanol-water mixtures (12). Approximate expressions for the constants obtained in this work are

$$\log \beta_1 = +15.3 - 3.25\sqrt{C_{H_2O}}$$
$$\log \beta_2 = 21.1 - 4.87\sqrt{C_{H_2O}}$$
$$\log \beta_3 = 23.75 - 7.55\sqrt{C_{H_2O}} \text{ for } C_{H_2O} < 0.5\text{M}$$
$$\log K_{so} = -20.0 + 3.25\sqrt{C_{H_2O}}$$
$$\log K_{s1} = -4.7$$
$$\log K_{s2} = +1.1 - 1.62\sqrt{C_{H_2O}}$$
$$\log K_{s3} = +3.75 - 4.3\sqrt{C_{H_2O}} \text{ for } C_{H_2O} < 0.5\text{M}$$

These equations give the experimental values of the constants within approximately ± 0.5 logarithmic units and are convenient for rough interpolation or extrapolation.

Figure 4 is a graphical representation of the results of this study, calculated using the above empirical expressions. Curves showing the solubility S of AgCl as a function of the concentration of added chloride C are drawn for solvents of various composition. In solutions of moderate chloride concentration (10^{-2} M), the solubility of AgCl decreases by about a factor of 20 as the solvent is changed from pure propylene carbonate to propylene carbonate containing 3M H_2O, and by an additional factor of 1000 as the solvent is changed to pure H_2O. It is curious coincidence, however, that the solubility of AgCl in the absence of added chloride (left of diagram) is almost exactly the same (2×10^{-5}M), independent of the composition of the solvent. This coincidence is all the more remarkable because in propylene carbonate the predominant species are undissociated AgCl molecules, and in water the predominant species are Ag^+ and Cl^- ions.

Although large changes are observed as the water concentration is increased from zero to the two-phase boundary (approximately 3.6M), the equilibrium constants for solubility and complex formation of silver chloride in this water-saturated propylene carbonate solution are still very different from those in pure water. Since the solutions on opposite sides of the miscibility gap are in equilibrium, this implies that similar dramatic changes in equilibrium constants would be found if small amounts of propylene carbonate were added to water.

A qualitative explanation of these large changes may be found in a discussion of the factors influencing the free energy of solvation of ions in the mixed solvents. The solubility product K_{so} reflects the free energy change for the reaction

$$AgCl(s) = Ag^+ + Cl^-$$

and is larger (less negative log K_{so}) the more strongly the ions are solvated. Thus a medium of higher dielectric constant, or stronger specific interactions be-

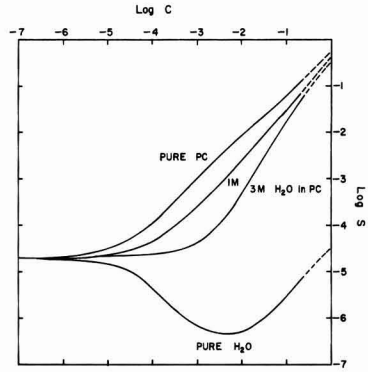

Fig. 4. Solubility (S) of silver chloride in propylene carbonate water mixtures containing excess chloride of concentration C. These curves were calculated using the equilibrium constants in Table IV.

tween the ions and solvent, would tend to increase K_{so}. As the medium is changed from propylene carbonate to water, the dielectric constant changes very little, but the hydrogen bonding of the solvent to chloride ions is very much less in propylene carbonate than in water. Thus we may attribute the changes in K_{so} which we observe largely to the differences in hydrogen bonding between chloride ion and solvent. Since propylene carbonate is probably a relatively weakly coordinating ligand, the free energy of solvation of the cation probably does not change very much as the composition of the solvent changes. Of course, the separation of the observed variation in K_{so} into contributions from solvation of cation or anion is a nonthermodynamic procedure, and we can discuss rigorously only the variation of the sum of the two free energies of solvation.

The other constant for which simple qualitative arguments may be clearly made is K_{s2}, which reflects the free energy change for the reaction

$$AgCl(s) + Cl^- = AgCl_2^-$$

Here we observe directly the difference in free energy of solvation for two anions. If there were no specific interactions with the solvent, we would expect K_{s2} to be somewhat greater than unity, simply because $AgCl_2^-$ is a larger ion than Cl^-. As the dielectric constant of the medium increases, we would expect the effect of size to be less, and thus expect K_{s2} to approach closer to unity. As is clear from Table IV, the observed values of K_{s2} decrease below unity at water concentrations around 0.5M, and are nearly five orders of magnitude smaller than unity in pure water (Table I). Hydrogen bonding of the solvent to Cl^- would tend to decrease K_{s2}, and this apparently causes the overwhelming change as the solvent is changed from propylene carbonate to water. Coordination of the solvent to silver would be expected to increase K_{s2}, and this may be a partial contribution to observed value $K_{s2} = 10$ in the anhydrous solvent, but is certainly a much smaller effect than hydrogen bonding. This observation tends to confirm our previous statement that most of the increase in K_{so} with increasing water content was attributable to increased solvation of Cl^- and not Ag^+.

The intrinsic solubility of AgCl ($K_{s1} = \beta_1 K_{so}$) reflects the free energy of solvation of the neutral complex AgCl, and this varies only slightly over the range from anhydrous propylene carbonate ($K_{s1} = 10^{-5}$) to water ($K_{s1} = 10^{-6.5}$). If anything, this variation implies that the coordinate bonding of propylene carbonate to silver is greater than water, but the effect is much smaller than the variations involving the solvation of the chloride ion.

Since these experiments were carried out in a constant ionic medium of 0.1M Et_4NClO_4, it is of interest to estimate the effect of the tetraethylammonium and perchlorate ions on the observed concentration equilibrium constants. The effect of ionic strength can be estimated from the Debye-Hückel theory and is essentially the same for all the solvent mixtures. At zero ionic strength, log β_1 and log β_2 would be approximately 0.35 units greater and log K_{so} would be approximately 0.35 units more negative. The effect of ionic strength on the constants β_3, K_{s1}, and K_{s2} is negligible in the range where the Debye-Hückel theory is applicable. Ion pairing with the supporting electrolyte would tend to increase β_1, β_2, and β_3, and decrease K_{so}, but have little effect on K_{s1}, K_{s2}, and K_{s3}. However, since the dielectric constant of these solvent mixtures is high, and since little evidence for ion pairing between alkali metal, tetraalkyl ammonium, halide, or perchlorate ions, has been observed in water, the effects of ion pairing on the measurements described here is probaby very small.

As is well-known (5-8), the solubility of AgCl can be suppressed by using electrolytes such as $LiAlCl_4$ which have a low concentration of free chloride ion. Studies are now in progress which are intended to elucidate the equilibria in such systems.

Acknowledgments

The authors thank Dr. Raymond Jasinski and Mrs. Susan Kirkland for providing us with samples of purified propylene carbonate, and Mr. Marcel Fajnzylber for assistance with preliminary experiments. This work was supported by but does not necessarily constitute the opinion of the Air Force Cambridge Research Laboratories, Office of Aerospace Research, under Contract No. AF 19(628)-6131.

Manuscript received Nov. 1, 1967; revised manuscript received Jan. 19, 1968. This paper was presented at the Chicago Meeting, Oct. 15-19, 1967, as Abstract 4.

Any discussion of this paper will appear in a Discussion Section to be published in the December 1968 JOURNAL

REFERENCES

1. W. S. Harris, Thesis, University of California, 1958. U.S. Atomic Energy Commission Report UCRL-8381.
2. J. N. Butler, *Anal. Chem.*, **39**, 1799 (1967).
3. I. Leden, *Svensk Kem. Tidskr.*, **64**, 249 (1952).
4. E. Berne and I. Leden, *ibid.*, **65**, 88 (1953).
5. R. J. Jasinski, "High Energy Batteries," Plenum Press, New York (1967).
6. J. E. Chilton, Jr., Report ASD-TDR-62-1, April 1962. AD 277 171.
7. H. F. Bauman, J. E. Chilton, W. J. Conner, and G. M. Cook, Report RTD-TDR-63-4083, Oct. 1963 AD 425 876.
8. J. E. Chilton, W. J. Conner, G. M. Cook, and R. W. Holsinger, Report AFAPL-TR-64-147, Feb. 1965. AD 612 189.
9. R. J. Jasinski, *J. Electroanal. Chem.*, **15**, 89 (1967).
10. R. J. Jasinski and S. Kirkland, *Anal. Chem.*, **39**, 1663 (1967).
11. N. Ingri and L. G. Sillen, *Acta Chem. Scand.*, **16**, 159 (1962).
12. C. L. LeBas and M. C. Day, *J. Phys. Chem.*, **64**, 465 (1960).

The Nickel Positive Electrode

II. Semiconduction and Electrode Performance

Donald Tuomi

Roy C. Ingersoll Research Center, Borg-Warner Corporation, Des Plaines, Illinois

and G. J. B. Crawford

Schlumberger Technology Corporation, Ridgefield, Connecticut

ABSTRACT

The anodic oxidation of nickel hydroxide in pure lithium hydroxide electrolytes produces an n-type semiconductor. The anodic oxidation involves lithium migration into the active material. The beta phase is characterized at room temperature by Seebeck coefficients near -100 μv/°K and electrical conductivities of 1 mho/cm. This is in contrast to the positive Seebeck coefficient for lithium nickelate.

The nickel hydroxide positive electrode is considered to involve a divalent $Ni(OH)_2$ and a trivalent nickelate discharge and charge state. The designation beta phase was used by Tuomi (1) to describe the oxidized state without giving an explicit chemical composition formulation. Variations in the electrochemical processing conditions can modify the beta phase structural characteristics. The beta phase, however, appeared to be consistently an n-type semiconductor through hot point probe tests. On the other hand, the beneficial effects of LiOH additions to the battery electrolyte frequently are attributed to "p" type semiconduction enhancement in the charged phase as noted in Li doped NiO.

The following brief electrical property study was performed to clarify the experimental problem.

Experimental

The oxidized product formed from crystalline $Ni(OH)_2$ during charge in pure LiOH electrolytes is structurally related to lithium nickelate (1). An Edison tubular positive electrode set was charged at 25° and 85°C in 5M LiOH using a 300 ma rate for 216 hr (69.8 amp-hr) to give complete oxidation to trivalent beta phase. After charging, the active material was removed, pulverized, and fractionated to beta plus nickel flake using magnetic separation. The beta powder was processed further to give the four samples: (*a*) C:uw, a 25°C charge unwashed; (*b*) C:w, a 25°C charge washed with distilled water; (c) H:uw, a 85°C charged unwashed; and (*d*) H:w, a 85°C charge washed with distilled water. The chemical analyses and x-ray diffraction examinations were performed on portions using earlier procedures (1). One sample set was fired in oxygen at 850°C for 16 hr.

Samples compressed into the annulus between two contact rings were used to measure the electrical properties. The Seebeck coefficient was calculated from the temperature and voltage differences measured when the center ring was heated. The electrical conductivity measurement involved a four point probe using very low frequency a-c current to minimize contact resistance effects.

The chemical analysis results are summarized in Table I, while the electrical and structural observations appear in Table II. The sample titled $Li_xNi_{1-x}O$ was formed by repeated grinding and refiring of a NiO-$LiC_2H_3O_2$ mixture at 850°C in oxygen for a 12 hr total time.

Discussion

The material structure depended on the processing. The initial product was identified as small particle size beta phase with the hexagonal lithium nickelate structure. Firing in oxygen converted three samples to the cubic NiO phase with $x < 0.3$ in $Li_xNi_{1-x}O$, and one to a hexagonal lithium nickelate at $x = 0.41$. The reaction product of NiO and $LiC_2H_3O_2$ was hexagonal nickelate at $x = 0.45$. The general observations are consistent with the prior investigators (2). However, the hexagonal unit cell volumes were 6% greater than anticipated.

The electrochemical oxidation in LiOH converted the $Ni(OH)_2$ to a trivalent oxide with a 2.86 to 3.07 valence as shown in Table I. This was accompanied by a nickel content decrease from 63.4% to 56-59%. This is higher than 53.9% for $HNiO_2 \cdot H_2O$ and less than 74% for $HNiO_2$ or 60.1 for $LiNiO_2$. Since no attempt was made to remove sorbed water the solid phase is more consistently viewed as an anhydrous oxide than a simple hydrate such as $Ni_2O_3xH_2O$.

The C:uw and C:w 25°C product has a lower lithium content than the 85°C material. The difference in Li content for the washed and unwashed materials could not readily be explained by extraneous Li_2CO_3 formation. The comparable product valence states suggest protons effectively exchange for Li. The data clearly indicate Li sorption during charge. A loaded tube impregnated with electrolyte and dried as above contained only 0.16% Li.

The lithium to nickel molar ratio varied from 0.2 to 0.7 for dried materials and did not change during 850°C firing. This ratio is not consistent with viewing the reaction product as $LiNiO_2$. On the other hand, the charged phase lithium content implies oxidation in LiOH electrolyte is best not simply viewed as proton migration out of $Ni(OH)_2$ to form an $HNiO_2$ phase. Rather hydroxyl at the double layer reacts with protons forming water while lithium ions make transitions into the active phase interior. Process details depend on the charge distribution through solid-electrolyte interphase.

The 850°C oxygen atmosphere firing process increased the nickel content to the 70% range with corresponding lithium percentage increases. By contrast, the nickel valence dropped to 2.2-2.5 from 3. The cubic fired products $Li_xNi_{1-x}O$ with $x < 0.3$ showed calculated x values based on both Li and Ni were consistent with the nickel valence determination. The fired H:uw sample with the highest Li content corresponded to hexagonal $Li_{0.41}Ni_{0.59}O$. After firing the measured and calculated (% Li in $Li_xNi_{1-x}O$) valence states are related as shown in Table III. The valence change and structural modifications are consistent with a $(H,Li)_xNi_{1-x}O$ containing sorbed H_2O transformation to $Li_xNi_{1-x}O$ accompanied by water and oxygen evolution.

The electrical measurements, Table II, provide more detailed insight into the problem complexity. Conventionally, the addition of lithium to NiO is viewed as introducing holes into the band structure (*i.e.*, Ni^{+3}

Table I. Chemical analyses and structural form for dried and fired anodic oxides as described in text

Sample		C:uw	C:w	H:uw	H:w	$Li_xNi_{1-x}O$
Ni Valence	Dried	3.07	2.97	2.97	2.86	—
	Fired	2.31	2.19	2.53	2.30	2.88
	δ	−0.76	−0.78	−0.44	−0.56	—
% Ni	Dried	55.86	59.28	55.62	56.84	—
	Fired	69.44	72.85	64.54	70.47	61.7
	δ	+13.58	+13.57	+8.92	+13.63	—
% Li	Dried	2.63	1.58	4.73	2.32	—
	Fired	3.25	1.82	5.35	2.99	5.70
	δ	+0.62	+0.24	+0.62	+0.67	—
Li/Ni Moles	Dried	0.398	0.225	0.719	0.343	—
	Fired	0.40	0.22	0.69	0.81	0.81
$Li_xNi_{1-x}O$	Dried	—	—	—	—	—
x =	Fired	0.29	0.18	0.41	0.26	0.45
Crystal	Dried	Hex	Hex	Hex	Hex	—
Symm.	Fired	Cubic NiO	Cubic NiO	Hex	Cubic NiO	Hex

Table II. Electrical data from dried and fired anodic oxide samples as described in text

Sample		C:uw	C:w	H:uw	H:w	$Li_xNi_{1-x}O$
S μv/°C	Dried	−107	−58	−92	−85	—
	Fired	+97	+137	+113	+99	+70
σ Mho/cm	Dried	3.3	4.5	0.68	0.92	—
	Fired	0.7	0.77	0.70	0.51	0.16

Table III. % Li in Li_x $Ni_{1-x}O$ valence states after firing

	Calc	Anal
C:uw	2.41	2.31
C:w	2.22	2.19
H:uw	2.69	2.53
H:w	2.36	2.30

local sites) and forming a p-type semiconductor (3). The anodic oxidation, however, converted the $Ni(OH)_2$ insulator to a high electrical conductivity n-type semiconductor. The reaction product has a negative Seebeck coefficient varying from −58 to −107 μv/°C at 0.7-5.0 mho/cm. The firing process produces the expected p-type conduction with S between +97 to +137 μv/°C and σ near 0.7 mho/cm. This compares to +70 μv/°C at 0.16 mho/cm for the direct reaction product $Li_{0.45}Ni_{0.55}O$. Lower nickel valence state fired products are also p-type. Thus, the LiOH electrolyte modification of the charged phase does not involve the anticipated semiconductor doping effect (4). It should be noted that Richardson (5) observed that the higher valence state precipitated nickelic oxides are also n-type semiconductors as has been previously noted for the KOH anodic oxidation product (6).

Even for a pure LiOH electrolyte the electrochemically oxidized $Ni(OH)_2$ is an n-type semiconductor beta phase. The semiconductor gross features are not under drastic control by alkali cation content. The n- to p-type transformation on heat treatment suggests the lattice or local electronic coordination imperfection depends on the hydrogen ion distribution effect on local band structure.

The characteristic $Li_xNi_{1-x}O$ composition formed by firing at 850°C is consistent with a trivalent nickel stabilization by local site symmetry conditions. The p-type conductivity for $O < x < 0.5$ is not simply interpretable as trivalent ion promotion through the local band electrostatic neutrality condition as in slightly Li doped NiO.

The recent results of Bosman and Crevecoeur (7) indicate a band model rather than the thermally activated carrier hopping model applies to nickel oxide. The detailed study of anodic oxidation products as well as the simple $Li_xNi_{1-x}O$ system could provide considerable insight into electronic processes in electrochemical systems. The local site symmetry constraints in high density, well-ordered, lithium nickelates are markedly stronger than in the less crystalline anodic product which frequently can approach an amorphous structure having only first and second nearest neighbor symmetry. The dilemma is accentuated when it is noted that the case of trivalent nickel oxidation to tetravalent alpha phase depends on electrolyte composition and electrode processing. Clearly interpreting chemical additive effects as altering semiconduction processes is questionable without detailed study.

The high electrical conductivity of the oxidized phase does not necessarily inhibit mass transport in the relevant electrochemical processes. A high electronically active site density is implied by the high conductivity with the probable low carrier mobility along with contact resistance in the fine grain material. Under such conditions, a variety of unusual behaviors related to imperfection densities would not be surprising. The space charge distributions within the compounds during cycling will depend partially on the electronic transport properties interactions with the mass transport as well as the interphase phenomena including Peltier effects, and the electronic-ionic exchange processes.

Detailed studies on the importance of impurity banding, metallic conduction, etc. to electrode behavior may be undertaken through a systems approach to the problem. The interpretation of n-type high conductivity in the anodic oxidation product with p-type in the cubic and hexagonal divalent-trivalent nickel solid solution of $Li_xNi_{1-x}O$ compounds requires a detailed knowledge of imperfection structure relationships to band structure. It should be emphasized that the semiconductor under consideration is an extremely complex chemical and structural system reflecting the formation conditions. A priori the system is not conceptually related to ceramic or single crystal cubic NiO. Rather the material represents a solid solution with nonstoichiometric characteristics and considerable disorder in the system Ni-O-Li-H. Mott's review (8) on electrons in disordered structures brings attention on to one class of problems to be solved. The mass and charge transport in the electrochemical oxidation-reduction process provides a general phase transformation kinetics problem.

Acknowledgments

The assistance of J. Bronson and L. Middlecamp in the experimental work is gratefully acknowledged. The analytical services were provided through the cooperation of B. D. Brummet. The research benefited from discussions with Drs. G. T. Croft, J. B. Johnson, and P. F. Grieger at the T. A. Edison Research Laboratory. The continued support of Dr. D. W. Collier is appreciated. Special acknowledgments are due to W. W. Smith and associates of the Electric Storage Battery Company for their encouragement and support during the preparation of this paper for publication.

Manuscript received June 19, 1967; revised manuscript received Dec. 11, 1967.

Any discussion of this paper will appear in a Discussion Section to be published in the December 1968 JOURNAL.

REFERENCES

1. D. Tuomi, *This Journal*, **112**, 1 (1965).
2. J. B. Goodenough, P. G. Wickham, and W. J. Croft, *J. Phys. Chem. Solids*, **5**, 107 (1958).
3. E. J. W. Verwey, "Semiconducting Materials," pp 151-161, Butterworths Scientific Pub. Ltd., London (1951).
4. R. L. Tichenor, *Ind. Eng. Chem.*, **44**, 973 (1952).
5. J. T. Richardson, *J. Phys. Chem.*, **67**, 1377 (1963).
6. D. Tuomi, *ibid.*
7. A. J. Bosman and C. Crevecoeur, *Phys. Rev.*, **144**, 763 (1966).
8. N. F. Mott, *Adv. in Physics*, **16**, 49 (1967).

The Electrolysis of Ammonium Bifluoride in Anhydrous Hydrogen Fluoride

Larry G. Spears*[1]

TRACOR, Inc., Austin, Texas

and Norman Hackerman*

The University of Texas, Austin, Texas

ABSTRACT

The electrolysis of ammonium bifluoride in anhydrous hydrogen fluoride (AHF) was investigated. Polarization curves of Monel in solutions of NH_4HF_2 in AHF did not show any diffusion-limited regions indicative of a potential-dependent stepwise reaction. The results of this study indicate that the fluorination of NH_4HF_2 in AHF occurs by a radical mechanism involving anodically generated fluorine. Chronopotentiometric data, current-potential curves, and product yields *vs.* time curves, indicate that the fluorinating agent, during electrolysis, is a "loose" complex between $\cdot F$ and NiF_2 and/or CuF_2. *Trans*-N_2F_2 was the only N-F product formed from the electrolysis of NH_4HF_2 in AHF.

The use of anhydrous hydrogen fluoride (AHF) as a solvent for the electrolysis of ammonium salts has not been investigated in much detail. Several investigators have reported using AHF as a solvent for the electrolysis of NH_4HF_2 (1, 2) but their results indicated that the solvent was not anhydrous. Several electrolyses (3, 4) have been performed using molten NH_4HF_2; however, they were not reported in much detail either.

Anhydrous HF has many properties which make it a valuable solvent system for studying the chemistry of both organic and inorganic fluorine-containing species. Among these are its ability to dissolve a variety of ionic and covalent compounds in significant amounts and its ionizing powers toward dissolved ionic species. In both of these aspects, it is very similar to water. Also, like water, its self-dissociation constant is small, so that the activity of ionic species contributed directly by AHF to a system under study will be low. Such properties are particularly valuable to an electrochemical approach for studying reaction kinetics in AHF, since the more "waterlike" the solvent system, the more applicable will be past electrochemical experience.

In this investigation an attempt was made to determine the electrochemical mechanism involved in the anodic fluorination of NH_4HF_2 dissolved in AHF. A free radical mechanism involving fluorine atoms has long been recognized by many workers as the mechanism involved in the electrochemical fluorination of organic materials in HF (5). Some workers claim the fluorinating agent is a higher valent metal fluoride or metal fluoride compound. Cotton (6) suggests that a nickel anode in HF and KF might form K_2NiF_6 and K_3NiF_6 which could act as fluorinating agents at the electrode surface. However, none of these higher valent fluorides have ever been identified. Of course, it is possible that these fluorides might be next to the metal and covered with the normal valency metal fluoride such that electron diffraction studies or other analytical devices would not detect them.

Experimental

The system developed for handling and storing the HF and the electrolytic cells used in this work has been previously described (7, 8). The electrolytic cells were constructed of Kel-F and Teflon with Teflon fittings and valves. All tubing in contact with the cells was either Teflon or Kel-F.

Anhydrous HF was prepared, using commercial HF, by a distillation and electrolysis procedure similar to that of Rogers, Johnson, and Evans (9). Conductivity of AHF prepared in this manner was usually around 10^{-5} ohm^{-1} cm^{-1}. Water concentration was estimated from an empirical relation given by Ukaji and Kageyama (10).

Monel (alloy No. 400), in the form of 0.125 in. rod, was used as the working electrode. Previously reported data (8, 11) indicates that Monel is probably the most desirable anode material for use in AHF. The Monel electrodes were prepared by mechanical sanding and buffing to a smooth surface. Then they were degreased in hot benzene, washed with distilled water, and vacuum dried. Nickel screen was used for the auxiliary electrode.

The reference electrode used was the Hg/Hg_2F_2 electrode. Initial work on this electrode was reported by Koerber and DeVries (12); details of construction and performance have been discussed previously (8, 13).

Volatile electrolysis products were analyzed using a Beckman IR 5-A infrared spectrometer, an F & M gas chromatograph (Model 720 with a nickel block), and a modified Electrodynamics Corporation mass spectrograph (Model 21-620). A description of the techniques involved in these analyses has been reported (7, 8). Cryogenic programming (using 2 coiled, 7 ft, ¼ in. OD Monel tubes) from −196°C to room temperature was used to separate the volatile products for identification by IR and mass spectral methods. A 70 ft column packed with 50% Halocarbon Oil 13-21 on 30-50 mesh Kel-F molding power at 0°C, was used for quantitative GC analysis of the volatile products (14). Irtran-2 (Eastman Kodak Company) was used as the liquid and gas IR cell window material.

A unique IR liquid cell was developed in this laboratory to analyze the soluble products (15).

All ammonia used for the NH_4HF_2-AHF solutions was double-distilled and all potentials were *vs.* Hg/Hg_2F_2 at −20°C.

Results

A typical steady-state polarization curve for Monel in AHF is shown in Fig. 1. The current increase past ~2.8v is due mainly to F_2 evolution. A hysteresis is noted when reverse polarization is done rapidly, indicating existence of a film on the electrode surface. The passive-type region between open circuit and

* Electrochemical Society Active Member.
[1] Present address: Gulf South Research Institute, New Iberia, Louisiana.

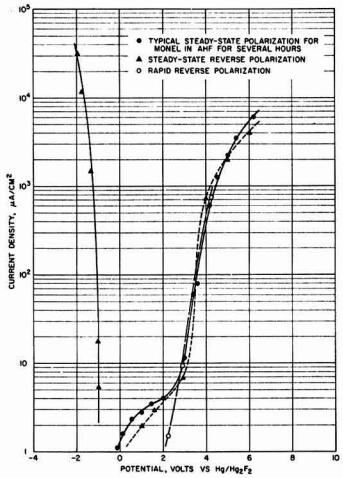

Fig. 1. Polarization curves for Monel in AHF

~2.8v is due mainly to formation of a metal fluoride film. Weight losses for Monel between open circuit and 2.8v were similar to those at open circuit. A typical anodic polarization curve for a Monel electrode in AHF for only 30 min is shown in Fig. 2. The current density peak at ~1.4v indicates an initial film formation. Curves run after an electrode had been in AHF for at least 2 hr did not exhibit this peak.

Anodic polarization curves were made in solutions of NH_3 dissolved in AHF to determine if the fluorination of NH_4^+ proceeded in a stepwise fashion as a function of potential. Liquid IR spectra showed that NH_3 dissolved in AHF formed NH_4HF_2 and possibly some $NH_4H_2F_3$ (7, 8). Two typical steady-state polarization curves made in a 1M solution of NH_4HF_2 in AHF are shown in Fig. 3. A plateau-like region can be seen between 3.4 and 3.8v. This current limited region was noted in all polarization curves run in AHF-NH_4HF_2 solutions; however, its magnitude was not dependent on the NH_4HF_2 concentration. Fast polarization curves were also made with a voltage increase of 0.9 v/min. Figure 4 shows two fast anodic polarization curves made in 0.1M NH_4HF_2 in AHF.

Galvanostatic cathodic reduction curves were made in an attempt to clarify the diffusion-limited region described above. Reduction curves for Monel, polarized anodically at 2, 4, 5, and 6v in 0.021M NH_4HF_2 in AHF, are shown in Fig. 5. The potential arrest at ~2.7v

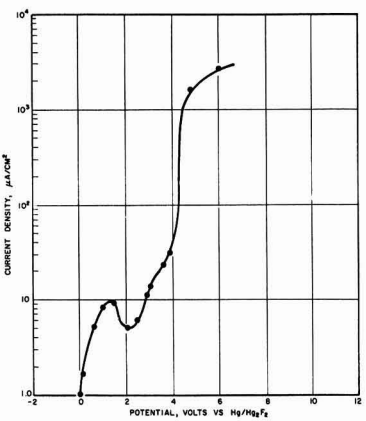

Fig. 2. Polarization curve for Monel (in AHF for 30 min)

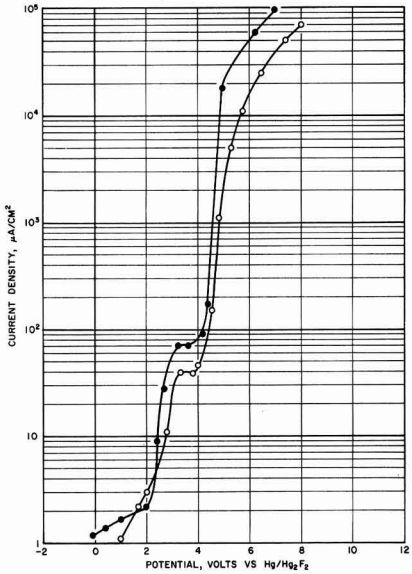

Fig. 3. Anodic polarization curves of Monel in 1M NH_4HF_2 in AHF

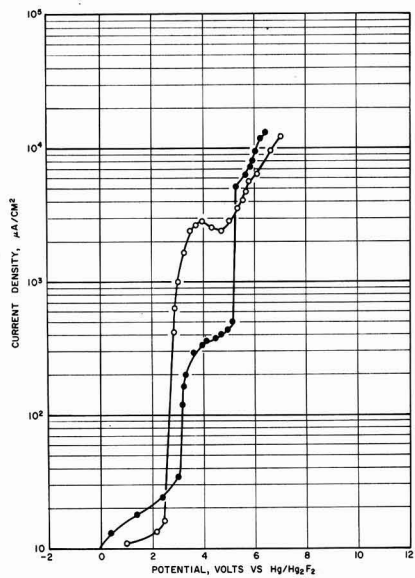

Fig. 4. Fast anodic polarization curves of Monel in 0.1M NH_4HF_2 in AHF.

is close to the reduction potential for fluorine according to Fig. 1. As shown in Fig. 6, the cathodic charge required for reduction appears to depend on the total charge passed at 6v rather than the increment of charge passed between reductions. These results indicated that a species other than the metal fluoride was being reduced during these reduction experiments.

If the potential arrest at ~2.7v was due to the reduction of fluorine, it should be possible to reach a state where the metal fluoride film would be saturated with fluorine. This effect is shown in Fig. 7. It should be noted that 154 coulombs were passed at 6.0v and a cathodic current applied until the potential returned to approximately the initial open circuit potential before the runs in Fig. 7 were made. Once the metal

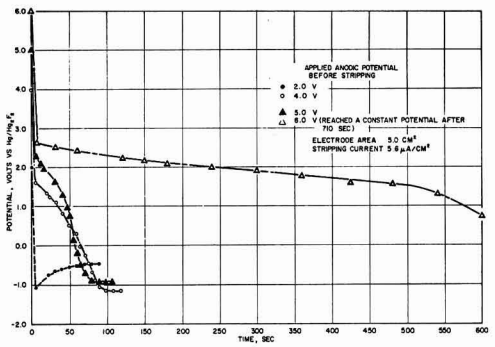

Fig. 5. Stripping curves for Monel electrodes polarized anodically in 0.021M NH_4HF_2 in AHF.

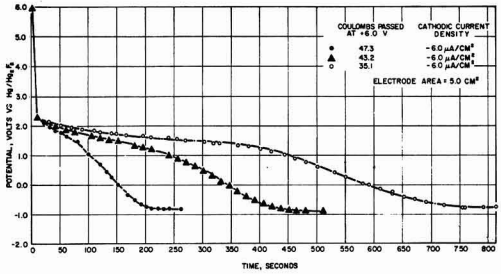

Fig. 6. Cathodic stripping of Monel electrodes from +6.0v in 2.13 X 10^{-2}M NH_4HF_2 in AHF.

fluoride film is saturated, it should be possible to decrease the applied anodic charge and thus have a decrease in the cathodic charge required to reduce the sorbed fluorine. This is shown in runs 3 to 8 of Fig. 7. In Table I, values obtained from reduction measurements in 0.01M NH_4HF_2 in AHF are given. It can be seen from the table that as the anodic charge decreases the ratio between the reduction charge and anodic charge begins to approach unity. Also, it should be noted that the anodic and cathodic charges for 6.0 v/2 sec and 4.0 v/30 sec were almost identical.

Constant potential electrolyses were performed using various concentrations of NH_4^+ and anodic potentials. Initially these electrolyses were made in order to identify the products formed. As described above, a cryogenic GC column was utilized for this work. After the volatile products were identified, the coulombic yields of the products were determined as a function of time using a 70 ft Halocarbon Oil Kel-F powder GC column.

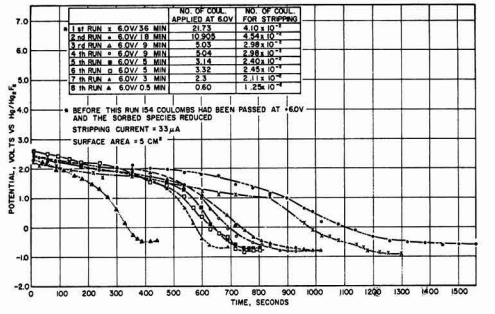

Fig. 7. Cathodic reduction curves for Monel in 2.16 X 10^{-3}M NH_4HF_2 in AHF.

Table I. Values obtained from the cathodic reduction measurements made on Monel in a solution of 0.01M NH_4HF_2 in AHF

Anodic potential/ sec applied	No. of reduction coul. required × 10^3 (C_1)	No. of coul. applied anodically (C_2)	$C_1/C_2 \times 100$
6.0 v/30 sec	5.95	2.55	0.233
6.0 v/15 sec	4.25	1.22	0.348
6.0 v/5 sec	2.96	0.35	0.845
6.0 v/2 sec	1.84	0.136	1.35
4.0 v/30 sec	1.87	0.135	1.36
4.0 v/15 sec	1.12	0.063	1.75
4.0 v/11 sec	0.918	0.044	2.09
4.0 v/5 sec	0.740	0.015	4.93
4.0 v/3 sec	0.442	0.008	5.46

None of the liquid IR spectra indicated the presence of any soluble electrolysis products (7, 8). Liquid spectra taken before and after extended electrolysis were identical except for the relative size of the NH_4^+ absorption bands.

Figures 8, 9, and 10 show the yields of the anodic products formed from the electrolysis of 0.1M and

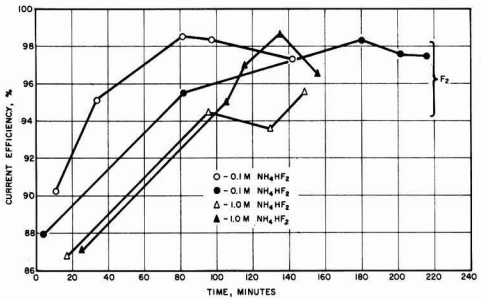

Fig. 8. Yield of 5.0v electrolysis products as a function of time

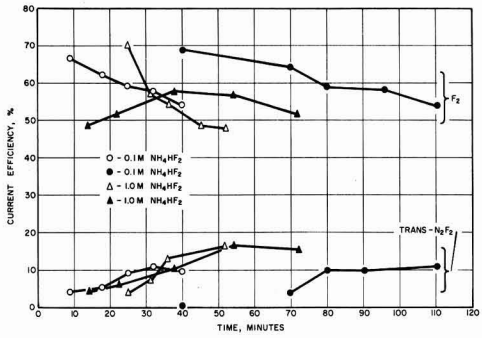

Fig. 9. Yield of 7.0v electrolysis products as a function of time

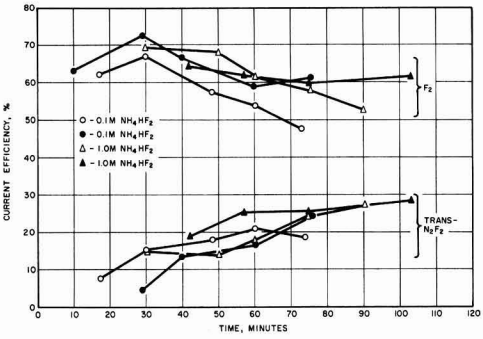

Fig. 10. Yield of 9.0v electrolysis products as a function of time

1.0M solutions of NH_4HF_2 in AHF at potentials of 5.0, 7.0, and 9.0v. Table II summarizes these results giving the net current efficiency for each of the electrolysis products. The equivalent weight of the metal fluoride was calculated assuming formation of NiF_2 and CuF_2. The current density range given in Table II is the variation of the observed current densities during electrolysis. Most of these runs had a lower current initially. During electrolysis, the current usually increased with time until a relatively constant current region was reached.

Discussion

Polarization curves of Monel in solutions of NH_4 HF_2 in AHF were made in an attempt to detect a potential-dependent stepwise reaction (see Fig. 3 and 4). A plateau-like region was noted around 4.0v; however, it did not appear to be dependent on the NH_4HF_2 concentration. Polarization curves of metals or alloys in solutions of ammonium salts in HF could not be found in the literature for comparison. Constant potential electrolyses at 5.0v, in 0.1M and 1.0M solutions of NH_4HF_2 in AHF, produced no volatile or soluble N-F or nitrogen containing species. Thus, it was concluded that the constant current region was probably due to a phenomena not directly related to the presence of NH_4HF_2.

Fast polarization curves were made to see if the lack of a thick fluoride film (the type formed during steady-state polarization) would result in different anodic polarization characteristics. The only differences noted were a broader plateau region around 4v and erratic behavior in the slope of the curve past the plateau region. Both of these changes are probably due to the inability of the system to reach equilibrium conditions during the fast scan (0.9 v/min.) Points taken for the steady-state curves were recorded after approximately 20 min at each potential.

The galvanostatic reduction curves presented above indicate that both metal fluoride and fluorine were formed on the electrode surface during anodic charging. When cathodic current was applied, only the trapped or sorbed fluorine was reduced. Continuous anodic charging resulted in more sorbed or trapped fluorine, this being due to the increasing film thickness. Experiments performed on nickel anodes in HF indicated similar phenomena (8, 16).

Constant potential electrolyses showed that *trans*-N_2F_2 was the only N-F species formed during the electrolysis of NH_4HF_2 in AHF. Previously reported data (7, 8) indicated that the formation of N_2F_2 decreased rapidly with the addition of increasing concentrations of water. Also, as the water concentration increased, increasing amounts of OF_2 and NF_3 were formed. The "induction period" (the time required for the yields to reach a constant value) noted in Fig. 10 and 11, are typical of electrolytic fluorination studies reported by other workers (1, 17, 18) including two studies on the electrolysis of molten NH_4HF_2 (3, 4).

The effect of increasing current density on the yield of N_2F_2 should be noted (see Table II). A previously reported study of the electrolysis of molten NH_4HF_2 (3) stated that a minimum current density of 30 ma/cm² was required in order to obtain N-F species.

From the data presented above, it is concluded that the electrolytic fluorination of NH_4^+ in AHF occurs by chemical reaction with anodically formed fluorine. A free radical mechanism is thought to occur in the electrochemical fluorination of organic materials in HF (5). Some workers claim that the fluorinating agent is a higher valent metal fluoride or metal fluoride compound (6). Another possibility for the identity of the fluorinating agent for this study is a loose complex between NiF_2, CuF_2, and $\cdot F$ or F_2 (5).

If the agent was a loose complex, fluorination would occur between the complex and the substrate adsorbed on the anodic film. This type process would thus require an induction period for buildup of the film containing the complexed NiF_2 and/or CuF_2. Initially, low yields of fluorinated species would occur due to the small amount of film on the anode. As the film increased, so would the concentration of fluorinating agent in the film, thus increasing the yield of fluorinated species.

If the fluorination process were due only to F_2 formed at the anode, there would be no need for the relatively long induction periods noted in Fig. 9 and 10. If fluorination occurred due to formation of higher metal fluorides, it is still difficult to explain the long induction periods. Of course, it is possible that the loose complex involved F_2 instead of $\cdot F$. However, if a complex is formed, the more active fluorine radical would be preferred to the molecule. This would also help to explain previously reported data (8, 16) where an anodically charged (in KF-AHF solution) Ni electrode was put under vacuum and then returned to the electrolytic cell and cathodically reduced. Very little of the sorbed fluorine had been removed from the film as a result of the vacuum.

Morrow and co-workers studied reactions between F_2 and NH_3 in a copper T-shaped reactor (19). They were able to form NF_3, N_2F_4, N_2F_2, and HNF_2 along with small amounts of N_2 and HF. With an excess of NH_3 only N_2F_4, N_2F_2 and HNF_2 were formed. When an excess of fluorine was used only NF_3 and NH_4F were formed. They concluded that the initial step in these reactions was the formation of $\cdot F$ from F_2. The copper reactor could have acted as a catalyst for the dissociation.

A reason for excess fluorine, in the above reactions, to hinder N_2F_2 formation might be that large amounts of fluorine result in relatively fewer fluorine radicals to react with NH_3. This might also explain the effect of water on the yields of NF_3 and *trans*-N_2F_2 in liquid HF. In aqueous HF, there should be fewer fluorine atoms in the film, thus decreasing the yield of any species dependent on $\cdot F$ for its formation.

Table II. Current efficiency of products formed from the electrolysis of NH_4 HF_2 in AHF

NH_4HF_2 concentration	Potential, v	Current density range, ma/cm²	Total charge passed, coulombs	% Yield of current passed		
				F_2	*Trans*-N_2F_2	Anode corrosion
0.1M	5	0.68-1.25	42.83	97.5	—	4.10
0.1M	5	0.32-0.44	7.58	97.3	—	7.44
1.0M	5	0.14-0.54	10.20	95.8	—	0.76
1.0M	5	0.81-2.10	39.77	96.5	—	2.24
0.1M	7	4.9-79.0	1082	54.0	11.20	27.36
0.1M	7	54.5-81.8	1086	56.8	10.01	30.10
1.0M	7	4.0-96.0	716	48.4	16.47	27.05
1.0M	7	48.8-97.6	1638	51.5	15.15	31.10
0.1M	9	113-191	818	47.7	19.0	27.30
0.1M	9	50-175	382	60.8	24.6	25.70
1.0M	9	26.7-233	1440	53.7	27.5	25.42
1.0M	9	63.8-264	1564	61.2	28.5	21.30

Conclusions

In view of the above data, the following mechanism is proposed for the formation of N_2F_2 in these studies. This mechanism is similar to that proposed by Morrow (19) and Colburn (4).

$$2NH_4HF_2 \rightarrow 2F\cdot + 2H^+ + 2e^- + 2NH_3 + 2HF \quad [1]$$

$$2NH_3 + 2F\cdot \rightarrow 2\cdot NH_2 + 2HF \quad [2]$$

$$2\cdot NH_2 + 2F_2 \rightarrow 2NH_2F + 2F\cdot \quad [3]$$

$$2NH_2F \rightarrow 2\cdot NF + 4H \quad [4]$$

$$2\cdot NF \rightarrow N_2F_2 \quad [5]$$

$$2F\cdot + 2H^+ + 2e^- + 4H + 2F_2 \rightarrow 6HF \quad [6]$$

$$2NH_4F_2 + 4F_2 \rightarrow N_2F_2 + 8HF \quad [7]$$

The first step in the mechanism above occurs at the electrode surface as a result of an anodic bias equal to or greater than the fluorine evolution poten-

tial. As a result of our experiments, it is felt that the fluorine radicals utilized in step [2] are associated in a loose complex with NiF_2 and/or CuF_2 in the anodic film. By use of bond dissociation energies given by Wilson (2), the following values were calculated (in units of kcal/mole) for the heats of formation of steps [2] to [6]: [2] —78, [3] —62.4, [4] 347.8, [5] —107.9, and [6] —662. Upon addition of these values, —562.5 kcal/mole is obtained for ΔH_f of the net equation given in step [7]. Another factor which makes this mechanism more probable is that NH_2F formation has never been observed. If fluorine gas were the fluorinating agent in step [2], the heat of formation would be reduced to —31 kcal/mole, making the initial step of this mechanism less favorable.

Why *trans*-N_2F_2 is formed instead of *cis*-N_2F_2 is difficult to explain. One answer might be that either the metals (Ni, Cu, Hg, or Pt) or metal fluorides present in the electrolytic cells catalyzed the formation of *trans*-N_2F_2 from any *cis*-N_2F_2 that was formed. It is also possible that under the experimental conditions used, the trans isomer required the least energy. *Cis*-N_2F_2 is reported to be the more active form of N_2F_2 (20).

Acknowledgments

This work was supported in part by the United States Navy, Office of Naval Research, under Contract Nonr-4054(00) with TRACOR, Inc., Austin, Texas. The authors also wish to express appreciation to E. S. Snavely, Jr., L. D. Fiel, W. E. Harrell, Jr., and J. O. Spears, for contributions to this project. One of the authors (N.H.) takes this opportunity to express his thanks to The Robert A. Welch Foundation, Houston, Texas, and to the Office of Naval Research, under Contract Nonr-375(15), for their support of the work in his laboratory which led in part to this work.

Manuscript received Nov. 16, 1967.

Any discussion of this paper will appear in a Discussion Section to be published in the December 1968 JOURNAL.

REFERENCES

1. H. H. Rogers, S. H. Evans, and J. H. Johnson, Contract Nonr-1818(00), Report No. R-5077, Rocketdyne (1963).
2. A. R. Young and S. I. Morrow, Contract Nonr-4364(00), ARPA Order No. 417, Report RMD 5043-Q2-64, Thiokol Chemical Corp. (1964).
3. M. Schmeisser and P. Satovi, *Angew. Chem.*, **71**, 523 (1959).
4. Colburn *et al.*, *J. Am. Chem. Soc.*, **81**, 6397 (1959).
5. M. Stacy, J. C. Tatlow, and A. Sharpe, "Advances in Fluorine Chemistry," Vol. I, p. 162, Butterworth, London (1960).
6. F. A. Cotton, "Progress in Inorganic Chemistry," Vol. II, p. 200, Interscience Publishers, Inc., New York (1960).
7. L. G. Spears, Ph.D. Dissertation, The University of Texas (1967).
8. E. S. Snavely, Jr., L. G. Spears, L. D. Fiel, J. L. Lindgren, and W. E. Harrell, Jr., Summary Report, Contract No. Nonr-4054(00), ARPA Order No. 399, TRACOR, Inc., (1966).
9. H. H. Rogers, S. H. Evans, and J. H. Johnson, *This Journal*, **111**, 701 (1964).
10. R. Ukaji and I. Kageyoma, *Bunseki Kogaku*, **9** 604 (1960).
11. N. Hackerman, E. S. Snavely, Jr., and L. D. Fiel, *Corrosion Science*, **7**, 39 (1967).
12. G. G. Koerber and T. J. DeVries, *J. Am. Chem. Soc.*, **74**, 5008 (1952).
13. R. M. Hurd and E. S. Snavely, Jr., Metal and metal/metal fluoride electrode systems in anhydrous hydrogen fluoride, ARPA Propellant Contractors Synthesis Conf. IIT Research Institute, Chicago, Illinois, 13-15 (April 1964).
14. L. G. Spears and N. Hackerman, To be published.
15. L. G. Spears and N. Hackerman, To be published.
16. L. D. Fiel, Ph.D. Dissertation, The University of Texas (1966).
17. O. Ruff and L. Staub, *Z. Anorg. Allgem. Chem.*, **198**, 32 (1938).
18. R. N. Hazeldine and F. Nyman, *J. Chem. Soc.*, 2684 (1956).
19. S. I. Morrow *et al.*, *J. Am. Chem. Soc.*, **82**, 5301 (1960).
20. J. N. Wilson, *et al.*, Contract DA-31-124-ARO(D)-54, ARPA No. 3910 ARO (D), Report No. 1, Shell Development Co. (1963).
21. A. Zletz, *et al.* Contract No. DA-31-224 ARO(D)-78, ARPA Order No. 402, Task 3, American Oil Co. (1965).

On the Mechanism of Formation of Thin Oxide Layers on Nickel

K. Hauffe,* L. Pethe,[1] and R. Schmidt
Institut für physikalische Chemie der Universität in Göttingen, Germany

and S. Roy Morrison
Stanford Research Institute, Menlo Park, California

ABSTRACT

It could be demonstrated that the initial period of oxidation of nickel at 400° and 500°C is governed by a logarithmic rate law. However, after approximately 5 hr at 400°C and 1 hr at 500°C the rate of oxidation changes into a fourth power rate law ruling in a special oxide-thickness region. This rate law can be understood if a negative space charge, caused by nickel-ion vacancies, in the growing NiO layer is assumed and if the current of nickel-ion vacancies from the surface of the oxide layer to the metal-oxide interface is caused predominantly by an electric field established over the layer. The experimental results of the oxidation of nickel are in fair agreement with the proposed mechanism.

During the oxidation of nickel, generally, the metal is covered with a practically pore-free coherent oxide layer of NiO in which the reacting components, nickel and oxygen, are spatially separated from one another so that one of the reactants, nickel or oxygen, or both, must diffuse through the oxide layer. The oxidation rate of nickel is slower than that of most other metals. Since nickel oxide is a p-type semiconductor, the assumption of the existence of electron holes $|e|^{\circ}$ and nickel-ion vacancies $|Ni|''$ in nickel oxide is

* Electrochemical Society Active Member.
[1] Present address: Chemistry Department, Marathwada University, Aurangabad, India.

justified (1). Accordingly, a preferred diffusion of nickel ions and electrons via vacancies and holes, respectively, should occur during the oxide growth causing a parabolic rate law if the oxide layer is thick enough so that this diffusion process is rate-determining. Such a rate law was found at high temperatures when a rather thick oxide layer was formed (2).

As could be demonstrated, however, the oxidation of nickel between 400° and 500°C in the thin oxide film region cannot be evaluated by a parabolic rate law. By a log-log representation of the oxide layer thickness *vs.* the time, a rate law was found to lie between $t^{1/3}$ and $t^{1/4}$ indicating that under these experimental conditions additional phenomena become predominant. Oxidation experiments with nickel at 400°C in oxygen at various gas pressures performed by Engell, Hauffe, and Ilschner (3) showed a rate law of the form

$$\xi \sim t^{1/3.7}$$

where ξ is the thickness of the oxide layer formed in time t. This rate law was found up to 1000Å thickness of the oxide. The kinetics of oxidation obtained at 475°C by Gulbransen and Andrew (4) also obeys this time law up to an oxide layer thickness corresponding to 13 μg/cm^2. For thicknesses larger than this value, a transition to the parabolic rate law has been found by us (3). In this investigation, however, such a transition could not be detected because the oxidation time was not long enough. Below 400°C, several authors could evaluate their experimental results by a logarithmic rate law, especially when the thickness of the oxide layer was very small (< 50Å) (5) or also larger than 200Å (6).

The nickel oxidation at 400°C was repeated and enlarged by 500°C experiments. As shall be demonstrated from the theoretical viewpoint below, the nickel oxidation in the thin oxide layer region can be described by a fourth power rate law ($\Delta\xi^4 \sim t +$ const). This was, indeed, the case for the oxidation experiments performed at 400° and 500°C at various oxygen pressures.

Experimental

A Sartorius vacuum microbalance was used which operated automatically and recorded the changes in the weight of the sample with time. The sensitivity of the balance could be varied between 1 and 100 μg for a maximum load of 1g. The balance was connected with a flexible red brass tube to enable a horizontal movement of the balance in order to center the sample, suspended by a glass fiber, in the glass reaction tube. The temperature of the latter was controlled to ±0.5°C by means of a regulated furnace. A grounded steel block was used near the constant temperature zone to minimize the temperature gradient in the reaction vessel. All experiments have been performed in oxygen with N_2 < 1%, in a static system, where H_2O and CO_2 have been removed by a cooling trap. Because of the large gas reservoir, the uptake of oxygen by the sample during oxidation did not cause a change of pressure in the reaction vessel. The vacuum system consisted of a mechanical pump and an oil diffusion pump with a cooling trap containing solid CO_2 in acetone.

Pressures higher than 1 Torr were read on a mercury manometer, separated from the rest of the system by another cooling trap while those between 1 and 10^{-3} Torr were measured with a thermotron valve supplied by Leyboldt. For pressures below 10^{-3} Torr an ionization gauge of Heraeus was used. In order to decrease the gas turbulence and convection currents in the system, the portion of the reaction vessel passing through the zone of the temperature gradient was made narrower than the rest by connecting a 20 cm long piece of 7 mm diameter glass tube above the reaction vessel of 32 mm diameter. In addition, such an arrangement prevents a significant flux of hot gas from the reaction chamber to the balance.

Pure nickel sheets (99.9% Ni), 0.2 mm thick, were supplied by the courtesy of Vacuumschmelze AG, Hanau, who provided the following analysis in weight per cent: 0.061 Fe, 0.001 Mn, 0.0045 Si, 0.001 Cu, 0.007 Co, 0.029 C, and 0.044 Mg. Specimens 2 x 2.7 cm^2, weighing nearly 950 mg were degreased and abraded under pure benzene with emery paper of 6/0. Subsequently, the grinding dust was wiped off by a piece of filter paper. They were then dried at room temperature in vacuum. Since before suspension, the sample had to pass through the hot zone of the reaction vessel, oxygen free pure nitrogen was continuously passed through the system during hanging in order to avoid any uncontrolled preoxidation.

After suspending the nickel sample, the reaction vessel was closed, evacuated, and the furnace moved into the required position. The sample was then reduced in hydrogen at 1 atm for 15 to 20 min and later annealed for 1 hr at a pressure of 10^{-3} Torr. Oxygen was then introduced into the reaction chamber to start the reaction. Experiments have been carried out at 400° and 500°C at various oxygen pressures between 50 and 700 Torr.

Since the attainment of pressure equilibrium in the system, after introducing oxygen, took nearly 2-3 min, the initial weight was found by extrapolation for the experiments at 400°C. The rate of oxidation at 500°C was fast enough to make the extrapolation inaccurate. Therefore, the initial readings were taken in an inert nitrogen atmosphere at the same pressure employed for oxidation.

Results

For illustration of our results, the rate of oxide growth is plotted both as weight increase per square centimeter, $\Delta m/A$, and as thickness, ξ, of the oxide layer *vs.* time. While $\Delta m/A$ is represented in μg/cm^2, the thickness ξ is in angström (Å) units. For the calculation of ξ, a roughness factor r of 2 has been assumed as an empirical average surface increase. Therefore, in all graphical representations, 1 μg/cm^2 of weight increase corresponds to 31.4Å.

Unfortunately, the oxidation experiments at 400°C had poor reproducibility of the order of ± 25%. The reason for the lack of reproducibility is not yet known. No oxygen-pressure dependence of the oxidation rate could be derived at 400°C since the expected change of the rate lies within the limits of reproducibility. At 500°C, however, a significant dependence of the oxidation rate on the oxygen pressure has been observed.

For the evaluation of the measurements, different rate laws have to be considered. The first period of oxidation is found best represented by a logarithmic rate law

$$\Delta m/A = k_1 \ln(t + t_o) + \text{const} \qquad [1]$$

k_1 is a constant and t_o must be evaluated by trial and error. In Fig. 1 and 2, the measuring data at 400° and 500°C are plotted in a semilogarithmic diagram. The constants k_1 and t_o are summarized in Table I. As can be seen from Fig. 3 and 4, the following larger periods of oxidation can be evaluated by a fourth power rate law

$$(\Delta m/A)^4 = k_o(t + t_o) \qquad [2]$$

According to Eq. [2], the measuring points are plotted as $(\Delta m/A)^4$ *vs.* the time t. The values of k_o in Table I have been calculated from the slopes of the straight lines in Fig. 3 and 4. Furthermore, the time t and the oxide-layer thickness ξ for the transfer from the logarithmic to the fourth power rate law are summarized.

As can be seen from Fig. 4, the kinetics of the oxidation obtained both by Gulbransen and Andrew and by us (4, 3), can be represented by the same rate law. While the absolute values of the rate of oxidation

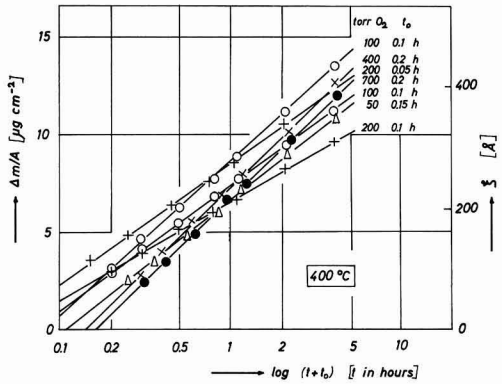

Fig. 1. Semi-logarithmic plot of the rate of oxidation of nickel at 400°C and various oxygen pressures. Only the first 5 hr of oxidation have been plotted since later on deviations from the straight lines occur. t_0 was determined by trial and error.

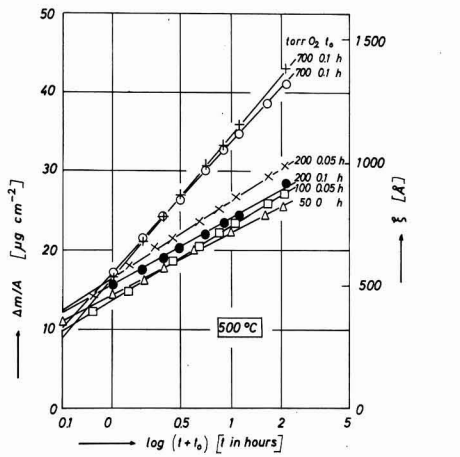

Fig. 2. Semi-logarithmic plot of the rate of oxidation of nickel at 500°C and various oxygen pressures. Only the first 2 hr of oxidation have been plotted since later on deviations from the straight lines occur. t_0 was determined by trial and error.

quoted in (3) are in fair agreement with the present data, those of Gulbransen and Andrew are smaller in spite of the higher temperature (475°C). Obviously, this discrepancy is caused by the higher iron content of our nickel samples. A high impurity of a trivalent metal causes an increase in the rate of oxidation but has no influence on the time law.

Finally, in Fig. 5 there is represented the oxygen-pressure dependence of the rate constant of the fourth power rate law. The reproducibility is not good. But the increase of the rate with increasing oxygen pressure can be clearly demonstrated.

Discussion

According to other oxidation experiments with nickel, the oxide layer growth was expected to follow a logarithmic rate law at the very beginning of oxidation. The period of this rate law becomes smaller with increasing temperature. At 500°C this period lasted only approximately 1 hr while at 400°C the period was about 4 hr. The isothermal logarithmic rate constants are nearly independent of the oxygen pressure (see Table I). The understanding of the logarithmic rate law is at present not satisfying in spite of the large effort in theoretical treatment (7-9, 11, 12). This

Table I. Oxidation of nickel with thin oxide layers at 400° and 500°C

Temperature of oxidation	Constants of the logarithmic rate law			Transition from the logarithmic to the fourth rate law at about		Rate constant k_0 of the fourth power rate law,
°C	P_{O_2}, Torr	t_0, hr	k_1, μg/cm²	Hour	Å*	μg⁴ cm⁻⁸ h⁻¹
400	50	0.15	3.0	6	380	$2.9 \cdot 10^3$
	100	0.1	2.8	5-9	390	$3.5 \cdot 10^2$
	100	0.1	3.4	7-10	490	$3.4 \cdot 10^3$
	200	0.1	2.2	5-6	330	$4.7 \cdot 10^2$
	200	0.05	2.7	5-10	420	$7.4 \cdot 10^2$
	400	0.2	3.6	5-6	440	$1.0 \cdot 10^1$
	700	0.2	3.7	6	430	$5.3 \cdot 10^3$
500	50	0	4.8	2	820	$1.0 \cdot 10^5$
	100	0.05	5.8	3-4	970	$1.7 \cdot 10^5$
	200	0.1	5.3	2-4	990	$2.1 \cdot 10^5$
	200	0.05	6.1	2-4	1050	$3.2 \cdot 10^5$
	700	0.1	9.8	3-4	1460	$9.9 \cdot 10^5$
	700	0.1	10.8	3	1510	$1.5 \cdot 10^6$

* Calculated with the estimated value for the surface roughness $r = 2$.

unsatisfying situation was discussed by Hauffe and Schottky (10).

After the logarithmic period of oxidation, the experimental data obtained at longer exposure time both at 400° and 500°C fit very well the relation of the fourth power rate law derived below. Furthermore, it is predicted by our theory that the validity of the fourth power rate law is limited. At a certain thickness of the oxide layer, it starts to obey the rate law and approximately after doubling the thickness of the oxide layer, the rate law is no longer valid. At 400°C, the validity of the fourth power rate law could

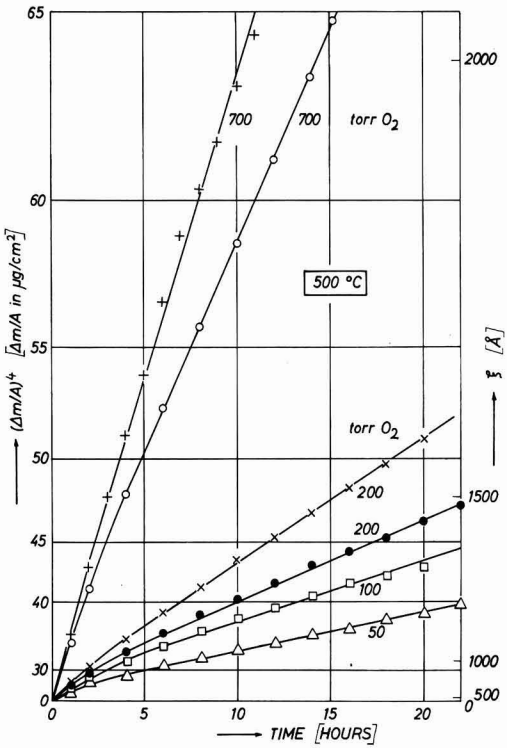

Fig. 3. Oxidation of nickel at 500°C and different oxygen pressures. In order to demonstrate the validity of the fourth power rate law, $(\Delta m/A)^4$ is plotted vs. time.

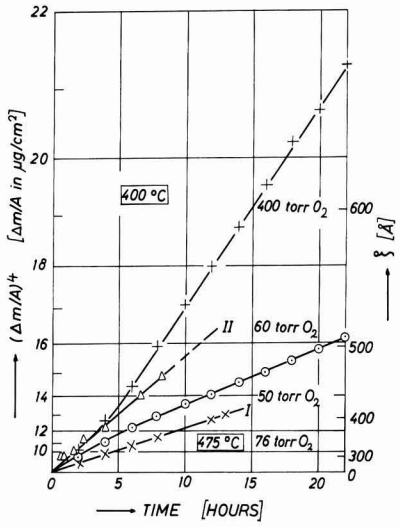

Fig. 4. Oxidation of nickel at 400°C. $(\Delta m/A)^4$ vs. time is plotted. The reproducibility of these experiments was unsatisfactory (±25%), but nevertheless, each experiment followed the fourth power rate law. Only two curves are represented as examples. As comparison to other measurements, the lines I and II are plotted from experimental data obtained by Gulbransen and Andrew and by Engell *et al.*, respectively.

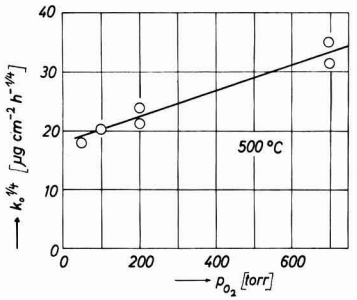

Fig. 5. Oxygen-pressure dependence of the rate of oxidation at 500°C. $k_0^{1/4}$ is plotted *vs.* p_{O_2}.

be observed after the thickness had reached about 500Å and at 500°C, about 1000Å. That is in rather good agreement with the theoretically predicted value given below. Since the oxidation rate became rather slow with increasing thickness of the oxide layer, we did not wait for the doubling of the initial thickness. The change into the parabolic rate law at longer oxidation time has been found.

In the present paper, the mechanism of the dependence of the rate of oxidation on the oxygen pressure is not discussed because more experimental data are necessary. In spite of the scattering of the values around the straight line in Fig. 5, the oxygen pressure dependence of k_0 is demonstrated.

The fourth power rate law.—Under the assumption that the corresponding chemical equilibrium is established at the phase boundaries O_2/NiO and NiO/Ni, the ambipolar diffusion and/or the electric field transport of nickel ions via nickel-ion vacancies $|Ni|''$ and electron holes $|e|^{\circ}$ must be the rate-determining step of the oxidation. The rate of oxidation is proportional to the flux of nickel ions, $j_{|Ni|''}$, via nickel-ion vacancies. In the following derived equations, x shall denote the local coordinate perpendicular to the surface (NiO/O_2) of the sample with $x = 0$ at the surface and $x = \xi$ at the interface NiO/Ni. As already discussed (10, 15), $j_{|Ni|''}$ can be written as a function of x

$$j_{|Ni|''}(x) = -D_{|Ni|''}\frac{dc_{|Ni|''}(x)}{dx} - c_{|Ni|''}u_{|Ni|''}\frac{dV(x)}{dx} \qquad [3a]$$

$D_{|Ni|''}$, $c_{|Ni|''}$, and $u_{|Ni|''}$ are the diffusion coefficient, the concentration, and the mobility of the nickel-ion vacancies, respectively, and V is the electrical potential. A similar equation can be employed for the description of the flux of holes. Both relations have to be combined with the Poisson equation

$$\frac{d^2V}{dx^2} = -\frac{1}{\epsilon\epsilon_0}(z_{|Ni|''}c_{|Ni|''} + c_+)e \qquad [3b]$$

which results in rather complex integro-differential equations (15, 10, 11). $z_{|Ni|''}$ $(= -2)$ is the valence of the nickel-ion vacancy, e the elementary charge, c_+ the concentration of electron holes, ϵ_0 the permittivity of free space, and ϵ the dielectric constant.

Since the mathematical evaluation yields in equations which cannot be tested directly by available experimental data, we have decided to introduce physically reasonable simplifications supplying time laws which can be employed for the evaluation of oxidation experiments.[2] Therefore, the following two cases have been introduced

$$c_+ >> z_{|Ni|''}c_{|Ni|''} \qquad [4a]$$

and

$$c_+ << z_{|Ni|''}c_{|Ni|''} \qquad [4b]$$

The first case is characterized by a strong chemisorption of oxygen and by a positive space charge in the NiO layer. This results in a cubic rate law (3). As can be seen from the experimental data, both in the former (3) and in the present paper, the obtained data fit better the $(\Delta m/A)^4 \sim t$ rate law which is derived below under the validity of condition [4b]. This condition is characterized by a negative space charge in the NiO layer usually involved in an ambipolar diffusion of ionic and electronic species. Under our experimental conditions, such space-charge layers can have a thickness of several hundreds or thousands of angströms depending on the disorder of the oxide lattice (16).

It is assumed, as in the metal semiconductor-rectifier theory, that the position of the valence band in NiO with respect to the Fermi level in the metal is independent of the thickness of the oxide, and, to our approximation, the doping of the oxide. It is, furthermore, similarly assumed that the surface state due to the oxygen ion pins the Fermi potential at the oxide-gas interface, independent of oxide thickness. Furthermore, it is speculated that the energy levels of electrons on the adsorbed oxygen are deep, so the Fermi potential is pinned near the valence band at the oxide-gas interface, closer than the pinning of the Fermi potential at the oxide-metal interface. It is also assumed that the acceptors in NiO are reasonably shallow.

In the mathematical analysis below, the p-type situation is specified, as the system to be analyzed, although of course the n-type case will be similar. In

[2] With this approximation we digress from the approach of Fromhold, who considered in detail the influence of space charge effects in oxide growth (11). In the cited work, no approximation was made and numerical methods of solution were therefore required. The present approximation, limiting the range of validity of the expression is not a drawback as the range of validity is where space charge effects show the strongest influence. Because of the approximation analytical methods become possible. The characterization of oxide growth is then separated into three parts, first the region of very thin oxide (parabolic), second an intermediate region dominated by space charge effects (present work), and third, the region of thick oxides dominated by diffusion (parabolic). Analysis of the laws for the transition between these regions requires numerical methods.

the following, we substituted $j_{|Ni|''}$ $c_{|Ni|''}$, etc. by j, c, etc. We assume the current of nickel-ion vacancies from the surface to the metal is predominantly driven by the electric field. Therefore, we write

$$\left| D \frac{dc}{dx} \right| << \left| c\, u \frac{dV}{dx} \right| \qquad [4c]$$

Thus with Eq. [3a] we obtain

$$j(x) = -c\, u\, dV/dx \qquad [5]$$

With the relation, fulfilled in the first approximation (10)

$$dj(x)/dx = 0$$

we obtain

$$\frac{dc}{dx}\frac{dV}{dx} + c\frac{d^2V}{dx^2} = 0$$

Inserting dV/dx from Eq. [5] and d^2V/dx^2 from the Poisson relation

$$\frac{d^2V}{dx^2} = -\frac{zce}{\epsilon\epsilon_0} \qquad [6]$$

yields

$$\frac{dc}{dx} = -\frac{\alpha}{2}c^3 \quad \text{with} \quad \alpha = \frac{2\,zeu}{j\epsilon\epsilon_0} \qquad [7]$$

Integration with the limiting condition that the density of nickel-ion vacancies is constant at the surface, *i.e.*

$$c = c_0 \text{ for } x = 0 \text{ at the interface gas/oxide}$$

supplies

$$c = 1/(\alpha x + 1/c_0^2)^{1/2} \qquad [8]$$

By insertion of Eq. [5], dV/dx and V itself become calculable

$$\frac{dV}{dx} = -\frac{j}{u}(\alpha x + 1/c_0^2)^{1/2} \qquad [9]$$

Integration with the boundary condition

$$V = 0 \quad \text{for} \quad x = 0$$

supplies

$$\beta V = (\alpha x + 1/c_0^2)^{3/2} - 1/c_0^3 \qquad [10a]$$

with

$$\beta = -\frac{3}{2j}\alpha u = -3\,zeu^2/(\epsilon\epsilon_0 j^2) > 0 \qquad [10b]$$

From our model we conclude that the difference of the valence band in NiO at both the interfaces, NiO/O_2 and NiO/Ni, is constant, which leads to a boundary condition of the form

$$V = V_0 \qquad \text{at } x = \xi$$

where V_0 is a constant potential (with respect to the potential at the surface) at the metal-oxide interface, and ξ represents the locus of the oxide-metal interface, *i.e.* ξ is the width of the NiO layer. Therefore, Eq. [10] can be reformulated

$$\beta V_0 = (\alpha\xi + 1/c_0^2)^{3/2} - 1/c_0^3 \qquad [11]$$

This equation is a fundamental one because it brings the interrelation between the cation flux j and the other entities c_0, V_0, and u as the dominant variables.

In order to avoid an equation of the 3rd order during the evaluation of j, the following reasonable assumption is allowed

$$c_0 >> (\alpha\xi)^{-1/2} \approx c(\xi)$$

which is equivalent to the relation

$$\alpha\xi >> 1/c_0^2 \qquad [12]$$

Therefore, Eq. [11] will be modified to

$$\beta V_0 = (\alpha\xi)^{3/2} \qquad [13]$$

By raising to second power and inserting α and β from Eq. [7] and [10], we obtain

$$j = \frac{9\,\epsilon\epsilon_0 u V_0^2}{8\,ze} \cdot \frac{1}{\xi^3} \qquad [14]$$

and with the relation

$$j = c_{Ni}\, d\xi/dt \qquad [15]$$

where c_{Ni} is the concentration of nickel ions in the oxide, finally, the fourth power rate law reads

$$\frac{d\xi}{dt} = \frac{k_0}{4} \cdot \frac{1}{\xi^3} \qquad [16]$$

with

$$k_0 = \frac{9\,\epsilon\epsilon_0 u V_0^2}{2\,zec_{Ni}} \qquad [17]$$

or integrated

$$\xi^4 = k_0(t + t_0) \qquad [18a]$$

or

$$\xi = k_0^{1/4}(t + t_0)^{1/4} \qquad [18b]$$

with t_0 as integration constant.

For further considerations, it is necessary to investigate the limits of the applicability of Eq. [18]. By inserting Eq. [5] into the dissimilar terms [4c] and substituting dc/dx by Eq. [7], then we obtain with the Nernst-Einstein relation

$$j^2 >> \frac{u^2\, kT\, c^3}{\epsilon\epsilon_0} \qquad [19]$$

Since in the interior of the oxide layer $c_0 \geq c(x)$, the applicability of this relation is permitted only if condition [19] is fulfilled. With Eq. [14], it follows

$$\xi^6 << \left(\frac{9}{8}\right)^2 \frac{(\epsilon\epsilon_0)^3 V_0^4}{(ze)^2\, kT\, c_0^3}$$

and we obtain for the upper limit of ξ

$$\xi < \gamma \left| \frac{3\,ze\,V_0}{kT} \right|^{1/6} \qquad [20]$$

with

$$\gamma = \left\{ \frac{3}{4} \left| \frac{\epsilon\epsilon_0 V_0}{zec_0} \right| \right\}^{1/2} \qquad [20a]$$

Correspondingly, we obtain under consideration of Eq. [14] with the relation [12] if α from Eq. [7] is inserted

$$\xi^4 >> \left(\frac{3}{4}\frac{\epsilon\epsilon_0 V_0}{zec_0}\right)^2$$

or with Eq. [20a]

$$\xi^4 >> \gamma^4$$

and finally, we obtain for the lower limit of ξ

$$\xi > \gamma \qquad [21]$$

Therefore, the validity of Eq. [18] is given by

$$|3\,ze\,V_0/kT|^{1/6} > \xi/\gamma > 1 \qquad [22]$$

From the relation [22], it can be concluded that the ξ^4 rate law is applicable only in a small region of oxide thickness. With the data $V_0 = 1$v, $c_0 = 10^{17}$ cm^{-3}, $\epsilon = 3$, $T = 800$°K, and $z = -2$, we obtain for

$$\gamma \approx 3 \cdot 10^{-6} \text{ cm}$$

and for

$$|3\,ze\,V_0/kT|^{1/6} = 2$$

By means of these values and Eq. [22], it can be seen that the law should be obeyed after an oxide thickness of 300Å has been built up. Furthermore, the thickness of the oxide layer where the validity of the ξ^4 rate law ceases, should be double the thickness at which it starts, *i.e.*, when the oxide layer has grown approximately by a factor of 2.

According to our experiments at 400°C, the kinetics of oxidation fit the relation ξ^4 *vs.* t rather well when

the thickness of the oxide layer has attained nearly 400Å. For higher temperatures, the validity region of this time law is shifted to lower thicknesses of the oxide layer. Engell, Hauffe, and Ilschner (3) have also found for the oxidation of nickel at 400°C a fourth power rate law ($\Delta m \sim t^{1/3.7}$-$t^{1/3.9}$) which changed later on to a parabolic one.

Another parabolic rate law should govern if the following relation is valid

$$\alpha\xi << 1/c_o^2 \qquad [12a]$$

instead of Eq. [12] which is a presupposition of the fourth power rate law. Such a parabolic rate law was first formulated by Cabrera and Mott (13). Relation [12a] is equivalent with

$$c = c_o \qquad [8a]$$

and

$$dV(x)/dx = -j/(uc_o) \qquad [9a]$$

Such a field-aided parabolic rate law could be found for the oxidation of zinc (14). Recently, Fromhold (18) has generalized the discussion on the validity of the parabolic rate law.

In order to compare our rate constant k_o to the data available in the literature, we tried to calculate k_o with the aid of the Nernst-Einstein equation and the relation between the tracer-diffusion coefficient and the component-diffusion coefficient D_{Ni} [3]

$$k_o = \frac{9\,\epsilon\epsilon_o\,D_{Ni}\,V_o^2}{2ckT}$$

D_{Ni} can be estimated from tracer-diffusion measurements carried out by Lindner and Åkerström (19) between 740° and 1400°C, by Choy and Moore (20) between 1000° and 1400°C, and by Klotsman, Timofeef, and Trakhtenberg (21) between 1200° and 1400°C if the diffusion data are extrapolated to 500° and 400°C, a procedure in many respects doubtful. From the extrapolation of the data of the last mentioned authors, the following values for D_{Ni} have been obtained: 10^{-19} (400°C) and 10^{-17} (500°C) cm²/sec. The corresponding values of Choy and Moore are an order of magnitude higher and those of Lindner and Åkerström an order of magnitude lower.

If we employ the data of $c_{|Ni|''} \equiv c$ published by Schlosser (22) ($c = 4\cdot10^{14}$ at 400°C and $c = 1\cdot10^{15}$ cm^{-3} at 500°C) and take $\epsilon = 3$ and $V_o = 1$v, then the following values for k_o are obtained

$$\left.\begin{aligned} k_o &= 1.2\cdot10^4\,\mu g^4\,cm^{-8}\,h^{-1} \text{ at } 400°C \\ k_o &= 4\cdot10^5\,\mu g^4\,cm^{-8}\,h^{-1} \text{ at } 500°C \end{aligned}\right\} \text{and 1 atm air}$$

As can be seen by comparison of these data with those in Table I, in spite of the rough extrapolation, the agreement is rather good.

Summarizing we may conclude that the oxidation of nickel should start in analogy to the oxidation of zinc (14) with a field-aided parabolic rate law and changes into a fourth power rate law. After this period, a parabolic rate law again rules, but now under the condition of a diffusion-controlled mechanism. Unfortunately, the kinetics of the nickel oxidation at the very beginning with oxide thicknesses below 300Å does not obey the parabolic plot as expected in analogy for the oxidation of zinc. But this result is not confusing since in the first period of oxidation, nucleation, and oxide needle formation can become predominant causing a logarithmic rate law (12). For the oxidation of bismuth (17), however, the rate of oxide layer growth between 175° and 250°C at 30 Torr oxygen can be represented from the very beginning up to 10-13 $\mu g/cm^2$ by a parabolic rate law and later on by a fourth power rate law.

[3] This relation has been derived explicitly by Schottky (10).

Acknowledgment

We are greatly indebted to the Deutsche Forschungsgemeinschaft for supplying the experimental equipment and the Max-Buchner-Forschungsstiftung for the financial support to one of us (R.S.) Furthermore, we wish to thank Hüttenwerk Oberhausen AG for the salary of Dr. L. Pethe during his stay at the Institute.

Manuscript received Oct. 19, 1967; revised manuscript received *ca.* Jan. 16, 1968.

Any discussion of this paper will appear in a Discussion Section to be published in the December 1968 JOURNAL.

REFERENCES

1. See for instance K. Hauffe, "Oxidation of Metals," p. 171 ff, Plenum Press, New York (1965).
2. C. Wagner and K. Grünewald, *Z. phys. Chem.* (B), **40**, 455 (1938).
3. H. J. Engell, K. Hauffe, and B. Ilschner, *Z. Elektrochem.*, **58**, 478 (1954).
4. E. A. Gulbransen and K. F. Andrew, *This Journal*, **101**, 128 (1954).
5. W. Campbell and U. Thomas, *Trans. Electrochem, Soc.*, **91**, 623 (1947); K. Hauffe and B. Ilschner, *Z. Elektrochem.*, **58**, 382 (1954).
6. H. H. Uhlig, J. Pickett, and J. MacNairn, *Acta Met.*, **7**, 111 (1959).
7. N. F. Mott, *Trans. Faraday Soc.*, **43**, 429 (1947).
8. P. T. Landsberg, *J. Chem. Phys.*, **23**, 1079 (1955).
9. H. H. Uhlig, *Acta Met.*, **4**, 541 (1956).
10. K. Hauffe and W. Schottky, Deckschichtbildung auf Metallen, in Halbleiterprobleme, Vol. 5, pp. 316-319, Braunschweig (1960).
11. A. T. Fromhold, Jr., *J. Chem. Phys.*, **38**, 282, 2041 (1963), **39**, 2278 (1963), **40**, 3335 (1964).
12. U. R. Evans, "The Corrosion and Oxidation of Metals," London (1960).
13. N. Cabrera and N. F. Mott, *Rept. Progress Physics*, **12**, 163 (1949).
14. H. J. Engell and K. Hauffe, *Metall.*, **6**, 285 (1952).
15. K. Hauffe and B. Ilschner, *Z. Elektrochem.*, **58**, 467 (1954).
16. B. Ilschner, *Z. Elektrochem.*, **59**, 542 (1955).
17. M. G. Hapase, V. B. Tare, and A. B. Biswas, *Acta Met.*, **15**, 131 (1967).
18. A. T. Fromhold, Jr., *J. Chem. Phys.*, **41**, 509 (1964).
19. R. Lindner and Å. Åkerström, *Disc. Faraday Soc.*, **23**, 133 (1957).
20. J. S. Choy and W. J. Moore, *J. phys. Chem.*, **66**, 1308 (1962).
21. S. M. Klotsman, A. N. Timofeef, and I. Sh. Trakhtenberg, *Fiz. Metal. i Metalloved.*, **14**, 428 (1962).
22. E. G. Schlosser, *Z. Elektrochem.*, **65**, 453 (1961).

Ignition Behavior of Plutonium Metal and Certain Binary Alloys

J. G. Schnizlein and D. F. Fischer

Argonne National Laboratory, Argonne, Illinois

ABSTRACT

The ignition behavior of plutonium and binary alloys containing nominally 2 a/o additives was studied by two methods in air and oxygen. Ignition temperatures in both air and oxygen lie in two regimes. Cubes, 5 mm on an edge, ignite near 500°C while thin foils, less than 0.2 mm thick, ignite near 300°C. The transition from one regime to the other occurs sharply at a specific area that depends on whether ignition takes place in air or in oxygen. The existence of two regimes is consistent with a change of oxidation kinetics between 300° and 400°C which is characterized by a minimum in oxidation rate near 400°C. The effects of additives are sometimes significant and must be considered in each regime and on the position of the transition between them. In the high temperature regime: (*i*) Increased resistance to ignition and oxidation is found on addition of aluminum, copper, gallium, or silicon; (*ii*) The same ignition and oxidation behavior as plutonium occurs with addition of nickel, chromium, uranium, cerium, or iron; and (*iii*) Decreased resistance to ignition and oxidation results from addition of carbon, cobalt or manganese. In the low temperature regime: (*i*) Increased resistance to ignition and oxidation is produced by additions of aluminum, cerium, carbon, cobalt, gallium, manganese or possibly chromium; (*ii*) The same ignition and oxidation behavior as plutonium is obtained with addition of nickel or silicon; and (*iii*) Decreased resistance to ignition and oxidation follows from addition of iron or uranium.

The transition from the high temperature regime to the low temperature regime does not occur in air for alloys of aluminum, cerium, carbon, or cobalt for specimens with specific areas of up to about 1 cm^2/g. Addition of silicon, nickel, manganese, or uranium have little influence on the transition in air which occurs at a specific area of 1.5 cm^2/g for pure plutonium. The presence of moisture had a negligible effect on the ignition temperatures of pure plutonium and the aluminum alloy.

The increasing use of plutonium in the nuclear energy program and the concomitant handling makes the development of safe handling procedures imperative. Accidental ignition of the metal is a hazard (1) per se and the possibility of dispersing extremely toxic fine particulate plutonium oxide extends the danger. Moreover, inordinately large expenses of time, money, and manpower in the past have been incurred in the decontamination procedures which must follow accidental ignition of the metal.

The literature on ignition of plutonium is largely restricted to reports of the USAEC and UKAEA. The first direct study of the ignition of plutonium was reported by Dempsey (2). Earlier, Dempsey and Kay (3) observed ignition during an experiment intended to be isothermal at 487°C. Ignition occurred after oxidation had proceeded for about 300 min. During a study of the particulate material produced during the burning of plutonium, Carter, Foy, and Stewart (4) observed ignition temperatures of turnings and small billets.

Thompson (5) observed ignitions to occur between 230° and 420°C in oxygen and between 310° and 505°C in air at 35% relative humidity. No positive correlations between temperature and weight, area, or rate of heating were observed. In atmospheres containing less than 6.5% oxygen in argon, no ignition occurred below 900°C. Above about 10% oxygen the ignition temperatures were between 400° and 500°C. Rhude (6) found that in a glovebox with only 5% oxygen in nitrogen the metal will burn readily. At the 1% level combustion will not continue unless heat is supplied. Cope (7) has developed a ternary eutectic salt mixture which shows promise (8) as a dry powder extinguisher for some plutonium fires. The problems of airborne particulate plutonium have recently been reviewed by Mishima (9) in the United States and Stewart (10) in Great Britain.

Although oxidation studies of plutonium alloys have been reported (11-14) at somewhat elevated temperatures, the only ignition studies of binary alloys are those by Dempsey (2) and Carter *et al.* (4) in which an aluminum additive was used to stabilize the delta phase of plutonium.

The present study of the ignition characteristics of plutonium and certain alloys was undertaken in conjunction with a study of the kinetics of isothermal oxidation (15) to aid in evaluating hazards in handling plutonium. Two experimental methods were developed for determining ignition temperatures. In addition to the study of pure plutonium, the influence of potential impurities and possible additives was appraised by the study of a series of binary alloys containing nominally 2 a/o (atom per cent) of various elements. Some elements were chosen because they are typical impurities in plutonium; other elements were chosen to study the effects of a given series in the periodic chart. Additives of aluminum, carbon, cerium, chromium, cobalt, copper, iron, gallium, magnesium, manganese, nickel, silicon, uranium, and zinc were used.

Materials and Procedures

Because of the extreme toxicity of plutonium, all experiments were performed in gloveboxes. To avoid accidental ignitions or oxidation of metal surfaces, a dry nitrogen atmosphere was used. Oxygen or air and helium were used directly from gas cylinders except in experiments where the moisture content was controlled. The contents of each cylinder used were analyzed by mass spectrometry to avoid accidental contaminants.

The plutonium and alloy cubes and foil specimens were prepared at Hanford.[1] Specially selected reactor

[1] Preparations were under the supervision of R. R. King, P. G. Pallmer, T. Nelson, R. W. Stewart, and O. J. Wick, General Electric Company, Hanford Atomic Products Division, Richland, Washington.

Table I. Plutonium analyses
Parts per million

Impurity element	Typical reactor grade plutonium	Alloys[a]	Unalloyed pure plutonium
C	50-400	200-500	90
O	100-600	50-200	50
Fe	50-1000	20-300	120
Ni	30-500	10-30	16
Mn	50-200	5-75	5
Cr	20-250	2-20	10
Mg	10-500	2-500	50
Al	20-100	<10	<10
Cu	10-80	5-70	20
Ca	5-250	5-50	10
Total metallic impurities	200-2900	50-1050	250

[a] Excluding intentional additive.

grade plutonium was used to minimize impurity content of both pure plutonium samples and binary alloy samples. Analyses of plutonium used for preparation of samples and of alloys are compared with typical reactor grade plutonium in Table I. Pure plutonium specimens were in the form of 5 mm cubes and 3 x 20 mm sections of foils having thicknesses ranging from 1 to 0.1 mm.

The binary alloys of plutonium contained nominally 2 a/o of various chosen elements. Additives of aluminum, carbon, cerium, chromium, cobalt, copper, iron, gallium, magnesium, manganese, nickel, silicon, uranium, and zinc were of the highest purity available. The additive element content was determined at Hanford by the most accurate method then known. The binary alloys were used in this study in the form of 5 mm cubes and such foils as it was possible to fabricate. For the manganese alloy it was possible to prepare samples with thickness down to 0.07 mm (17.2 cm^2/g specific area), whereas for the uranium alloy, the thinnest foil that could be produced was 0.89 mm thick (1.9 cm^2/g specific area).

The ignition experiments are a kind of thermal analysis originally used by Fassel (16) for magnesium alloys. Two methods were used: The first, in which the oxidizing gas was present during the heating, is called a burning-curve experiment; the second method is called a shielded ignition experiment because the oxidizing gas was excluded by helium until the test temperature was reached. These methods have previously been used for the study of ignition of uranium and its alloys (17-19) and were found to provide reproducible results. Burning-curve and shielded-ignition experiments were performed with air or oxygen.

In the burning-curve experiment, the specimen was supported on a thermocouple in a vertical tube furnace and was heated at a programmed rate in a flowing oxidizing gas until ignition occurred. The programming was such that the temperature of an inert sample increased at a uniform rate (usually 10 deg/min). The heat of oxidation of a reactive sample caused an increase of temperature (self-heating) above the control temperature. An increase of oxidation rate caused an increase of the slope of the temperature-time trace. When ignition occurred, the slope rapidly approached an infinite value and the sample usually self-heated to its maximum burning temperature. The ignition temperature was determined graphically from the temperature-time trace as the intersection of the pre-ignition heating curve with the post-ignition self-heating curve. Some thermogravimetric experiments were performed in this manner on a thermobalance equipped with a transducer to permit simultaneous weight and temperature measurement (20). A platinum crucible was hung under the sample to avoid loss of weight due to dropping oxide.

In a shielded-ignition experiment the sample was heated to the test temperature in a protective atmosphere of helium. The protective gas was then rapidly replaced by the oxidant to determine whether ignition occurred at the test temperature. For these experiments the ignition temperature is reported as the range between the highest temperature at which ignition did not occur and the lowest temperature at which ignition did occur.

Experimental Results

Comparison of the temperature-time curves of various samples in an oxidizing atmosphere provides a measure of the relative oxidation rate and ignition behavior. The relative oxidation rate can be assessed by the extent of self-heating or temperature increase above the control temperature at a particular time. The ignition behavior of various samples can be compared by consideration of the temperature or time of sudden temperature increase. Burning curves in air for 5 mm cubes of plutonium and a plutonium-silicon alloy are illustrated in Fig. 1. The ignition temperature for pure plutonium was found to be 508°C and for the silicon alloy, 544°C.

After ignition in air the resulting oxide was considerably larger than the original metal sample and had numerous protuberances. Figure 2 illustrates the appearance of a 5 mm cube in the platinum crucible before and after ignition at 508°C in air.

Pure plutonium.—Burning-curve and shielded-ignition experiments were performed with pure plutonium specimens in both air and oxygen. The specimens were 5 mm cubes and 3 x 20 mm sections of foils having thickness of 1, 0.5, 0.22, 0.17, and 0.13 mm. Ignition temperatures determined by both methods in air and oxygen are listed in Table II. In most cases ignition temperatures determined by the shielded method are somewhat lower than those obtained by the burning-curve method. Ignition temperatures obtained by the burning-curve method are plotted as a function of specific area of the sample in Fig. 3. Ignition data from Dempsey and Kay (3) and from Carter, Foy, and Stewart (4) are also included for comparison. The variation of ignition temperature with specific area yields a step function instead of a gradual change over the range studied. Ignition occurs in one of two regimes, one at about 300°C (282°-322°) and the other at about 500°C (468°-535°). The transition from one regime to the other occurs at a specific area of

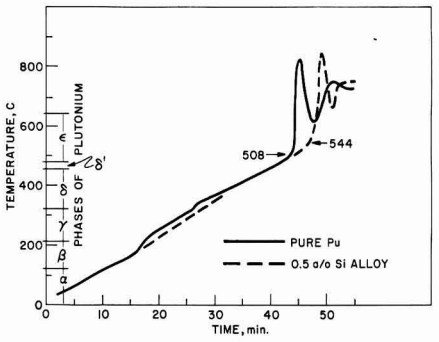

Fig. 1. Burning curves in air

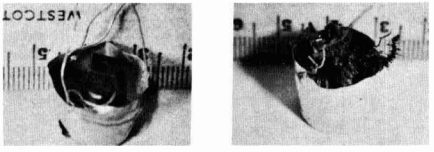

Fig. 2. Plutonium cube before and after ignition at 508°C in air.

Table II. Ignition temperatures of plutonium in air and oxygen

Foil thickness, mm	Specific area, cm^2/g	Burning curve ignition temperatures, °C Air	O_2	Shielded-ignition temperatures,[a] °C Air	O_2
~5 (cube)	0.65	520	512	442-492	—
		508	494		
1.0	1.5	492	490	378-408	327-374
		322			
0.52	2.5	310	468	303-337	353-398
		314	505		
0.22	5.3	518	524	375-403	322-350
		520	527		
		535			
		519[b]			
		521[b]			
0.17	6.7	282	299		
0.13	11.0	282	305	266-280	273-284

[a] Indicated as the highest temperature at which ignition did not occur and the lowest temperature at which ignition did occur.
[b] Samples were polished with 600 grit SiC paper; all others as received.

1.5 cm^2/g in air and at 6.0 cm^2/g in oxygen. The sharpness of the change is illustrated in Fig. 4 where two burning curves for 1.0 mm thick (1.5 cm^2/g) foil specimens heated in air are shown. At this specific area the ignition might occur in either regime although the difference of specific area of the two samples was indistinguishable. It will be noted that the thermal effects of plutonium phase transitions can be detected on the curves. These were observed in most experiments and provide assurance of good contact between the thermocouple and the sample.

The 0.22 mm thick foil gave anomalous results in air. Its ignition temperature in air was consistently in the high temperature regime even though its specific area, 5.3 cm^2/g, was considerably greater than the 1.5 cm^2/g point of transition for other foil samples. No explanation for this anomalous behavior was found.

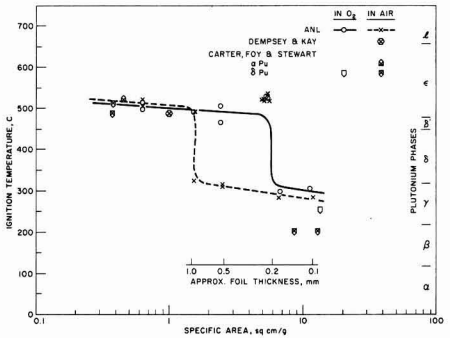

Fig. 3. Ignition temperatures of plutonium by the burning-curve method.

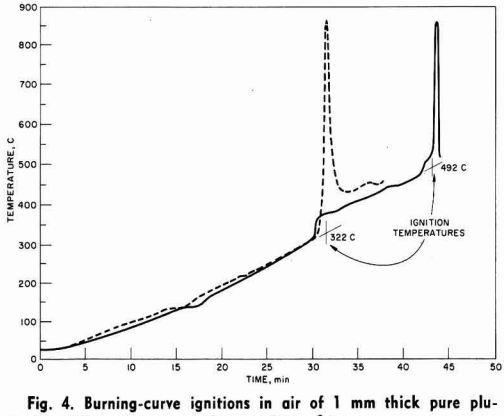

Fig. 4. Burning-curve ignitions in air of 1 mm thick pure plutonium foil specimens, specific area 1.5 cm^2/g.

In air the ignition temperatures in the low temperature regime are somewhat lower than in oxygen. However, in the high temperature regime no difference is observed. Ignition results reported by Dempsey and Kay (3) and by Carter, Foy, and Stewart (4) were generally consistent with the other results plotted in Fig. 3.

Shielded-ignition temperatures (Table II) are appreciably lower than burning-curve ignition temperatures in the high temperature regime but are only slightly lower in the low temperature regime.

Plutonium binary alloys.—All chosen alloys were available in the form of 5 mm cubes. However, it was impossible to fabricate some of the alloys into foils as thin as was desired. Burning-curve experiments were performed in both air and oxygen for all cubes and foils. Shielded-ignition experiments were performed in both air and oxygen for most foils. Because of the large number of samples required to define a narrow temperature range between ignition and nonignition, only a few cubes were studied in this manner; the range of shielded-ignition temperature for a few of the foils is also larger than desirable.

Results of ignition temperature determinations for the alloys are presented in Table III. The additive elements were intended to be 2 a/o but in some cases segregation, evaporation, or reaction with crucible material altered the final concentration. The analyzed (or estimated if no satisfactory analytical procedure was available) content of the additive and the specific area of the samples are included.

For samples in the form of 5 mm cubes ignition temperatures lie in the high temperature regime, and additives have only small effects on the ignition temperature; the greatest effects were found for aluminum, nickel, and cobalt. The ignition temperature of the 3.4 a/o aluminum-plutonium alloy was 60° higher than that of the plutonium base metal. The 2 a/o gallium-plutonium, 2.4 a/o copper-plutonium, and the 1.2 a/o silicon-plutonium alloys ignited at temperatures about 30° higher than did the base metal. In contrast, the 1.8 a/o cobalt and 1.8 a/o nickel alloy ignition temperatures were 30°-40° lower than that of the plutonium base metal. Additives of cerium, carbon, chromium, iron, magnesium, manganese, uranium, and zinc had little effect.

Appraisal of the effect of variation of specific area on ignition temperature for most of the alloys is possible by considering the data on foils. Ignition temperatures were plotted as a function of the logarithm of specific area and a composite trace of the behavior in air for the various additives is presented in Fig. 5. The shapes of the curves are similar to those for pure plutonium except for alloys of aluminum, cerium, carbon, cobalt, and gallium. The transition from the high temperature regime to the low temperature regime does not occur for samples of these alloys with specific areas up to about 10 cm^2/g. The addition of silicon to plutonium causes a shift of the transition in air from a specific area of 1.5 cm^2/g for pure plutonium to 4 cm^2/g for the alloy. Additions of nickel, manganese, and uranium to plutonium cause no change in the transition region in air.

In oxygen the transition to the low temperature regime for the alloys occurs at lower specific areas than it does for pure plutonium.

Effect of moisture on ignition behavior of plutonium and plutonium 3.4 a/o aluminum alloy.—To appraise the effect of moisture on the ignition of plutonium and its alloys, burning curves have been obtained in air saturated with moisture at room temperature (20,000 ppm water). Isothermal studies (15) have shown

Table III. Ignition data for plutonium alloys
Nominally 2 a/o additives

Additive	Analyzed content, a/o	Foil thickness, mm	Specific area, cm^2/g	Burning-curve ignition temperature, °C: Air	Burning-curve ignition temperature, °C: O_2	Shielded-ignition[a] temperature, °C: Air	Shielded-ignition[a] temperature, °C: O_2
Al	3.4	5 (cube)	0.79	588, 590	576		
	1.8	0.26	4.4	544	555		350-388
	3.4	0.26	4.8	557	546	250-388	375-407
	8	0.24	5.6	620	590, 604		382-455
	11	0.82	1.7	425	390		400-432
	11	0.13	10	412	440		398-402
Ce	0.5[b]	5 (cube)	0.64	510	485		
	0.5[b]	0.96	1.6	488	478	398-436	406-442
	0.5[b]	0.11	11.0	478	481	325-351	299-342
C	2[b]	5 (cube)	0.65	498	486		
	1.55	5 × 5.6 diam rod	0.63	295, 459	208, 447, 455		
	2[b]	0.97	1.6	474	478	401-440	287-328
	0.9	0.28	4.1	370	330		270-300
	2[b]	0.16	7.8	469	466	386-428	275-309
Co	1.8	5 (cube)	0.67	474	462		
	1.8	0.93	1.7	456	465	410-477	380-413
	1.8	0.23	5.2	465	462	346-389	340-390
Cr	2[b]	5 (cube)	0.65	512, 514	498, 507		
	2[b]	1.01	1.70	513	503	325-375	
	2[b]	0.15	7.5	575	527	380-421	268-380
	2[b]	0.08	14.5	No ign.	517	243-292	
	0.2	0.21	5.8	380	No ign., 320		275-307
Cu	2.4	5 (cube)	0.65	555	533, 546		
Fe	1.8	5 (cube)	0.65	548	515		
	1.8	0.85	1.71	596	266		
	1.8	0.39	3.33	589	567	327-377	
	1.8	0.21	5.7	602	289	271-315	243-287
					No ign.		
	1.8	0.11	11.5	352	253	246-288	
	2.0	5 × 5.7 diam rod	0.60	476, 485	520		
				490, 516			
	2.5	0.26	4.88	372	330		307-348
	2.0	0.25	5.16	358	310		
	2.0	0.19	6.60	550	532, 537, 539		
Ga	2	5 (cube)	0.78	550	534		
		0.25	5.1	546, 539	523, 598	381, 405	350-375
		0.25 (cold rolled)	5.1	546	528		391-416
Mg	0.2	5 (cube)	0.7	520	512		
Mn	2.7	5 (cube)	0.66	499	477		
	2.7	1.0	1.6	496	482	362-406	249-294
	2.7	0.53	2.7	293	320	221-258	240-288
	2.7	0.24	5.3	365, 598	293	257-288	276-300
	2.3	0.21	5.6	330	247		214-230
	2.7	0.10	12.1	No ign.[c]	289	282-317	242-278
	2.7	0.07	17.2	No ign.[c]	279	251-258	251-282
Ni	1.8	5 (cube)	0.66	490, 529	468		
	1.3	5 (cube)	0.64		489, 509		
	1.8	1.05	1.55	486	470	420-263	367-422
	3.2	0.24	5.1	325	316		297-317
	1.8	0.24	5.4	No Ign.[d]	288		
	1.8	0.25	5.4	302			
	1.8	0.15	7.6	No ign.	467	282-335	238-282
Si	0.3	5 (cube)	0.65	544, 548, 548	525, 537, 537	462-511	412-467
	1.2[b]	5 (cube)	0.72	553	540		
	1.2	0.95	1.67	528	515		
	1.2	0.28	4.29	202, 286, 295	318		
	1.2	0.20	5.85	537	310	281-325	265-297
U	2[b]	5 (cube)	0.65	510, 513	490		
	2[b]	0.89	1.9	252, 550	242	(e)-443	(e)-233
Zn	1.03	5 (cube)	0.7	528	523		
	0.40	5 (cube)	0.7	528	503		

[a] Indicated as the highest temperature at which ignition did not occur and the lowest temperature at which ignition did occur.
[b] Estimated content, no satisfactory analysis performed.
[c] Sample completely oxidized or disintegrated before ignition occurred.
[d] There was a thermal spike of 150° at 309°C with no visual ignition. Another spike of 80° was observed at 610°C with no visual ignition.
[e] Insufficient samples were available to determine lower limit of shielded ignition range.

that the presence of moisture increases the linear rate of oxidation at temperatures below 200°C, but has negligible effects at higher temperatures.

Although burning curves indicate that ignition occurs in slightly shorter periods of time in moist air, the graphic method of defining ignition temperatures yields values for experiments carried out in dry air which are essentially identical with those for experiments carried out in moist air. These temperatures, determined by the burning-curve method, are given in Table IV.

Discussion and Summary

Two experimental procedures were used to define the temperatures at which the ignition of plutonium occurs. The first, which is a thermal analysis of the sample heated in an oxidizing atmosphere, is called a burning-curve experiment. In the second, the temperature at which ignition occurs if suddenly exposed to an oxidizing gas, is called shielded-ignition temperature.

Pure plutonium.—The ignition temperatures determined by the burning-curve method for pure plutonium in air or oxygen lie in two regimes: about 500°C for large samples with low specific area, and at about 300°C for thin foils with high specific areas. The existence of these two ignition temperature regimes is consistent with the isothermal oxidation behavior of plutonium (15). A change in the oxidation kinetics occurs just above 300°C. The oxidation rate decreases sharply between 350° and 450°C and the oxide is more protective above 400°C. Evidently, the rate of heat generation by oxidation in the region of 300°C is just sufficient to cause ignition of specimens having large specific areas. Specimens having smaller specific areas have greater thermal inertia, and the temperature increase caused by self-heating occurs more slowly. This allows the formation of a more protective oxide at temperatures near 400°C, where there is a minimum in the oxidation rate. The decreased oxidation rate prevents ignition from occurring until the sample temperature is increased by external heating beyond 450°C whereupon the oxidation rate again rapidly increases with increasing temperature.

For samples igniting in the high temperature regime with the burning-curve method, shielded-ignition tem-

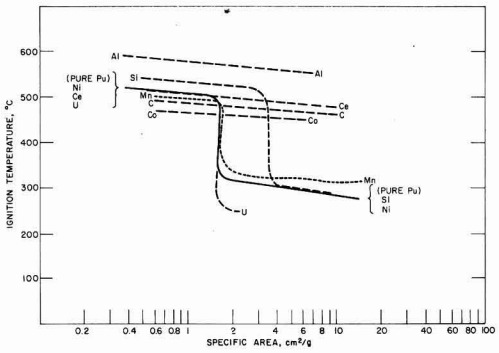

Fig. 5. Effect of additives on ignition behavior in air of plutonium. Each curve labeled with additive element present nominally at 2 a/o conc.

peratures are noticeably lower. In the low temperature regime shielded- and burning-curve experiments provide similar ignition temperatures.

Binary alloys.—Because the ignition temperatures fall in two regimes (consistent with the two regimes observed in the isothermal oxidation), it is necessary to consider the influence of an additive on each regime and on the transition region.

In the high temperature regime the influence of the additives (using the behavior of pure plutonium as the standard for comparison) were as follows:

(*i*) Increased resistance to ignition and oxidation; aluminum, copper, gallium, and silicon.

(*ii*) The same ignition and oxidation behavior as plutonium; nickel, chromium, uranium, cerium, and iron.

(*iii*) Decreased resistance to ignition and oxidation; cobalt, carbon, and manganese.

In the low temperature regime, the influence of the additives was as follows:

(*i*) Increased resistance to ignition and oxidation; aluminum, cerium, carbon, cobalt, gallium, manganese, and possibly chromium.

(*ii*) The same ignition and oxidation behavior as plutonium; nickel and silicon.

(*iii*) Decreased resistance to ignition and oxidation; iron and uranium.

The transition from the high temperature regime to the low temperature regime does not occur in air for alloys of aluminum, cerium, carbon, and cobalt for specimens with specific areas of up to approximately 10 cm^2/g. The addition of silicon to plutonium causes a shift of the transition in air from the specific area of 2 cm^2/g for pure plutonium to 4 cm^2/g for the alloy. Additions of nickel, manganese, and uranium to plutonium caused no change in the transition point from that of pure plutonium.

Moisture.—The presence of moisture in air has negligible effect on ignition temperatures of plutonium and of a plutonium-3.4 a/o aluminum alloy as determined by burning-curve experiments. Because isothermal studies (15) have shown that the presence of moisture has negligible effects on the oxidation kinetics above 220°C, ignition temperatures of samples above 220°C in dry air will not be affected by moisture. It must be pointed out that it does not follow that long term corrosion by moist air or water vapor will not influence the ignition of plutonium.

Table IV. Temperature determined by burning-curve method

		Burning-curve ignition temperature, °C	
		In dry air	In wet air
Pu	5 mm cube	524	522
Pu	0.11 mm foil	283	282
Pu-3.4 a/o Al	5 mm cube	585, 590	569

Acknowledgments

The encouragement of R. C. Vogel, the advice of L. Baker, Jr., and the assistance of J. D. Bingle are gratefully acknowledged. In addition, the authors appreciate the services of the many persons who maintained the glovebox facility, obtained materials, and performed analyses.

Manuscript received March 20, 1967; revised manuscript received *ca.* Nov. 16, 1967.

Any discussion of this paper will appear in a Discussion Section to be published in the June 1968 JOURNAL.

REFERENCES

1. R. B. Smith, *Nucleonics*, **14**, 28 (1956).
2. E. Dempsey, British Report No. 0-49/58, December 1958.
3. E. Dempsey and A. E. Kay, *J. Inst. Metals*, **86**, 379 (1958).
4. R. F. Carter, B. Foy, and K. Stewart, British Report AERO Conf/8 (1960).
5. M. A. Thompson, USAEC Report RFP 491, March 12, 1966.
6. H. V. Rhude, USAEC Report TID 16826, July 1962.
7. L. H. Cope, UKAEA Report DEG 29 (also British Patent 884,946, December 20, 1961).
8. R. F. Powell, E. Demsey, and J. Holliday, UKAEA-AWRE Report No. 0-45/60.
9. J. Mishima, USAEC Report HW 83668 (1964).
10. K. Stewart, in "Progress in Nuclear Energy," Series IV, Vol. 5, p. 535, Pergamon Press, New York (1963).
11. J. T. Waber, W. M. Olson, and R. B. Roff, *J. Nucl. Mat.*, **3**, 201 (1961).
12. M. J. F. Notley, E. N. Hodkin, and J. A. C. Davidson, UKAEA Report AERE-R-4070, June 1962.
13. D. M. Poole, J. K. Critchley, J. A. C. Davidson, P. M. French, E. N. Hodkin, and M. J. F. Notley, "Plutonium 1960," p. 627, Cleaver-Hume Press, London (1961).
14. G. Picton and J. F. Sackman, *J. Nucl. Mat.*, **18**, 292 (1966).
15. J. G. Schnizlein and D. F. Fischer, *J. Electrochem. Soc.*, **114**, 23 (1967).
16. W. M. Fassel *et al.*, *J. Metals*, **3**, 522 (1951).
17. J. G. Schnizlein *et al.*, USAEC Report ANL-5974, 1959.
18. L. Baker, Jr., J. G. Schnizlein, and J. D. Bingle, *J. Nucl. Mat.*, **20**, 22 (1966).
19. J. G. Schnizlein, L. Baker, Jr., and J. D. Bingle, *ibid.*, **20**, 39 (1966).
20. J. G. Schnizlein, John Brewer, and D. F. Fischer, *Rev. Scientific Instruments*, **36**, 591 (1965).

A Film-Thickness Determination of Nitrogen Diffusion in Zirconium Nitride

C. J. Rosa* and W. C. Hagel*

Metallurgy Division, University of Denver Research Institute, Denver, Colorado

ABSTRACT

Calculations of the diffusion coefficient for nitrogen in zirconium nitride are given in terms of a unidirectional, two-phase, volume-diffusion model. These calculations require the knowledge of both the thicknesses of nitride films and of nitrogen diffusion coefficients in the underlying zirconium metal. The values obtained can be represented by $D_{N\rightarrow ZrN} = 7.87 \times 10^{-5} \exp(-35{,}900/RT)$ cm²/sec for the temperature range of 650°-850°C. Zirconium nitriding kinetics for extended exposures up to 900 hr are also reported. The portion of nitrogen confined to the α-zirconium phase amounts to about 80 w/o of the total nitrogen consumed during the over-all nitriding process.

The zirconium-nitrogen reaction has not attracted the interest of many investigators. Gulbransen and Andrew (1) described this metal-gas reaction in the temperature range of 400°-825°C and Dravnieks (2) studied the kinetics at 862°-1043°C. Mallett *et al.* (3) measured the rate of surface reaction of zirconium with nitrogen in the range of 975°-1640°C at 1 atm pressure. All these investigators report that the reaction conformed strictly to a parabolic relationship and that the reaction rate was much slower than with oxygen. These experiments were carried out for short time exposures, up to 7 hr.

More recently, Rosa and Smeltzer (4) investigated nitriding kinetics in terms of models based on the growth of the reaction product layer and simultaneous dissolution of the reactant in the metal substrate. They found that over the temperature range 750°-1000°C, and for exposures up to 170 hr, the reaction obeys the parabolic rate law. Using microhardness measurements, they determined the diffusion coefficient of nitrogen in α-zirconium as $D_N{}^{\alpha-Zr} = 0.15 \exp(-54{,}100/RT)$ cm²/sec, which to the best knowledge of the present authors is the only relationship available at this time.

The purpose of this investigation is to evaluate the diffusion coefficients of nitrogen in hypostoichiometric zirconium nitride for the temperature range of 650°-850°C in terms of data from nitriding kinetics and from the growth rates of the nitride layer. A comprehensive model relevant to the forthcoming calculations is presented.

Experimental

The commonly used gravimetric method has been employed for measuring nitriding kinetics of 2 × 1 × 0.2 cm, 99.93 w/o (weight per cent) pure, zirconium samples. High-purity, better than 99.9 v/o (volume per cent) pure, nitrogen was passed through a cold trap and glass columns containing silica gel and phosphorous pentoxide to remove residual water vapor. Before exposing to nitrogen at a pressure of 400 Torr, specimens were treated by wet abrasion on 200 through 600-grit silicon carbide papers followed by final polishing on 8 and 1μ diamond-dust impregnated laps, acetone washing, and careful drying to avoid water stains.

To prevent formation of a gap between the metal and mounting material, whenever microscopic measurements of nitride thicknesses had to be taken, all samples are cold mounted in "Hysol" self-setting epoxy resin and prepared for metallography by using methods advised by Cprek (5) and Evans (6). Final polishing, for scale thickness measurements, was performed by 1μ diamond-dust and vibrator polishing with 0.05μ gamma-alumina solution.

To accentuate the mount/specimen interface, the nitrided surfaces were coated with dyed "Eastman 910" adhesive diluted in "GA-1A" accelerator and allowed to harden for a few hours. Dark blue recorder ink was used as a dye. Measurements of nitride thicknesses were made by projection on a metallographic glass screen or by using a filar micrometer eyepiece on sections cut at an angle of 6° with respect to the normal surface.

The zirconium nitride, although quite thin, covered the metal substrate uniformly, and no appreciable edge or corner effects could be observed. X-ray analyses, using Ni-filtered Cu radiation, showed that the yellow film formed on heating zirconium in nitrogen was ZrN having $a_o = 4.56$Å for the fcc structure. This evidence then eliminated the possibility of formation of $ZrO(NO_3)_2 \cdot 2H_2O$, $Zr_2O_3(NO_3)_2 \cdot 5H_2O$, and $Zr(NO_3)_4 \cdot 5H_2O$ nitrates reported by Elinson and Petrov (7).

Theoretical

Figure 1 shows schematically the zirconium-nitrogen equilibrium phase diagram and the associated semi-infinite diffusion couple formed during nitriding of zirconium at temperature T. Assuming that the nitrogen diffusion coefficients D_{II} and D_I are independent of nitrogen concentration, c, the equations for the two concentration curves in the nitride and in the metal can be obtained from solution of Fick's second law. These are given by

$$c_I = k_1 - B_I \operatorname{erf}(x/2\sqrt{D_I t}) \text{ at } 0 < \times < \infty \qquad [1]$$

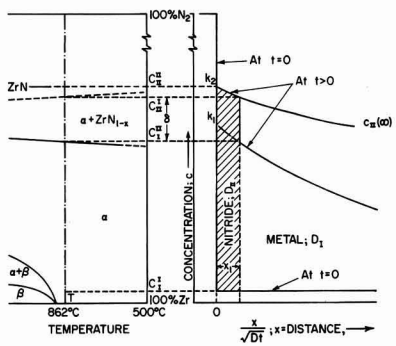

Fig. 1. Schematic presentation of zirconium-nitrogen equilibrium phase diagram and associated diffusion couple formed during nitriding of zirconium at temperature T and for time $\infty > t > 0$.

* Electrochemical Society Active Member.

for the metal phase (I) and

$$c_{II} = k_2 - B_{II} \text{ erf } (x/2\sqrt{D_{II}t} \text{ at } 0 < \times < x_1 \quad [2]$$

for the zirconium nitride phase (II).

In terms of the nomenclature used in these equations, k_1 and k_2 represent the values of c's at the surface, *i.e.*, where $x = 0$. D_{II} and D_I are diffusion coefficients of nitrogen in phases II and I, respectively, and $B_{II} = k_2 - c_{II}(\infty)$ and $B_I = k_1 - C_I^I$. All remaining symbols used follow directly from inspection of Fig. 1.

Diffusion analysis applicable to this type of a system has been advanced by Wagner (8) and applied by many investigators (4, 9, 10). At time $0 < t < \infty$, subject to boundary conditions, Eq. [1] and [2] must satisfy

$$c_I = k_1 \text{ and } c_{II} = k_2 \cong C_{II}^{II} \quad [3]$$

for $x = 0$, and similarly at $x > 0$

$$c_I = C_I^I \text{ and } c_{II} = c_{II}(\infty) \quad [4]$$

for $t = 0$.

Considering the flux at the α-zirconium/zirconium nitride interface x_1, one can write for the mass balance that

$$D_I \frac{\partial c_I}{\partial x}\bigg|_{x=x_1+0} - D_{II}\frac{\partial c_{II}}{\partial x}\bigg|_{x=x_1-0} = \delta \dot{x}_1 \quad [5]$$

where $\delta = C_{II}^I - C_I^{II}$ and $\dot{x}_1$ is the rate of movement of x_1.

In a previous investigation (4) describing the partition of nitrogen between metal and the nitride phase, it has been shown that the portion of nitrogen confined to the α-zirconium phase can be expressed as

$$(k_p)_{\alpha-Zr} = 2 B_I \sqrt{D_I/\pi} \exp(-\gamma^2 D_{II}/D_I) \quad [6]$$

In this equation, $(k_p)_{\alpha-Zr} = \Delta m/A\sqrt{t}$ represents the parabolic rate constant for nitrogen weight gain (Δm) per unit area (A) within time (t). γ is a proportionality constant as in Eq. [8] and

$$B_I = k_1 - C_I^I = \frac{C_I^{II} - C_I^I}{\text{erfc } (x_1/\sqrt{D_I t})} \quad [7]$$

which can be evaluated if the movement of interface x_1 and D_I are known.

Should one neglect the small volume change associated with conversion of zirconium metal to zirconium nitride (calculated Pilling-Bedworth ratio: $V_{ZrN}/V_{\alpha-Zr} = 1.05$), then the two values of x in Eq. [1] and [2] become equal at the nitride/metal interface. Consequently, it follows directly from Eq. [6] that

$$\gamma'\sqrt{D_I} = \gamma\sqrt{D_{II}} = \gamma_{expt'l}/2 \quad [8]$$

where $\gamma_{expt'l}$ is the experimentally measured slope of x_1 *vs.* $\sqrt{t}$, and

$$\gamma' = [\ln (2 B_I \sqrt{D_I/\pi}) - \ln (k_p)_{\alpha-Zr}]^{1/2} \quad [9]$$

In terms of conditions implied by Eq. [3] and [8] we can express the difference of nitrogen concentration as a function of distance x from the surface. Thus at $x = x_1$ we have

$$C_I^{II} - C_I^I = (k_1 - C_I^I)(1 - \text{erf } \gamma') \quad [10]$$

for the metal phase, and similarly for the nitride phase

$$C_{II}^{II} - C_{II}^I = B_{II} \text{ erf } \gamma \quad [11]$$

Differentiating Eq. [1] and [2] with respect to x and making use of the mass balance Eq. [5], one obtains in terms of relationship [8] that

$$\frac{(C_{II}^{II} - C_{II}^I)(\text{erf } \gamma)'}{\gamma \text{ erf } \gamma} - \frac{(C_I^{II} - C_I^I)(\text{erf } \gamma')'}{\gamma' \text{ erfc } \gamma'} = 2\delta \quad [12]$$

where the index "prime" behind parentheses is being used to designate the derivative of the respective error functions, *e.g.* $(\text{erf } \gamma)' = 2(\pi)^{-1/2} \exp -\gamma^2$.

Equation [12] may be simplified by introducing the following arbitrary definitions

$$\xi(\gamma) = (\text{erf } \gamma)'/2\gamma \text{ erf } \gamma \quad [13]$$

and

$$\xi(\gamma') = (\text{erf } \gamma')'/2\gamma' \text{ erf } \gamma' \quad [14]$$

and therefore

$$(C_{II}^{II} - C_{II}^I)\xi(\gamma) - (C_I^{II} - C_I^I)\xi(\gamma') = \delta \quad [15]$$

Knowledge of D_I and $\gamma_{expt'l}$ allows one to evaluate the proportionality constant γ' from Eq. [8], and consequently calculation of $\xi(\gamma')$ becomes possible. For a given value of $\xi(\gamma')$, one obtains a corresponding value of $\xi(\gamma)$ by virtue of Eq. [15] because the nitrogen concentration differences are known. The unique value of γ satisfying relationship [13] may be obtained by means of a graphical solution, *e.g.*, by plotting $\exp(-\gamma^2)/\sqrt{\pi}\,\gamma\,\xi(\gamma)$ and erf γ *vs.* γ. Consequently, we can determine the diffusion coefficient, D_{II}, of nitrogen in zirconium nitride from relationship [8].

Evaluation of Nitrogen Diffusivity in ZrN

Nitriding kinetics for α-zirconium in the temperature range 650°-850°C are shown in Fig. 2 together with the evaluated portion of nitrogen confined to the metal phase. Zirconium exhibits an exceptionally large solubility for nitrogen, above 20 a/o (atomic per cent), and accordingly the amount of nitrogen taken up by the metal is about 80 w/o of the total nitrogen consumed during the nitriding process.

Figure 3 is a plot of ZrN thicknesses formed at different temperatures as a function of nitriding time. Visual inspection of these figures indicates that, to a good approximation, parabolic relationships are obeyed for both the nitride growth and nitrogen dissolution in the metal. This then implies that volume diffusion of nitrogen may be the controlling factor in the nitriding mechanism of zirconium.

Densities of α-zirconium and ZrN are 6.5 (11) and 7.09 (12) g/cm^3, respectively. The boundary concentrations of nitrogen in zirconium nitride and in the metal saturated with nitrogen are summarized in Table I and were obtained from the Zr-N_2 equilibrium phase diagram (13). The initial concentration of nitrogen in the zirconium samples used was $C_I^I = 0.65 \times 10^{-5}$ gN/cm^3. Values for nitrogen diffusion coefficients in α-zirconium were taken from ref. (4) and those for $\gamma_{expt'l}$ from Fig. 3.

Knowledge of these experimental data makes possible the evaluation of the remaining parameters: γ';

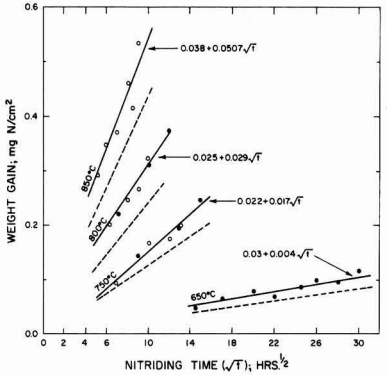

Fig. 2. Nitriding rates of zirconium at different temperatures. Solid lines, total nitrogen uptake; dashed lines, nitrogen dissolved in α-zirconium; open circles, from ref. (4); closed circles, from this study.

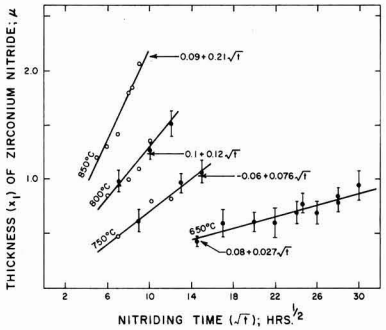

Fig. 3. Zirconium-nitride thicknesses for various nitriding times and temperatures. Open circles, from ref. (4); closed circles, from this study.

$\xi(\gamma')$; $\xi(\gamma)$; $B_I(x=0)$ and hence $(k_p)_{\alpha-Zr}$. The numerical values thus obtained are summarized in Table II.

Figure 4 shows the graphical solution of Eq. [13] for arbitrary values of γ. The unique results for γ, at various temperatures, which satisfy this equation are obtained from intersections of the exponential functions and are also recorded in Table II.

The values for diffusion coefficients of nitrogen in hypostoichiometric ZrN, obtained under conditions of nitriding polycrystalline α-zirconium for exposures up to 900 hr, are represented in Fig. 5 in Arrhenius form. The method of least squares has been employed to obtain an expression for the diffusion coefficient, this is

$$D_{II} = 7.87 \times 10^{-5} \exp(-35{,}900/RT) \text{ cm}^2/\text{sec} \quad [16]$$

for the temperature range of 650°-850°C

While deriving the mathematical expressions it was tacitly assumed that the treatment of semi-infinite plate is applicable to the 2 mm-thick zirconium samples. Figure 6 which is a plot of concentration of nitrogen within the metal phase, at limiting temperatures of 850° and 650°C, provides satisfactory justification for this premise.

Discussion of Results

In the absence of other measurements of nitrogen diffusion in zirconium nitride it is difficult to assess how closely the calculated values of D_{II} approximate those from experimental evidence. The knowledge of

Table I. Summary of experimental data used for evaluation of nitrogen diffusivities in zirconium nitride

	Temperature, °C			
	650	750	800	850
C_I^I; gN/cm^3	0.65 × 10^{-5}	0.65 × 10^{-5}	0.65 × 10^{-5}	0.65 × 10^{-5}
C_I^{II}	0.239	0.260	0.268	0.274
C_{II}^I	0.938	0.933	0.929	0.925
C_{II}^{II}	0.945	0.945	0.945	0.945
δ	0.699	0.673	0.661	0.651
D_I; cm^2/sec	2.32 × 10^{-14}	4.20 × 10^{-13}	1.39 × 10^{-12}	4.60 × 10^{-12}
γ_{expt+1}; cm^2/sec	0.45 × 10^{-7}	0.13 × 10^{-6}	0.21 × 10^{-6}	0.35 × 10^{-6}

Table II. Compilation of values obtained from theoretical evaluations

Parameter	Temperature, °C			
	650	750	800	850
γ'; Eq. [8]	14.8 × 10^{-2}	9.80 × 10^{-2}	9.47 × 10^{-2}	8.14 × 10^{-2}
$\xi(\gamma')$; Eq. [14]	4.48	6.42	6.62	7.61
$\xi(\gamma)$; Eq. [15]	2.53 × 10^2	1.95 × 10^2	1.52 × 10^2	1.37 × 10^2
γ; Fig. 4	4.50 × 10^{-2}	5.00 × 10^{-2}	5.75 × 10^{-2}	6.05 × 10^{-2}
D_{II}; Eq. [8]	2.5 × 10^{-13}	1.6 × 10^{-12}	3.6 × 10^{-12}	8.4 × 10^{-12}
B_I; Eq. [7]	0.287	0.293	0.300	0.302
$(k_p)_{\alpha-Zr}$; Eq. [9], gN/cm^2 sec$^{1/2}$	4.81 × 10^{-8}	2.12 × 10^{-7}	3.96 × 10^{-7}	7.28 × 10^{-7}

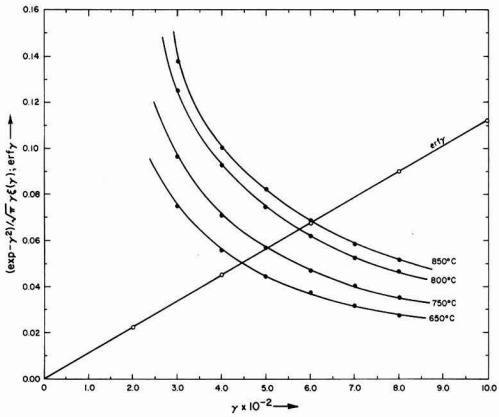

Fig. 4. Plots of exp $(-\gamma^2)/\sqrt{\pi}\ \gamma\ \xi(\gamma)$ and erf γ vs. γ for different temperatures.

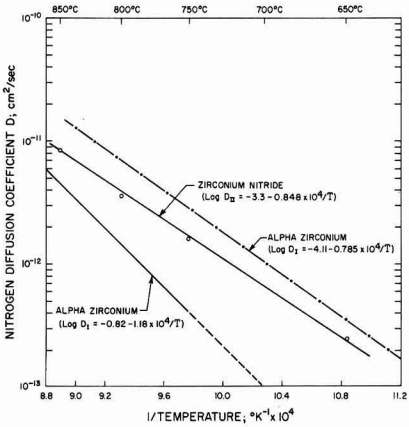

Fig. 5. Arrhenius plots for nitrogen diffusion in zirconium nitride and α-zirconium (4). Dot-dash line is for values obtained from kinetic studies; see Appendix.

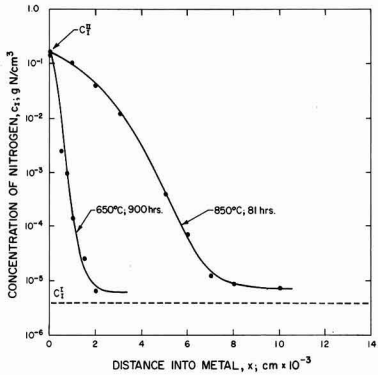

Fig. 6. Theoretical distribution curves for nitrogen in α-zirconium as functions of nitriding time and distance into the metal. Points shown were calculated from Eq. [1] with $k_1 = C_I^{II}$.

error arising by considering the diffusion coefficient D_{II} as a concentration independent factor would be of particular interest.

The accuracy of evaluation of D_{II} depends on the precision with which the value of D_I is known. Com-

parison of the latter value from microhardness measurements with that from kinetic data shows appreciable discrepancy as depicted by Fig. 5. The D_I value from microhardness determinations is lower by a factor of 4 to 22 for the temperature range of interest. A question then arises which of these two values should be employed in evaluating D_{II}.

Results from Fig. 2 indicate that as much as 80% of the total amount of nitrogen consumed is confined to the metal phase. Consequently, when evaluating D_I (see appendix), omission of the thin ZrN film formed in the initial stages of nitriding seems to be plausible. However, inspection of Eq. [4A] in the appendix reveals that D_I is strongly dependent on the accuracy with which the total nitrogen uptake, M_I, can be measured, and unfortunately this is not very high. The following example will accentuate this point. Reference (2) gives for the total nitrogen uptake $M_I = 3.91 \times 10^{-5}$ for 2-hr exposure at 862°C, or $M_I \cong 3.0 \times 10^{-5}$ gN/cm² if extrapolated to 825°C. This value is to be compared with $M_I = 8.32 \times 10^{-5}$ gN/cm² at 825°C for 2 hr exposure from ref. (1). It means that at the temperature considered D_I can vary from 1.04×10^{-11} to about 1.5×10^{-12} cm²/sec. The latter value is in close agreement with that from microhardness determinations. Due to the paucity of precise and consistent kinetic studies, the value of D_I resulting from microhardness measurements has been employed for evaluating D_{II}.

Some mention should be made about the accuracy of D_{II} in terms of errors in C_{II}^I. The α + ZrN_{1-x}/ZrN_{1-x} phase boundary is drawn as a dashed line indicating poor accuracy. This phase boundary has been determined from the limited x-ray investigations by Domagala *et al.* (14), who believe that its position is accurate within ± 0.5 w/o N for the temperature range of 1600°-1850°C and that it reaches nearly stoichiometric ZrN at temperatures below 600°C. Unfortunately, for the temperatures of this study, it is impossible to evaluate the errors attached to D_{II} by considering the positive deviation from C_{II}^I, because this would mean the presence of hyperstoichiometric ZrN and the existence of such a compound has never been reported. It is, however, possible to account for the negative value of —0.5 w/o N, and thus, *e.g.*, at 850°C the value of $D_{II} = 3.1 \times 10^{-12}$ cm²/sec as compared with $D_{II} = 8.4 \times 10^{-12}$ for the average value of C_{II}^I.

The value of 35.9 kcal/mole for the diffusion activation energy could indicate an interstitial type of diffusion. This, however, seems to be highly improbable if we consider the relatively closely packed ZrN fcc lattice. The formation of hypostoichiometric zirconium nitride during the nitriding process provides a vacancy-type structure, and accordingly diffusion of nitrogen via nitrogen vacancies appears to be a more plausible mechanism for diffusion. In this case, the activation energy will consist of two terms: the energy of formation of vacancies and the energy required to move the diffusing species across these vacancies.

Diffusion across the α-zirconium structure is seen to be very sensitive to temperature change, in accord with what one would expect from the rate of diffusion through hcp lattice of the metal.

Acknowledgments

The authors wish to express their gratitude to Dr. C. B. Magee for valuable comments and suggestions during the course of this work. The technical assistance and financial support by the University of Denver Research Institute are greatly appreciated.

Manuscript received Nov. 13, 1967; revised manuscript received *ca.* Jan. 15, 1968. This paper was presented at the Dallas Meeting. May 7-12, 1967, as Abstract 212.

Table III. Diffusion coefficients obtained from kinetic measurements

Temperature, °C	Exposure time, hr	ZrN thickness, μ	C_I^{II}, gN/cm³	D_I, cm²/sec
825	2	0.17-0.30	0.270	1.1×10^{-11}
800	2	0.17	0.268	5.5×10^{-12}
700	2	0.038-0.11	0.252	8.4×10^{-13}
600	2	—	0.230	1.1×10^{-13}

Any discussion of this paper will appear in a Discussion Section to be published in the December 1968 JOURNAL.

APPENDIX

According to Fick's first law the quantity of nitrogen M_I, which penetrated metal per unit area at the end of time t can be expressed as

$$M_I = -D_I \int_o^t \left(\frac{\partial c_I}{\partial_x} \right)_{x=x_1} dt \qquad [1A]$$

If we assume that the concentration of nitrogen $C_I^I = 0$ (about 1 ppm in our samples), then we can write in terms of Eq. [1] that

$$\frac{\partial c_I}{\partial x_1} = -\frac{k_1}{\sqrt{\pi D_I t}} \exp -(\gamma')^2 \qquad [2A]$$

for $x_1 = 2\gamma'\sqrt{D_I t}$.

Substituting [2A] into [1A] yields

$$M_I = \frac{2k_1\sqrt{D_I t}}{\sqrt{\pi}} \exp -(\gamma')^2 + C \qquad [3A]$$

where $C = 0$ if $t = 0$.

Expressing $k_1 = C_I^{II}$ when $x_1 = 0$ (*i.e.*, no nitride film) we have

$$D_I = \pi M_I^2 / 4t \, (C_I^{II})^2_{x_1=0} \qquad [4A]$$

This relationship is of the form sometimes used for evaluation of diffusivity in the metal assuming that the film thickness is negligible. We shall utilize this equation in determining D_I for nitrogen diffusion in α-zirconium for short exposure times.

As already mentioned in the text, Gulbransen and Andrew obtained a strictly parabolic relationship for nitriding kinetics up to 2-hr exposures. In view of the present investigation, the estimated thicknesses of nitride films formed on their samples are given in Table III. Included also are values for D_I resulting from solution of Eq. [4A]. Utilizing the principle of least squares, the diffusion coefficient for nitrogen diffusion in α-zirconium may be represented as $D_I = 5 \times 10^{-4} \exp(-38{,}000/RT)$ cm²/sec.

REFERENCES

1. E. A. Gulbransen and K. F. Andrew, *Metals Trans.*, **185**, 515 (1949).
2. A. Dravnieks, *J. Am. Chem. Soc.*, **72**, 3568 (1950).
3. W. M. Mallett, J. Belle, and B. B. Cleveland, *This Journal*, **101**, 1 (1954).
4. C. J. Rosa and W. W. Smeltzer, *Electrochem. Technol.*, **4**, 149 (1966).
5. E. R. Cprek, *Trans. ASM*, **55**, 369 (1962).
6. W. Evans, *Can. Mining and Met. Bull.*, **53**, 897 (1960).
7. S. V. Elinson and K. I. Petrov, Zirconium-Chemical and Physical Methods of Analysis, AEC-tr-5373, 22 (1960).
8. C. Wagner, "Diffusion in Solids, Liquids, Gases," p. 72, W. Jost, Editor, Academic Press, New York (1960).
9. G. Beranger and P. Lacombe, *J. Nucl. Materials*, **16**, 190 (1965).
10. T. Smith, *This Journal*, **112**, 39 (1965).
11. C. J. Smithells, "Metals Reference Book," London, Vol. 2, p. 696 (1962).
12. C. D. Hodgman, R. C. Weast and S. M. Selby, "Handbook of Chemistry and Physics," p. 687, Cleveland (1960).
13. M. Hansen and K. Anderko, "Constitution of Binary Alloys," p. 996, McGraw-Hill, New York (1958).
14. R. F. Domagala, D. J. McPherson, and M. Hansen, *Trans. AIME*, **206**, 98 (1956).

The Properties of Oxide Films Formed on a Zirconium-2.7 w/o Niobium Alloy in the Temperature Range 300°-500°C

M. G. Cowgill[1] and W. W. Smeltzer*

Department of Metallurgy and Materials Science, McMaster University, Hamilton, Ontario, Canada

ABSTRACT

Electron microscopy techniques were employed to determine the morphologies and structures of oxide films formed on martensitic and Widmanstatten alloys in an oxygen atmosphere. Morphological development of a film in the very early stages of its formation was dependent on surface preparation, the substructure of an alloy being replicated by the film formed on a pickled specimen. Pustules occurred in the oxide films with their growth being confined to the α'-Zr phase of Widmanstatten alloys. Also, films on this alloy phase in comparison to those on a martensitic specimen commenced cracking at smaller thicknesses. The films consisted of monoclinic zirconia and, in addition, a second phase which was either tetragonal zirconia or an intramolecular oxide of zirconia and niobium pentoxide. This latter oxide occurred as small crystallites 50-150Å in diameter.

The reaction kinetics were previously reported for martensitic and several Widmanstatten alloys oxidized at temperatures in the range 300°-500°C (1). Little difference was found between the oxidation rates of these alloys in the early stages of the reaction, but prolonged exposures demonstrated that the martensitic alloys consisting of α'-Zr oxidized much more rapidly in the range of linear kinetics, the linear kinetics of the Widmanstatten alloys decreasing with increasing amounts of proeutectoid α-Zr. This latter phase oxidized at much slower rates than α'-Zr. The oxide layer consisted essentially of monoclinic zirconia, and the formation of oxide pustules on martensitic specimens was the only distinct feature indicating a difference in the mode of oxide formation on differently structured alloys. The purpose of this investigation was to gain more detailed information by the techniques of electron microscopy on the structural properties of the oxide films and on their role as barriers to oxidation processes.

Experimental

The electron microscopy studies were of two types: replication studies of oxide film surfaces and transmission microscopy of oxide films stripped from the alloys. For the former, two-stage replication was used, the parlodion film being shadowed at 20° to the surface with gold-palladium, before carbon evaporation at right angles to the surface. Transmission studies necessitated first coating the oxidized surface of the specimen with carbon in order to strengthen the thin film. The stripping of the oxide from the metal was then performed with a solution of 10% bromine in ethyl acetate held at 75°C.

Microscopy was carried out on a Siemens Elmiskop I operating with voltages of 80 kv for replicas and 100 kv for thin oxide films. In order to facilitate accurate measurement of lattice spacings by selected area diffraction, gold was evaporated on the oxide to provide a standard diffraction pattern. Distance measurements on the patterns were made with a Joyce recording densitometer.

The alloy material, the procedures for preparing alloys in martensitic and Widmanstatten structures, surface preparation, and oxidation of specimens in oxygen at 1 atm pressure have been described in a previous paper (1). The aqueous pickling solution, 30 v/o H_2SO_4, 30 v/o HNO_3, and 10 v/o HF, was held at a temperature in the range 68°-75°C. Weight gains of specimens by oxidation were converted to approximate average film thicknesses based upon the factor $1\mu g\ O/cm^2 = 62Å$.

* Electrochemical Society Active Member.

[1] Present address: Atomic Power Division, Westinghouse Electric Corporation, Madison, Pennsylvania.

Results

Oxide film morphologies.—The changes in the topographies of specimens oxidized at 400°C were studied from the initial protective stage of film formation, through the transition region, and into the final stage where oxidation approximated to linear kinetics (1).

Representative surfaces of martensitic specimens and the film at various stages of oxidation are shown in Fig. 1-3. Although the surfaces of mechanically polished specimens were featureless, surfaces of pickled specimens showed areas of selective etching at the boundaries of the martensite plates. Irrespective of

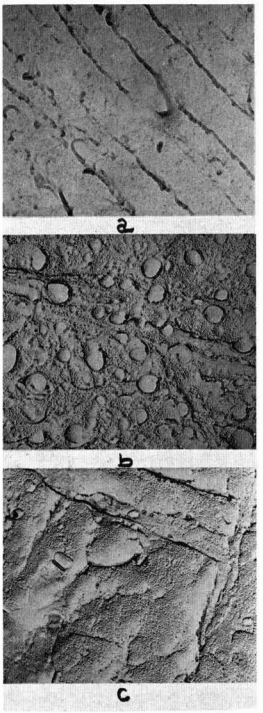

Fig. 1. Surface replicas of pickled martensitic alloy surfaces after oxidation at 400°C. Oxygen uptake: top, unoxidized, 26,665X; middle, 0.10 mgO/cm², 14,665X; bottom, 0.20 mgO/cm², 14,665X.

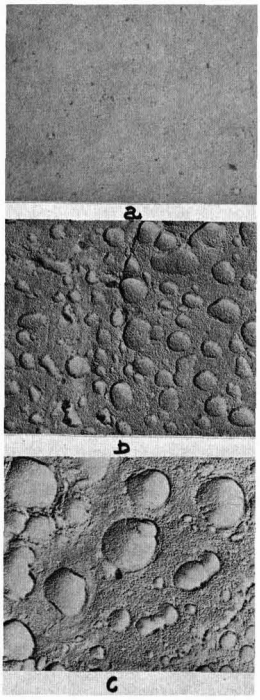

Fig. 2. Surface replicas of mechanically polished martensitic alloy surfaces after oxidation at 400°C. Oxygen uptake: top, unoxidized; middle, 0.09 mgO/cm^2; bottom, 0.15 mgO/cm^2. 14,665X.

Fig. 3. Typical surface replica of martensitic specimen oxidized to the range of linear kinetics. Oxygen uptake: 1.56 mgO/cm^2. 14,665X.

surface treatment, the films were uneven in the initial stages of the reaction, Fig. 1b and 2b, exhibiting pustular growths with sizes varying from grain to grain. In addition to pustules, fine cracks were to be observed in the films as the specimens were progressively oxidized into the period for transition to linear kinetics, Fig. 1c and 2c. At long times, a film exhibited an uneven surface populated with cracks, Fig. 3.

A similar series of micrographs for the Widmanstatten alloys is illustrated in Fig. 4. There was not a noticeable difference between the pickled and unpickled surfaces, other than that, with the former type of specimen, the alloy structure could be more easily distinguished. Micrographs of films formed on both alloy phases, Fig. 4b, demonstrated that the films were considerably thicker on the α'-Zr phase even at small oxygen uptakes. Moreover, the films formed on this phase were characterized by pustules as previously shown for the martensitic specimens. Cracking of this oxide became very extensive before any evidence was found for cracking of the oxide formed on the α-Zr phase, Fig. 4c, and even occurred in films thinner than those formed on martensitic specimens. For example,

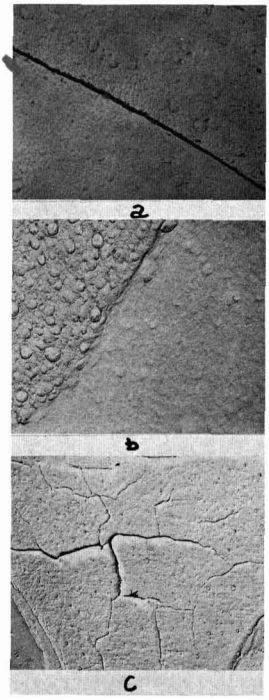

Fig. 4. Surface replicas of mechanically polished Widmanstatten alloy surfaces after oxidation at 400°C. Oxygen uptake: top, unoxidized, 25,330X; middle, 0.01 mgO/cm^2, 14,665X; bottom, 0.2 mgO/cm^2, 2,665X. The pustular oxide and extensively cracked oxide occur on the α'-Zr alloy phase.

cracks were readily observable in a 1500Å film on an alloy containing 30 v/o α-Zr, whereas evidence was only found for the initiation of cracking in films corresponding to approximately 2500Å on martensitic specimens.

Oxide film structures.—Films formed at 300°C and with thicknesses varying from 100 to 800Å were examined by the transmission technique. Their appearance was dependent on the surface preparation of the specimens. A film stripped from a specimen whose surface was mechanically polished was relatively featureless. On the other hand, the films stripped from pickled specimens exhibited structures related to the alloy microstructures. The microstructures of the martensitic and Widmanstatten alloys replicated by their oxide films are illustrated in Fig. 5. Absence of electron transmission through the films at alloy transformation boundaries indicated enhanced oxide growth in these regions.

Selected area diffraction spot patterns obtained from films formed on alloy pickled surfaces could often be indexed as monoclinic zirconia (2-4). It was also possible to index some patterns as a mixture of monoclinic zirconia and another phase. Most of the spots could be accounted as coming from the monoclinic oxide, but one pair of spots arose from planes with d-spacing of 2.95Å. Such a lattice spacing would be compatible with the (111) spacing of tetragonal zirconia (5), or, possibly, of the mixed oxide $6ZrO_2 \cdot Nb_2O_5$ (6). A typical diffraction pattern from a film containing both oxides is illustrated in Fig. 6. In the case of a mechanically polished surface, the diffraction patterns were those of a polycrystalline oxide and they could be indexed generally as monoclinic zirconia.

In the earlier reported paper (1), examination by a recording x-ray diffractometer of the surfaces of

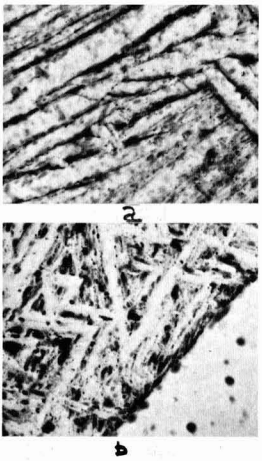

Fig. 5. Electron transmission micrographs of oxide films stripped from pickled alloys oxidized at 300°C: top, martensite, 0.001 mgO/cm^2; bottom, Widmanstatten structure, 0.002 mgO/cm^2. 13,330X.

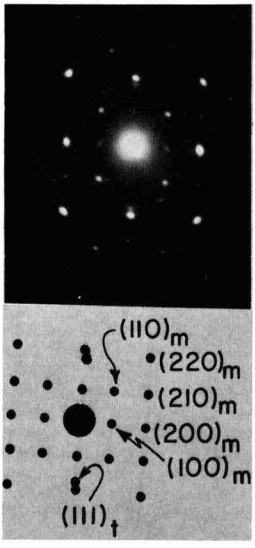

Fig. 6. Selected area diffraction pattern from film formed on pickled martensitic alloy oxidized at 300°C. Oxygen uptake: 0.004 mgO/cm^2. Symbols m and t refer to monoclinic and tetragonal oxide, respectively.

specimens oxidized for extended exposures to form scales demonstrated that monoclinic zirconia was the major reaction product, little evidence being found for the existence of another oxide phase. To gain more detailed information, powder x-ray diffraction experiments were carried out on scales formed at the temperatures of 300°, 400° and 500°C on both martensitic and Widmanstatten specimens. The patterns from oxide formed under all these conditions were similar and reflections were consistently obtained from a plane with lattice spacing 2.94-2.95Å in addition to those of monoclinic zirconia. This is the same value as that found by electron diffraction from thin films and the existence of a tetragonal oxide in both monoclinic zirconia films and scales is considered definite.

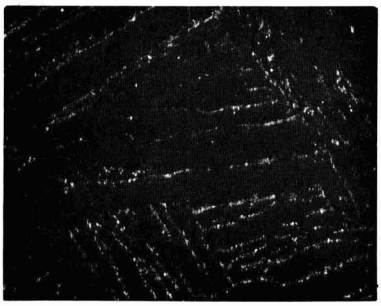

Fig. 7. Dark field transmission micrograph from oxide film formed on pickled martensitic alloy oxidized at 300°C showing crystallites of tetragonal oxide at alloy transformation boundaries. 20,000X.

Attempts were made to locate the tetragonal crystallites in the films formed on pickled specimens by dark field electron microscopy. This was done using the diffraction spots from the (111) plane of this phase as all other planes gave rise to spots coincident, or nearly coincident, with spots from monoclinic zirconia. Examination of many films demonstrated that this oxide was distributed as small crystallites in a size range between 50 and 150Å at areas bounding transformation boundaries in a martensitic alloy, Fig. 7, and over the main surface, the distribution appearing to be dependent on the orientation of the alloy matrix surface. Although several films stripped from specimens with Widmanstatten structures were composed of both monoclinic and tetragonal oxide, it was impossible to form conclusions regarding the distribution of crystallites.

Discussion

Oxide pustules in the films on martensitic specimens were found previously by light microscopy to be the only distinct feature indicating a difference in the mode of oxide formation on different structured alloys (1). The current observations at the high magnifications of an electron microscope show that pustules also occur in films on Widmanstatten alloys, albeit not on such a large scale and then only on α'-Zr. The size of these pustules was restricted to about 0.1-0.2μ, whereas those on martensitic specimens ranged upwards to 0.5μ by electron microscopy and 500μ by light microscopy. Apparently both the mode of oxide formation and the properties of the films differ. Film growth on martensitic alloys was characterized by the lateral growth of pustules. On the other hand, pustules in the α'-Zr phase of the Widmanstatten specimens attained smaller ultimate size before cracking of the film occurred at a relatively small thickness.

Film growth was uneven on all alloy structures with enhanced oxide growth occurring about the transformation boundaries in the alloy microstructures. These latter regions would exhibit niobium enrichment brought about during quenching and/or tempering at reaction temperatures. This enrichment would eventually lead to the segregation of β-Nb (92 w/o Nb) which may play a role in oxide formation in these regions. Since the crystallites of the tetragonal oxide phase, an allotropic modification of zirconia or the double oxide, $6ZrO_2 \cdot Nb_2O_5$ were distributed both around transformation boundaries and on the martensitic plates, niobium may only dissolve in the tetragonal zirconia, without leading to the formation of the double oxide.

The crystallite size of the tetragonal oxide was small lying in the range 50 to 150Å. This observation stimulates comparison with other work despite the limitation of not being able to distinguish whether this phase

was an allotropic modification of zirconia or an intramolecular oxide. A tetragonal oxide was reported by Schwartz *et al.* (7) to occur on zirconium oxidized in water at 400°C and by Korobkov *et al.* (8) on zirconium and alloys containing titanium, aluminum and tin oxidized in air at temperatures between 300°-1100°C. Its transformation to a monoclinic structure was suggested by these investigators as the cause for film breakdown. This supposition would not appear to be valid for the alloy of the present investigation because the films formed before the breakaway region in a reaction curve consisted largely of monoclinic zirconia with only small amounts of tetragonal oxide.

To account for the diverse features of film formation, account must be given to the alloy phases upon which oxide is forming. The films on the α-Zr phase of Widmanstatten alloys, which would be most homogeneous with respect to niobium concentration, were more uniform than those on the α'-Zr phase or the fully martensitic alloy. The niobium content of α'-Zr depends upon the annealing treatment for the alloy and was approximately 4 w/o compared with 2.7 w/o for martensite. Thus a higher degree of niobium enrichment in the zirconia film on α'-Zr is to be expected. The oxide in this film may exhibit the same properties as shown by Douglass (9) for zirconia where metal additives decreased its plasticity. A similar decrease in oxide plasticity possibly played a role in determining the most extensive cracking of the film on the α'-Zr phase at the earliest stage of reaction. It would appear, however, that the cracks observable by electron microscopy did not play a dominant role in determining the protective properties of the total film because the linear oxidation kinetics of a martensitic alloy were much larger than those for the Widmanstatten alloys (1).

Acknowledgments

The authors were indebted to D. J. Embury for many helpful discussions on electron microscopy techniques. This research was completed under the auspices of the Atomic Energy of Canada Limited and the Defence Research Board of Canada.

Manuscript received Nov. 20, 1967; revised manuscript received *ca.* Jan. 10, 1968. This paper was presented at the Chicago Meeting, Oct. 15-19, 1967, as Abstract 88.

Any discussion of this paper will appear in a Discussion Section to be published in the December 1968 JOURNAL.

REFERENCES

1. M. G. Cowgill and W. W. Smeltzer, *This Journal*, **114**, 1089 (1967).
2. J. D. McCullough and K. N. Trueblood, *Acta Cryst.*, **12**, 507 (1959).
3. J. Adam and M. D. Rogers, *ibid.*, **12**, 951 (1959).
4. W. B. Pearson, "A Handbook of Lattice Spacing and Structures of Metals and Alloy," p. 246, Pergamon Press (1964).
5. L. N. Komissarova, Yu. P. Simanov, and Z. A. Vladimirova, *Russ. J. Inorg. Chem.*, **5**, 687 (1960).
6. R. S. Roth and L. W. Coughanour, *J. Research Natl. Bur. Standards*, **55**, 209 (1955).
7. C. M. Schwartz, D. A. Vaughan, and G. C. Cocks, BMI-793 (Dec. 1952).
8. I. I. Korobkov, D. V. Ignatov, A. E. Evstyukhin, and V. S. Emelyanov, *Proc. 2nd. U. N. Conf. on Peaceful Uses of Atomic Energy*, **5**, 60 (1958).
9. D. L. Douglass, *Corrosion Sci.*, **5**, 255 (1965).

The Attraction of Liquids by Electric Fields

E. P. Damm, Jr.

Systems Development Division, International Business Machines Corporation, Poughkeepsie, New York

ABSTRACT

The attraction of liquids by electric fields is studied. The time between application of electric field and liquid contact with electrode (response time) serves as the basis for determining the effects of various system parameters. Variation of response time with electrode voltage and with air gap is plotted for a high-dielectric-constant liquid. It is shown that response time is largely independent of the liquid's conductivity, solids concentration, particle size and particle polarity of dissolved or dispersed solids in water. Response time does vary significantly with viscosity, and, up to certain field strengths, with the surface tension of the liquid. Also, for the liquids used in these experiments, response times were lowest for liquids having highest dielectric constants and highest for those with lowest dielectric constants, if viscosity effects are taken into consideration. The evaporation rate or the presence of vapor molecules of a volatile nonpolar or only slightly polar liquid also appears to increase the response time. However, the presence of polarizable materials dispersed in a liquid of low polarity such as toluene produces a decrease in the response time of the liquid.

It has long been known that liquids can be influenced by electric fields. The phenomenon of "ink flying" in the printing industry (1) and the rise of the level of the liquid with oil-insulated high-tension equipment are examples. Swan (2), Schott and Kaghan (3) have also reported some interesting experiments with this phenomenon.

Pohl (4-8) and Kok (9) have experimented with and tried to develop a theoretical mechanism for the motion of particles in dielectric liquids by high-intensity divergent fields. The motion of these particles was, at least initially, the result of a phenomenon which Pohl called dielectrophoresis. The term dielectrophoresis was defined as the motion of electrically polarized matter in a nonuniform field, in contrast to electrophoresis, which is defined as the phenomenon of the migration of charged particles through a fluid under the influence of an electric field. While both phenomena were known, the experiments of Pohl served to emphasize that polarization effects, while somewhat neglected in the area of particle motion in an electric field, were of practical use and could account for certain occurrences which otherwise might be loosely accounted for only by electrophoresis. There is little record (10) of work on the attraction of highly conducting liquids by divergent electric fields and

especially on the quantitative comparison of their characteristics with those of dielectric liquids under an applied electric field.

This paper describes several experiments with liquids of varying dielectric constant and conductivity. The system variables of electrode voltage and gap are discussed, as well as the liquid variables of conductivity, surface tension, viscosity, particle polarity, solids concentration, and particle size of the dissolved or dispersed phase. The importance of the dielectric constant of the liquid and the evaporation rate of liquids with extremely low dielectric constant are also shown. The response time of the liquid is used as the dependent variable to quantitatively define the system behavior. Response time in this paper refers to the time interval between the initiation of the attraction voltage and the contact of the attraction electrode by liquid.

A Simple Model

In attempting to understand how response time is related to the properties of dielectric liquids and the electric fields that attract them, the equation for the force between a point charge and an unbounded, planar dielectric medium provides useful clues. This equation is given by (11)

$$F = \frac{1}{4\pi K_0 K_1} \frac{K_1 - K_2}{K_1 + K_2} \frac{q^2}{a^2}$$

where K_0 = the permittivity of free space; K_1 = the dielectric constant of the material between the point charge and the plane; K_2 = the dielectric constant of the planar dielectric medium; q = the charge at the point; and a = the distance between the point charge and the plane of the dielectric.

While more rigorous equations can be developed to explain the phenomenon whereby, for example, the geometry of one of the equipotential surfaces of the point charge is assumed to be the geometry of the attraction electrode, the simple model does illustrate that, for a given q and a, the attractive force decreases significantly only when K_2 approaches K_1. For example, if the medium between the point charge and the planar surface is air ($K_1 = 1$) and the dielectric is water ($K_2 = 80$), the attractive force is 79/81 = 97.5% of the force available if K_2 were infinite. For the case of glycerine (98%) ($K_2 = 43$), the force is 42/44 = 95.5% of that available if K_2 were infinite. Hence, it could be expected that response time, which is inversely related to the attracting force, will not vary significantly for different liquids of low viscosity and high dielectric constant. Also, from this simple model one would expect that changes in conductivity, liquid depth, and solids concentration in a high-dielectric-constant liquid will not radically affect response time. On the other hand, it may be expected that surface tension and viscosity, which are not shown in this equation, might be important factors affecting the response time.

In the case of low-dielectric-constant liquids such as toluene ($K_2 = 2.4$), any factors which significantly alter the dielectric constant of either the liquid or the air gap would be expected to seriously affect response time. For example, condensation in the air could alter K_1 enough to cause a significant change in response time.

High-Dielectric-Constant Liquids

Characteristic curves.—In our initial experiments, we studied the response time of a high-dielectric-constant liquid as a function of air gap and applied voltage. A 1% aqueous solution of the colloidal electrolyte, crystal violet, extra pure,[1] was chosen as representative of this class of liquids. In order to minimize the effect of surface tension, we added a surfactant to the solution. With 1% Fluorochemical L-1006[2] (nonionic) it was possible to bring the surface tension as low as 23.4 dynes/cm (measured with a DuNuoy-type tensiometer).

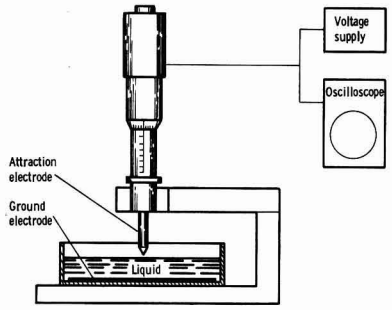

Fig. 1. Responsometer

To measure response times, an instrument called a responsometer was devised (Fig. 1). A petri dish contains the liquid to be tested and a brass, flat-disk electrode. The upper, attracting electrode is a micrometer head ground to a conical tip (0.021 in. radius, 45° taper) to provide a divergent electrical field. The accuracy of the vertical adjustment is to the nearest 0.0001 in. A 5000v d-c power supply with a 10-Mohm current-limiting resistor is used to supply the voltage, which is controlled with a standard powerstat. An oscilloscope connected to the attracting electrode is used to monitor the voltage.

When voltage is applied to the micrometer head, the oscilloscope trace rises accordingly and remains at the upper level until the attracted liquid makes contact with the electrode. At this time the circuit is electrically shorted, and the trace drops back to zero. Response times can be measured directly from photographs of the oscilloscope trace (Fig. 2). We found that the response times of reasonably polar liquids having specific conductivities as low as 2×10^{-8} mho/cm could be directly measured with this instrument.

The characteristic curves of the water and crystal violet solution are given in Fig. 3 and 4, which show response time as a function of air gap and applied voltage, respectively.

Effect of solution properties.—Since surface tension and viscosity resist the attracting force of the electric field, they were expected to have an important effect on response time. The response time *vs.* surface tension characteristic was determined for the aqueous crystal violet solution. Different amounts of surfactant were added to vary the surface tension over the range from 76 to 23.4 dynes/cm. Figure 5 shows that the variation in surface tension has a significant effect on response time only for low values of applied voltage. Above 500v, the slopes of the response time *vs.* surface tension curves are close to zero. The limiting effect of the restraining forces at low surface tension is observed in Fig. 6, which shows the maximum gap through which the aqueous crystal violet solution with minimum surface tension can be attracted for various voltages.

The effect of viscosity on response time was measured in an experiment which used different concentrations of glycerine in water to provide a range of viscous solutions. Figure 7 shows that response time increased linearly by a factor of about 3 as the viscosity was increased from 1.7 to 360 centipoise.

Other solution properties that were checked included conductivity, concentration of colloidal particles, and size of dissolved or dispersed particles. Response time was virtually independent of these properties. To test the effect of conductivity, potas-

[1] A product of du Pont de Nemours & Co., Wilmington, Delaware.

[2] A product of the 3M Corporation, St. Paul, Minnesota.

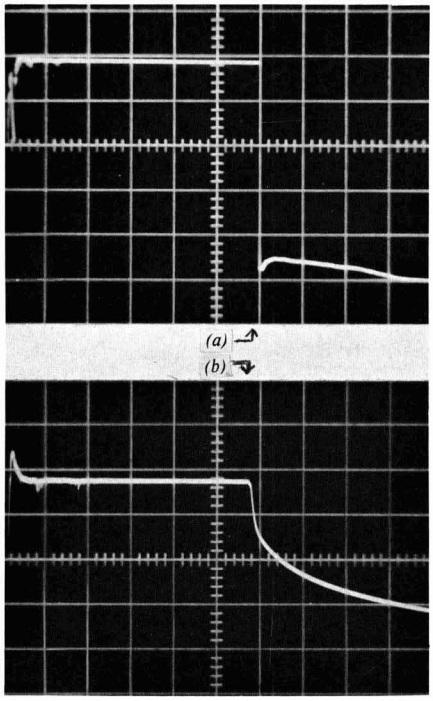

Fig. 2. Typical curves: *(a)* response curve displayed by a conductive liquid. Vertical axis = applied potential, horizontal axis = time; *(b)* capacitance-type decay curve displayed by demineralized water and polar liquids of high resistivity.

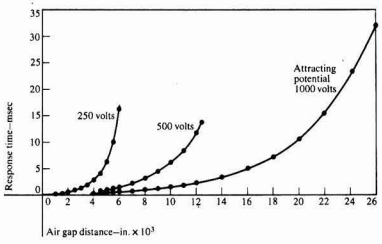

Fig. 3. As air gap distance increases, the response time increases.

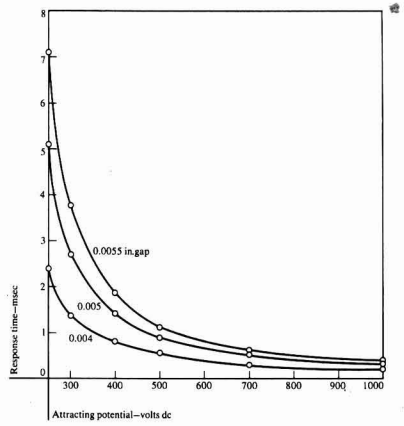

Fig. 4. At small gaps, the response time decreases rapidly as attracting potential increases in the range from 250 to 500v (aqueous solution).

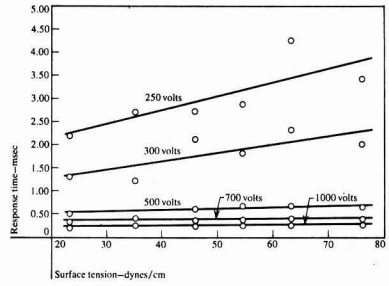

Fig. 5. Effect of surface tension on response time decreases with increasing voltage (0.004 in. gap, aqueous solution).

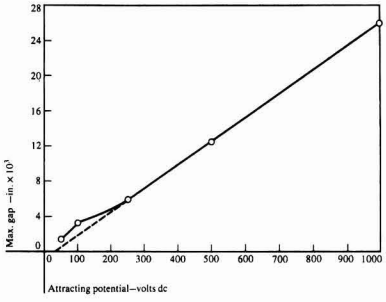

Fig. 6. As attracting potential increases, the maximum gap at which liquid will jump increases (aqueous solution).

sium chloride was titrated into demineralized water. As the conductivity of the solution was varied from 6 to 3000 μmhos (monitored during titration by a conductance bridge with dip-type cells), response time remained relatively constant (Fig. 8).

The concentration of crystal violet in water was varied from 0 to 1% to test the possibility that the concentration of colloidal electrolyte in a liquid could significantly affect response time. It did not (Fig. 9).

In none of the experiments with solution properties of high-dielectric-constant liquids was there a difference in response time which could be attributed to the size of the particles in solution. The solutions studied had particles that ranged from ions to colloidal electrolytes to colloids to coarse particles.

Effect of electric field properties.—The simple model of the attraction process assumes a point electrode. Electrode geometry, however, is important in a real system. Therefore, variations in the electrode geometry and their effect on response time were studied. When the electrode was altered from a conical tip with 0.021 in. radius to a hemisphere with 0.115 in. radius to a flat surface, the response time increased accordingly. The effect of these gross changes is to make the attracting force weaker by reducing the divergence of the field and the results in Table I are not unexpected based on a model using a dielectric-constant relationship. However, a much subtler change in electrode geometry produced an interesting result. When the radius of the tip of the conical micrometer head was reduced from 0.021 to 0.008 in., the response time was significantly higher for the smaller tip (Table II). This seems to indicate the

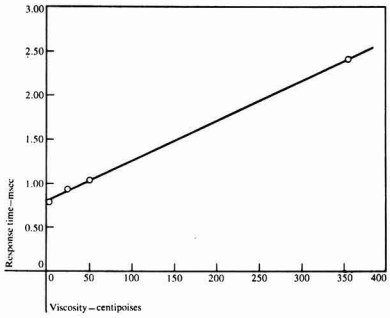

Fig. 7. Response time increases with increasing viscosity (surface tension corrected to 39.1 dynes/cm, 0.004 in. gap, aqueous solution).

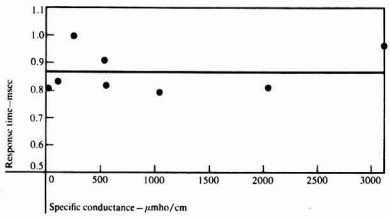

Fig. 8. Specific conductance has no effect on response time in the range from 6 μmhos/cm to 3000 μmhos/cm (0.004 in. gap, surface tension corrected to 75.0 dynes/cm).

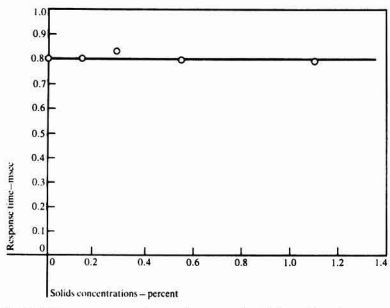

Fig. 9. Solid concentration of crystal violet dye has no effect on response time (0.004 in. gap, aqueous solution).

existence of an inflection point in the variation of response time with electrode diameter. Perhaps the divergence of the electric field with the smaller-radius electrode is great enough to result in such a substantial decrease in the field near the surface of the liquid that the high acceleration caused by the field near the tip is not enough to compensate.

Also, to find out whether variation in liquid depth would change the shape of the field, we measured response time at several liquid depths from 0.2509 to 0.0076 in. No change was noted. It was concluded that for relatively conductive liquids, the liquid surface itself could be assumed to act as the ground electrode. In fact, removing the brass-disk electrode from the

Table I. Effect of gross changes in electrode geometry

Electrode shape	Response time in msec applied voltage +500v	−500v
Point	0.52	0.29
Hemisphere	0.63	0.57
Flat	0.77	0.73

Table II. Effect of small change in electrode geometry

Radius of conical tip in inches	Response time in msec air gap in inches			
	0.004	0.006	0.008	0.010
0.021	0.56	1.16	2.42	4.85
0.008	0.70	2.40	5.90	14.31

petri dish has almost no effect on response time as long as the liquid makes contact with an electrical ground.

Finally, an experiment was run to test the possibility that a negatively charged attraction electrode would produce different response times than did the positively charged ones. Different behavior would not be unexpected since it has been observed in the breakdown voltages of point-plane surfaces in air (12) and in some work with liquids (13, 14) where large changes in the refractive index of the liquids occurred with a negatively charged point but not with a positively charged point. Figure 10 shows that, in general, response times obtained with negative potential on the attraction electrode were lower than those with positive potential. However, response times were much more erratic for the negative potentials. In addition, in our experiments, response time results already obtained for the aqueous crystal violet solution at an attracting voltage of +500v were compared with those response times obtained for the negatively charged colloidal electrolyte, Amaranth Red U.S.P. in a 1% aqueous solution at +500v. For equivalent surface tensions they were identical.

Low-Dielectric-Constant Liquids

If the simple model suggested earlier for the liquid attraction process is at all realistic, a large increase in response time should be noticed as the dielectric constant of liquids closely approaches that of air. Our experiments with low-dielectric-constant liquids bore out this suggestion. However, it was necessary to use a different means of measuring response time for these liquids. Since low-dielectric-constant liquids have low conductivity, no change in voltage could be observed on the oscilloscope when the liquid made contact with the attracting electrode. So, a detection system utilizing a high-speed movie camera was used. In this system a timer on the camera triggered the electrode voltage after the film had accelerated to a reasonably constant speed. Timing lights were used to determine the speed of the film at the time of attraction. An oscilloscope trace identifying the time at which voltage was applied to the electrode was superimposed on the

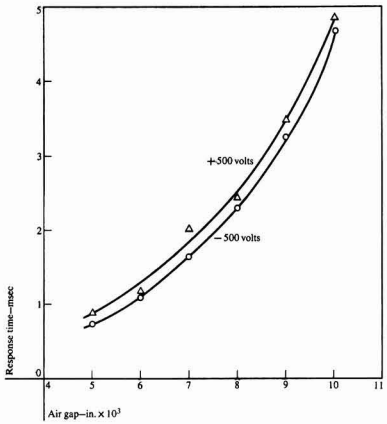

Fig. 10. Negative potentials give lower (but more erratic) response times than do positive potentials (aqueous solution).

film by means of a side-viewing port of the camera (Fig. 11).

Effect of liquid properties.—Viscosity is a measure of the internal friction of the liquid. Therefore, if the attraction phenomenon is dependent on dipole forces, the relaxation time of the dipoles can become very important in viscous liquids having low dielectric constants. The polarization forces in an electric field can be separated into two components: one slow-acting and the other fast. The fast polarization consists largely of electronic distortion because of the displacement of electrons relative to the positive nucleus. The slow polarization consists of dipole orientation in the electric field and in some respect depends on the frictional resistance of the medium to changes in molecular orientation.

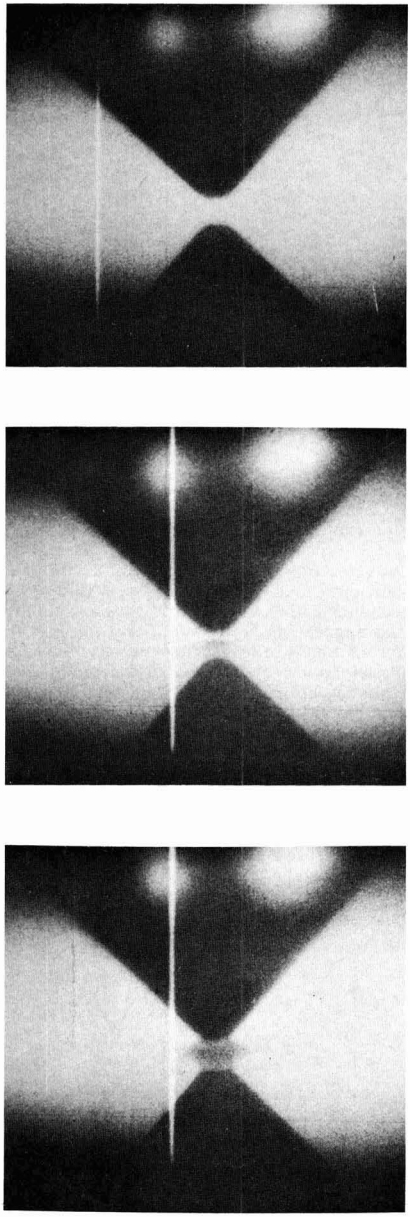

Fig. 11. Photographs of high-speed movies taken with a Fastax Model WF-17 camera. Film speed was 8000 frames per second. The dark area in the upper portion of the photo is the attraction electrode. The lower dark area is the reflection of the attraction electrode in the liquid. The white line in the left of center is the oscilloscope trace which was superimposed on the film. The shift in the position of this line took place at the time of the application of the pulse. Top, 0 sec; center, 3.0 msec; bottom, 4.5 msec.

With small-chain polar molecules, the dipole forces are usually strong enough to overcome viscosity forces in a short period of time, *e.g.*, 10^{-11} to 10^{-6} sec. With nonpolar or only slightly polar liquids, however, dipole forces are quite small. Thus the dipoles of very viscous nonpolar and slightly polar liquids can remain in a semi-oriented state minutes after the external field is removed. This is especially true of long chain molecules. Further complications arise because trace polarizing materials, including air bubbles, can change the effective dipole moment and thus the relaxation time of the molecules (15).

We ran into trouble in experimenting with the effect of viscosity on response time for low-dielectric-constant liquids. We had thought that the dimethyl silicones would be useful liquids for this type of study because their viscosity can be varied over a wide range without changing the dielectric constant by much. However, the results obtained were very unreliable, apparently because of the hysteresis effects mentioned above. Toluene ($K_2 = 2.4$), the liquid we used for several subsequent experiments, could not be used to study viscosity. Also, it was not possible to vary surface tension and conductivity significantly, so the effects of these properties were not studied either.

The significance that various additives have on the response time of toluene is shown in Table III. Materials having different particle sizes and solubilities were dissolved or dispersed in toluene. It appears that response time decreases accordingly as the particles have greater polarizing power. The most marked effect on response time was produced by the presence of colloid particles.

Table IV shows that ambient conditions also have a great effect on the response time of toluene. It is possible that the variation is caused by water condensed from the atmosphere by evaporating molecules of the liquid. This condensation could change the dielectric constant of the air gap enough to significantly alter the attracting force on the liquid. Another explanation is that air-vapor electrophoresis-dielectrophoresis occurring at high relative humidity and/or high vapor pressure of solvent produces a down pressure [the "electric wind" described by Pohl (5)]. The importance of evaporation rate was noted when hexane ($K_2 = 1.9$), which has a high evaporation rate, was

Table III. Effect of additives in toluene on response time

Additive	Response time in msec
1% Amaranth dye (large particle)	53.0
1% Foron blue (partial solution plus flocculated particles)	46.2
1% Acetate red (partial solution plus large particles)	17.9
1% Oil red (solution)	11.7
1% Crystal violet, extra pure (colloidal plus medium-sized particles)	4.36

Table IV. Effect of temperature and humidity on response time of toluene

Temperature in °F	Relative humidity, %	Response time in msec
78	30	10.7
72.5	42	14.2
70.3	52	30.2

Table V. Effect of gross changes in electrode geometry

Electrode shape	Maximum gap in inches applied voltage +500v	−500v
Point	0.0130	0.0130
Hemisphere	0.0187	0.0180
Flat	0.0283	0.0273

compared with toluene. The maximum gap across which the hexane could jump at 500v was only 0.0025 in. as compared with 0.0123 in. for toluene. Furthermore, when the level of the toluene was raised to the top of the container, response time increased sharply, no matter where the ground electrode was placed. Hence, it appears that for low-dielectric-constant liquids an increase in evaporation rate, whether it is inherent or caused by greater exposure of the liquid to air currents, increases response time.

Electric field effects.—The effect of electrode geometry on the maximum gap of toluene was also studied (Table V). The electrodes were the same as those used in the electrode geometry study for liquids with high-dielectric constants. The results showed that the maximum gap through which the liquid could be attracted increased in this order: pointed, rounded, and flat attraction electrode. This seemed to indicate that for these three electrodes, the more uniform the field, the longer the response time, but the higher the maximum gap through which the liquid can be attracted. One possible reason is that while more-divergent fields produce a higher acceleration, less force is available at the surface of the liquid to overcome surface tension. It should be kept in mind that the mass of the liquid attracted may be varying with the radius of the attraction electrode.

As another consideration, if electrode-to-electrode distance is very critical, a difference in maximum gap should be noticed as the depth of toluene is varied. While the surface of a conductive liquid can be expected to act as a ground electrode, this is certainly not true for the low-conductivity liquids. No great difference in maximum gap was noticed when the depth of toluene was varied from 0.250 to 0.019 in. at 500v. Furthermore, when the ground disk was removed from the petri dish the liquid continued to jump under the applied potential. This indicates that for the depths of liquid studied, as long as some reference ground is present, the electrode-to-liquid distance is more important than electrode-to-electrode distance.

A study of some liquids having dielectric constants in the range between what have been called high- and low-dielectric-constant liquids was performed. Response times of these liquids are given in Table VI.

Conclusion

It has been shown that response time is largely independent of the conductivity, solids concentration, and particle size of dissolved or dispersed materials in a highly polar liquid such as water, although response time does vary with the surface tension and viscosity of the liquid. However, above a certain field strength, surface tension plays a minor role in determining the rate of attraction. In addition, studies with high-, intermediate-, and low-dielectric constant liquids, have shown that response time appears to be lowest for liquids with high-dielectric constants and *vice versa*. Also, the evaporation rate or the presence of vapor molecules of a volatile nonpolar or only slightly polar liquid appears to increase the response time. However, the presence of particles capable of producing polarization effects in a low-polarity liquid reduces this effect and produces a decrease in the response time of the liquid.

Table VI. Response times for liquids with intermediate dielectric constants

Liquid	Surface tension in dynes/cm	Viscosity in centipoise	Dielectric constant	Response time in msec
Methyl alcohol	22.6	0.59	33.0	4.1
Acetone	23.7	0.33	21.3	4.7
G. E. nitrile silicone XF-1150	36.7	800-1300	19.6	18.5
G. E. nitrile silicone XF-1112	23.6	100 ± 20	7.2	4.1
G. E. nitrile silicone XF-1112 plus crystal violet extra pure	—	—	—	3.0
G. E. nitrile silicone XF-1105	21.9	100 ± 20	4.7	10.6
G. E. nitrile silicone XF-1105 plus dispersed dye Foron blue	—	—	—	10.4

Based on the above data and the fact that the effects of electrical polarity within the liquid appear to be negligible or at least quite obscure, a stand can be taken that the phenomenon studied was largely dielectrophoresis. An analogy can be drawn to the work of Pohl (4-8) if the air between the attraction electrode and the liquid is considered as the fluid of low-dielectric constant and the liquid attracted is considered as a large, easily deformable particle.

Acknowledgment

The author acknowledges the contribution of E. R. Mondou, who performed most of the measurements reported here.

Manuscript received Nov. 28, 1967. This paper was presented at the Chicago Meeting, Oct. 15-19, 1967, as Abstract 151.

Any discussion of this paper will appear in a Discussion Section to be published in the December 1968 JOURNAL.

REFERENCES

1. A. Voet, "Ink and Paper in the Printing Process," p. 81, Interscience Publishers, New York (1952).
2. J. W. Swan, *Proc. Royal Soc.*, **62**, 38 (1897).
3. H. Schott and W. S. Kaghan, *Appl. Phys.*, **36**, 3399 (1965).
4. H. A. Pohl, *ibid.*, **22**, 869 (1951).
5. H. A. Pohl, *ibid.*, **29**, 1182 (1958).
6. H. A. Pohl and J. P. Schwar, *ibid.*, **30**, 69 (1956).
7. H. A. Pohl and C. E. Plymale, *This Journal*, **107**, 386 (1960).
8. H. A. Pohl, *Scientific American*, p. 107 (December 1960).
9. J. A. Kok, "Electrical Breakdown of Insulating Liquids," p. 40, Philips Technical Library, Netherlands (1961).
10. W. F. Pickard, "Electrical Force Effects in Dielectric Liquids," in "Progress in Dielectric," p. 24, J. B. Birkes and J. Hart, Editors, Academic Press, New York (1965).
11. G. P. Harnwell, "Principles of Electricity and Magnetism," p. 74, McGraw-Hill Book Co. Inc., New York (1949).
12. J. M. Meek and J. D. Craggs, "Electrical Breakdown of Gases," Clarenden Press, Oxford, (1953).
13. B. Farazmand, *Brit. Appl. Phys.*, **12**, 251 (1961).
14. S. S. Hakim and J. B. Higham, *Nature*, **189**, 996 (1961).
15. C. P. Smyth, "Dielectric Behavior and Structure," p. 52, McGraw-Hill Book Co., Inc., New York (1955).

Evidence of Nickel Phosphide Ni_2P in As-plated Electroless Nickel

J.-P. Randin and H. E. Hintermann*

Laboratoire Suisse de Recherches Horlogères, Neuchâtel, Switzerland

ABSTRACT

The dissolution rate of as-plated electroless nickel containing between 3.2 and 12.5 w/o phosphorus is studied in hydrochloric acid. Two reaction rates can be distinguished: first the dissolution of the nickel phase (fast), second that of a phase containing 21 w/o phosphorus whose stoichiometry corresponds to the composition of the nickel phosphide Ni_2P (slow). The Ni_2P content of the as-plated electroless nickel corresponds to the entirety of phosphorus bonded to nickel.

In a previous publication (1) the study of electroless nickel by differential thermal analysis revealed that the heat evolution during the heating corresponds to 11-17% of the heat of formation of Ni_3P, which is the final reaction product. According to this data and the findings of Graham, Lindsay, and Read (2) we proposed that as-plated electroless nickel might be a supersaturated solid solution of phosphorus in nickel. This state could be considered as a metastable intermediate state between that of a mixture of nickel plus phosphorus and that of the equilibrium system of nickel plus Ni_3P. We suggested (1) that the intermediate state could include phosphorus atoms chemically bonded to nickel atoms as a phosphide since 83-89% of the heat of formation of the stable state of nickel plus Ni_3P is released.

In this study it is shown how the dissolution rate of electroless nickel in hydrochloric acid allows to establish the nature of the chemical state of phosphorus in the as-plated alloy.

Experimental Procedure

Preparation of deposits.—An acid bath of the following composition was used: $NiCl_2 \cdot 6H_2O$: 30 g/l; $CH_2(OH)COOH$: 30 g/l; $COOH(CH_2)_2COOH$: 10 g/l; NaF: 3 g/l; NaOH to adjust the desired *p*H. The reducing agent was sodium hypophosphite, added to the bath as a concentrated solution of 500 g/l at constant rate. The temperature of the bath was 94°C. If the *p*H and the nickel concentration are kept constant during the entire deposition time, coatings of uniform phosphorus distribution are obtained (3). By adjusting the *p*H of the bath between 5.0 and 4.0, deposits with phosphorus contents between 3.5 and 11.4 w/o (weight per cent) are produced for an introduction rate of the hypophosphite of 0.05 M/hr. For the deposition at *p*H 5.0, the concentration of the glycolic acid has to be increased in regard to the concentration at lower *p*H to prevent the precipitation of the orthophosphite. At *p*H 5.0 the bath of the aforementioned composition was used and the nickel concentration was kept constant during the entire reaction time by addition of a solution containing: 500 g/l $NiCl_2 \cdot 6H_2O$, 500 cm^3 of a 56 w/o aqueous solution of glycolic acid completed to 1000 cm^3 with demineralized water. For lower *p*H, an aqueous solution of $NiCl_2 \cdot 6H_2O$ at a concentration of 800 g/l was used. If the orthophosphite which precipitates during the deposition from the bath with normal concentration is dissolved in the bath at *p*H $\simeq$ 4, the residue of dissolution in 7.8*N* hydrochloric acid at room temperature contains about 23 w/o phosphorus whereas it contains only 21 w/o if the solvent is at boiling temperature. As will be seen further on, the phosphorus content of the residue represents 21 w/o for both solution temperatures, providing that the orthophosphite precipitation in the bath is prevented.

Powdery samples were prepared by seeding the bath with palladium chloride. The powders used were previously ground and screened to obtain particles smaller than 37 μm (400 mesh ASTM).

Dissolutions and analyses.—The dissolutions of electroless nickel are made in hydrochloric acid either at room temperature and slightly agitated, or at boiling temperature. The amount of hydrochloric acid used is twice as high as that required assuming that electroless nickel contains only nickel. The acid concentrations reported in this work always are the initial values. During the dissolution these concentrations may decrease by one half if all the powder is dissolved. For each run, the amount of electroless nickel used is 5 or 10 mM depending on the acid concentration.

After the test, the residue is filtered on Millipore,[1] then oxidized with the filter in nitric acid. The Millipore filters have been used because the as-plated deposit of electroless nickel consists of very small crystals. Moreover the oxidation of the residue with the filter is more practical and safer (avoiding any loss of substance) than the use of ordinary filters. By the Tyndall effect, we made sure that the filtration was efficacious, *i.e.*, that no solid particles of colloidal size of the residue had passed the filter.

The nickel and the phosphorus are spectrophotometrically determined by the dimethylglyoxime oxidizing agent method (4) and the molybdenum blue method using the ascorbic acid as a reducing agent (5), respectively. The relative error is of $\pm 1\%$ for each element.

We verified that, under our experimental conditions, no phosphine PH_3 was produced, or in negligible amounts only.

The nickel and the phosphorus of both the residue and the filtrate of one particular test were determined in order to check the material balance. In further experiments the nickel and the phosphorus were determined only from the residue.

Moreover, we verified that the sum of the phosphorus plus the nickel corresponds to the weight of the residue. At this point, difficulties have arisen with the residues from electroless nickel with initial phosphorus contents of about 4 w/o. These residues, washed with demineralized water then dried in air at 70°C, present a difference from 10 to 17% between their weight and the sum nickel plus phosphorus analytically determined. The reason for this discrepancy is the oxidation of the residue during its drying. It could be shown that the oxidized precipitate can be reduced at 600°C in hydrogen. The undesired oxidation can be avoided by maintaining the residue during and after the filtration continuously under a film of water. The wet slurry is then transferred into an oven and

* Electrochemical Society Active Member.

[1] Millipore Filter Corporation, Bedford, Massachusetts, (Type GS WP 04700, Mean Pore Size 0.22 μm.)

dried at 700°C during 1 hr under vacuum, and cooled when still under reduced pressure. By the heat treatment the powder is recrystallized and its activity and ease to oxidize are decreased. For powders thus treated the analytical results for nickel and phosphorus add up to 100% of the weighed sample. The reactivity of the residue is unique for electroless nickel deposits containing about 4 w/o phosphorus. This phenomenon certainly comes from the following fact. After a certain time of deposition at pH 5.0, a spontaneous seeding of the bath occurs and leads to a deposition of much finer particles than those issuing from the palladium nucleates.

Results

As-plated electroless nickel.—The dissolution of electroless nickel in hydrochloric acid is studied as a time dependent function with the acid concentration, the initial phosphorus contents of the deposited alloys, and the solvent temperature as parameters.

Influence of the HCl concentration at room temperature.—Figure 1 shows that for an initial phosphorus content of 3.26 w/o, the rate of dissolution at the beginning of the reaction is the faster the higher the concentration of the acid. After a certain time, a maximum of the rate of dissolution occurs for a concentration of 2.0*N*. For a concentration of 7.8*N* (azeotropic mixture, $d = 1.12$ g/cm^3), the curve is composed of two linear sections of different slope. Figure 2 shows the phosphorus content in the residue which increases rapidly with the dissolution time to approach a limiting value. After a certain time, the residue has the same composition as what is analyzed in the solution. Therefore the dissolution curve showing two intersecting straight lines (Fig. 1) can be explained by the successive dissolutions of two phases: first the nickel one and second a phase containing about 21 w/o phosphorus, that is to say a compound with the stoichiometry of the nickel phosphide Ni_2P (20.87 w/o P). The linear extrapolation at time zero of the second section of the straight line (Fig. 1) yields the initial content of the phosphide phase present in the alloy. The calculated value obtained by supposing that all phosphorus initially present in the alloy is bonded to the nickel as the nickel phosphide Ni_2P, indicated down at right of Fig. 1, agrees well with the extrapolated value.

Influence of the initial phosphorus content of electroless nickel at room temperature.—The results obtained with a sample containing 3.26 w/o phosphorus are reported on Fig. 1 and 2; Fig. 3 shows the same types of curves combined in a single figure for a sample containing 6.85 w/o phosphorus dissolved in 7.8*N* hydrochloric acid. Again the limiting value for the phosphorus content in the residue reaches about 21 w/o corresponding to the nickel phosphide Ni_2P. The extrapolated value pertinent to the initial Ni_2P content present in the electroless nickel and drawn from the time when the phosphorus content of the residue varies no more, corresponds well to the calculated value for 6.85 w/o phosphorus, supposing the totality of the initial phosphorus is bonded to nickel at Ni_2P.

For phosphorus contents higher than 8 w/o, the dissolution time is very long and the separation less efficacious than for alloys with lower phosphorus contents.

Influence of the HCl concentration at boiling temperature.—As an example the dissolution of electroless nickel of 12.5 w/o initial phosphorus content in boiling acid is reported. For acid concentration $\leq 2N$ it is found that the higher the acid concentration, the more rapid the dissolution rate (Fig. 4). For a concentration of 7.8*N*, the dissolution rate is more rapid initially than for an acid concentration of 2.0*N*. The most efficacious separation of the two phases initially present in the as-plated alloy is realized at boiling temperature with an acid concentration of 7.8*N*. The

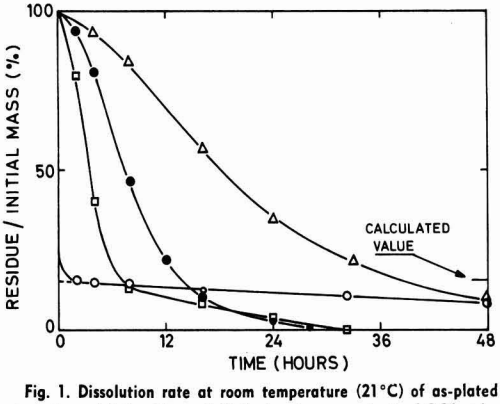

Fig. 1. Dissolution rate at room temperature (21°C) of as-plated electroless nickel with an initial phosphorus content of 3.26 w/o. ○ HCl 7.8*N*, □ HCl 2.0*N*, ● HCl 0.78*N*, △ HCl 0.20*N*.

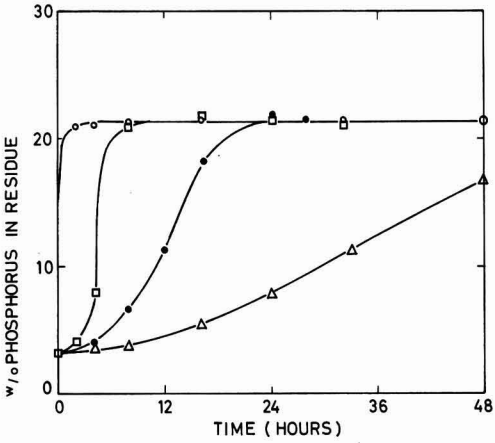

Fig. 2. Phosphorus content of the residue as a function of the time of dissolution at room temperature (21°C) for as-plated electroless nickel with an initial phosphorus content of 3.26 w/o. Legend same as Fig. 1.

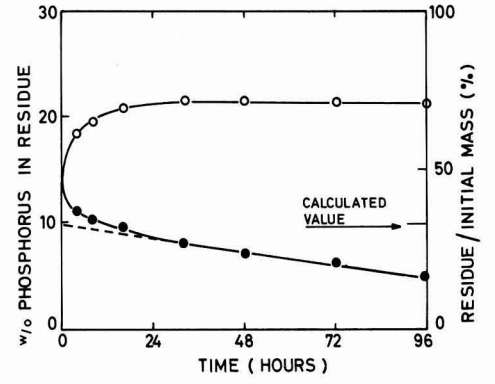

Fig. 3. Phosphorus content of the residue as a function of the time and dissolution rate of as-plated electroless nickel with an initial phosphorus content of 6.85 w/o at room temperature (21°C) in 7.8*N* HCl. ○ w/o P in residue, ● residue/initial mass in per cent.

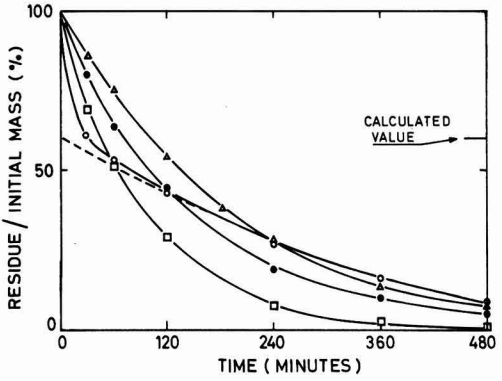

Fig. 4. Dissolution rate at boiling temperature of as-plated electroless nickel with an initial phosphorus content of 12.5 w/o. Legend same as Fig. 1.

same phenomenon was already observed with samples dissolved at room temperature (Fig. 1). The phosphorus content of the residue as a function of the time of dissolution shows that the limiting value reaches 20.9 w/o phosphorus which exactly corresponds to the stoichiometric composition of the nickel phosphide Ni_2P (Fig. 5). Again, the extrapolated value of the initial content of the Ni_2P phase corresponds to the calculated one, assuming that all the phosphorus is present as Ni_2P. In the case under discussion, the curve is not a segment of a straight line any longer hence the extrapolation has to be made from the time when the phosphorus content of the residue varies no more (upper curve of Fig. 6).

Influence of the initial phosphorus content of electroless nickel at boiling temperature.—Samples containing 8.78, 6.85, and 3.26 w/o phosphorus are studied in an acid concentration of 7.8*N* (Fig. 6, 7, and 8). For all these contents, the dissolution leads to the isolation of a Ni_2P phase. The extrapolated values of the initial contents of Ni_2P phase in the as-plated alloys agree well with the calculated values, assuming that all phosphorus is present as Ni_2P.

Heat-treated electroless nickel.—The method of dissolution in hydrochloric acid is applied to heat-treated electroless nickel, whose structure and chemical composition are well established. The heat treatment was conducted under a vacuum better than 10^{-3} Torr for 5 hr, at 800°C.

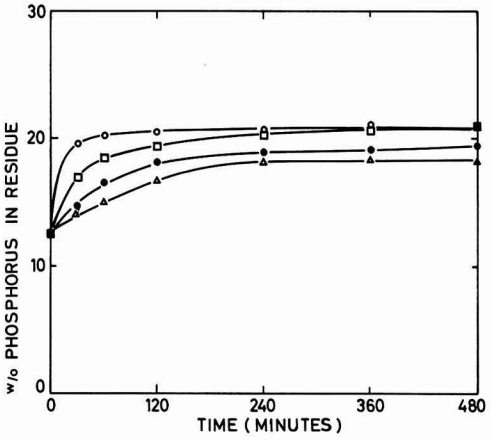

Fig. 5. Phosphorus content of the residue as a function of the time of dissolution at boiling temperature for as-plated electroless nickel with an initial phosphorus content of 12.5 w/o. Legend same as Fig. 1.

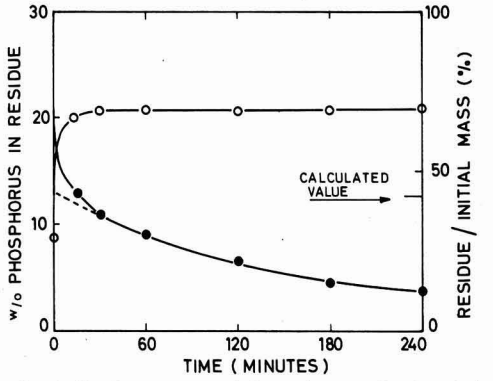

Fig. 6. Phosphorus content of the residue as a function of the time and dissolution rate of as-plated electroless nickel with an initial phosphorus content of 8.78 w/o at boiling temperature in 7.8*N* HCl. Legend same as Fig. 3.

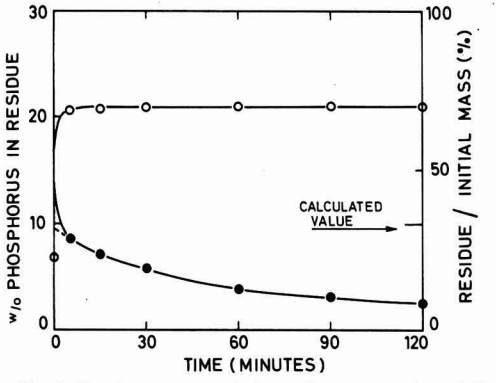

Fig. 7. Phosphorus content of the residue as a function of the time and dissolution rate of as-plated electroless nickel with an initial phosphorus content of 6.85 w/o at boiling temperature in 7.8*N* HCl. Legend same as Fig. 3.

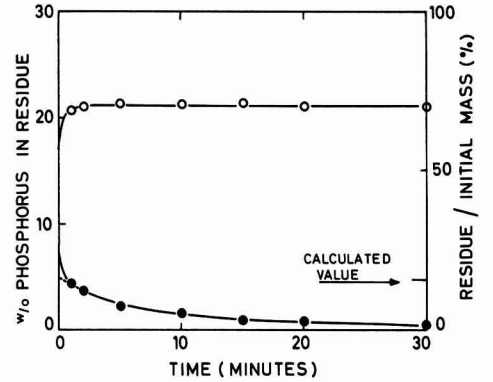

Fig. 8. Phosphorus content of the residue as a function of the time and dissolution rate of as-plated electroless nickel with an initial phosphorus content of 3.26 w/o at boiling temperature in 7.8*N* HCl. Legend same as Fig. 3.

Samples containing 3.71, 8.78, and 12.5 w/o phosphorus are dissolved in 7.8*N* hydrochloric acid (Fig. 9, 10, and 11). For each of these phosphorus contents,

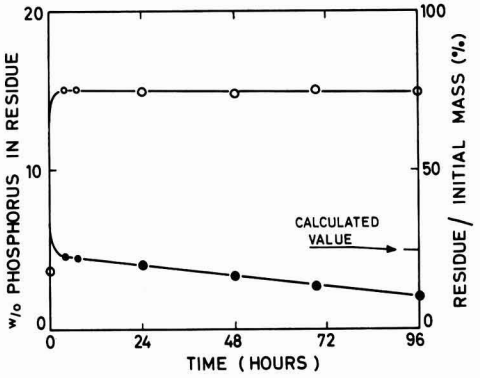

Fig. 9. Phosphorus content of the residue as a function of the time and dissolution rate of heat-treated electroless nickel with an initial phosphorus content of 3.71 w/o at room temperature (24°C) in 7.8*N* HCl. Legend same as Fig. 3.

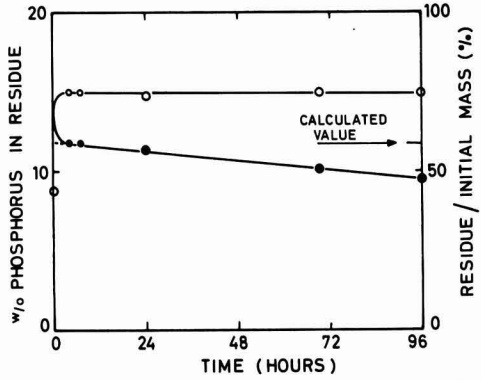

Fig. 10. Phosphorus content of the residue as a function of the time and dissolution rate of heat-treated electroless nickel with an initial phosphorus content of 8.78 w/o at room temperature (24°C) in 7.8*N* HCl. Legend same as Fig. 3.

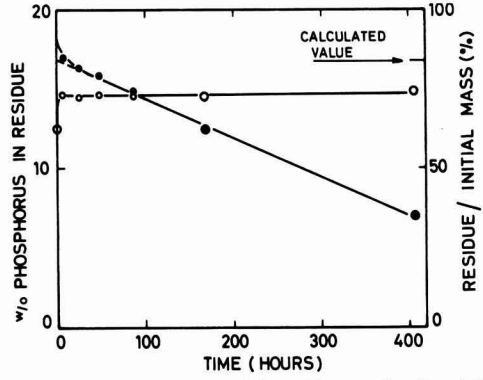

Fig. 11. Phosphorus content of the residue as a function of the time and dissolution rate of heat-treated electroless nickel with an initial phosphorus content of 12.5 w/o at room temperature (24°C) in 7.8*N* HCl. Legend same as Fig. 3.

the dissolution leads to the isolation of a phase containing about 15 w/o phosphorus in good agreement with the stoichiometry of the nickel phosphide Ni_3P (14.96 w/o P). The extrapolated values of the initial contents of the Ni_3P phase in the heat-treated electroless nickel correspond well to the calculated values, supposing all the phosphorus is present as Ni_3P. These results confirm those obtained by the x-ray method (1).

Discussion and Conclusions

For all the phosphorus contents of the electroless nickel studied, and independently of the temperature of dissolution, a nickel phosphide phase whose stoichiometry corresponds to Ni_2P could be isolated. In as-plated electroless nickel, nickel phosphide Ni_2P is best separated from nickel by using 7.8*N* hydrochloric acid as a solvent, for low phosphorus alloys at room temperature, and for high phosphorus alloys at boiling temperature. The Ni_2P content of the as-plated electroless nickel accounts for all the phosphorus present in the samples.

The identification of the nickel phosphide Ni_2P as such is the residue of dissolution of as-plated electroless nickel was also attempted by x-ray diffraction analysis and DTA.

The x-ray diffraction study of the residue of dissolution leads to the results of Table I. The small number of lines observed and the accuracy of their position for the nonheat-treated residue do not allow one to assert the presence of Ni_2P only. The x-ray diagram obtained from a sample annealed for 24 hr at 800°C in hydrogen confirms the previously found line positions for the nonheat-treated residue. It reveals however an additional number of diffraction lines of Ni_2P as well as some of $Ni_{12}P_5$ which is formed during the heat treatment. The positions of the lines measured on the residue of dissolution and the calculated values of Ni_2P agree within 1 °/₀₀. The relative intensities of the observed values on the residue compare reasonably well with those tabulated. Thus, the residue of dissolution of as-plated electroless nickel consists of Ni_2P; it contains no nickel and no other nickel phosphide.

A DTA curve of the residue of dissolution does not show any deviation. An as-plated electroless nickel alloy containing about 8 w/o phosphorus was reconstituted by mechanically mixing a residue of dissolution and a carbonyl-nickel powder, then studied by DTA. The exothermic energy evolved between 520° and 640°C corresponds to about 5.7 kcal/mole Ni_3P, the reaction product being identified as Ni_3P. In a previous work (1) a DTA study of electroless nickel revealed two reaction areas in the energy *vs.* temperature diagram: one below 300°C, the other above 300°C. The reaction heat of the former was called Q_1, that of the latter Q_2. The heat $Q_2 = 5.9$ kcal/mole Ni_3P is proportional to the phosphorus content of the electroless nickel. Q_1 passes through a maximum at about 8 w/o phosphorus and vanishes thereafter at a concentration higher than 10 w/o. The total heat of reaction $Q_1 + Q_2$ for alloys with less than 8 w/o phosphorus is 8.9 kcal/mole Ni_3P.

Table I. Comparison of observed line spacings and intensities of residue against calculated values of Ni_2P

d (Å) measured on residue	d (Å) measured on residue heat-treated 24 hr, 800°C	d (Å) Ni_2P Pearson (6)	I/I_o measured on residue	I/I_o measured on residue heat-treated 24 hr, 800°C	I/I_o Ni_2P ASTM (7)	Reflection hkl
2.214	2.217	2.216	100	100	100	111
2.028	2.031	2.031	85	50	80	201
1.914	1.918	1.919	69	40	80	120
—	1.692	1.693	—	28	70	300/002
—	1.670	1.670	—	15	40	121
1.39*	1.408	1.409	24	20	40	310
—	1.300	1.300	—	40	40	311
1.26*	1.271	1.270	48	67	60	212
1.18*	1.197	1.199	30	55	60	302
—	1.188	1.189	—	24	—	401
—	1.101	1.102	—	100	88	231
—	1.083	1.083	—	20	40	132

* Less accurate measurement.

The heats Q_1 and Q_2 obtained below 400°C are difficult to compare with the value reported in the present work which was measured between 520° and 640°C, since specific heat data of nickel phosphides are not available. However, the energy of 5.7 kcal/mole Ni_3P evolved during heating of a mixture of Ni_2P plus nickel corresponds to the heat previously called Q_2, *i.e.*, 5.9 kcal/mole Ni_3P. The energy of the reaction

$$Ni_2P + Ni = Ni_3P + 8.4 \text{ kcal (at 630°C)} \quad (8)$$

more or less corresponds to the heat previously called $Q_1 + Q_2$, *i.e.*, 8.9 kcal/mole Ni_3P.

The comparison of results of the dissolution rates with those obtained by DTA (1) leads to the following comments. The DTA study (1) revealed two reaction areas for phosphorus contents below 10 w/o while only one such area was observed above this concentration. According to the results of the present study showing that the as-plated electroless nickel has the same qualitative composition for any phosphorus content, the two reaction areas previously observed for phosphorus contents below 10 w/o could eventually correspond to the formation of Ni_5P_2 from Ni_2P and of Ni_3P from Ni_5P_2. This hypothesis would not explain the case of phosphorus contents higher than 10 w/o. In order to verify this supposition, samples containing 3.26, 7.32, and 12.5 w/o phosphorus, respectively, were analyzed after heating up to 285°C under the same conditions as those used in the DTA study, *i.e.*, a heating rate of 2°/min. This temperature delimits the two reaction areas. After dissolution in 7.8*N* hydrochloric acid at boiling temperature, the three samples lead to a residue with the stoichiometry of Ni_2P. These very samples further investigated under the same experimental conditions after heating up to a temperature high enough to allow a complete reaction, *i.e.*, 500°C, leave a dissolution residue whose stoichiometry corresponds to that of Ni_3P. The intermediate state of the Ni_5P_2 does not represent any one of the two reaction areas and, therefore, cannot be isolated by controlling merely the temperature of the heat treatment.

As a consequence, the heat previously called Q_2 which is proportional to the phosphorus content of the electroless nickel may correspond to the reaction: $Ni_2P + Ni = Ni_3P$, though the measured energy is only 5.9 kcal/mole Ni_3P, *i.e.*, about 70% of that indicated by Weibke and Schrag (8). This hypothesis is supported by the fact that the energy evolved during the rise of temperature of a reconstituted electroless nickel alloy from Ni_2P plus nickel leads to a value close to the heat Q_2. The discrepancy between our energy result and that of Weibke and Schrag can possibly be explained by the fact that the heats of formation cannot be compared at the same temperature (see above). The heat previously called Q_1 could be explained by the reaction of a little amount of phosphorus as a solid solution in the nickel producing a nickel phosphide Ni_2P or/and Ni_3P. The maximum energy of the heat Q_1 which occurs for phosphorus contents of about 8 w/o, could correspond to a free phosphorus content <0.5 w/o.

The accuracy of the analytical results concerning the Ni_2P phase content in the as-plated alloys would allow the presence of a little amount of phosphorus not bonded to nickel. The presence of elementary phosphorus in the freshly prepared residue of dissolution, in amounts more important than only traces, cannot be measured either by reaction with sodium hydroxide, or by solubility in absolute alcohol. In carbon disulfide, the maximum solubility observed in a dissolution residue of electroless nickel with an initial phosphorus content of 4.41 w/o in 7.8*N* hydrochloric acid at room temperature is <0.02 w/o phosphorus in regard to the initial mass of electroless nickel. Therefore it might be concluded that the as-plated electroless nickel contains only very little phosphorus in the elementary state, the rest being bonded to nickel as nickel phosphide Ni_2P.

The temperature at which the electroless nickel is deposited, in this study at 94°C, has perhaps an influence on the nature of the chemical bond between phosphorus and nickel in the as-plated state. This parameter has not been investigated.

Acknowledgment

The authors wish to thank Professor P. Dinichert, Director of the L.S.R.H. for his advice and interest in this work and permission to publish this paper. They also thank Mr. J.-P. Renaud and Dr. M. Delaloye for helpful discussions and for providing facilities. They acknowledge the valuable assistance of Mr. J. C. Jaquet in the x-ray analysis and of Mr. A. Verbay in differential thermal analysis.

Manuscript received Nov. 8, 1967; revised manuscript received Jan. 22, 1968.

Any dicussion of this paper will appear in a Discussion Section to be published in the December 1968 JOURNAL.

REFERENCES

1. J.-P. Randin, P. A. Maire, E. Saurer, and H. E. Hintermann, *This Journal*, **114**, 442 (1967).
2. A. H. Graham, R. W. Lindsay, and H. J. Read, *ibid.*, **112**, 401 (1965).
3. J.-P. Randin and H. E. Hintermann, *Plating*, **54**, 523 (1967).
4. E. B. Sandell, "Colorimetric Determination of Traces of Metals," p. 671, Interscience Publishers, New York (1959).
5. L. Duval, *Chim. Anal.*, **45**, 237 (1963).
6. W. B. Pearson, "A Handbook of Lattice Spacings and Structures of Metals and Alloys," Vol. 2, p. 1132, Pergamon Press, New York (1967).
7. ASTM X-Ray Powder Data File, ASTM Special Technical Publication 48-J, 3-0953 (1960).
8. F. Weibke and G. Schrag, *Z. Elektrochem.*, **47**, 222 (1941).

Electroless Nickel Plating on Silicon

Hitoo Iwasa, Masami Yokozawa, and Iwao Teramoto

Research Laboratory, Matsushita Electronics Corporation, Takatsuki, Osaka, Japan

ABSTRACT

In the study of electroless Ni plating of Si wafers with p-n junctions using conventional solutions, a pronounced difference in plating rate between p- and n-type surfaces is observed. Further experiments show that rate difference probably should not only be attributed to the photovoltaic effect generated at the p-n junctions but also to the electronegativity difference between p- and n-type Si. The latter effect can be changed by addition of such material as NH_4SCN or $2NH_4$-EDTA to the plating solution. Whereas SCN^- addition increases the rate difference, EDTA addition decreases it. This fact which can be put to practical use gives an extra support for the explanation given above.

Electrical connections to Si transistors up to now are often made by Au-Al thermocompression bonds. Another technique uses a simple method: electroless Ni plating followed by soldering. Advantages are the excellent chemical and mechanical properties of the connections. Also the cost of the processing is much lower than of the thermocompression bonding technique. However, this latter technique is not now widely used.

Since Sullivan and Eigler (1) first applied the electroless Ni plating to Si, one of the difficulties often found for actual Si devices has been the difference in plating rate between adjacent p- and n-type surfaces. Silverman (2) reported that, during Au plating by autocatalytic reduction, the difference in plating rate between adjacent p- and n-type Si surfaces was changed by strong illumination owing to the created photovoltaic effect at the p-n junction. We observed a similar effect in the electroless Ni plating as have other observers.

The theory of electroless plating has not been well defined yet, although many explanations have been proposed. For example, Gutzeit's explanation (3), based on the autocatalytic reduction of Ni ions, may be clear for the acidic solution, but in an alkaline solution hypophosphite is spontaneously oxidized at an elevated temperature. Moreover, the effect of photovoltage on plating rate can hardly be explained by the argument that a nickel ion is reduced only by an atomic hydrogen.

One of the most promising models for the process in an alkaline bath (4) may be that in which the reactions involved are divided into anodic and cathodic reactions, forming many local cells at the interface between substrate and solution, as indicated in Fig. 1. The different reaction occurring can be summed up as follows:

1. Diffusion of reactants to the interface
2. Oxidation of $H_2PO_2^-$ (anodic)

$$H_2PO_2^- + H_2O \rightharpoonup H_2PO_3^- + 2e + 2H^+ \qquad [1]$$

3. Migration of the electrons in the substrate
4. Reduction of Ni^{++} and H^+ (cathodic)

$$Ni^{++} + 2e \rightharpoonup Ni \qquad [2]$$

$$2H^+ + 2e \rightharpoonup H_2 \qquad [3]$$

5. Diffusion of reaction products from the interface into the solution. Similar oxidation and reduction processes may occur if instead of electrons, holes move in the opposite direction in the substrate. The electron (or hole) migration in the substrate and the transfer through the interface will be determined by: (*a*) electron concentration within the substrate; (*b*) thin oxide layers on the substrate; (*c*) photovoltage at the p-n junctions; (*d*) electronegativity of the substrate. If electron (or hole) migration determines the deposition rate, one can easily imagine that this rate will be different for adjacent p- and n-type substrate materials. For this reason we studied the possibility of diminishing the difference in plating rate by transferring the rate-determining step from the migration in the substrate to one of the other steps of the reaction occurring inside the solution.

Results of experiments carried out to analyze the effect of each of these factors are reported below.

Experimental Procedures

The composition of the plating bath used in the present experiment is substantially the same as that of the Brenner solution (5), that is

$NiCl_2 \cdot 6H_2O$	30 g/l
NH_4Cl	50 g/l
$(NH_4)_2HC_6H_5O_7$	65 g/l
$NaH_2PO_2 \cdot H_2O$	10 g/l

The bath is heated to a temperature of 90°C, at which temperature about 200 cc of NH_4OH is added to 1000 cc of the plating solution; the bath temperature is then elevated to 95°C, at which temperature the Si sample is immersed in the bath for 30 sec. Ni films plated in this way were 1000-2000Å thick.

Si wafers with polished surfaces were used as samples; they were cleaned by etching slightly and rinsing with distilled water and methyl alcohol. Then the wafers were stored in isopropyl alcohol. Prior to plating, the wafer was dipped in NH_4F solution (50%) for 30 sec and again rinsed thoroughly with methyl alcohol. The whole process was carried out without drying the wafer surfaces until the plating was completed to protect the Si surfaces from oxidation and staining.

The Ni film thickness for thick films was measured by the conventional interference method. For thin films the autoradiographic method was applied by making use of radioactive Ni^{63} in the plating bath.

Electrode potentials were measured using a saturated calomel electrode as the standard electrode. The

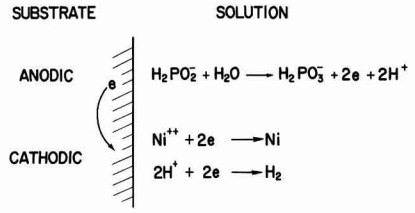

Fig. 1. Schematic representation of the "local cell" model

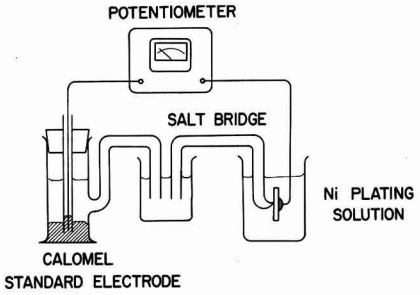

Fig. 2. Experimental arrangement for measuring electrode potentials.

schematic arrangement for this measurement is shown in Fig. 2; the electrical connection on the back side of the Si wafer was made by means of Ni plating and soldering.

The reduction potential of Ni^{++} in the plating solution was estimated by measuring the current-voltage characteristics of the solutions without the hypophosphite. The current through two Pt plates with an area of 1 cm^2, placed 1 cm apart from each other, as a function of applied voltage was traced on an X-Y recorder.

Results

Migration of charge carriers in the Si *substrate.—Thin oxide films on silicon.*—A p-type surface is more likely covered with an oxide film than an n-type surface. Plating on a p-type surface was hardly possible without a cleaning treatment to remove the oxide. Cleaning the surface with HF or NH_4F solution or adding 0.1 to 0.2 mol/l of F^- to the plating bath made the plating reproducible (6), and Ni film was easily plated even on p-type surface. However, any cleaning treatment could not eliminate the difference in plating rate between p- and n-type surfaces.

Electron concentration in silicon.—If electrons would act as charge carriers in the substrate, the plating rate on p-type should be much smaller than that on n-type Si. However, a rather small difference in plating rate was found between separated p- and n-type surfaces.

Strong illumination on semiconductors generates electron and hole pairs and makes the conduction type intrinsic. The plating rate on p-type silicon was not affected by illumination, showing that the electron concentration above a certain value has only small effect on the plating rate.

Photovoltage at the p-n junction.—With illumination on a p-n junction the plating rate on adjacent p- and n-type materials proved to be different. The difference increases with an increase of illumination density, suggesting a contribution of the photovoltaic effect. The plating rate on the n-type material was found to be higher than on the adjacent p-type material. However, an appreciable small difference was still found under weak room light.

Electronegativity of silicon.—The electronegativity of p-type Si is greater than that of n-type Si. It seems feasible that the electronegativity difference between p- and n-type Si causes a difference in rate of electron transfer from Si to Ni^{++} and consequently gives rise to a difference in plating rate.

Summarizing we may say that the difference in plating rate observed between adjacent p- and n-type surfaces as far as the substrate is concerned is due to the photovoltage generated at the p-n junction, and possibly to the difference in electronegativity between p- and n-type Si.

Rate limitations imposed by the solution.—Effect of Ni *concentration.*—The concentration of $NiCl_2$ in the plating solutions was reduced. It was found that the ratio of the plating rates on adjacent p- and n-type materials changed only slightly with Ni^{++} concentration.

Effect of additives in the plating solution.—The ammonium salt of EDTA was added to the plating solution. The observed plating rate and its ratio on adjacent p- and n-type materials are shown in Fig. 3 and Fig. 6, respectively. The ratio increased to unity with increasing concentration of EDTA. The plating rate on p-type showed a maximum at an EDTA concentration of 5 g/l, whereas on n-type material it was constant. Further addition of EDTA resulted in a remarkable decrease in plating rate, and no films were grown at an EDTA concentration above 10 g/l, corresponding to one third of Ni^{++} concentration; film growth stopped completely. Figure 4 represents autoradiographs of plated Ni: (a) without EDTA and (b) with EDTA (6 g/l). Figure 5 shows the thickness of films on both types of the p-n junction (a) without EDTA, (b) with EDTA (6 g/l) and (c) with EDTA (10 g/l).

The electrode potential of the half-cell of the system

$$Ni^{++} + 2e \rightleftharpoons Ni \qquad [2']$$

was measured. Addition of EDTA to this system made the potential more negative, as shown in Fig. 7.

The relative deposition voltages of Ni were obtained from the I-E characteristics of different $H_2PO_2^-$-free solution. The results shown in Fig. 8 indicate a tendency similar to those based on the half-cells in solutions with $H_2PO_2^-$.

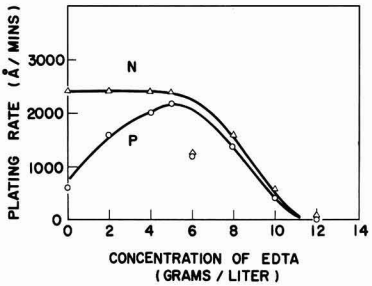

Fig. 3. Plating rate on p- and n-type Si as a function of concentration of EDTA added to the solution.

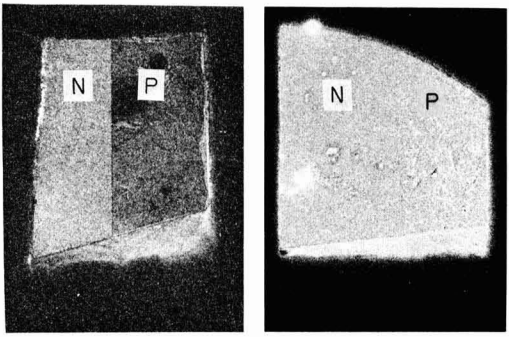

Fig. 4. Autoradiographs of plated Ni on Si: (a) with the EDTA-free solution, (b) with the EDTA-added solution (6 g/l).

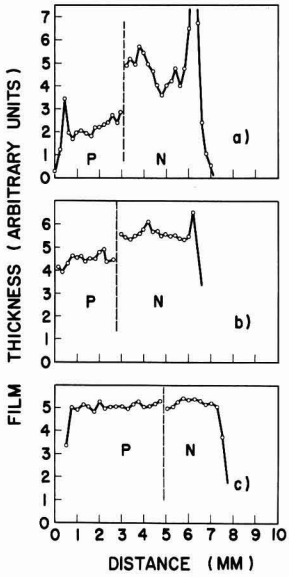

Fig. 5. Relative thickness of Ni films plated on p- and n-type Si: (a) with the EDTA-free solution, (b) with the EDTA-added solution (6 g/l), (c) with the EDTA-added solution (10 g/l).

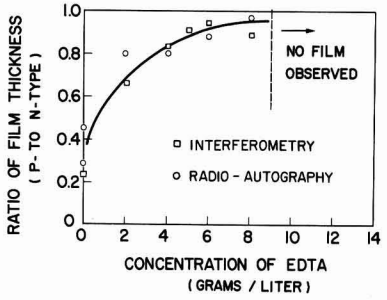

Fig. 6. Thickness ratio of Ni films plated p- and n-type Si as a function of concentration of EDTA added to the solution.

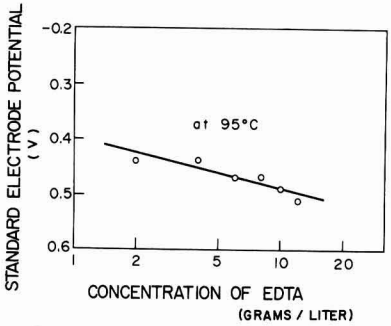

Fig. 7. Electrode potential as a function of concentration of EDTA aded to the solution.

Ni-EDTA^{++} gives a larger negative value to the electrode potential than $Ni(NH_3)_4^{++}$. One may expect that the addition of SCN^- to the plating solution will cause an opposite effect to EDTA, and that the difference in plating rate will increase with increasing SCN^- concentration. Figure 9 shows a photograph

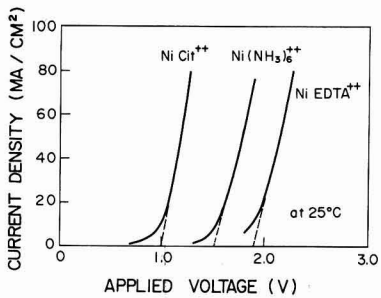

Fig. 8. Dependence of the electrode potential on complex formers, citrate, NH_3, and EDTA, added to the solution.

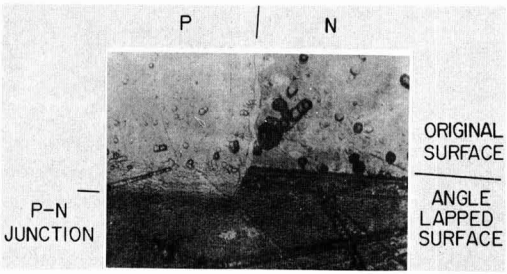

Fig. 9. Photograph of the plated Ni with the SCN^--added solution.

of an SCN^- solution; the difference was remarkably enhanced and the p-n junction was plainly revealed.

Discussion

The difference in plating rate of electroless nickel between p- and n-type surfaces under strong illumination can be attributed substantially to the photovoltage generated at p-n junctions. However, this may not be the only cause for the rate difference, because the appreciable difference was observed in plating rate even under weak room light, where the photovoltage is negligibly small. Two different causes, as previously described, would be considered. One concerns the surface condition of substrate silicon. The surface of silicon is usually covered with thin oxide layers, which impede the plating reaction. However, it was found that careful cleaning can prevent the effect of oxide. The alternative cause is due to redox potential of the substrate. With some exceptions, electroless nickel plating is more easily applied to less noble materials. In other words, the plating rate is higher on less electronegative materials, being consistent with the result observed on p- and n-Si. Thus, both the photovoltage generated at p-n junctions and the electronegativity difference between p- and n-substrates may affect the plating rate in a similar way. The effect of potential difference between p- and n-types, however, will appear relatively to the potential of nickel ions. When the potential required for reduction of nickel ions is larger than the potential difference between the substrates, the plating rates on both surfaces are small and consequently the rate difference becomes negligible in comparison with the plating rates.

From this view point, the effect of addition of EDTA can be explained as follows. By addition of EDTA salt to the plating solution, the nickel complex ion changes its form from $Ni(NH_3)_4^{++}$ to Ni-EDTA^{++} making the potential more negative (or less noble). The potential difference between p- and n-type surfaces relative to the reduction potential of the complex ions apparently decreases, resulting in diminished difference in plating rate.

On the contrary, $Ni(SCN)_2$ formed by addition of SCN salt makes the potential more positive. This gives rise to faster plating and enhanced rate difference between p- and n-substrates.

Conclusion

It is probable that the difference in plating rate between adjacent p- and n-type surfaces may be attributed to the electronegativity difference between p- and n-type Si as well as to the photovoltage generated at p-n junctions. This difference can be suppressed by addition of EDTA to the plating solution. The stable $Ni\text{-}EDTA^{++}$ complex then formed in the solution elevates the redox potential to such a high value that the electronegativity difference and the photovoltage will have a negligible effect.

Manuscript received Feb. 23, 1967; revised manuscript received Nov. 13, 1967.

Any discussion of this paper will appear in a Discussion Section to be published in the December 1968 JOURNAL.

REFERENCES

1. M. V. Sullivan and J. H. Eigler, *This Journal*, **104**, 226 (1957).
2. S. J. Silverman and D. R. Benn, *ibid.*, **105**, 170 (1958).
3. G. Gutzeit and G. Goldstein, *ibid.*, **104**, 104 (1957).
4. S. Ishibashi, *J. Metal Finishing Soc. Japan*, **12** 447 (1961).
5. A. Brenner, *Metal Finishing*, **52**, [11] 68 (1954).
6. S. L. Matlow and E. L. Ralph, *Solid State Electronics*, **2**, 202 (1961).

The Measurement of Diffusion Coefficients in Binary Liquid Metals with a Concentration Cell

John B. Edwards,† Edward E. Hucke* and Joseph J. Martin

Department of Chemical and Metallurgical Engineering, The University of Michigan, Ann Arbor, Michigan

ABSTRACT

An experimental technique has been developed for measurement of diffusion coefficients in liquid metals. A liquid metal concentration cell was designed to measure cell potential and discharge current while insuring that diffusion in the cathode was the over-all rate limiting process. The technique was used to obtain diffusion coefficients in three binary liquid metal systems; potassium-mercury, sodium-lead, and sodium-tin.

Unlike the study of diffusion in aqueous and in organic systems, it is not possible to use optical methods to study diffusion in liquid metals. The principal advantage of optical methods is that it is possible to determine the rate at which material enters the diffusion path. From this rate, anomalies such as disturbances during the initial stages of the experiment can be detected. A number of methods have been developed to measure diffusion coefficients for liquid metals in which only the over-all concentration change and/or the total quantity of diffusate is accessible. One of the authors has presented an extensive review and critique of these methods (1).

In this paper the development of a new technique for measuring diffusion coefficients of binary liquid metal systems is described. A liquid metal concentration cell with a capillary cathode is discharged at constant potential. The diffusion coefficients are calculated from the cell potential and discharge current. The unique contribution of this technique is that it allows measurement of the rate at which diffusate enters the diffusion path, and thus, detection of anomalies in the diffusion process. The technique has been utilized for measurement of coefficients in three binary systems; potassium-mercury, sodium-lead, and sodium-tin.

Experimental

Technique.—A liquid metal concentration cell may be constructed with a pure alkali metal anode, A, a fused salt electrolyte containing cations of A^+ only, and an alloy of A with a heavier metal B. The cell is written as

$$A \mid A^+ \mid A(B)$$

For a given metal couple, the reversible (open circuit) potential of such a cell, theoretically depends only on its temperature and the atomic fraction of A in the cathode alloy at the cathode-electrolyte interface. When current flows, reversible conditions no longer exist and the cell potential differs from its equilibrium value due to resistance, concentration and activation polarization.

A concentration cell of this type, together with the appropriate solution of Fick's second law, may be utilized to determine the diffusion coefficient of A through the alloy A(B) if the following conditions are met. First, the cell design must insure that diffusion of A through A(B) in the cathode is rate controlling. Second, the relationship between discharge current and quantity of alkali metal transferred from anode to cathode must be known. Third, the relationship between reversible cell potential and cathode composition must be known.

Table I summarizes the liquid metal systems investigated, the fused salt electrolytes used, and the temperature ranges studied.

Thermodynamic data are available for each of the metal couples (2) from which the equilibrium cell potential may be calculated as a function of cathode composition. Concentration units of gram atoms alkali metal per cubic centimeter of alloy were used. Alloy densities were obtained from (3, 4) for potassium amalgams. For the sodium-lead and sodium-tin al-

Table I. Summary of the liquid metal systems

Diffusion couple	Anode	Electrolyte	Cathode	Temp, °K
K in K (Hg)	K	KOH-KI-KBr	K (Hg)	500, 550, 600
Na in Na (Pb)	Na	NaOH NaI-NaCl	Na (Pb)	625 853, 903
Na in Na (Sn)	Na	NaOH NaI-NaCl	Na (Sn)	625 853, 903

† Electrochemical Society Student Member.
* Electrochemical Society Active Member.

loys, experimental data were not available, and densities were estimated by linear interpolation of the pure component densities on a mole fraction basis.

High current efficiencies with respect to A^+ were obtained by the use of discharge potentials well below the decomposition potentials of the fused salts, and by selection of salts with cations of A^+ only. The ionization potentials of sodium and potassium reveal that oxidation states greater than +1 did not occur. The solubility of alkali metals in the fused salts over the temperature ranges investigated was not large enough to affect the current efficiencies appreciably. The current densities obtained in this investigation were less than 1 amp/cm^2, while exchange currents in metal-metal ion systems are often 1-4 amp/cm^2. Therefore, activation polarization was assumed not to be rate limiting. The high specific conductivities of the molten salts gave low values of resistance polarization. Finally, the capillary cathode geometry was used to insure that concentration polarization of A diffusing through A(B) was the over-all limiting step during cell discharge.

Apparatus.—A typical diffusion cell is shown in Fig. 1. To preclude phase inversions the most dense phase must be located on the bottom and the least dense on the top. The cathode compartment was constructed from quartz tubes. These were examined under a binocular microscope, only sections with uniform bore were selected. The activity of the alkali metal in the cathode was lowered by the heavy metal addition, and the alloy did not attack the quartz. The anode compartment which was exposed to pure alkali metal was constructed of alumina. A new cell was constructed for each experiment.

The lead or tin was heated in a graphite crucible to remove surface oxides and dissolved gases. The sodium was weighed under dry box conditions and transferred under n-pentane with the lead or tin to the furnace. The heated charge was stirred to assure uniform composition after which the cathode compartments were filled by submerging them in the alloy and applying a positive pressure. The potassium amalgams were prepared in quartz rather than graphite crucibles since potassium readily forms lamellar compounds with graphite (6). The fused salts were prepared from reagents weighed in the dry box and heated in graphite crucibles. The matrices were impregnated by immersing them in the melt and pressurizing with argon. Each cell was assembled under dry box conditions.

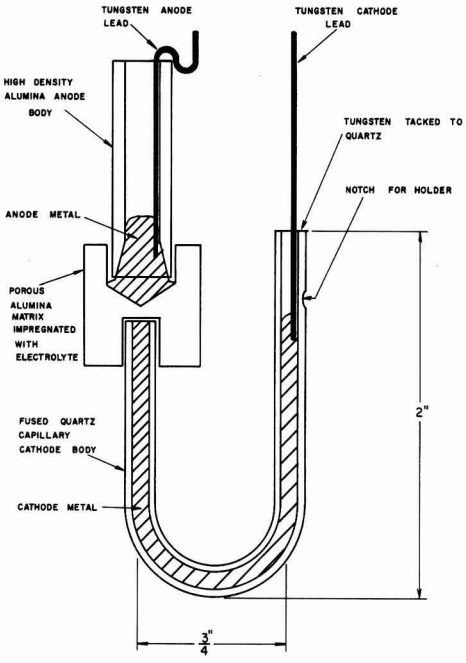

Fig. 1. Diffusion cell

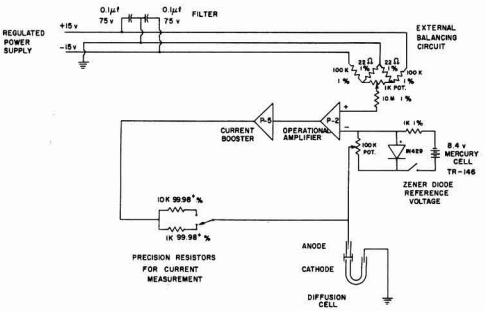

Fig. 2. Potentiostat circuit

Constant discharge potentials were obtained with a voltage follower circuit as shown in Fig. 2. This was constructed from a differential input operational amplifier and a current booster amplifier. This negative feedback circuit was capable of handling discharge currents to 20 ma. A Zener reference source was used to select the discharge potential. The discharge current was determined by measuring the potential drop across a precision resistor in the feedback circuit.

The 3-in. diameter furnace had three independently controlled windings. Power to the furnace was regulated with a proportional controller such that it was possible to maintain a stable gradient of 0.5°C/in. in the central portion of the furnace. The Vycor sleeve used to contain the cell was evacuated to less than a micron before pressurizing with high-purity argon.

Mathematical formulation.—For the case where concentration polarization of the cathode is rate limiting, the capillary may be treated as a one-dimensional semi-infinite diffusion path. Fick's second law applies.

$$\frac{\partial C}{\partial t} = D\frac{\partial^2 C}{\partial x^2} \qquad [1]$$

If the cathode-electrolyte interface is the origin and the cell is discharged at constant potential, the concentration profile in the cathode at any point x and time t is (7)

$$C(x,t) = \left[C_o + (C_s - C_o)\ \mathrm{erfc}\frac{x}{2\sqrt{Dt}} \right] \qquad [2]$$

where C_o and C_s are, respectively, the initial cathode alloy concentration and the concentration at the cathode-electrolyte interface for time greater than zero. The flux J $(0,t)$ at the interface is obtained by differentiating Eq. [2]

$$J(0,t) = (C_s - C_o)\left(\frac{D}{\pi t}\right)^{1/2} \qquad [3]$$

In this solution it is assumed that the diffusion coefficient is independent of concentration and that no volume changes occur during diffusion. Experimentally the error due to these assumptions is minimized by using small concentration intervals $(C_s - C_o)$.

At small times Eq. [3] predicts $J(0,t) \rightarrow \infty$ as $t \rightarrow 0$. However, for small times the resistance polarization in the electrolyte becomes small compared to the over-all cell potential. This occurs as the concentration gradient in the cathode becomes progressively smaller.

The one-dimensional treatment above implies the cathode-electrolyte interface is planar and perpendic-

ular to the axis of the capillary. Surface energy will lead to a nonplanar interface. A contact angle of 127° has been reported for a lead drop on a quartz surface covered with KCl-NaCl (8). Few data on other systems are available. Based on the single result for the lead-salt couple, the cathode-electrolyte interface would tend to be convex with respect to the cathode alloy. The perturbations introduced by a nonplanar interface were investigated by considering the diffusion path to be a semi-infinite cylinder terminating in a hemispherical surface at the bounded end. An analytical solution of Fick's law for this geometry is greatly complicated by the boundary conditions at the bounded end. A computer solution, however, was obtained using the implicit alternating direction technique (9). Figure 3 compares the flux obtained for the case of the hemispherical nonlinear interface to that for the one-dimensional case. A diffusivity of 1×10^{-5} cm²/sec was used. For a hemispherical interface, initially the flux is larger than Eq. [3] predicts due to the contribution of radial diffusion. However, for times in excess of a few hundred seconds the two become indistinguishable as diffusion in the cylindrical capillary becomes rate limiting.

Results and Discussion

A typical current-time discharge curve is shown in Fig. 4. The general shape conforms to that predicted by mathematical analysis. For small times, $t < 10$ sec, the flux (current/diffusion path area) is smaller than Eq. [3] predicts due to ohmic polarization in the electrolyte. For the time interval $10 < t < 100$ sec, the flux is greater than Eq. [3] predicts due to the contribution of the larger area of a nonplanar interface. For $t > 100$ sec, the discharge current behaves as is expected for one-dimensional diffusion. Equation [3] was solved to obtain the diffusion coefficient, D, explicitly. Calculation of the coefficients was based on that portion of the curve which is a straight line on a plot of log i *vs.* log t. The open-circuit potential of the cell was not stable. Presumably this was due to the small but finite solubility of the alkali metal anode in the fused salt electrolyte.

Activation polarization was assumed to be negligible and the current efficiency was taken as 100%. Both these assumptions seem reasonable in view of available data in the literature for liquid metal concentration cells. Concentration intervals ($C_s - C_o$) of from 4 to 8 m/o (mole per cent) alkali metal were used. This lower limit was determined by the smallest concentration interval which gave stable cell discharge characteristics. In each of the systems investigated two or more cells were run at a common point to insure reproducibility and to compare results from cells with 1.0 and 1.6 mm diameter diffusion paths. In no case was the path diameter found to affect the results significantly.

Coefficients for the diffusion of potassium in potassium-amalgams are shown in Fig. 5. The values of the diffusion coefficient at infinite dilution were calculated from the Stokes-Einstein equation using the viscosity reported in (10) and the Pauling ionic radius of potassium (11). The results are compared with the smoothed data of Bonilla *et al.* (3). Both investigations report a maximum in the diffusion coefficient close to $N_K = 0.30$. The phase diagram (2) shows a congruently melting compound Hg_2K at $N_K = 0.33$. Thermodynamic data (2) reveal that negative deviations from Raoult's law exist for this system. Diffusion coefficients have been measured as a function of composition for two other systems which show negative deviations from Raoult's law, Hg-Tl (12) and Bi-Pb (13). In both cases a maximum exists.

For the range $0.25 < N_K < 0.35$, Bonilla *et al.* report much higher values than were found in the present investigation. Diffusion coefficients over a wide range of compositions have been reported for the following binary liquid metal systems; Hg-Tl (12), Bi-Sn (13), In-Sn (14, 15, 16), Bi-Pb (13, 17, 18), Zn-Hg (19), Pb-Sn (13), and Na-Pb (20). With the exception of one investigation, Pb-Bi (13), in no case did the diffusion coefficients vary by more than a factor of 2.2 over the composition range. In this exception the variation was more than an order of magnitude. However, the investigators noted that large concentration gradients inherent in the experimental method probably gave rise to convection currents. Large variations in the value of the diffusion coefficient with composition are common in solids where marked structure changes can occur. In liquids where the atoms are less rigidly bound the variations are not expected to be as pronounced. Variations of an order of magnitude are not expected. Several investigators (21-24) have observed convection effects with liquid metals in diffusion paths of greater than 2-mm diam-

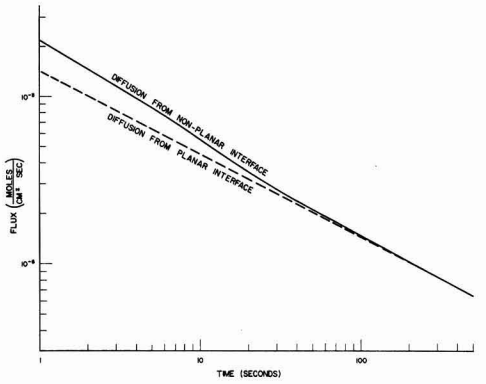

Fig. 3. Flux for coupled diffusion problem

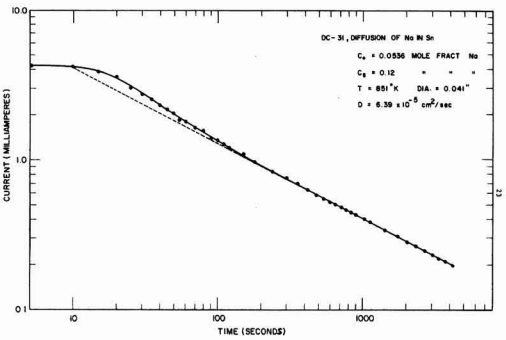

Fig. 4. Typical discharge curve

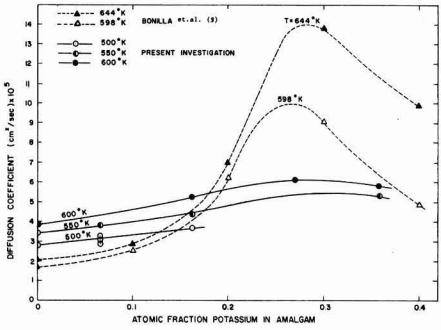

Fig. 5. Diffusion coefficients for potassium in potassium amalgams.

Table II. Activation energy and pre-exponential, D_o

System	N	D_o, cm²/sec	E, cal/g atom
K-Hg	0.165	3.7×10^{-4}	2100
Na-Pb	0.120	2.0×10^{-4}	2500
Na-Sn	0.160	1.9×10^{-4}	1900

eter. Convection may result from the presence of vibrations or from negative temperature gradients (top end cooler) as small as 0.1°C/cm (25). The data of Bonilla *et al.* were obtained in paths of ½ and ¼-in. diameter which greatly increases the possibility of convection. They maintained a small positive temperature gradient to reduce the possibility of convection as was done in the present investigation. However, the potassium-mercury system is strongly exothermic and liberation of heat occurs during diffusion of the components. This heat liberation is most likely to be pronounced where compounds exist in the solid state, such as Hg_2K, and may persist into the liquid state. Analogous thermal generation conditions exist in the electromobility experiments where internal heat liberation results from ohmic heating by the high current densities. Several investigators have noted the existence of convection in liquid metals under these conditions (26-29). On the basis of these considerations, the explanation for the inordinately high coefficients reported by Bonilla *et al.* in the range $0.25 < N_K < 0.35$ may be convection resulting from a combination of a large diameter diffusion path and exothermic heat liberation causing local temperature disturbances. The discrepancy between the coefficient of diffusion at infinite dilution reported in the two investigations is explained by the choice of different sources for the viscosity data used in the calculation.

The coefficients obtained for diffusion of sodium in sodium-lead are shown in Fig. 6. The values at infinite dilution were calculated from the Stokes-Einstein equation using viscosity data from (30) and the Pauling ionic radius of sodium (11). Results are compared with values reported by Morachevsky (20) who used the capillary reservoir technique and sectioned the path after diffusion for chemical analysis. His concentration gradients were as large as 40 a/o (atom per cent) sodium. The sodium-lead system exhibits large negative deviations from Raoult's law. The minimum in Morachevsky's data is not consistent with this as explained earlier. Rather, a maximum as was obtained in the present investigation is expected.

The coefficients obtained for the diffusion of sodium in sodium-tin are shown in Fig. 7. No other investigators have reported diffusion coefficients for this system.

The data for each of the three systems can be represented by the Arrhenius equation

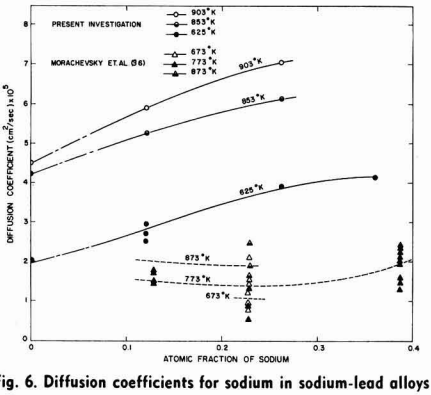

Fig. 6. Diffusion coefficients for sodium in sodium-lead alloys

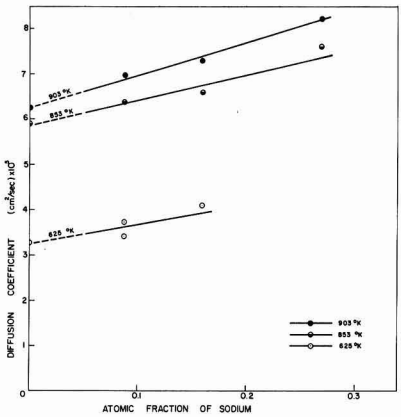

Fig. 7. Diffusion coefficents for sodium in sodium-tin alloys

$$D = D_o e^{-E/RT} \qquad [4]$$

The activation energy, E, and the pre-exponential, D_o, are given in Table II for each of the systems at the indicated mole fraction of alkali metal, N.

Summary

A method has been developed of measuring diffusion coefficients in binary liquid metals. This method, unlike others available, allows observation of the rate at which diffusate enters the diffusion path and detection of anomalous effects which may occur particularly in the early stages of the experiment. The electrical measurements of current and potential are substituted for the traditional chemical or radiochemical analyses. Since very small quantities of diffusate enter the diffusion path during an experiment, typically 10^{-4}g, the advantage of measuring electrical quantities over chemical analysis for this small a composition change is apparent. The method has been tested on three liquid metal systems, potassium-mercury, sodium-lead, and sodium-tin. It was found to give results consistent with available thermodynamic data and theoretical models. The concentration cells were discharged at constant potential in this investigation. They could, however, be discharged at constant current providing the appropriate solution of Fick's law is used in analysis of the data.

Acknowledgments

The authors are grateful to the United States Atomic Energy Commission who supplied the support for this project under contract AT (11-1)-1352.

Manuscript received Sept. 14, 1967; revised manuscript received Dec. 8, 1967.

Any discussion of this paper will appear in a Discussion Section to be published in the December 1968 JOURNAL.

REFERENCES

1. J. B. Edwards Ph.D. Thesis, The University of Michigan, Ann Arbor, December 1961.
2. R. Hultgren, R. L. Orr, P. D. Anderson, and K. K. Kelly, "Selected Values of Thermodynamic Properties of Metals and Alloys," John Wiley, & Sons, Inc., New York (1963).
3. C. F. Bonilla, Do-ik Lee, and P. J. Foley, Advances in Thermophysical Properties at Extreme Pressures and Temperatures, 3rd Symposium, March 22-25, 1965, pp. 207-15.
4. J. Degenkolbe and F. Sauerwald, *Z. anorg. und allgem. Chem.*, **270**, 317 (1952).
5. "Handbook of Chemistry and Physics," 40th ed., C. D. Hodgeman, Editor, Chemical Rubber Publishing Co., Cleveland (1958).
6. M. L. Dzurus and G. R. Henning, "Carbon—Proceedings of the Fifth Conference," **1**, 139, Pergamon Press (1962).

7. J. Crank "Mathematics of Diffusion," Oxford University Press, Fair Lawn, N.J. (1956).
8. L. T. Gul'din and A. V. Buzhinskaya, Surface Phenomena in Metallurgical Processes, Proceedings of an Inter-institute Conference, Edited by A. I. Belgaev, Consultants Bureau, New York, 1965, pp. 177.
9. B. Carnahan, H. A. Luther, and J. O. Wilkes, "Applied Numerical Methods," Preliminary Edition, Vol. II, Chap. 7, John Wiley & Sons, Inc., New York (1964).
10. A. V. Grosse, *J. Phys. Chem.*, **68**, 3419 (1964).
11. L. Pauling, *J. Am. Chem. Soc.*, **49**, 765 (1927).
12. W. T. Foley and L. E. Reid, *Can. J. Chem.*, **41**, 1782 (1963).
13. K. Niwa, M. Shimoji, S. Kado, Y. Watanabe, and T. Yokokawa, *J. Metals*, **9**, 96 (1957).
14. G. Careri, A. Paoletti, and M. Vincentini, *IL Nuovo Cimento*, **X**, 1088 (1958).
15. A. Paoletti and M. Vincentini, *J. Appl. Phys.*, **32** 22 (1961).
16. M. Vincentini and A. Paoletti, *IL Nuovo Cimento*, **XIV**, 1373 (1959).
17. R. E. Grace and G. Derge, *J. Metals*, **6**, 839 (1955).
18. S. J. Rothman and L. D. Hall, *ibid.*, **8**, 1580 (1956).
19. H. W. Schadler and R. E. Grace, *Trans AIME*, **215**, 559 (1959).
20. A. C. Morachevsky, E. A. Cherespanova, and A. F. Alabysher, *Isvestiia. VUZ-Tsvetnaya Metallurgiya*, **70**, (1960).
21. D. W. Morgan and J. A. Kitchner, *Trans. Faraday Soc.* **51**, 51 (1954).
22. S. J. Rothman and L. D. Hall, *J. Metals*, **8**, 199 (1956).
23. J. W. Gorman and G. W. Preckshot, *Trans. Met. Soc. AIME*, **212**, 367 (1958).
24. G. W. Preckshot and R. E. Hudrlik, *ibid.*, **212**, 516 (1960).
25. G. Careri, A. Paoletti and F. L. Salvetti, *IL Nuovo Cimento*, **X**, 399 (1954).
26. J. C. Angus, Ph.D. Thesis, The University of Michigan, 112, (1960).
27. A. R. E. Lodding, "Isotope Transport Phenomena in Liquid Metals, Gothenburg Studies in Physics," Nils Ryde, Editor. Acta Universitatis Gothoburgensis (1961).
28. J. Rohlin and A. Lodding, *Z. Naturforsch.*, **17a**, 1081 (1962).
29. J. D. Verhoeven, *Metals*, **1**, 26 (1966).
30. E. Rothwell, *J. Inst. Metals*, **90**, 389 (1961-62).

The Mechanism of Oscillatory Behavior During the Anodic Oxidation of Formaldehyde

Herbert F. Hunger*

U. S. Army Electronics Command, Fort Monmouth, New Jersey

ABSTRACT

Galvanostatic studies of formaldehyde half-elements in sulfuric acid at room temperature were made. In addition to kinetic measurements with constant bulk concentration of formaldehyde, adsorption and desorption experiments were performed. The oscillatory behavior is described in terms of current-potential characteristics and potential transients. Two reaction sequences are postulated to explain the oscillations. In path I a catalytic decomposition step and in path II a diffusion-readsorption step are suggested as the coupling steps which are required to continue the oscillations. At potentials of or above +0.8v *vs.* SHE, the participation of the oxidized platinum surface in the oxidation of formaldehyde becomes noticeable. From adsorption and desorption experiments it can be concluded that readsorption from a liquid film on top of the ad-layer is essential for the occurrence of the first oscillation. This excludes the coupling mechanism of path I.

In previous papers we have reported on oscillation phenomena occurring during the anodic oxidation of formaldehyde in sulfuric acid at platinum electrodes and room temperature (1, 2). The objective of this paper is to report on further work concerning the reaction mechanism.

Experimental

The half element investigated can be presented by the scheme

$$Pt|1M\ CH_2O,\ 3.75M\ H_2SO_4 \qquad [1]$$

and the cell used to study the oscillation phenomena by

$$(-)\ Pt|1M\ CH_2O,\ 3.75M\ H_2SO_4/1M\ CH_2O,\ 3.75M\ H_2SO_4|Pt\ (+) \qquad [2]$$

It contained either a smooth or platinized platinum electrode in an anolyte consisting of 1M formaldehyde in 3.75M sulfuric acid. The anolyte was separated by a cation exchange membrane (Nepton CR-61 from Ionics Incorporated) or a sintered glass disk from a catholyte of the same composition. A smooth platinum cathode was placed into the catholyte. Both smooth and platinized platinum electrodes were made from platinum-foil (0.076 cm thickness with a geometrical cross section area of 1 cm^2, except otherwise noted). A hydrogen reference electrode of the type described by Giner was arranged in a separate electrolyte compartment (3.75M H_2SO_4) and connected with a properly arranged Luggin capillary to the anode (3). The Giner hydrogen electrode was 26 mv negative to SHE. One type of experimental cell was constructed from Lucite except the gasketing material (Teflon or rubber) (4). The adsorption and desorption experiments were performed in glass-H-cells (E. H. Sargent & Company) with standard glass joints and controlled atmosphere (CO_2 or argon). The electrodes were platinized in a controlled manner (5). Nominal amounts up to 30 mg platinum black per square centimeter of geometrical area were electrolytically deposited. These nominal amounts correspond to the electrical charge passed during platinization. Corrections for the Faradaic efficiency showed that 10 mg platinum/cm^2 nominal correspond to 3.05 mg/cm^2 and 30 mg/cm^2 nominal to 7.5 mg/cm^2. The experiments were conducted at controlled temperature conditions (21° and 25°C). The chemicals used to prepare the electrodes and the electrolytes were of highest purity grade commercially available.

* Electrochemical Society Active Member.

A precision current source (Model CS-12, North Hills, Electronics, Inc.) was used to control the current (1 μa-999 ma) between the working anode and the counter electrode. A potentiometric recorder (Model FW 5A-3332 from Texas Instruments, Inc.) was used for measuring the stationary anode potentials and the potential transients *vs.* the reference electrode.

In addition to the kinetic measurements with constant bulk concentration of formaldehyde, adsorption experiments, similar to those performed by Pavela and Breiter for methanol were made (6, 7). Adsorption of formaldehyde at platinized platinum took place from the electrolyte (1M CH_2O in 3.75M H_2SO_4) under open circuit conditions. Adsorption times were in the range of 1 to 900 sec. After adsorption the electrodes were dipped shortly in 3.75M H_2SO_4 in order to remove the adherent liquid and transferred immediately into the anode chamber of the cell which contained in this case only 3.75M sulfuric acid as the electrolyte. A preset circuit permitted to oxidize the adsorbed organic species immediately at constant current just above the threshold current for the oscillations (50 ma). The voltage maxima of the pulsations under these conditions were about 0.78v *vs.* SHE. Thus, as shown later, strong participation of an oxidized surface state in the mechanism was avoided.

The dipping procedure described above did not completely eliminate the adherent liquid film as desorption experiments showed; however, this technique proved to be useful to obtain a defined amount of organic species at the electrode.

Desorption experiments in order to determine the amount of adherent liquid film in addition to the ad-layer after rinsing were also made. For this purpose the adsorption time was held at 300 sec, a time which was required to obtain constant amounts (saturation coverage plus liquid film) of organic species at the electrodes. After adsorption the electrode was dipped for time periods of 1-10,980 sec in H_2SO_4 to obtain removal of the adherent film and desorption of the ad-layer. The remaining organic amount was stripped off as described before. It was noticed from a plot of log μC/cm^2 of anodically oxidized organic species *vs.* time that up to 15 sec of desorption a significant amount of liquid film was still present. A rapid decrease in the amount of organic species was observed up to 300 sec. After that the curve followed the desorption relationship

$$\log(\mu C/cm^2)_t = \log(\mu C/cm^2)_{t=0} - k_D t \qquad [3]$$

Extrapolation of the straight line to $t=0$, permitted to measure the $(\mu C/cm^2)_{t=0} = 182$ μC/cm^2. We shall refer to this value in the following as the ad-layer in contrast to the amount of organic species at the electrode which can consist of the ad-layer plus a liquid film. Rinsing for one second reduced the original liquid film ($t=0$, no rinsing) from about 1443 μC/cm^2 to 976-1020 μC/cm^2 corresponding to about 5.5 ad-layers.

Before each adsorption or desorption experiment, the electrochemical surface area of the electrode was estimated. The following procedure was used. The electrode was submitted to cathodic charging at 50 ma for 1 min, followed immediately by an anodic current of 50 ma. The voltage trace was recorded. The transients permitted to determine the electrical charges corresponding to the anodic oxidation of hydrogen (0-0.3v *vs.* SHE) and that of the anodic oxidation of the platinum surface, noticeable at about +0.8v and ending at about +1.6v with the evolution of oxygen. All these events are clearly marked by a change in the slopes of the transient. The length of the latter region corresponds to the build up of a monolayer of oxygen. Using the value of 420 μC/cm^2 corresponding to one oxygen monolayer, the absolute electrochemical surface area could be estimated. This theoretical value of 420 μC/cm^2 was found to be in excellent agreement with our experimental data. When cathodic hydrogen transients were compared with anodic oxygen transients, it was found that an oxygen coverage corresponding to one monolayer was reached at about 1.6v *vs.* SHE. In this comparison a hydrogen monolayer corresponded to 210 μC/cm^2 of real platinum surface (8).

It was further checked to what degree the charge in the oxygen transient depended on the current density used. The current was varied between 5 and 500 ma, corresponding to a current density range of 2-200 μa/cm^2 (the average real surface area of the electrode being $2.5 \cdot 10^3$ cm^2). Between 5 and 200 ma the mean error was 2.87%. Negative deviations up to —23.3% were observed at 500 ma. The current of 50 ma normally used in the surface area determination corresponds to 13.8 — 50 μa/cm^2 for the range of surface areas observed for platinum black in our experimentation (10^3 — $3.2 \cdot 10^3$ cm^2) per electrode.

Results and Discussion

Kinetic measurements with constant bulk concentration of formaldehyde.—The current-potential curves, both for smooth and platinized platinum are shown in Fig. 1 and 2. The open circuit potentials of the formaldehyde anodes are varying from +0.07 to +0.49v, specifically for smooth platinum, and from +0.175 to +0.33v for platinized platinum. Analogy

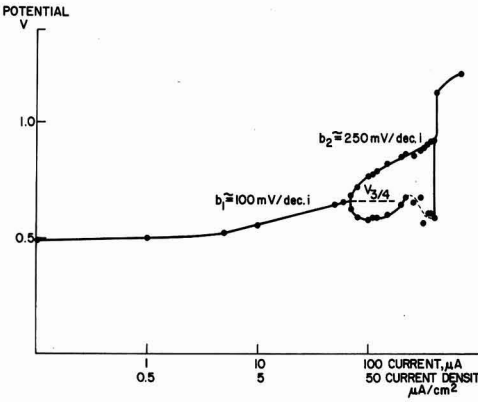

Fig. 1. Galvanostatic current-potential curve for smooth platinum electrode (1 cm^2 cross section) in 1M CH_2O, 3.75M H_2SO_4 at 21°C. Potential measured *vs.* hydrogen reference electrode (—0.026v).

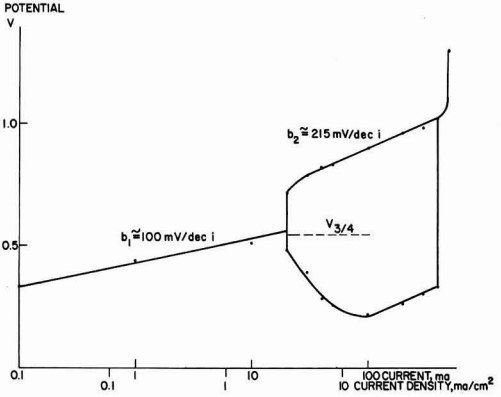

Fig. 2. Galvanostatic current-potential curve for platinized platinum electrode (3 cm^2 cross section) in 1M CH_2O, 3.75M H_2SO_4 at 21°C. Potential measured *vs.* hydrogen reference electrode (—0.026v).

with formic acid supports the hypothesis that these potentials are mixed potentials caused perhaps by the simultaneous low-potential anodic oxidation of the organic specie with cathodic deposition of hydrogen (9, 10).

The current-potential curves, both for smooth and platinized platinum, showed a stationary region up to a threshold current of 70 μa and 20 ma, respectively. The slope b, in the stationary region is 100 $\pm$ 5 mv per decade of current for all three types of electrodes, corresponding approximately to a 2.3 ($2RT/F$) value. Since the slopes for smooth platinum and platinized platinum are identical, no effects of electrode porosity on the value of the slope were observed (11). Thus the platinized platinum electrodes can be considered essentially as nonporous. The estimated exchange current density values, obtained by extrapolation of the stationary Tafel slopes to the reversible potential for formaldehyde oxidation were 10^{-11} a/cm^2 for smooth platinum and 7.5 10^{-9} a/cm^2 as an average value for platinized platinum. Similar data are reported for the anodic oxidation of formic acid at platinum electrodes. (9, 12).

Oscillatory behavior expressed in periodic voltage transients was observed at higher current densities. For platinized platinum these potential transients range from +0.22 to +1.02v *vs.* the hydrogen reference electrode. An upper and a lower curve limit the oscillation region. These two curves represent stable states according to the theory of stability of electrode states (13).

The slope of the upper curve, b_2, is about 215 mv per decade of current for platinized platinum and approximately 250 mv for smooth platinum. Such slopes obtained under nonsteady-state conditions, however, can not be used as a diagnostic tool for the reaction mechanism.

The lower boundaries of the oscillation planes approach at first more negative potentials when the current is increased. Above 100 ma the potentials become again more positive in the case of platinized platinum. The new slope corresponds approximately to that of the upper boundary. In the case of smooth platinum, a similar behavior is observed up to 220 μa. Then the lower boundary becomes ill-defined.

A second transition region is observed at higher currents, at about 400 μa for smooth platinum and between 400 and 500 ma for platinized platinum, indicating electrode surface oxidation and leading finally to oxygen evolution.

It was noticed that the intersection between the stationary part of the V — log i curve and the threshold current gave another interesting characteristic which we termed $V_{3/4}$ potential.

In analyzing the potential transients in the oscillation region (Fig. 3 and 4), the following approach was used. Besides measuring the coulombs per oscillation cycle, the coulombs corresponding to $\frac{3}{4}\tau$ (τ = time for one cycle) were determined for various currents and the corresponding potential values were registered. They were found to be identical with the $V_{3/4}$ potentials. The $V_{3/4}$ potential levels shown in Fig. 1 and 2 divide the initial oscillation planes in two parts. The upper part corresponding to $\frac{3}{4}\tau$ and the lower one to $\frac{1}{4}\tau$, a $3e^-/1e^-$ ratio.

For smooth platinum the results are recorded in Table I. In the last column, the process frequency is noted. The $V_{3/4}$ level, average value calculated from Table I: $\overline{V_{3/4}} = +0.654$.

Results for platinized platinum are given in Table II. The voltage transients are larger than in the case of smooth platinum and $\overline{V_{3/4}} = +0.542$v.

Figure 5 relates the upper oxidation potential (last figure in column 3, Table I and II) to the millicoulombs per cycle. A strong increase in the amount of species oxidized occurs above +0.8v in the case of smooth platinum and above +0.9v in the case of platinized platinum. This increase in millicoulombs per cycle is related to the onset of increasing oxygen coverage and participation of the oxidized electrode surface in the oxidation of organic species. Breiter and Becker report that anodic oxidation of platinum in acid electrolytes becomes noticeable at +0.7 and the surface coverage becomes a monolayer at about +1.5v (14).

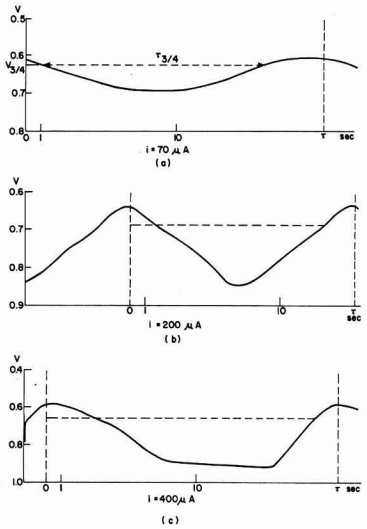

Fig. 3. Potential transients. Smooth platinum electrode potential V measured *vs.* hydrogen reference electrode (—0.026v), recorder speed 24 in./min: (a) i = 70μa, (b) i = 200 μa, and (c) i = 400 μa.

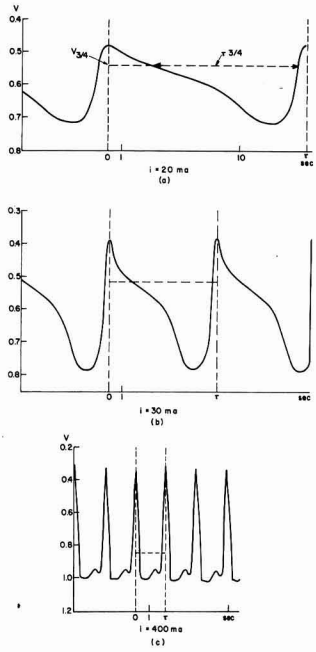

Fig. 4. Potential transients. Platinized platinum electrode potential measured *vs.* hydrogen reference electrode (—0.026v), recorder speed 24 in./min: (a) i = 20 ma, (b) i = 30 ma, and (c) i = 400 ma.

Table I. Coulombic analysis of galvanostatic potential transients

1M CH_2O, 3.5M H_2SO_4; smooth platinum; 1 cm^2 cross section; 21°C

i, μA	m Cbs/cycle	V	$V_{3/4}$	ν, Hz
0		0.49		
1		0.5		
5		0.522		
10		0.55		
50		0.642		
60		0.651		
70	1.4	0.62-0.68	0.65	0.05
80	1.59	0.585-0.715	0.61	0.051
100	1.8	0.575-0.76		0.056
110	1.96	0.585-0.77	0.62	0.056
120	2.13	0.585-0.785	0.615	0.056
150	2.47	0.595-0.815	0.63	0.061
200	3.0	0.64-0.845	0.685	0.067
220	3.27	0.67-0.855	0.703	0.067
260	3.6	0.65-0.85	0.692	0.072
300	4.12	0.67-0.87	0.71	0.073
320	4.71	0.56-0.885	0.64	0.068
350	6.82	0.6-0.9	0.67	0.051
370	7.05	0.6-0.91	0.67	0.053
400	7.76	0.58-0.915	0.66	0.052
420		1.12		
500		1.16		
700		1.2		

Table II. Coulombic analysis of galvanostatic potential transients

1M CH_2O, 3.5M H_2SO_4, platinized platinum; 10 mg platinum/cm^2, 3 cm^2 cross section; 21°C

i, ma	m Cbs/cycle	V	$V_{3/4}$	ν, Hz
0		0.212		
10^{-3}		0.221		
10^{-2}		0.235		
10^{-1}		0.331		
1		0.44		
10		0.51		
20	303	0.48-0.715	0.54	0.049
30	246	0.39-0.79	0.52	0.091
40	407	0.28-0.82	0.53	0.099
50	257	0.255-0.83	0.545	0.194
100	383	0.22-0.9	0.576	0.262
200	813	0.26-0.96	0.66	0.246
300	1028	0.3-0.98	0.82	0.292
400	1082	0.33-1.02	0.84	0.37
500		1.3		

With the increase in millicoulombs per cycle a change in the shape of the voltage transients is observed (Fig. 3 and 4): For smooth platinum at 70 μa, a symmetrical transient and at 400 μa, a flat, extended potential maximum. For platinized platinum a relatively slow attainment of a potential maximum is observed at low current densities and the return to less positive potentials is rapid (Fig. 4a, b). At higher current densities this return is delayed by an additional small pulsation next to the potential maximum (Fig. 4c).

Certain conclusions with respect to the mechanism of the oscillations can be made from the kinetic behavior: The oscillatory behavior of formaldehyde at platinum electrodes is a special case of a general phenomenon, the periodic electrode process. At least two electrode processes have to occur simultaneously to result in a periodic process (15). Periodic behavior can also be observed by coupling more than two parallel reactions. Coupling means that the reaction rates depend mutually on the condition of the parallel reactions, following a periodic function of time. The rate determining step of the periodic process has therefore also to be time dependent.

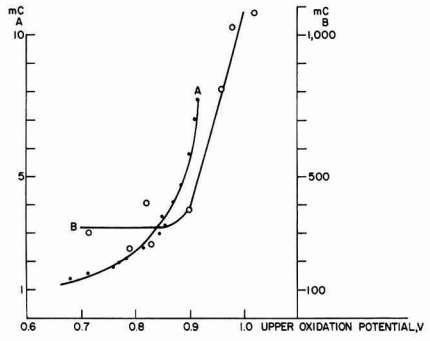

Fig. 5. mCb/cycle *vs.* upper oxidation potential: (a) smooth Pt, (b) platinized Pt.

The complete anodic oxidation of formaldehyde is a $4e^-$ process

$$CH_2(OH)_2 \rightarrow CO_2 + 4H^+ + 4e^- \qquad [4]$$

The occurrences within the low current region of the oscillation plane can be formulated by two postulated reaction sequences:

The postulated reaction path I considers a chemical step as the coupling step, path II a diffusion-adsorption step. The coupling step is required to continue the periodic electrode process and is the reason for the reverse of the potential during oscillations.

Path I is an extension to the mechanisms proposed by Mueller and Conway for the anodic oxidation of formic acid (12, 16-18)

Path I

$CH_2(OH)_2$ ads	$\rightarrow A + H^+ + e^-$	(a)
A	$\rightarrow B + H^+ + e^-$	(b)
B	$\rightarrow HCOO + H^+ + e^-$	(c)
B^-	$\rightarrow HCOO + e^-$	(c^1)
HCOO	$\rightarrow CO_2 + H$	(d)
H	$\rightarrow H^+ + e^-$	(e)
$CH_2(OH)_2$ sol	$\rightarrow CH_2(OH)_2$ ads	(f)

The anodic oxidation of formaldehyde occurs through the electron transfer steps (a), (b), (c), or (c^1) and results in formation of adsorbed formate radicals, sometimes identified with the so-called "blocking intermediate." Build up of the blocking intermediate occurs up to a critical surface concentration (17). After this is reached, rapid catalytical decomposition of this specie to carbon dioxide and hydrogen occurs. This leads to a rapid change in surface coverage from partially oxygenated organic species to hydrogen in step (d), the coupling step. The anodic oxidation of hydrogen occurs at a less positive potential. Anodic oxidation of hydrogen has been observed in that potential region during periodic phenomena (19). Partially oxygenated hydrocarbons as methanol and formic acid adsorb at platinum from acid solutions in the potential region of +0.1 to +0.6v *vs.* SHE (7, 20). The surface coverage is high at the less positive potentials, but decreases with increasing positive potential. Thus readsorption of organic species (f) can occur in this potential region simultaneously with step (e) and the oscillations are continued.

Path II postulates the stepwise anodic oxidation of formaldehyde with participation of the anodically oxidized platinum surface at the more positive potentials.

Path II

$CH_2(OH)_2$ ads	$\rightarrow A + H^+ + e^-$	(a)
A	$\rightarrow B + H^+ + e^-$	(b)
B	$\rightarrow C + H^+ + e^-$	(c)
C	$\rightarrow CO_2 + H^+ + e^-$	(g)
$CH_2(OH)_2$ sol	$\rightarrow CH_2(OH)_2$ ads	(f)

Steps (a), (b), (c), and (g) are charge transfer steps. Step (f) is a diffusion-adsorption step. Coupling occurs here as a consequence of step (g) through step (f).

From experiments in which the anode was driven by an external emf, the behavior during simultaneous current and voltage oscillations was studied (1, 2). It was observed that the anodic current decreases with increasing anodic polarization during one oscillation cycle. This indicates inhibition of the oxidation of

the organic species by a small, but increasing coverage of the electrode with oxygen species. Since adsorption of organic species is known to occur at the less positive potentials, adsorption will decrease with increasing positive potential during a cycle and finally become zero. Then only the previously adsorbed amount of organic species becomes completely oxidized in step (g) and depletion of the surface of organic species leads finally to readsorption at less positive potentials through step (f). The original maximum current is observed and a new cycle starts. These occurrences are also reflected in the potential transients (Fig. 3) and marked in Fig. 4.

Above +0.8v noticeable surface oxidation was observed probably by discharge of water. Such reactions shift the three to one electron ratio observed previously to a higher value. An analysis of the potential transients above +0.9v showed ratios up to $13e^-/1e^-$ for the original $V_{3/4}$ level. These occurrences explain the change in the shape of the potential transients with increasing positive potential (Fig. 3c, Fig. 4c). Correspondingly the apparent increase of the $V_{3/4}$ potential above an upper oxidation potential of 0.9v (Table II) is due to these reactions.

Adsorption and desorption experiments, discussed in the following, permitted to distinguish between the coupling steps of the mechanisms.

Adsorption and desorption experiments.—Two general types of potential transients were noted after adsorption of formaldehyde. In case of short adsorption times (1 to 5 sec in case of electrode A), no oscillations were observed, but after longer periods one to four pulses, depending on the length of the adsorption time, were obtained (Fig. 6a, b). In the first case (a), the potential rose fast from open circuit potential to about +0.7v, followed by a plateau region and above +0.8v by platinum surface oxidation. The latter was marked by a change in the slope of the transient. Above +1.62v visible oxygen evolution occurred. In the second case (b), potential oscillations between +0.47 and +0.78v replaced the plateau region. The average potential for start of visible carbon dioxide evolution was +0.757v for the given current density. At about +1.05v, this gas evolution ceased. In the case of electrode B, which had a larger surface area than A, up to ten pulses were observed. The frequency of the oscillations decreased somewhat with the order of the pulses.

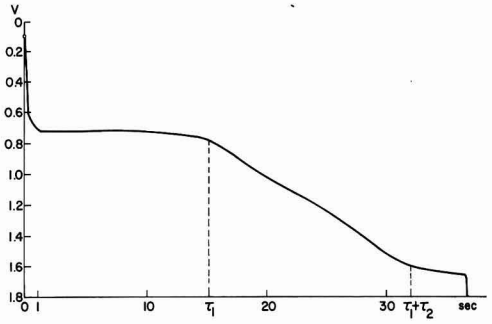

Fig. 6a. Potential transient. Platinized platinum electrode adsorption time: 5 sec, i = 50 ma. Potential measured vs. hydrogen reference electrode (—0.026v), recorder speed 24 in./min.

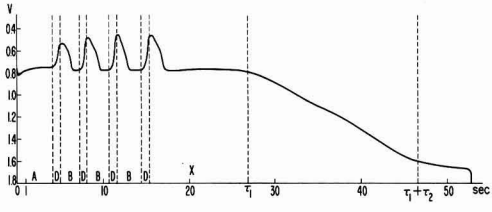

Fig. 6b. Potential transient. Platinized platinum electrode adsorption time: 420 sec, i = 50 ma. Potential measured vs. hydrogen reference electrode (—0.026v), recorder speed 24 in./min.

The millicoulombs of organic species oxidized between open circuit potential and onset of surface oxidation (time τ_1) are a function of the adsorption time.

The amounts of organic species oxidized during various phases of the oscillations were estimated by dividing the potential transients in certain segments (Fig. 6b). Segment A was termed the preoscillation period, D the (potential) decrease period, B the (potential) build up period, and X the after oscillation period. B plus D form one oscillation cycle. A and B were found to be identical. Coulometric analysis of the segments was done in two ways. For electrode A only the averaged values of D, B, and X over all oscillations were computed. For electrode B this was done also, but in addition a range of values for D, B, and X considering the frequency dampening effect observed for the pulses with higher order was calculated. The results are given in Table III.

Desorption experiments with electrode C were also evaluated coulometrically as in the case of electrode B. The results are compared with those of the adsorption experiments in Table III. In detail the pulse analysis of the desorption experiments gave the results shown in Table IV.

Analysis of the data yielded the following conclusions concerning the mechanism of the oscillations.

The after oscillation period ranges from 174 to about 400 $\mu C/cm^2$. The first oscillation occurred when a total organic amount of about 400 $\mu C/cm^2$ had adsorbed or was still adsorbed at the electrode. Thus the critical amount required at the electrode to make one oscillation lies around 400 $\mu C/cm^2$. Any amount in surplus of the critical one led to additional oscillations and/or an after oscillation period in accordance with Table III.

Relating these data to specific coverage estimates leads to the following. Assuming complete oxidation of formaldehyde to carbon dioxide (4), one coulomb corresponds to $7.78 \cdot 10^{-5}$g CH_2O. One CH_2O molecule weighs 5.10^{-23}g. The area requirement for one formaldehyde molecule adsorbed on the platinum surface,

Table III. Coulometric analysis of the segments of the voltage transients

Surface area, cm^2	Electrode A $1.94 \cdot 10^3$	Electrode B $3.05 \cdot 10^3$	Electrode C $2.46 \cdot 10^3$
Oscillation period $\mu C/cm^2$	76	84*	94*
Decrease period $\mu C/cm^2$	20	27.9	—
Build up period $\mu C/cm^2$	56	56.1	—
After oscillation period $\mu C/cm^2$	200	278-400	174-346

* Considering the frequency dampening effect, the value observed for the first oscillation was at 46 $\mu C/cm^2$ for B and 59 $\mu C/cm^2$ for C, respectively.

Table IV. Coulometric analysis of desorption experiments

Desorption time, sec	Number of pulses	Total pulse-charge (τ_1-x), $\mu C/cm^2$	After oscillation period (X), $\mu C/cm^2$	Average $\mu C/cm^2$/ pulse
0	14	1451	174	104
0	10	934	346	93
1	8	645	322	81
3	4	337	313	85
7	3	353	244	118
15	1	84	322	84
30	0		258	

attached to two surface atoms, is about 15Å². On one square centimeter of absolute surface area we can accommodate $6.66 \cdot 10^{+14}$ molecules of formaldehyde. This corresponds to $3.33 \cdot 10^{-8}$g CH_2O or $4.28 \cdot 10^{-4}$ Cb. Thus the electrical charge connected with the anodic oxidation of formaldehyde if a 2 site adsorption would occur is 428 $\mu C/cm^2$. If one site attachment occurred, the formaldehyde monolayer would give 856 $\mu C/cm^2$.

According to these data, the value of the ad-layer (182 $\mu C/cm^2$) indicates that the platinum surface is only partially covered with the adsorbed organic species (to about 21%). During one pulse about one half of the ad-layer is oxidized. The critical amount about doubles the value of the ad-layer.

This means that readsorption from a liquid film on top of the ad-layer is essential for the occurrence of the first oscillation. This excludes the coupling mechanism of path I where the first oscillation would occur by self-decomposition of the "blocking" intermediate formed by partial oxidation of the ad-layer. The coupling mechanism suggested in path II is therefore probable.

Acknowledgment

The author gratefully acknowledges the continued interest and support of Dr. E. A. Gerber, Director, Electronic Components Laboratory, U.S. Army Electronics Command, Fort Monmouth, New Jersey. The author wishes also to thank Miss R. Rinaldi for her technical assistance.

Manuscript received March 1, 1967; revised manuscript received Nov. 4, 1967. This paper was presented at the Dallas Meeting, May 7-12, 1967, as Abstract No. 110.

Any discussion of this paper will appear in a Discussion Section to be published in the December 1968 JOURNAL.

REFERENCES

1. H. F. Hunger, J. E. Wynn, and N. J. Sanfilippo, *Proc.* 19th Ann. Power Sources Conf., Atlantic City (1965).
2. H. F. Hunger, *Proc.* Journees Int. D'Etude des Piles Combustible, Bruxelles (1965).
3. J. J. Giner, *This Journal*, **111**, 3, 376 (1964).
4. H. F. Hunger, J. E. Wynn, and N. J. Sanfilippo, Technical Report ECOM-2670, March 1966.
5. H. F. Hunger, J. E. Wynn, and N. J. Sanfilippo, Technical Report ECOM-2520, Oct. 1964.
6. T. O. Pavela, *Ann. Acad. Sci. Fennicae*, Series A, II Chemica 59 (1954).
7. W. M. Breiter and S. Gilman, *This Journal*, **109**, 622 (1962).
8. F. G. Will and C. A. Knorr, *Z. Elektrochem.*, **64**, 258 (1960).
9. M. H. Gottlieb, *This Journal*, **111**, 465 (1964).
10. M. W. Breiter, *ibid.*, **111**, 1298 (1964).
11. L. G. Austin, "Fuel Cells" V II, p. 100, C. J. Young, Editor (1963).
12. B. E. Conway and M. Dzienciuch, *Can. J. Chem.*, **41**, 21, 38, 55 (1963).
13. U. F. Franck, *Z. f. Phys. Chem., N.F.*, **3**, 183 (1955).
14. M. Breiter and M. Becker, *Z. Elektrochem.*, **60**, 1080 (1950).
15. K. F. Bonhoeffer, *ibid.*, **51**, 24 (1948).
16. E. Mueller, *ibid.*, **29**, 264 (1923).
17. E. Mueller and G. Hindemith, *ibid.*, **33**, 561 (1927).
18. E. Mueller and S. Tanaka, *ibid.*, **34**, 256 (1928).
19. J. A. V. Butler and G. Armstrong, Disc., Faraday Soc., **1**, 122 (1947).
20. S. B. Brummer and A. C. Makrides, *J. Phys. Chem.*, **68**, 1448 (1964).

Seebeck Coefficient of a $(ZrO_2)_{0.85}(CaO)_{0.15}$ Electrolyte Thermocell*

R. J. Ruka, J. E. Bauerle, and L. Dykstra

Westinghouse Research Laboratories, Pittsburgh, Pennsylvania

ABSTRACT

The Seebeck coefficients of thermocells of the type

$$x,Pt \underset{T_1}{||} (ZrO_2)_{0.85}(CaO)_{0.15} \underset{T_2}{||} Pt,x$$

were measured at temperatures near 1000°C. In these cells x represents any of several oxygen-inert gas or hydrogen-water-inert gas mixtures. It was found that the change in Seebeck coefficient corresponding to a change in the partial molar entropy of oxygen in the gas at the electrodes agreed closely with the values predicted from irreversible thermodynamic theory. Two principal assumptions were made in applying the theory to these cells: (*i*) that the transported entropy of the oxygen ions in the electrolyte was constant for the different gas mixtures used, and (*ii*) that gas-solid reactions were at equilibrium at each electrode. The temperature dependence of the Seebeck voltage was found to be small.

An electrochemical cell with identical electrodes develops an emf when the electrodes are at different temperatures. The thermal emf per degree temperature difference is termed the Seebeck coefficient. Holtan (1) and others (2, 3) have derived equations based on irreversible thermodynamics for the Seebeck coefficient in such thermocells.

Measurement of the Seebeck coefficient gives information on the simultaneous transfer of charge and heat in the oxide electrolyte, allowing us, *e.g.*, to calculate the Peltier-type heat transfer during isothermal operation of a related galvanic cell.

The purpose of this paper is a comparison of the experimentally with theoretically determined difference in Seebeck coefficient which results from a change in the partial molar entropy of oxygen in the gas phase at the electrodes of a thermocell with $(ZrO_2)_{0.85}(CaO)_{0.15}$ electrolyte and gas-platinum electrodes. The temperature dependence of the Seebeck voltage is also examined briefly. $(ZrO_2)_{0.85}(CaO)_{0.15}$ is

Key words: Seebeck coefficient; zirconia; thermocell.
* Supported by ARPA through the Office of Naval Research.

an attractive oxide for this study since necessary experimental information on transference numbers of ions and electrons in the oxide and on electrode reactions of corresponding galvanic cells is already available. Several studies of this electrolyte are of particular significance for the interpretation of the present paper. These include contributions by Wagner and coworkers (4) on cell emf, Rhodes and Carter (8) on cation diffusion, Kingery and co-workers (5) on oxygen ion diffusion, Weissbart and Ruka (6) on oxygen concentration cells, and Schmalzried (7) on electrolyte stability to oxidizing and reducing atmospheres. Essential information from these papers for consideration of our current experiments is that conduction in the oxide is due almost 100% to oxygen vacancy or ion migration (4, 8, 5) over the temperature range of interest to the present experiments, *i.e.*, 700°-1280°C, that electrode reactions with oxygen or hydrogen-water using this oxide as electrolyte of a galvanic cell with platinum electrodes can be made essentially reversible (6) and that the oxide is stable to oxidizing or reducing atmospheres at oxygen partial pressures between 1 atm and the order or 10^{-22} atm (7).

Reinhold and co-workers (9) and Holtan (1) have experimentally measured the thermal emf of several halogen-containing solid electrolytes. Holtan concludes from this data that transported entropy terms are either small or absent in these cells. On the other hand, Patrick and Lawson (10), and Christy and co-workers (11) present Seebeck coefficient data for pure and doped AgBr and AgCl thermocells with Ag electrodes which apparently contain sizable entropy of transport terms at some temperatures. Significant data on oxide thermocells for comparison has not been available.

Consider the following thermocell

$$x_{O_2},Pt \,||\, (ZrO_2)_{0.85}(CaO)_{0.15} \,||\, Pt,x_{O_2} \qquad [A]$$

where x_{O_2} is an oxygen containing atmosphere at the electrodes such as pure O_2, air, an H_2-H_2O mixture, etc., Pt represents the platinum electrodes and leads, and $(ZrO_2)_{0.85}(CaO)_{0.15}$ is the oxide electrolyte with conductivity resulting almost exclusively from diffusion of $O^=$ ions.

The measured value of the thermal emf $\Delta\phi$ in this thermocell is a function of three individual potentials as given by the relationship

$$\Delta\phi = \Delta\phi_{(O^=,E)} - \Delta\phi_{(e^-,Pt)} + \Delta\phi_c \qquad [B]$$

where $\Delta\phi_{(O^=,E)}$ is an emf across the electrolyte resulting from the thermally induced flow of $O^=$ ions, $\Delta\phi_{(e^-,Pt)}$ is an emf across the platinum metal electrodes and leads, due to thermally induced flow of electrons, and $\Delta\phi_c$ is the difference between contact potentials of the two electrolyte-electrode interfaces at the two temperatures.

Holtan (1), Lidiard and co-workers (2, 3) have derived general equations for thermal emf in thermocells, and we list below pertinent equations for the above thermocell as adapted from their considerations.[1] The equations are simplified by assuming that electronic conductivity is nil, that chemical diffusion gradients do not occur, and that $O^=$ is the only diffusing ionic species. The treatment assumes that the reference frame for diffusion is a plane in the lattice. This is also consistent with a choice of the positive ions as reference since these remain essentially immobile. For a small difference in electrode temperatures

$$\Delta\phi_{(O^=,E)} = \frac{\Delta T}{\mathbf{F}}\left[\frac{1}{2}\overset{\approx}{S}_{O^=} - \frac{1}{2}\bar{s}_{O^=}\right]$$

Thermal emf across electrolyte [1]

$$\Delta\phi_{(e^-,Pt)} = \frac{\Delta T}{\mathbf{F}}\left[\overset{\approx}{S}_{(e^-,Pt)} - \bar{s}_{(e^-,Pt)}\right]$$

Reverse thermal emf across platinum electrodes and leads [2]

$$\Delta\phi_c = \frac{\Delta T}{\mathbf{F}}\left[-\frac{1}{4}\bar{S}_{O_2} + \frac{1}{2}\bar{s}_{O^=} - \bar{s}_{(e^-,Pt)}\right]$$

Difference between contact potentials at the two electrodes [3]

By combining expressions [1], [2], and [3] into Eq. [B], we obtain

$$\frac{\Delta\phi}{\Delta T} = \frac{1}{\mathbf{F}}\left[\frac{1}{2}\overset{\approx}{S}_{O^=} - \overset{\approx}{S}_{(e^-,Pt)} - \frac{1}{4}\bar{S}_{O_2}\right]$$

Seebeck coefficient[2] of thermocell [4]

where ΔT is the temperature of the hot electrode minus that of the cold electrode, $\mathbf{F}$ is the Faraday, $\overset{\approx}{S}_{O^=}$ and $\overset{\approx}{S}_{(e^-,Pt)}$ are the transported entropies of $O^=$ ions and electrons, respectively, in the electrolyte, and platinum electrode (and leads), respectively, $\bar{s}_{O^=}$ and $\bar{s}_{(e^-,Pt)}$ are the partial molar entropies of oxygen ions and electrons, respectively, in the electrolyte and platinum electrode, respectively, and $\bar{S}_{O_2}$ is the partial molar entropy of O_2 in the gaseous atmosphere at the electrodes. With the restrictions listed, $\bar{S}_{O_2}$ represents the partial molar entropy of oxygen in a pure oxygen atmosphere or in a gas mixture such as H_2-H_2O-N_2. In the latter mixture the calculation of $\bar{S}_{O_2}$ involves the reacting species, namely O_2, H_2O, and H_2 of the gas mixture, but is independent of the "inert" component N_2. For the purpose of calculation, $\bar{S}_{O_2}$ is defined in a conventional way as the change in entropy of the oxygen-containing gas mixture at the electrode per mole of oxygen added, with the addition being made at constant temperature and pressure and in such small quantity that the composition of the gas mixture remains essentially the same.

While the absolute Seebeck coefficient cannot as yet be calculated, the Seebeck coefficient difference for two gas mixtures $(d\phi/dT)_{\text{gas 1}} - (d\phi/dT)_{\text{gas 2}}$ can in principle be calculated for a range of oxygen partial pressures over which the electrolyte and electrode material remain invariant. Under these conditions $\overset{\approx}{S}_{O^=}$ is constant, and applying Eq. [4] to two different gas atmospheres at the same temperature, we obtain by subtraction

$$\left(\frac{d\phi}{dT}\right)_{\text{gas 1}} - \left(\frac{d\phi}{dT}\right)_{\text{gas 2 (ref.)}} = \left(\frac{\bar{S}_{O_2}}{4\mathbf{F}}\right)_{\text{gas 2 (ref.)}} - \left(\frac{\bar{S}_{O_2}}{4\mathbf{F}}\right)_{\text{gas 1}} \qquad [5]$$

where in our present experiments gas 2 is a convenient reference gas, pure O_2 at atmospheric pressure, and where the electrode reaction is written to involve a reversible 4-electron step

$$O_2 + 4e^- \rightleftarrows 2\,O^=$$

Relation [5] contains no entropy of transport terms and $\bar{S}_{O_2}$ values can be calculated from data available in standard thermodynamic tabulations.

$\overset{\approx}{S}_{O^=}$, the transported entropy of the oxygen ion, cannot be directly calculated from present theory. However, the quantities measured in the current experiments enable us to obtain from Eq. [4] experimental values for $\overset{\approx}{S}_{O^=}$, since $\bar{S}_{O_2}$ is a known value and

[1] It is of interest to note that the derivations of Eq. [1-4] involve electrochemical potentials, and there is a term $e\phi'$ in each electrochemical potential for the usually accidentally occurring electrical state of the system. However, these terms all cancel in the final results and the partial molar entropies of the ions or electrons in Eq. [1-5] do not contain the extra term $e\phi'$ which would otherwise give an indeterminate character to the entropy terms.

[2] $\Delta\phi/\Delta T$, the Seebeck coefficient is considered positive if the hot terminal is positive.

$\tilde{\bar{S}}_{(e^-,Pt)}$ is known from experimental and theoretical considerations of others based on comparison with a lead superconductor which serves as a reference having a Seebeck coefficient of zero (13). $\tilde{\bar{S}}_{O^=}$ is composed of both kinetic and thermodynamic terms which are related to the heat of transport Q^* by

$$\tilde{\bar{S}}_{O^=} = + \frac{Q^*_{O^=}}{T} + \bar{s}_{O^=} \cong \frac{Q^*_{O^=}}{T} + s_{O^=}{}^{vib.} + \bar{s}_{O^=}{}^{config.} \quad [6]$$

where $\bar{s}_{O^=}$ is the partial molar entropy of the oxygen ion, $\bar{s}_{O^=}{}^{vib.}$ and $\bar{s}_{O^=}{}^{config.}$ are the partial molar entropies of vibration and configurational entropy respectively of the $O^=$ ion, and $Q^*_{O^=}$, the heat of transport, is a kinetic term depending on details of the heat transfer by the $O^=$ ion diffusing along the temperature gradient.

No satisfactory theoretical treatment has yet been proposed to evaluate quantitatively the heat of transport term in any systems of this nature. Haga (12) proposed a "thermodynamic" treatment which appears to give semiquantitative agreement between experimental and theoretical results for some silver halide systems. However, Haga's use of the Zener-Wert analysis has been criticized both from the standpoint of mathematics (15) and applicability to the framework of the derivation (16). Agreement found by Haga thus would appear to be fortuitous or at best of an empirical nature. To account properly for the continuous interactions of the diffusing ionic species with the lattice, a theory based on lattice dynamics rather than purely thermochemical reasoning appears to be necessary.

Wirtz (14) proposed a physical model of the transport process, but gave no quantitative treatment.

Gonzalez and Oriani (18) criticize the Wirtz model and discuss Q^* in terms of the mechanism by which activation energy is dissipated back into the lattice. They conclude that the ratio of the heat of transport to the activation energy for migration is a function of the ratios of the mean free paths of phonons and electrons to the jump distance of the diffusing atom. Q^* may be positive or negative according to this concept.

Experimental

Specimens.—Three specimens of $(ZrO_2)_{0.85}(CaO)_{0.15}$ were used in the measurements. Specimen 1 was prepared by fusing $(ZrO_2)_{0.85}(CaO)_{0.15}$ powder in an arc image furnace to give a dense polycrystalline sample. The powder used for this was prepared by sintering and grinding a properly proportioned mixture of ZrO_2 (major impurity, 0.1% Si) and $CaCO_3$ (major impurity, 0.1% Sr). Specimen 2 was prepared by sintering the appropriate mixture of ZrO_2 (major impurity, < 0.09% Fe) and $CaCO_3$ (major impurity, 0.1% Sr). The sintering treatment consisted of 2 hr at 1400°C, 12 hr at 2000°C, and an annealing of 2 days at 1400°C, all in O_2 atmosphere. Specimen 3 was purer, containing about 50 ppm combined impurities of Fe, Si, Mg, Al, and Cu, and was sintered in the arc image furnace to eliminate contamination by furnace wall materials. Specimens were ground to a disk form of 1 mm thickness and 9 mm diameter.

Atmospheres.—In the course of the measurements a variety of atmospheres were used, each flowed through the system at a rate of approximately 250 cc per minute. The volume of the system was about 500 cc.

For the O_2-inert gas atmospheres, tank gas mixtures, made to specification by the Matheson Company were employed.

For the H_2-H_2O inert gas atmospheres, tank gas mixtures of H_2-inert gas were passed through a cooled water bubbler which introduced the H_2O component but avoided saturation.

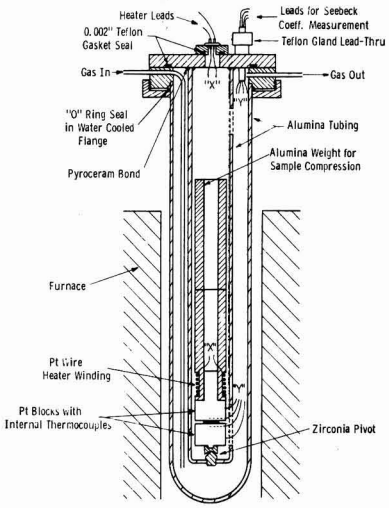

Fig. 1. Apparatus for high temperature Seebeck coefficient measurements.

The constitution of each atmosphere was checked by mass spectrometric analysis of a sample. Water content of the atmospheres was determined by standard adsorption and weighing methods on the effluent gases from the system.

Apparatus and technique.—Seebeck coefficient measurements were carried out with the apparatus shown schematically in Fig. 1. The specimen was situated between the polished faces of two platinum blocks. On the upper block a close-fitting alumina cylinder acted as a compression weight and in addition carried a heater winding for controlling the temperature gradient of the specimen. The lower block was supported by a calcia stabilized zirconia cone pivot which insured that the specimen and blocks were aligned for uniform contact pressure at all times.

The specimen thermal emf was measured by means of 0.020 in. Pt wires attached to the Pt blocks. To measure the temperature of each block at a point as near to the specimen as possible, a 0.020 in. Pt-10% Rh wire was led into the block through alumina-insulating tubing. The end of this wire was then bonded to the block by means of two small Pt plugs. This produced an internal junction near the interface, whose lead wires were the Pt-10% Rh wire and the previously mentioned Pt wire. These details are shown in Fig. 1.

Each measurement was taken at two or more specimen temperature gradients which corrects for thermocouple mismatch and eliminates other stray thermal or galvanic emf's (17). With this procedure a change of one microvolt in the specimen Seebeck coefficient was easily detectable.

Results and Discussion

Equation [5] has been experimentally verified over a wide range of gas compositions as shown by the data in Fig. 2. In Fig. 2 the Seebeck coefficient difference $(d\phi/dT)_{(mixture)} - (d\phi/dT)_{(pure\ O_2)}$ at open circuit, atmosphere pressures of $730_{\pm 2}$ Torr and about 1005°C, is plotted *vs.* $[\bar{S}_{O_2(mix.)} - \bar{S}_{O_2(pure\ O_2)}]$ for several mixtures of oxygen and inert gas, and for water-hydrogen-nitrogen mixtures. The solid line in this figure is a theoretical line calculated from Eq. [5] assuming the following over-all reversible electrode reactions for the O_2-inert gas and H_2-H_2O-N_2 mixtures respectively

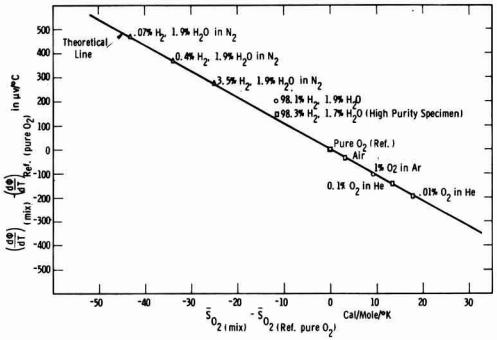

Fig. 2. Difference in Seebeck coefficient *vs.* difference in partial molar entropy of oxygen for various gas mixtures for thermocell $X(\bar{S}_{O_2})$, Pt || $(ZrO_2)_{0.85}(CaO)_{0.15}$ || Pt, $X(\bar{S}_{O_2})$. Temperature range 1000°-1005°C, ~730 Torr—Total pressure for all atmospheres. Experimental points: ○ specimen 1, △ specimen 2, □ specimen 3 (high purity). S_{O_2} in calories per mol per degree K.

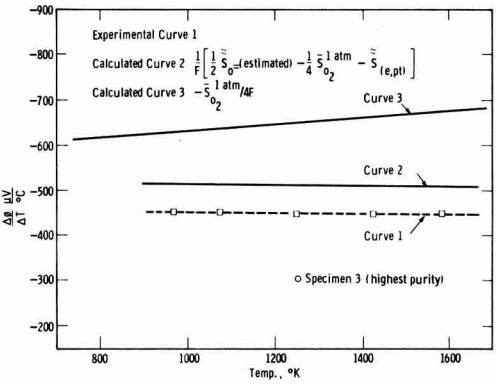

Fig. 3. Effect of temperature on the Seebeck coefficient

$$O_2 + 4e^- \rightleftarrows 2\,O^= \qquad [7]$$

$$2H_2O + 4e^- \rightleftarrows 2H_2 + 2\,O^= \qquad [8]$$

All experimental points in Fig. 2 fit the calculated line within the probable error of measurement and gas analysis except for the points at 1.9% H_2O-98.1% H_2 and 1.7% H_2O-98.3% H_2. These mixtures are the most reducing atmospheres used (equivalent equilibrium oxygen partial pressure is $\sim 10^{-18.1}$ atm at 1000°C), and it is possible that the electrolyte is being slightly altered chemically. Since data of Schmalzried (7) indicate that appreciable reduction does not occur until about 10^{-22} atm O_2 partial pressure for this electrolyte, it is possible that impurities are at least in part responsible for the deviation. The highest purity specimen used, No. 3, gave a much smaller deviation from the theoretical value which is consistent with this viewpoint.

The information obtained in these measurements indicates that our assumption of a constant transported entropy, $\tilde{\bar{S}}_{O^=}$, for a wide range of partial pressures of oxygen is valid. This allows us to determine an "experimental" value of $\tilde{\bar{S}}_{O^=}$ directly from Eq. [4] since the other terms of the equation can be measured or calculated.

While the difference values $(d\phi/dT)_{(\text{mixture})} - (d\phi/dT)_{(\text{pure } O_2)}$ were, except for the point noted, consistent for all specimens, the experimental value of $\tilde{\bar{S}}_{O^=}$ in cal deg^{-1} mole^{-1}, varied from 10.3 to 10.9 for specimens from batches 1 and 3 to 11.7 for specimen 3, the highest purity specimen. Part of these differences may be linked to subtle temperature-dependent structural changes which are suggested by neutron diffraction and conductivity studies of others (22, 23). To check this point, specimen 1 was cycled between 1250° and 800°C and held for periods up to 14 days. Slow changes of 3 to 5% in $\tilde{\bar{S}}_{O^=}$ were measured. These changes and effects arising from impurities, inhomogeneities (21), differences in crystalline character of the oxides and other sources may contribute to the spread in the values.

An unusual feature of the data is the relatively small temperature dependence of the Seebeck coefficient. As shown in Fig. 3 curve 1, $\Delta\phi/\Delta T$ changes only a few per cent between temperatures of 700° and 1280°C.

Referring to Eq. [4] and [6], it appears that the term most likely to introduce a large temperature dependence is Q^*/T. To illustrate this more clearly, Fig. 3 curve 2 gives values of $\Delta\phi/\Delta T$ as a function of temperature based on the values of $\bar{S}_{O_2}$ calculated from JANAF thermochemical tables (19), $\tilde{\bar{S}}_{(e^-,\text{Pt})}$ for the platinum electrode from the data of Cusack and Kendall (13) and a "calculated" value of $\tilde{\bar{S}}_{O^=}$ based on Eq. [6], except that $Q^*_{O^=}/T$ is neglected, $\bar{s}_{O^=}^{\text{config.}}$ is assumed to be given by the ideal relation of the form R ln $1-C/C$ where C is the fraction of filled $O^=$ sites based on the perfect fluorite lattice, and $\bar{s}_{O^=}^{\text{vib.}}$ is estimated on the basis of equipartition of entropy between ions of the oxide. For lack of specific data on the mixed oxide the entropy is assumed to be about that of a simple mixture of 85 m/o (mole per cent) ZrO_2 (tetragonal) and 15% CaO using thermochemical data assembled by Kelly and King (20) for ZrO_2 and CaO. This simple procedure does not take into account such problems as electronic contribution to the entropy at high temperatures, entropy differences of ions next to vacancies, effect of specimen inhomogeneities (21), possible preferred conduction paths due to the high vacancy concentration and other effects. As a consequence we may expect large errors in the absolute value of $\tilde{\bar{S}}_{O^=}$ calculated in this way. However, it would seem that the error due to variation of $\Delta\phi/\Delta T$ with temperature may be small which would suggest the relative importance of the $Q_{O^=}*/T$ term which might be expected to have a large temperature dependence. It is seen that the temperature dependence of curve 2 is small, similar to the actual experimental data indicating either that Q^*/T is small or not appreciably temperature dependent. This is clearly speculation, however, since, as indicated, curve 2 can at best give only a poor estimate of the absolute value of this collection of terms due to uncertainties in the procedure for estimating $\tilde{\bar{S}}_{O^=}$. Figure 3 curve 3 shows the relative contribution of the term $\bar{S}_{O_2(1\text{ atm})}/4\mathbf{F}$ calculated from thermodynamic data (19) for reference.

This analysis suggests that further information on the problem might come from experimental measurements at lower temperatures where a temperature dependence of Q^*/T could result in a larger contribution to the Seebeck coefficient and from measurements of contact potentials for the cell and the work function of electrons in platinum as a function of temperature which would give experimental information for evaluating $\bar{S}_{O^=}$.

Acknowledgment

The authors wish to thank D. Watt for help with part of the measurements, J. Hrizo and T. Y. Tien for part of the sample preparations, and R. Ure, P. Klemens, and A. Panson for helpful discussions.

Manuscript received Sept. 11, 1967; revision received Jan. 19, 1968.

Any discussion of this paper will appear in a Discussion Section to be published in the December 1968 JOURNAL.

REFERENCES

1. Hans Holtan, Jr., *Koninkl. Ned. Akad. Wetenschap. Proc.*, **56B**, 498 (1953); H. Holtan Jr., P. Mazur, and S. R. DeGroot, *Physica*, **19**, 1109 (1953).
2. A. B. Lidiard, "Reports on Progress in Physics" (1964).
3. R. E. Howard and A. B. Lidiard, *Disc. Faraday Soc.*, **23**, 113 (1957).
4. Kalevi Kiukkola and Carl Wagner, *This Journal*, **104**, 379 (1957).
5. W. D. Kingery, J. Pappis, M. E. Doty, and D. C. Hill, *J. Am. Chem. Soc.*, **42**, 394 (1959).
6. J. Weissbart and R. Ruka, *Rev. Sci. Instr.*, **32**, 593 (1961).
7. H. Schmalzried, *Z. Elektrochem.*, **66**, 572 (1962).
8. W. H. Rhodes and R. E. Carter, "Ionic Self-Diffusion in Calcia Stabilized Zirconia," Abstract in *Bull. Am. Ceram. Soc.*, April 1962.
9. H. Reinhold, *Z. Physik Chem.* (Leipzig), **B11**, 321 (1930); H. Reinhold and A. Blachny, *Z. Electrochem.*, **39**, 290 (1933).
10. L. Patrick and A. W. Lawson, *J. Chem. Phys.*, **22**, 1492 (1954).
11. R. W. Christy, E. Fukushima, and H. T. Li, *ibid.*, **30**, 136 (1959); R. W. Christy, *ibid.*, **34**, 1148 (1961).
12. Eijiro Haga, *J. Phys. Soc. Japan*, **15**, 1949 (1960).
13. N. Cusack and P. Kendall, *Proc. Phys. Soc. (London)*, **72**, 898 (1958).
14. K. Wirtz, *Phys. Z.*, **44**, 221 (1943).
15. A. B. Lidiard, Personal communication.
16. C. Zener, Personal communication.
17. R. W. Ure, Jr., in "Thermoelectricity," p. 321, Interscience Publishers, New York (1961).
18. O. D. Gonzalez and R. A. Oriani, *Trans. Met. Soc. AIME*, **233**, 1878 (1965).
19. JANAF Thermochemical Tables PB 168370-1, U.S. Dept. of Commerce Oxygen (Diatomic), Sept. 30, 1965.
20. K. K. Kelly and E. G. King, Bureau of Mines Bulletins 584 and 592.
21. Conyers Herring, *J. Appl. Phys.*, **31**, 1939-1953 (1960).
22. T. Y. Tien and E. C. Subbarao, *J. Chem. Phys.*, **39**, 1041-1047 (1963).
23. W. L. Roth, "Structure and Vacancy Ordering in Calcia-Stabilized Zirconia," Abstract presented at Am. Cryst. Assoc. Meeting, July 1964; R. E. Carter and W. L. Roth, "The Decomposition of Calcia-Stabilized Zirconia," Abstract presented at 31st Annual Chemical Engineering Symposium, A.C.S., at University of Michigan, November 1964.

Poisson's Equation as a Condition of Equilibrium in Electrochemical Systems

H. A. Christopher* and C. W. Shipman

Worcester Polytechnic Institute, Worcester, Massachusetts

ABSTRACT

The available analyses of the conditions for equilibrium in electrochemical systems do not consider the electrostatic field as a possible variable. Since there is a voltage difference between the electrodes in an electrochemical system, an electrostatic field must be present, and this field must be considered in the treatment of equilibrium because it affects the internal energy of the system. This paper presents an analysis in which the electric displacement vector is included as a possible variable. The results show that Poisson's equation is a condition of equilibrium in addition to the usual conditions of uniformity of the electrochemical potential, the pressure, and the temperature.

The conditions of equilibrium in electrochemical systems (systems which contain charged species and in which there may be electrostatic fields) have been discussed by several authors. In each case the proof is incomplete. Gibbs (1) uses a variational treatment but does not consider the electrostatic field as a possible variation. Guggenheim (2) states that uniformity of the electrochemical potential is a requirement for equilibrium but does not give a detailed proof. He also does not consider the electrostatic field as a possible variable in the system although he later shows that variation of the electric displacement vector can alter the internal (intrinsic) energy. Kirkwood and Oppenheim (3) use a variational analysis but assume as a starting point that the electrochemical potential is the intensive factor for variations in energy with mass addition. Here again, consideration of the electric displacement vector as a possible variable is omitted.

The fact that in an electrochemical cell there is a voltage difference between the electrodes means that there is an electrostatic field present in the system, and this electrostatic field is not always applied but can arise spontaneously. This means that the consequences of variations in the electric displacement vector must be considered when the equilibrium is considered.

Both ref. (2) and (3) discuss at some length the fact that separate measurement of the electrostatic and chemical potentials cannot be made and that separation of these potentials is, therefore, "nonoperational." Gibbs (1), on the other hand, considers these two potentials separately in his analysis, but in a later note (4) points out that separate measurement is impossible. The present authors take the position that the question of separate measurement is a consequence of rather than a basis for the equilibrium analysis. Further, the use of separate terms for the chemical and electrostatic potentials facilitates the treatment of mass transfer in electrochemical systems (5).

Finally, it is noted that the usual criteria for equilibrium involve terms of the form $(dE)_{S,V}$, $(dS)_{E,V}$, or $(dG)_{p,T}$, and, therefore, require that some purely thermodynamic property of the system be fixed at the outset. This is restrictive because these restraints cannot be imposed experimentally by direct control.

The present analysis considers the electric displacement vector as a possible variable, and does not require, at the outset, the fixing of any purely thermo-

* Electrochemical Society Active Member.

dynamic property except as a controlled boundary condition. Separate terms for the chemical and electrostatic potentials are retained for the reasons cited earlier.

The Conditions for Equilibrium

A general criterion of equilibrium is:

If a system be in such state that any possible variation from that state, within the restrictions that the first law of thermodynamics and any physical constraints be satisfied, requires a violation of the second law of thermodynamics, then such variation cannot occur, and the system is at equilibrium.

The most convenient form of the second law for the present purpose is the inequality of Clausius which, for a real process, is

$$dS - (\delta Q/\tau) > 0 \qquad [1]$$

(A table of nomenclature is included at the end of the paper.) In a derivation of this statement by Phillips as quoted by Keenan (6), it is shown that τ is the temperature of that part of the system to which heat is transmitted. This does not imply uniformity of temperature in the system or constancy of τ, only that there are not multiple sources of heat for the system at different temperatures simultaneously. The entropy term is for the entire system. Equation [1] is, of course, restricted to systems of fixed total mass.

To apply the criterion of equilibrium, we consider a system of constant total mass confined by a piston at an applied pressure, P. The system will consist of several phases, Φ in number (*e.g.*, as a minimum two electrode phases and an electrolyte phase; or for a fuel cell, a fuel phase, an anode phase, an electrolyte phase, a cathode phase, and an oxidant phase). For simplicity, magnetic and gravitational fields are excluded, surface phenomena are neglected, and any variations are in one dimension only. No current passes to an external circuit from the system (*i.e.*, attention is restricted to open-circuit conditions). The system contains several chemical species, J in number, each of which has a charge per unit mass, z_j. (The possibility that $z_j=0$ is not excluded.) Such a system is shown schematically in Fig. 1. In this figure X is the total length of the system from the fixed boundary at the left to the piston on the right and may vary as the piston moves to maintain the applied pressure, P; $x_{1,\phi}$ and $x_{2,\phi}$ are the boundaries of one of the phases; δx is an incremental length of the system within one of the phases; and x is the distance from the fixed boundary to the plane considered. The locations of $x_{1,\phi}$ and $x_{2,\phi}$ may, of course, be altered as the system varies. The heat source (or sink) is at the left where the temperature of the system is τ. (This heat source may be viewed as a constant temperature bath, but this is unnecessarily restrictive.)

In the system as described several variables are not controlled directly, and changes in these are, therefore,

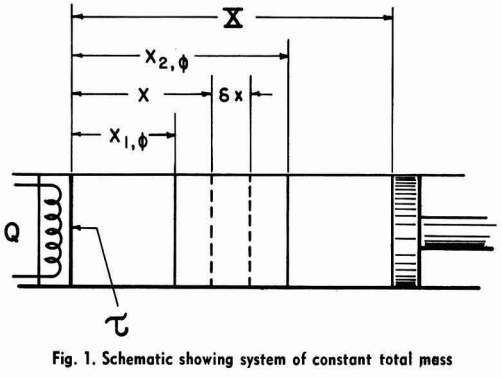

Fig. 1. Schematic showing system of constant total mass

"possible." (The term possible variation is used in the sense indicated, *i.e.*, not specified by a fixed parameter. This means that some variations considered possible herein are restricted by the laws of thermodynamics and the material balances.) These possible variations are:

1. The electrostatic field vector, $\vec{\mathcal{E}}$ and the corresponding electrostatic potentials.
2. Chemical composition. (Changes may be a consequence of migration of a species from one part of the system to another or of chemical reaction.)
3. Thermodynamic properties: entropy, internal (intrinsic) energy, specific volume, pressure, etc.
4. The total volume of the system.

We now seek the state of the system such that for any of the possible variations, there results

$$(\delta Q/\tau) - dS \geqq 0 \qquad [2]$$

i.e., violation of the second law of thermodynamics.

The possible variations in the system are subject to restraint by: (*a*) the first law of thermodynamics, (*b*) the material balances, and (*c*) the functional relations among the thermodynamic properties. These will be discussed in turn.

(*a*) The first law of thermodynamics, for the fixed mass system considered herein, may be written

$$\delta Q = d\sum_{\phi=1}^{\Phi}\int_{x_{1,\phi}}^{x_{2,\phi}} \bar{E}_{\phi}\rho_{\phi}A\delta x + d\sum_{\phi=1}^{\Phi}\int_{x_{1,\phi}}^{x_{2,\phi}} (\Psi_{\phi}\rho_{\phi}\sum_{j=1}^{J} z_j\chi_{j,\phi})A\delta x + P\,d\int_0^X A\delta x \qquad [3]$$

$$j = 1, 2, \ldots, J$$

$$\phi = 1, 2, \ldots, \Phi$$

The integral forms have been used to allow for the point-to-point variations in the integrands within a phase, as in electrolyte composition and electrostatic potential. The summations over the various phases are considered because properties may not be continuous at phase boundaries, *e.g.*, electrodes. The only work term is that resulting from expansion of the movable boundary against the fixed, applied pressure, P. (Note: P is the pressure applied to the system by the piston, not the pressure of the system at some point inside.) Changes in the internal energy have been distinguished from changes in the potential energy of charged masses in the electrostatic field which may be computed from Coulomb's law. It is important that these latter variations be distinguished from those due to the electrostatic field alone because variations in the electrostatic field will affect the internal energy. While the two effects are not always physically independent (changing the position of a charged particle can alter the electrostatic field vector), they are described by different physical laws.

(*b*) Any variations in composition must be consistent with the appropriate material balance expressions. A quantitative statement of the material balance is

$$d\sum_{\phi=1}^{\Phi}\int_{x_{1,\phi}}^{x_{2,\phi}} \rho_{\phi}\chi_{j,\phi}A\delta x - \sum_{\phi=1}^{\Phi}\sum_{r=1}^{R} \nu_{j,r}d\xi_{r,\phi} = 0 \qquad [4]$$

(J equations)

The possibility that some of the species, j, do not react chemically ($\nu_{j,r}=0$) is not excluded. The quantities $\nu_{j,r}$ are the stoichiometric coefficients of the j^{th} chemical species in the r^{th} independent stoichiometric relation of the form

$$\sum_{j=1}^{J} \nu_{j,r}M_j = 0 \qquad (r = 1, 2, \ldots, R) \qquad [5]$$

The quantities $\xi_{r,\phi}$ are the parameters representing variations due to chemical reaction as indicated by the r^{th} stoichiometric relation (extent of reaction parameters). These are, in Eq. [4], integral averages over a phase.

It should be noted that either mole or mass units may be used in these equations so long as one is consistent. That is, ρ is either a mole or mass density, χ_j is mole or mass fraction, and z_j is the charge per mole or per unit of mass of j. The stoichiometric coefficients, $\nu_{j,r}$, must, of course, be changed accordingly.

(c) In order to relate the specific internal energy, $\bar{E}$, to the other properties of the system, the necessary relationships among the thermodynamic properties must be given. Further, because these relations are to be applied to individual volumes of the entire system, and because the total mass of the individual volumes may vary, the applicable relationships must apply to variable mass systems. Since these relations are not available elsewhere, the derivations will be given in some detail.

In general the internal energy, E, is related to the other properties of the system in the usual way, *viz.*

$$E = E(S,V,m_j,\vec{D}) \qquad [6]$$

(It should not be inferred that S, V, m_j, and $\vec{D}$ are the independent variables of the electrochemical system considered; only that fixing S, V, m_j, and $\vec{D}$ fixes the value of E.) The relevant form for variations of the internal energy is

$$dE = TdS - pdV + \sum_{j=1}^{J} \mu_j dm_j + \vec{V\mathcal{E}} \cdot d(\vec{D}) \qquad [7]$$

where the last term on the right represents variations in the internal energy due to variations in the electrostatic field (7). Recognizing that the electric displacement vector, $\vec{D}$, is related to the electric intensity, $\vec{\mathcal{E}}$, by

$$\vec{D} = \epsilon \vec{\mathcal{E}} \qquad [8]$$

one may write Eq. [7] in the alternative forms

$$dE = TdS - pdV + \sum_{j=1}^{J} \mu_j dm_j + (\vec{VD}/\epsilon) \cdot d\vec{D} = TdS$$

$$- pdV + \sum_{j=1}^{J} \mu_j dm_j + d(\vec{VD}^2/2\epsilon) - (\vec{D}^2/2)\, d(V/\epsilon) \qquad [9]$$

It is important to recognize that Eq. [7] and, therefore, Eq. [9] can be applied only to regions in which the coefficients are single-valued.

Equations [9] may be integrated over a region for which the intensive factors (T, p, μ_j, $\vec{D}$) are constant to give

$$E = TS - pV + \sum_{j=1}^{J} \mu_j m_j + \vec{VD}^2/2\epsilon - (\vec{D}^2/2)\,(V/\epsilon)$$

$$= TS - pV + \sum_{j=1}^{J} \mu_j m_j \qquad [10]$$

(It is striking that in this integration the terms involving the electrostatic field drop out. This is a consequence of the fact that the expression is being applied to a region in which the intensive factors are uniform. While it is clear that the internal energy is altered by the presence of the electrostatic field, the other thermodynamic properties are also altered. Note also that in the integration we are not computing the work required to establish the electrostatic field; it is already present.)

We consider next variations in the properties of the system generally by differentiating [10], *viz.*

$$dE = TdS - pdV + \sum_{j=1}^{J} \mu_j dm_j + SdT - Vdp + \sum_{j=1}^{J} m_j d\mu_j$$

Comparison of this equation with [9] requires that

$$0 = SdT - Vdp + \sum_{j=1}^{J} m_j d\mu_j - (\vec{VD}/\epsilon) \cdot d\vec{D} \qquad [11]$$

For purposes of utilization in the energy balance (Eq. [3]), the relationships among the specific properties for variable mass systems are required. Such relationships may be obtained by dividing Eq. [10] and [11] by the total mass to obtain

$$\bar{E} = T\bar{S} - p\bar{V} + \sum_{j=1}^{J} \mu_j \chi_j \qquad [12a]$$

$$0 = \bar{S}dT - \bar{V}dp + \sum_{j=1}^{J} \chi_j d\mu_j - (\bar{\vec{VD}}/\epsilon) \cdot d\vec{D} \qquad [12b]$$

Differentiation of Eq. [12a] and subtraction of [12b] from the result gives the desired expression.

$$d\bar{E} = Td\bar{S} - pd\bar{V} + \sum_{j=1}^{J} \mu_j d\chi_j + (\bar{\vec{VD}}/\epsilon) \cdot d\vec{D} \qquad [13]$$

(The reader will note that obtaining Eq. [13] by division of Eq. [9] by the total mass restricts the result to a system of fixed mass. The seemingly circuitous route herein used avoids that problem and makes the result more general.) Equations [12] and [13] constitute the necessary relations among the specific properties. It is emphasized that the chemical potentials, μ_j, are functions of the electric displacement, $\vec{D}$, and represent the change of internal energy with mass of j with all of the other variables held constant.

$$\mu_j = (\partial E/\partial m_j)_{S,V,\vec{D},m_{k\neq j}}$$

It is important to recognize that an electrostatic field can be imposed on the system without changing its composition.

Returning, now, to the conditions for equilibrium, the nonproperty term, δQ, may be eliminated from the criterion expression [2] by substitution from the energy balance [3]. After multiplication by τ the result is

$$d\sum_{\phi=1}^{\Phi} \int_{x_{1,\phi}}^{x_{2,\phi}} \bar{E}_\phi \rho_\phi A \delta x + d\sum_{\phi=1}^{\Phi} \int_{x_{1,\phi}}^{x_{2,\phi}} \Psi_\phi \rho_\phi \left(\sum_{j=1}^{J} \chi_{j,\phi} z_j \right) A \delta x$$

$$+ P\, d\int_0^X A\delta x - \tau\, d\sum_{\phi=1}^{\Phi} \int_{x_{1,\phi}}^{x_{2,\phi}} \bar{S}_\phi \rho_\phi A \delta x \geqq 0 \qquad [14]$$

By carrying out the indicated differentiations of Eq. [14] one obtains

$$\sum_{\phi=1}^{\Phi} \int_{x_{1,\phi}}^{x_{2,\phi}} \Big(d\bar{E}_\phi + \Psi_\phi \sum_{j=1}^{J} z_j d\chi_{j,\phi} + d\Psi_\phi \sum_{j=1}^{J} z_j \chi_{j,\phi} - \tau d\bar{S}_\phi \Big) \rho_\phi A dx + \sum_{\phi=1}^{\Phi} \int_{x_{1,\phi}}^{x_{2,\phi}} \Big(\bar{E}_\phi + \Psi_\phi \sum_{j=1}^{J} z_j \chi_{j,\phi} - \tau \bar{S}_\phi \Big) d\rho_\phi A \delta x + \sum_{\phi=1}^{\Phi} \Big(\bar{E}_\phi \rho_\phi + \Psi_\phi \rho_\phi \sum_{j=1}^{J} z_j \chi_{j,\phi} - \tau \rho_\phi \bar{S}_\phi \Big)_{x_{2,\phi}} A dx_{2,\phi} - \sum_{\phi=1}^{\Phi} \Big(\bar{E}_\phi \rho_\phi + \Psi_\phi \rho_\phi \sum_{j=1}^{J} z_j \chi_{j,\phi} - \tau \rho_\phi \bar{S}_\phi \Big)_{x_{1,\phi}} A dx_{1,\phi} + P A dX \geqq 0 \quad [15]$$

The internal energy may be eliminated from [15] by means of Eq. [12a] and[13] to give

$$\sum_{\phi=1}^{\Phi} \int_{x_{1,\phi}}^{x_{2,\phi}} \Big((T_\phi - \tau) d\bar{S}_\phi + \sum_{j=1}^{J} (\mu_{j,\phi} + z_j \Psi_\phi) d\chi_{j,\phi} + \bar{V}_\phi \vec{\mathcal{E}}_\phi \cdot \vec{dD}_\phi + \Big(\sum_{j=1}^{J} z_j \chi_{j,\phi} \Big) d\Psi_\phi \Big) \rho_\phi dx + \sum_{\phi=1}^{\Phi} \int_{x_{1,\phi}}^{x_{2,\phi}} (-p_\phi \rho_\phi d(1/\rho_\phi) - (p_\phi/\rho_\phi) d\rho_\phi) \delta x + \sum_{\phi=1}^{\Phi} \int_{x_{1,\phi}}^{x_{2,\phi}} \Big((T_\phi - \tau) \bar{S}_\phi + \sum_{j=1}^{J} (\mu_{j,\phi} + z_j \Psi_\phi) \chi_{j,\phi} \Big) d\rho_\phi \delta x + \sum_{\phi=1}^{\Phi} \Big((T_\phi - \tau) \bar{S}_\phi \rho_\phi + \sum_{j=1}^{J} (\mu_{j,\phi} + z_j \Psi_\phi) \chi_{j,\phi} \rho_\phi \Big)_{x_{2,\phi}} dx_{2,\phi} - \sum_{\phi=1}^{\Phi} \Big((T_\phi - \tau) \bar{S}_\phi \rho_\phi + \sum_{j=1}^{J} (\mu_{j,\phi} + z_j \Psi_\phi) \chi_{j,\phi} \rho_\phi \Big)_{x_{1,\phi}} dx_{1,\phi} - \sum_{\phi=1}^{\Phi} \Big([p_\phi (1/\rho_\phi) \rho_\phi]_{x_{2,\phi}} dx_{2,\phi} - [p_\phi (1/\rho_\phi) \rho_\phi]_{x_{1,\phi}} dx_{1,\phi} + P dX \Big) \geqq 0 \quad [16]$$

The area term, A, has been divided out. Note that the second integral on the left of [16] is identically zero. Note also that the sum of the changes in the volumes of the separate phases must be the change in volume of the system.

$$dX = \sum_{\phi=1}^{\Phi} (dx_{2,\phi} - dx_{1,\phi})$$

By means of this expression the last three terms on the left of [16] may be combined, *viz.*

$$- \sum_{\phi=1}^{\Phi} \Big((p_\phi - P)_{x_{2,\phi}} dx_{2,\phi} - (p_\phi - P)_{x_{1,\phi}} dx_{1,\phi} \Big)$$

The variations ($d\bar{S}_\phi$, $d\chi_{j,\phi}$, $\vec{dD}$, $d\Psi_\phi$, etc.) in Eq. [16] are not all independent. The variations in $\chi_{j,\phi}$ and ρ_ϕ are restricted by Eq. [4] and by the requirement that at any point

$$\sum_{j=1}^{J} \chi_{j,\phi} = 1 \quad \text{or} \quad \sum_{j=1}^{J} d\chi_{j,\phi} = 0 \qquad [17]$$

Equation [16] as modified, [17], and [4] then indicate an extremum with two conditions of restraint. The inequality [16] indicates that the equilibrium condition is at the minimum value of the function whose variation is given by the left side of [16] with restraints represented by Eq. [4] and [17]. Lagrange's method of multipliers may be used. After carrying out the indicated differentiations in Eq. [4] (there are J equations) and multiplying each by the arbitrary functions λ_j, and after multiplying the differential form of [17] by λ_{17}, the results are subtracted from [16] to yield

$$\sum_{\phi=1}^{\Phi} \int_{x_{1,\phi}}^{x_{2,\phi}} \Big[(T_\phi - \tau) d\bar{S}_\phi + \sum_{j=1}^{J} (\mu_{j,\phi} + z_j \Psi_\phi - \lambda_j - \lambda_{17}) d\chi_{j,\phi} + \bar{V}_\phi \vec{\mathcal{E}}_\phi \cdot \vec{dD}_\phi + \Big(\sum_{j=1}^{J} z_j \chi_{j,\phi} \Big) d\Psi_\phi \Big] \rho_\phi \delta x + \sum_{j=1}^{J} \sum_{\phi=1}^{\Phi} \sum_{r=1}^{R} \lambda_j \nu_{j,r} d\xi_{r,\phi} + \sum_{\phi=1}^{\phi} \int_{x_{1,\phi}}^{x_{2,\phi}} \Big((T_\phi - \tau) \bar{S}_\phi + \sum_{j=1}^{J} (\mu_{j,\phi} + z_j \Psi_\phi - \lambda_j) \chi_{j,\phi} \Big) d\rho_\phi \delta x + \sum_{\phi=1}^{\Phi} \Big((T_\phi - \tau) \bar{S}_\phi + \sum_{j=1}^{J} (\mu_{j,\phi} + z_j \Psi_\phi - \lambda_j) \chi_{j,\phi} \Big)_{x_{2,\phi}} \rho_{x_{2,\phi}} dx_{2,\phi} - \sum_{\phi=1}^{\Phi} \Big((T_\phi - \tau) \bar{S}_\phi + \sum_{j=1}^{J} (\mu_{j,\phi} + z_j \Psi_\phi - \lambda_j) \chi_{j,\phi} \Big)_{x_{1,\phi}} \rho_{x_{1,\phi}} dx_{1,\phi} - \sum_{\phi=1}^{\Phi} \Big((p_\phi - P)_{x_{2,\phi}} dx_{2,\phi} - (p_\phi - P)_{x_{1,\phi}} dx_{1,\phi} \Big) \geqq 0 \qquad [18]$$

The values of the functions λ_{17} and λ_j will be chosen so that the variables in Eq. [18] which are not independent will be eliminated. The function λ_{17} is chosen such that for some particular species, say k, it is identically equal to the function $(\mu_{k,\phi} + z_k \Psi_\phi - \lambda_k)$ at all points in the system. The values of the functions λ_j are chosen so that the functions $(\mu_{j,\phi} + z_j \Psi_\phi - \lambda_j)$ are identically zero at some point in the system. This procedure effectively eliminates the dependent variables from Eq. [18]; either the variables $d\bar{S}_\phi$, $d\chi_{j,\phi}$, $d\rho_\phi$, $d\Psi_\phi$, etc., are independent or their coefficients are identically zero. Satisfaction of Eq. [18] for regions wherein "j" is an actual component ($d\chi_{j,\phi}$ can take any sign) requires that

I. $T_\phi = \tau$

II. $p_{x_{1,\phi}} = P \qquad p_{x_{2,\phi}} = P$

III. $\mu_{j,\phi} + z_j \Psi_\phi = \lambda_j \qquad (j = 1, 2, \ldots, J)$

IV. $\sum_{j=1}^{J} \nu_{j,r} \lambda_j = 0 \qquad (j = 1, 2, \ldots, J) \quad (r = 1, 2, \ldots, R)$

V. $\bar{V}_\phi \vec{\mathcal{E}}_\phi \cdot \vec{dD}_\phi + \Big(\sum_{j=1}^{J} z_j \chi_{j,\phi} \Big) d\Psi_\phi = 0$

These five conditions must obtain at equilibrium. Con-

dition I requires that the temperature be uniform; condition II requires that the pressure at each phase boundary be the pressure applied to the system; condition III is the familiar requirement of unitormity of the electrochemical potential; condition IV (combined with condition III) is the familiar form for chemical equilibrium except that the electrochemical potential $(\mu_j + z_j\Psi)$ appears instead of the chemical potential alone.

Condition V is new and is a consequence of considering the effect of the electrostatic field. Actually condition V reduces to Poisson's equation for a medium of constant permittivity. This may be easily demonstrated by considering adjacent parts of the system and applying condition V in one-dimensional form. Using Eq. [8] and the definition

$$\vec{\mathcal{E}}_\phi = -\text{ grad }(\Psi_\phi)$$

one finds

$$\overline{V}_\phi\,(-d\Psi_\phi/dx)\,\frac{d}{dx}\left(-\epsilon_\phi\frac{d\Psi_\phi}{dx}\right) + \left(\sum_{j=1}^{J} z_j\chi_{j,\phi}\right)(d\Psi_\phi/dx) = 0 \quad [19]$$

For constant permittivity this becomes

$$d^2\Psi_\phi/dx^2 = -\left(\sum_{j=1}^{J} z_j\chi_{j,\phi}\right)/(\epsilon_\phi\overline{V}_\phi) \quad [20]$$

which is Poisson's equation. Thus, Poisson's equation is a consequence of the equilibrium analysis if the permittivity of the medium is constant. Since permittivity is, in general, dependent on composition, use of [20] implies uniform composition.

The expression deduced directly from [19] without assumption is

$$\frac{d}{dx}(\vec{D}_\phi) = \left(\sum_{j=1}^{J} z_j\chi_{j,\phi}\right)/\overline{V}_\phi \quad [20a]$$

which may be obtained directly from Maxwell's equations (8). Since the electrostatic field term in Eq. [7] was also obtained by use of Maxwell's equations (5) such a result is not surprising.

Condition V may also be used to develop relations between the electrochemical potential and the other thermodynamic properties. For example, substitution of condition V into Eq. [12b] yields

$$0 = \overline{S}dT - \overline{V}dp + \sum_{j=1}^{J}\chi_j d(\mu_j + z_j\Psi) \quad [21]$$

which is the analog of the Gibbs equation for electrochemical systems. Note that according to Eq. [21] the equilibrium requirements of uniformity of the electrochemical potentials and of the temperature mean that the pressure must also be uniform.

Use of condition V in Eq. [7] gives the relation

$$dE = TdS - pdV + \sum_{j=1}^{J}\mu_j dm_j - \left(\sum_{j=1}^{J} z_j m_j\right)d\Psi \quad [22]$$

or in Eq. [13]

$$d\overline{E} = Td\overline{S} - pd\overline{V} + \sum_{j=1}^{J}\mu_j d\chi_j - \left(\sum_{j=1}^{J} z_j\chi_j\right)d\Psi \quad [23]$$

By adding the quantity

$$d\left(\Psi\sum_{j=1}^{J}(z_j m_j)\right)$$

to both sides of [22] one obtains

$$d\left(E + \Psi\sum_{j=1}^{J} z_j m_j\right) = TdS - pdV + \sum_{j=1}^{J}(\mu_j + z_j\Psi)\,dm_j \quad [24]$$

Equations [21] and [23] may be used to obtain interrelationships among the various properties by relations of the Maxwell type in the usual way.

Equation [24] is effectively the fundamental expression used by Kirkwood and Oppenheim (3) except that their symbol E represents the group in parenthesis on the left of [24]. The present treatment makes this a consequence of the equilibrium analysis. Kirkwood and Oppenheim state in developing [24] that they make the assumption that the quantity denoted by the symbol E as used herein depends only on the pressure, temperature, and composition and not on the charge, and point out that verification of the assumption has been obtained from experiment. The present analysis shows that such an assumption is unnecessary. It is emphasized that E is, in virtue of Eq. [17], dependent on $\vec{D}$ (5).

Finally, in obtaining conditions I through V it was assumed that all chemical species, j, are present in all phases. For species which are not actually present in some particular phase, ϕ_1, the sign of $d\chi_{j,\phi_1}$ can only be positive, and therefore, Eq. [18] will be satisfied if

$$\mu_{j,\phi_1} + z_j\Psi_{\phi_1} \geqq \lambda_j \quad [25]$$

Conclusions

The results of an equilibrium analysis in which the electric displacement vector is considered as a possible variable show that the usual conditions of equilibrium involving uniformity of temperature, pressure, and electrochemical potential are unaffected. The treatment also shows that the usual conditions of equilibrium will apply across regions where the electric displacement vector is varying. Furthermore, the analysis yields Poisson's equation (or rather its more general equivalent) as a condition of equilibrium.

Acknowledgment

The authors gratefully acknowledge the financial support of the Research and Advanced Development Division of the AVCO Corporation. Dr. Christopher was supported by an NDEA (Title IV) Fellowship. The helpful comments of Professors J. P. van Alstyen, B. A. Wooten, and M. V. Evans of the Worcester Polytechnic Institute, and Jeong-long Lin of Boston College are also appreciated.

Manuscript received May 3, 1967; revised manuscript received Jan. 19, 1968.

Any discussion of this paper will appear in a Discussion Section to be published in the December 1968 JOURNAL.

REFERENCES

1. J. W. Gibbs, "Collected Works," Vol. I, p. 331 *et seq.*, Yale University Press, New Haven (1948).
2. E. A. Guggenheim, "Thermodynamics," 2nd ed., p. 330 *et seq.*, Interscience, New York (1950).
3. J. G. Kirkwood and I. Oppenheim, "Chemical Thermodynamics," p. 205, McGraw-Hill, New York (1961).
4. J. W. Gibbs, *op. cit.*, p. 429.
5. P. L. T. Brian, *et al.*, *A.I.Ch.E. Journal*, **10**, 727 (1964).
6. J. H. Keenan, "Thermodynamics," p. 79, John Wiley & Sons, Inc., New York (1941).
7. E. A. Guggenheim, *op. cit.*, p. 361.
8. J. A. Stratton, "Electromagnetic Theory," p. 5, McGraw-Hill, New York (1941).

NOMENCLATURE

A	Cross-sectional area (see Fig. 1)
$\vec{D}$	Electric displacement vector

d Differential operator (small change in operated quantity)
E Internal (intrinsic) energy
$\vec{G}$ Electric intensity vector
J Total number of chemical species
m Mass of subscript species
P Pressure applied to the system
p Pressure in the system
Q Heat added to the system
R Number of independent stoichiometric relations
S Entropy
T Temperature
V Volume
X Length of the system (see Fig. 1)
x Dummy variable, length in the system (see Fig. 1)
z Charge per unit mass of subscript species

Greek
δ Differential operator (small amount of operated quantity)
ϵ Permittivity
λ Lagrangian multiplier (a function)
μ Chemical potential of subscript species
$\nu_{j,r}$ Stoichiometric coefficient of j^{th} species in r^{th} reaction
ξ Reaction parameter
ρ Density
τ Temperature of that part of the system in contact with heat source
Φ Total number of phases present
χ Mass (or mole) fraction of subscript species
Ψ Electrostatic potential

Subscripts
j Species index
k Species index
r Reaction index
ϕ Phase index
1 Lower limit of phase boundary
2 Upper limit of phase boundary

Superscripts
— (overscore) Denotes quantity per unit mass or per mole

Brief Communications

The Standard Potential of the Silver-Silver Chloride Electrode in N-N Dimethylacetamide at 25°C

Bruno Scrosati, Gianfranco Pecci, and Gianfranco Pistoia

Istituto di Chimica Fisica ed Elettrochimica, Università di Roma, Roma, Italy

Although interest in nonaqueous electrolytes has been greatly increased in the last few years because of their use in high energy battery systems, relatively few determinations of standard potentials of suitable reference electrodes have been carried out in nonaqueous solvents (1-10).

In this work we extend the series to report the behavior of the silver-silver chloride electrode in N-N-Dimethylacetamide (DMA) at 25°C, with respect to the normal hydrogen electrode using the following cell

$$\text{Pt, } H_2/\text{HCl (m) in DMA/AgCl, Ag} \qquad [1]$$

From the emf data of cell [1] activity coefficients of HCl solutions in DMA at 25°C have been calculated.

DMA (C. Erba reagent grade) was purified by fractional distillation under reduced pressure (2 mm Hg). The final product had a specific conductance of 4×10^{-7} ohm^{-1} in good agreement with the value given in the literature (11).

The HCl gas was obtained by dropping concentrated H_2SO_4 on reagent grade NaCl and passing the evolved gas first through concentrated H_2SO_4 and finally through two traps at dry ice temperature. The solutions used in cell [1] were prepared by passing HCl gas into DMA. The concentration of HCl was determined by Mohr titrations, after neutralizing with sodium bicarbonate. The reliability of volumetric titrations in DMA has been shown by Pistoia and Scrosati (12).

The cell was an all glass type of the design recommended by Ives and Janz (13). The silver-silver chloride electrodes were of the thermal type and were prepared according to the method described by Ives and Janz (13). Hydrogen electrodes were prepared in the usual manner (13).

Hydrogen gas was purified by Engelhard Hydrogen Purifier Mod. 0-50 and passed through the cell at a rate of 1-2 bubbles/sec. The emf measurements were made at 25.00° ± 0.05°C by a differential voltmeter Keithley 662. The emf readings were taken 30 min after starting the hydrogen flow.

The emf values of cell [1], corrected to 760 mm of pressure, are given in Table I as a function of HCl molality.

The standard potential of the silver-silver chloride electrode was determined by the use of the function E', defined by the equation

$$E' = E + \frac{2(2.3026)RT}{\mathbf{F}} \log m - \frac{2(2.3026)RT}{\mathbf{F}} \alpha\sqrt{m} = E^\circ - \frac{2(2.3026)RT}{\mathbf{F}} \beta m \qquad [2]$$

Table I. Emf data and activity coefficients for HCl solutions in N-N-dimethylacetamide at 25°C

mHCl	E (volt)	E' (volt)	$\gamma_\pm$
0.0052	0.4305	0.1475	0.818
0.0064	0.4183	0.1444	0.843
0.0145	0.3814	0.1422	0.763
0.0204	0.3617	0.1359	0.796
0.0260	0.3500	0.1334	0.784
0.0319	0.3389	0.1297	0.793
0.0348	0.3336	0.1275	0.806
0.0425	0.3224	0.1229	0.821
0.0500	0.3120	0.1178	0.854
0.0584	0.3022	0.1127	0.885

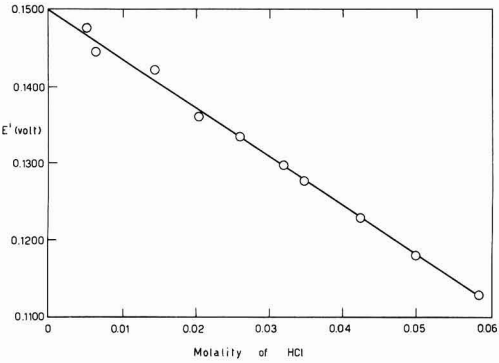

Fig. 1. E' as a function of HCl molality

where the Debye-Hückel constant α for DMA at 25°C is 1.526. Figure 1 shows the values of E' *vs.* the corresponding values of m. Extrapolation to zero molality by the method of least squares gives the standard potential of the Ag, AgCl electrode in DMA at 25°C, $E°$, as $0.1500^x \pm 0.0006$v. The best fit of the data corresponds to a straight line with a slope of −0.640 and, consequently, the value of β in Eq. [2] is 5.410. The mean molal activity coefficient, $\gamma_\pm$, of HCl in DMA at 25°C may be calculated by the equation

$$\log \gamma_\pm = \frac{E° - E}{0.1183} - \log m \qquad [3]$$

The values of $\gamma_\pm$ obtained by Eq. [3] are listed in Table I. Studies on the properties of the silver-silver chloride and other reference electrodes are being extended in this laboratory to other nonaqueous solvents.

Manuscript received Jan. 18, 1968.

Any discussion of this paper will appear in a Discussion Section to be published in the December 1968 JOURNAL.

REFERENCES

1. H. S. Harned and T. R. Paxton, *J. Phys. Chem.*, **57**, 531 (1953).
2. L. M. Mukherjee, *J. Am. Chem. Soc.*, **79**, 4040 (1957).
3. D. H. Everett and S. E. Rasmussen, *J. Chem. Soc.*, **1954**, 2812.
4. H. Taniguchi and G. J. Janz, *J. Phys. Chem.*, **61**, 688 (1957).
5. I. T. Oiwa, *ibid.*, **60**, 754 (1956).
6. R. K. Agawarl and B. Nayak, *ibid.*, **70**, 2568 (1966).
7. M. Mandel and P. Delcroly, *Nature*, **182**, 794 (1958).
8. M. De Rossi, G. Pecci, and B. Scrosati, *Ric. Sci.*, **37**, 342 (1967).
9. W. Sen, K. K. Kundu, and M. N. Das, *J. Phys. Chem.*, **71**, 3665 (1967).
10. L. R. Dawson, R. C. Sheridan, and H. C. Eckstrom, *ibid.*, **65**, 1829 (1961).
11. G. Lester, T. Grover, and P. Sears, *J. Phys. Chem.*, **60**, 1076 (1956).
12. G. Pistoia and B. Scrosati, *Ric. Sci.*, in press.
13. D. J. G. Ives and G. J. Janz, "Reference Electrodes," Academic Press, New York (1961).

Mechanism of the Formation of Zinc Dendrites

A. R. Despic,[1] J. Diggle, and J. O'M. Bockris*

Electrochemistry Laboratory, University of Pennsylvania, Philadelphia, Pennsylvania

During Zn dendrite formation at constant overpotential, the current grows exponentially with time, the time constant decreasing with increasing overpotential, concentration of zincate, and temperature.

This is consistent with a model of dendrite initiation according to which the rate of deposition onto any part of a microrough surface entering deeper than the average surface into the diffusion layer, relative to the rate of growth of the average surface, increases exponentially with time. The relative height of a protrusion can be shown to be

$$y = y_0 \exp\left(\frac{t}{\tau}\right) \qquad [1]$$

where the time constant τ, given by

$$\tau = \frac{\left[\frac{(i_L)_0}{i_0 f_c(\eta)} + \delta_0\right]^2}{\frac{M}{\rho n F}\left[1 - \frac{f_a(\eta)}{f_c(\eta)}\right](i_L)_0} \qquad [2]$$

and where y_0 is the original protrusion height at $t = 0$, $f_a(\eta) = \exp\left(\frac{(2-\beta)F}{RT}\eta\right)$, $f_c(\eta) = \exp\left(-\frac{\beta F}{RT}\eta\right)$, $(i_L)_0 = nFD_0C_0$, and δ_0 is the diffusion layer thickness. Thus the height of the protrusion increases exponentially with time (Fig. 1) until it becomes comparable to the diffusion layer thickness. After this initial process, the protrusion forms its own diffusion layer, the conditions of spherical diffusion to the tip are established, and growth becomes governed by a law of the type derived by Barton and

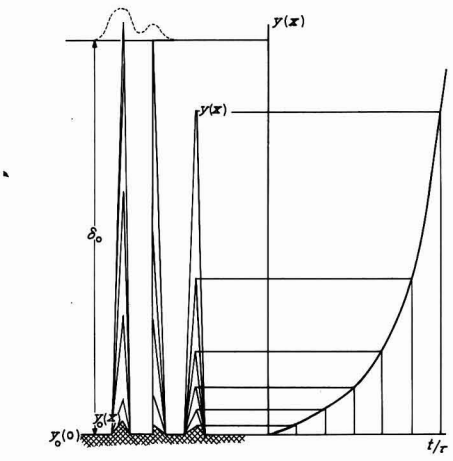

Fig. 1. Height of protrusions at equal time intervals exhibiting exponential dependence.

* Electrochemical Society Active Member.
[1] On leave of absence from the University of Beograd (Yugoslavia).

Bockris (1). Such a model avoids the concept of dendrite nucleation.

To test the model, its consequences on the current flowing through the interface, at a given overpotential, were evaluated. It was shown that the current should follow a relationship similar to Eq. [1], *i.e.*,

$$i = i_{\text{init.}}\left\{1 + \left[\frac{y_0}{\dfrac{(i_L)_0}{i_0 f_c(\eta)} + \delta_0}\right]\exp\left(\frac{t}{\tau}\right)\right\} \qquad [3]$$

where

$$i_{\text{init.}} = \frac{(i_L)_0}{\dfrac{(i_L)_0}{i_0 f_c(\eta)} + \delta_0}\left(1 - \frac{f_a(\eta)}{f_c(\eta)}\right) \qquad [4]$$

The time constants, τ, were extracted from experimental plots, by plotting log $(i - i_{\text{init.}})$ *vs.* t with $i_{\text{init.}}$ being taken as equal to the initial current density for that overpotential ($t = 0$). Good straight lines were obtained with slope 2.3τ.

The dependence of τ on overpotential, concentration, and temperature was found to follow quantitatively the dependence predicted from analyzing Eq. [2] in those directions. The diffusion layer thickness was found to be $\sim 10^{-3}$ cm, which is in the expected range.

To interpret the growth rate data, the Barton-Bockris theory was extended to encompass mixed activation and diffusion control of the current density in the nonlinear regions ($\eta > 10$ mv) and this for two cases of deposition mechanisms: (*a*) the single electron discharge of univalent ions (pertinent to silver) and (*b*) a two-step single electron discharge (pertinent to zinc and other divalent metal depositions). The current density at the dendrite tip, *i.e.*, the rate of propagation of the dendrite, is
for (*a*)

$$i_n = \frac{f_c(\eta)\exp(-1/r_n) - f_a(\eta)_a \exp(1/r_n)}{K/i_0 + f_c(\eta) r_n \exp(-1/r_n)} \qquad [5]$$

and for (*b*)

$$i_n = \frac{f_c(\eta) - f_a(\eta)\exp(1/r_n)}{K/i_0 + f_c(\eta) r_n} \qquad [6]$$

where $i_n = i/K$, $\tau_n = \dfrac{RT}{2\gamma V}\cdot r$ and $K = RTnFDC_0/2\gamma V$,

γ being the surface tension at the metal-solution interface.

The observed rates of growth for Zn were found to follow relation [6] as far as the dependence on potential concentration and temperature implicit in [6] is concerned.

Important conclusions can be made from an analysis of Eq. [5] and [6], which can be understood from analyzing the graphs in Fig. 2.

(*a*) The curves showing the relation between tip c.d. (*i.e.*, growth rate) and the tip radius for different overpotentials are found to cross a line indicating the value of the limiting current density $(i_{L,l})_n$ in Fig. 2 for linear diffusion onto a flat surface at overpotentials coinciding remarkably well with the experimentally observed critical overpotentials (*e.g.*, from Fig. 2b, dendritic growth for Zn would start at 60 mv as experimentally observed). Hence, the criterion for a critical current density of the dendrite tip which grows under activation control, past which the conditions for dendritic growth are established, as well as the criterion for critical overpotential are defined as

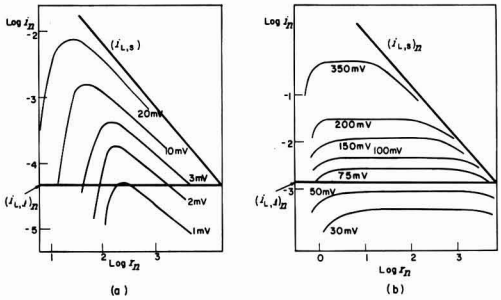

Fig. 2. Dependence of the tip current density on tip radius at different constant overpotentials (a) in the case of silver; (b) in the case of zinc. $i_{L,l}$ is the limiting current density for diffusion onto a flat surface; $i_{L,s}$ the limiting current density of spherical diffusion.

$$i_c = i_0[f_c(\eta) - f_a(\eta)] \geqq i_{L,l} \qquad [7]$$

and

$$-\eta_c \geqq \frac{RT}{\beta F}\ln\left(\frac{i_{L,l}}{i_0}\right) \qquad [8]$$

The critical current density depends solely on the conditions of diffusion to the flat surface, while the critical overpotential depends also on i_0 for the deposition process.

(*b*) The difference in mechanism, and even more so the difference in i_0, results in a significant difference in the range of tip radii in which dendrite formation can occur for the two systems: those for silver show sharp peaks of growth rate in a narrow range of tip radii, while those for zinc show broad plateaus over a wide range of tip radii. This explains the observed difference in the character of the deposit for the two metals: the dendrites of silver are propagating fast at low overpotentials but are scarce, since the probability of the protrusions falling into the right range of radii is small; zinc dendrites are propagating slowly, but they are more abundant because of the high probability of the appearance of a protrusion with radii in the required range.

Acknowledgments

The authors thank the National Science Foundation for their support under Grant No. GK-1724.

Manuscript received Jan. 8, 1968.

Any discussion of this paper will appear in a Discussion Section to be published in the December 1968 JOURNAL.

REFERENCE

1. J. L. Barton and J. O'M. Bockris, *Proc. Royal Soc. London*, **A268**, 485 (1962).

Field Ion Microscopical Studies of Exchange Current Density on Iridium

Leonard Nanis

School of Chemical Engineering, University of Pennsylvania, Philadelphia, Pennsylvania

and Philippe Javet

Institute for Direct Energy Conversion, University of Pennsylvania, Philadelphia, Pennsylvania

The recently developed technique of field ion microscopy (FIM) is a powerful tool for the investigation of metal surfaces. In many instances, resolution of individual atoms in the metallic lattice has been possible (1). Recent progress in electrode kinetics has shown the need for models on a true atomic scale for the interpretation of phenomena occurring at the electrified interface.

The use of FIM for electrochemistry provides an opportunity to observe surface effects on a scale in which the elementary electrochemical steps occur. Experiments have been performed based on the sequence:

1. image iridium tip (after shaping to almost perfect hemispherical form and atomic smoothness by field induced evaporation);
2. bring to atmospheric pressure and remove tip from FIM;
3. immerse for specified time in electrolyte with iridium ions;
4. rinse electrolyte from tip;
5. return to FIM and image again.

Changes on the surface have been photographically recorded and compared with those occurring in a "blank" experiment during which the tip is treated in a similar electrolyte, but free of iridium ions.

The rate of exchange of charge at the equilibrium potential between a metal and its ions is the exchange current density, a central concept of electrode kinetics (2). Thus, rearrangement of a previously smooth surface should be expected as atoms from the metal become involved in the exchange of charge. The extent of this perturbation is expected to be an increasing function of the time of contact of the metal with the electrolyte and of the magnitude of the exchange current. FIM prepared iridium tips have been immersed for various times in acid solution ($2N$ H_2SO_4) containing 10^{-6}M iridium ion. A blank experiment using the same acid without iridium ions has shown that the surface perturbation following a treatment of up to 10 min in electrolyte and 10 min in air extends to a depth of only 3 ± 1 atom layers. An example of a blank experiment is shown by comparing Fig. 1 and 2. The field evaporated (111) region of an iridium tip is shown in Fig. 1. After the tip was brought to atmospheric pressure, it was removed from the FIM, dipped for 3 min in $1N$ H_2SO_4 and then returned to the FIM. After reestablishment of the vacuum, one atomic layer was removed by field evaporation, leading to the structure shown in Fig. 2.

The numerous bright spots superimposed on the previous features are most probably displaced iridium atoms. After evaporation of two more atomic layers, bright spots no longer appear and the original image, as in Fig. 1, is obtained. When a field evaporated tip is exposed to air only, bright spots similar to those shown in Fig. 2 appear, but the original image is generally restored after the field evaporation of only two layers.

For the solution containing iridium ions, however, the perturbation extends very much deeper than for blank experiments. The relationship between the time of contact with solution and the depth of penetration (corrected for blank) is shown in Fig. 3. Correlation of the observed atom redistribution with time of immersion, exchange current density, and, *e.g.*, crystallographic factors is now under study. However, two important features are readily obtained from the immersion experiments:

(*A*) For brief times of contact (less than 5 min), comparison of the damage which occurs in various crystallographic directions permits ordering of relative exchange current density on different crystal faces as

$$J_o(111) < J_o(100) < J_o(210)$$

A similar order

$$J_o(111) < J_o(100) < J_o(110)$$

has been determined for copper (fcc, as is iridium) by Damjanovic *et al.* (3) in a study of electrodeposition kinetics.

(*B*) With prolonged contact (greater than 5 min) between the metal and its ions, the formation of "spikes" on the surface has been observed.

Figure 4 shows a field-evaporated clean iridium tip with a central (100) region. The fourfold symmetry decoration is caused by field-stabilized protruding atoms in the [110] directions. The nearly hemispherical tip has an average radius of curvature of about 800Å.

Following imaging, this tip was immersed for 10 min in iridium ion solution as mentioned above. Figure 5 shows the image of the treated tip after the removal of 10 atom layers by field evaporation.

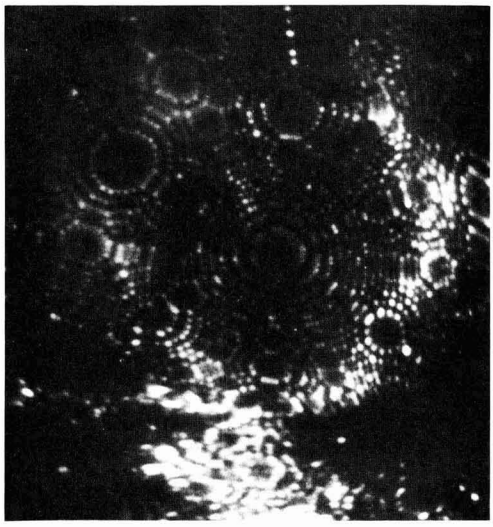

Fig. 1. Field evaporated iridium tip with central (111) region before blank treatment.

Fig. 2. Same as Fig. 1 following 3-min immersion in 1*N* H_2SO_4

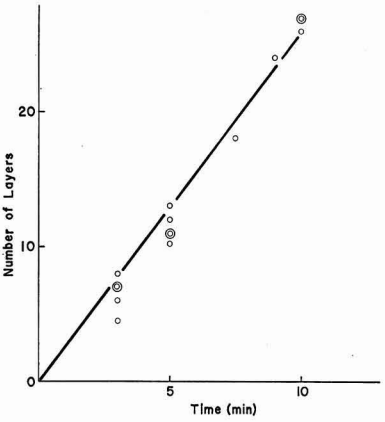

Fig. 3. Number of perturbed layers on iridium tip as a function of time of contact with iridium ions.

The two spike regions centered around the [310] direction have smaller radius of curvature than the original tip, *i.e.*, the radius in the upper region of Fig. 5 is 450 to 500Å with an even smaller radius for the lower region.

The field enhancement associated with the decreased local radius produces an effective increase in image magnification and resolution and permits imaging at much lower potential than for Fig. 4. At the reduced potential, imaging does not occur for the remainder of the tip because of the reduced field. Further field evaporation restores the original image as in Fig. 4. Figure 6 shows the tip after the removal of twenty atom layers from the protruding (310) plane. Features of the original structure (Fig. 4) are increasingly evident. The last traces of over-all irregularities disappear completely after evaporation of the 29th layer.

By postulating a simple model for the transfer of material on the surface, an estimate for the magnitude of the exchange current density may be obtained. It has been observed that a general roughening of the entire surface occurs during the first 5 min of immersion, followed by a growth pattern which favors

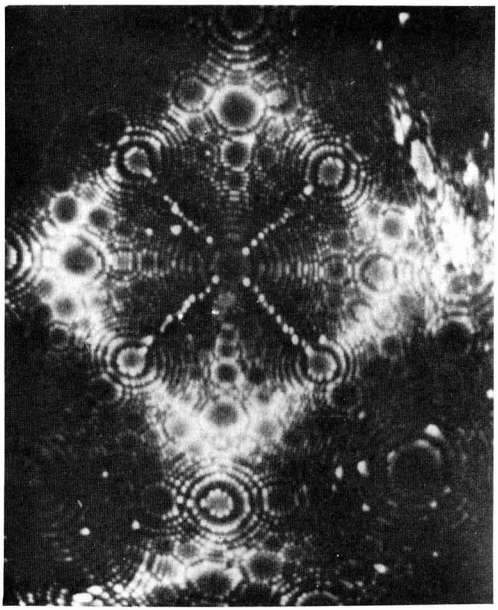

Fig. 4. Field ion image of smooth, field evaporated iridium tip before electrochemical treatment; (100) plane in center, (111) planes in picture corners. Image potential 17.3 kv; imaging gas helium 2 μm Hg.

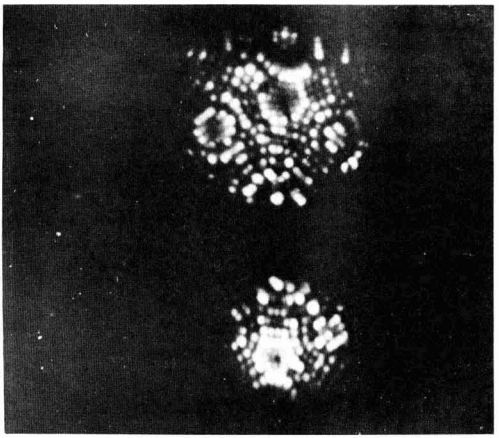

Fig. 5. Iridium tip, same as Fig. 4, after 10 min contact with solution, 10^{-6}M Ir, followed by return to FIM and field evaporation of 10 atomic layers. The two "spike" growth features are each centered on [310] directions. Imaging potential 11.5 kv.

specific directions (Fig. 5). Accordingly, suppose that all discharge of ions after five minutes takes place at the favored position, causing this region to grow, *i.e.*, a hypothetical separation of the cathodic and anodic components of the exchange current density.

The approximate volume of the spike region may be readily computed from direct measurements of the area at different levels as layers are removed by field evaporation. Using Fig. 4, 5, 6 and images at other levels, assuming a tetravalent iridium ion, an upper limit of 10^{-4} Acm^{-2} for the exchange current density is obtained.

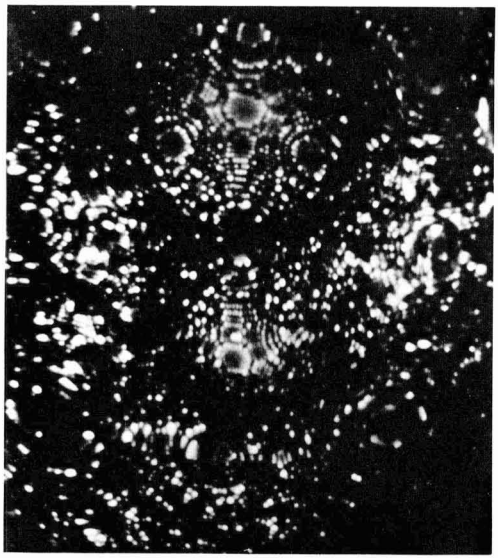

Fig. 6. Iridium tip, same as Fig. 5 after field evaporation of 20 layers. The structure of Fig. 4 has partially reappeared. Imaging potential 15.5 kv.

It is expected that direct FIM observation of treated electrode surfaces will be helpful in devising models for electrochemical reactions, not only by the observation of the changes induced on the surface by electrochemical treatment, but also through consideration of the analogy between the field used for image formation and the field at the electrode-electrolyte interface.

Although there is evidence for the existence of vacancies in Fig. 5, spiral dislocations are apparently absent. Provided the imaging field following electrochemical treatment does not interact to remove dislocations, the mechanism presently accepted for the initiation and continuation of electrolytic growth, requiring spiral dislocations intersecting the growth surface, bears re-examination.

Some of the well-known features of the FIM method such as field-stabilized protruding atoms (fourfold decoration in Fig. 4) and field-induced mechanical stresses require incorporation in models of the electrochemical interface.

Acknowledgment

This work was supported by NASA Grant NSG-316.

Manuscript received Jan. 23, 1968; revised manuscript received Feb. 19, 1968.

Any discussion of this paper will appear in a Discussion Section to be published in the December 1968 JOURNAL.

REFERENCES

1. E. Müller, *Advances in Electronics,* **13,** 89 (1960).
2. H. Gerischer, *Z. Elektrochem.,* **54,** 362 (1950); **55,** 98 (1951); **59,** 604 (1955).
3. A. Damjanovic, T. H. V. Setty, and J. O'M. Bockris, *This Journal,* **113,** 429 (1966).

Electrochemical Books in Print

John Wiley Publications In-Print

The following are books developed and sponsored by The Electrochemical Society and published by John Wiley & Sons Inc., 605 Third Ave., New York, N. Y., 10016. Members of the Society can receive a 33 1/3% discount by ordering from Society Headquarters. Book and invoice mailed by the publisher. Nonmembers (including subscribers) must order direct from the publisher.

Corrosion Handbook. Edited by Herbert H. Uhlig. Published 1948, 1188 pages, **$21.00.**

Modern Electroplating, Second Edition. Edited by Frederick A. Lowenheim. Published 1963, 769 pages, **$16.00.**

Electrochemistry in Biology and Medicine. Edited by Theodore Shedlovsky. Published 1955, 369 pages, **$12.50.**

Arcs in Inert Atmospheres and Vacuum. Edited by W. E. Kuhn. Published 1956, 188 pages, **$7.50.** A 1956 Spring Symposium.

The Structure of Electrolytic Solutions. Edited by Walter J. Hamer. Published 1959, 441 pages, **$19.50.** A 1957 Spring Symposium.

Ultrafine Particles, Editor-in-Chief—William E. Kuhn. Published 1963, 561 pages, **$15.00.**

First International Conference on Electron and Ion Beam Science and Technology. Edited by R. Bakish. Published 1965, 945 pages, **$24.50.** (Sponsored by the Electrothermics and Metallurgy Division of The Electrochemical Society and the Metallurgy Society of AIME.)

The Electron Microprobe. Edited by T. D. McKinley, K. F. J. Heinrich, and D. B. Wittry. Published 1966, 1035 pages, **$27.50.** A 1964 Fall Symposium.

Chemical Physics of Ionic Solutions. Edited by B. E. Conway and R. G. Barradas. Published 1966, 622 pages. **$25.00.** A 1964 Spring Symposium.

Vapor Deposition. Edited by C. F. Powell, J. H. Oxley, and J. M. Blocher, Jr. Published 1966, 725 pages, **$19.95.**

The Stress Corrosion of Metals by Hugh I. Logan. Published 1966, 306 pages; **$13.95.**

High Temperature Oxidation of Metals by Per Kofstad. Published 1966, 340 pages; **$13.50.**

The Corrosion of Light Metals, by H. P. Godard, W. B. Jepson, M. R. Bothwell, and R. L. Kane. Published 1967, 360 pages; **$13.95.**

High-Temperature Materials and Technology. Edited by I. E. Campbell and E. M. Sherwood. Published 1967, 1022 pages, $27.50.

Out-Of-Print Volumes Available from University Microfilm

The following volumes are out-of-print from the publisher but can be obtained from University Microfilm, 300 N. Zeeb St., Ann Arbor, Mich., as soft bound volumes. Book and invoice mailed by the publisher.

The Surface Chemistry of Metals and Semiconductors. Edited by Harry C. Gatos, with the assistance of J. W. Faust, Jr., and W. J. La Fleur. Published 1960. Reprinted 1967. 526 pages, **$21.50.** A 1959 Fall Symposium.

Transactions of the Symposium on Electrode Processes. Edited by Ernest Yeager. Published 1961. Reprinted 1967. 374 pages, **$15.50.** A 1959 Spring Symposium.

Vapor Plating (The Formation of Metallic and Refractory Coatings by Vapor Deposition), by C. F. Powell, I. E. Campbell, and B. W. Gonser. Published 1955. Reprinted 1967. 158 pages, **$6.50.**

Mechanical Properties of Intermetallic Compounds. Edited by J. H. Westbrook. Published 1959. Reprinted 1967. 435 pages, **$17.50.** A 1959 Spring Symposium.

Iodide Metals and Metal Iodides, by Robert F. Rolsten. Published 1961. Reprinted 1967. 441 pages, **$18.00.**

Technology of Columbium (Niobium). Edited by B. W. Gonser and E. M. Sherwood. Published in 1958. Reprinted 1967. 120 pages; **$5.00.**

Zirconium and Its Alloys. Published 1966. c. 250 pages; **$6.00.** A 1965 Fall Symposium.

Measurement Techniques for Thin Films. Edited by B. Schwartz and N. Schwartz. c. 380 pages; **$15.00.** 1965 and 1966 Fall Symposia

---

Other ECS Publications

The following books are available through The Electrochemical Society and various other publishers. Consult each listing for ordering instructions.

Vacuum Metallurgy, third printing, 1958, Edited by J. M. Blocher, Jr.; 216 pages; **$5.00,** less a 20% discount to ECS members only. Available from Electrochemical Society Headquarters, 30 East 42 St., New York, N. Y. 10017. A 1954 Fall Symposium.

Rhenium. Edited by B. W. Gonser. Published by Elsevier Publishing Co., 1962; 225 pages; **$12.50.** A 1960 Spring Symposium. ECS Members can obtain a 30% discount by sending their orders directly to Society Headquarters, 30 East 42 St., New York, N. Y. 10017. Remittance, made payable to American Elsevier Publishing Co., 52 Vanderbilt Ave., New York, N. Y. 10017 should accompany the order. Nonmembers must order direct from the publisher.

Iron Ore Reduction. Edited by R. R. Rogers. Published by Pergamon Press Ltd., New York and London, 1962; 359 pages; **$12.50** A 1960 Spring Symposium. Send all orders to The Macmillan Co., 60 Fifth Ave., New York, N. Y.

Stress Corrosion Cracking and Embrittlement. Edited by W. D. Robertson. Published 1956 by John Wiley & Sons Inc., New York. 202 pages **$2.50** (Hard cover book originally priced at **$7.50.**) Distributed by Dover Publications, Inc., 180 Varick St., New York. Send all orders to Dover Publications, Inc.

Electrode Processes. Published by The Electrochemical Society, 1966. c. 160 pages; **$5.00.** Edited from invited papers and full discussion presented by the Theoretical Electrochemistry Division, and supported by the United States Air Force Office of Scientific Research, at the Spring Meeting held May 1-5, 1966 in Cleveland, Ohio. Order direct from Society Headquarters.

Electrolytic Rectification and Conduction Mechanisms in Anodic Oxide Films. Published by The Electrochemical Society, 1967. Edited by P. F. Schmidt and D. M. Smyth. c. 230 pages; **$7.00.** Papers presented at the Dielectrics and Insulation Division Symposium on Anodic Oxides at the 131st Spring Meeting held in Dallas, Texas. Order direct from Society Headquarters.

Electrets and Related Electrostatic Charge Storage Phenomena. 1968. **$11.00.** A 1967 Fall Symposium. Order directly from Electrochemical Society Headquarters, 30 East 42 St., New York, N. Y. 10017.

Dielectrophoretic and Electrophoretic Deposition. 1968. **$9.00.** A 1967 Fall Symposium. Order directly from Electrochemical Society Headquarters, 30 East 42 St., New York, N. Y. 10017.

Electron and Ion Beam Science and Technology—Third International Conference. 1968. **$21.00.** A 1968 Spring Symposium. Order directly from Electrochemical Society Headquarters, 30 East 42 St., New York, N. Y. 10017.

JOURNAL OF THE ELECTROCHEMICAL SOCIETY

SOLID STATE SCIENCE

MAY 1968

Journal of The Electrochemical Society is the fundamental research journal serving the interdisciplinary interests of chemistry, physics, electronics, biology, medicine, and engineering *as they pertain to electrochemistry* and to electrochemical phenomena. Written for the research scientist in industry, government, the independent laboratory and the university, it publishes contributed Technical Papers, Technical Notes and Brief Communications describing current basic research of original character, and is edited in two sections: 1) ***Electrochemical Science*** including such areas as batteries, fuel cells, corrosion and corrosion mechanisms, electrothermics and metallurgy, electrodeposition, electroorganic reactions and phenomena, and allied work of theoretical electrochemical nature. 2) ***Solid State Science*** including such areas as dielectrics and insulation, electrothermics and metallurgy, semiconductors, luminescence and related solid state investigations.

Effect of Ionic Additives on the Heterocharge in Carnauba Wax Thermoelectrets

Preston V. Murphy

Thermo Electron Corporation, Waltham, Massachusetts

ABSTRACT

Thermopolarization and depolarization studies have been carried out on Carnauba wax electrets with controlled impurity content. While the initial impurity content was found to have little influence on the density of heterocharge, the addition of certain inorganic salts, in 10-50 ppm concentration, increased the heterocharge by factors of 2-5. The temperature dependence of electrical conductivity varied considerably with ion doping, but the heterocharge density in all samples showed the same thermal activation energy for polarization.

Carnauba wax, being a mixture of compounds, is not as ideal a choice as pure compounds. However, its dielectric properties have been studied for many years, and the electret effect has been studied more extensively in Carnauba wax than in any other material. Among the many studies on this material are the early papers of Eguchi (1) which described the main features of the electret effect including charge reversal, existence of a volume polarization, and long polarization lifetime for electrets in short-circuit. Adams (2), who proposed one of the early phenomenological theories, used Carnauba. Gross (3) likewise used the material while developing the currently accepted theories on heterocharge and homocharge (3). Wiseman *et al.* (4) carried out experiments which substantiated the two charge theory of Gross. Gubkin (5), at the same period, studied the effects of short circuiting on charge stability in Carnauba and other materials. In more recent studies, Gross (6) showed that the heterocharge is distributed uniformly throughout the volume of Carnauba electrets. Murphy *et al.* (7) have reported on Carnauba radio-electrets, and Perlman *et al.* (8) extended earlier phenomenological theories on the electret effect in Carnauba.

Carnauba Wax

Carnauba wax is a natural product obtained from the palm Copernicia Cerifera Martins (9). It consists primarily of long-chain esters (10). About two-thirds of these are n-alkanoic acid esters composed predominantly of the n-alcohols, C_{32}, C_{34}, and C_{27}, (listed in decreasing abundance) and the n-acids C_{24}, C_{28}, C_{26}, and C_{20}. The remaining third are esters of the ω-hydroxy n-alkanoic acids, C_{28}, C_{24}, and C_{26}.

The dielectric constant of Carnauba wax measured at 1 kHz increases from 2.5 at room temperature to a maximum of 3.0 at the melting point (79°-80°C). Dielectric measurements (11) have shown that the ω-hydroxy acid esters are oriented in a trans-trans configuration, and that rotation about the chain axis occurs in the solid state.

The highest grade of Carnauba, #1 yellow, has been used in this investigation as well as in earlier work including that of Gross (3). It is common practice to filter the wax to remove dark, particulate matter. However, there have been no reports on the nature of the contaminants, neither the portion removed by filtration nor the portion that inevitably remains in the filtrate. The inorganic contaminant might be expected to contribute significantly to the internal polarization of the wax by providing mobile ions or polarizable, colloidal aggregates.

Samples of Carnauba have been purified by simple filtration, by filtration with diatomaceous silica, and by zone refining. The resultant levels of inorganic impurities are shown in Table I. After purification, the wax was cast in the shape of small disks and machined to a size of 1.75 in. diameter by 0.079 in. thickness. Electrodes of Aquadag were applied to the flat surfaces.

Heterocharge Measurement

The heterocharge was measured by the thermodepolarization technique which was developed by Frei and Groetzinger (12) and used extensively by Gross (3). A rather sophisticated, automatic measuring system shown in Fig. 1 was employed.

Four disks of Carnauba wax were mounted in the chrome-plated copper block, C, (Fig. 1), and measurements of both conductivity and polarization were made. The upper and lower electrodes, of chrome-plated copper, were both mounted symmetrically on ⅛ in.-diameter sapphire spheres which maintained a leakage resistance in excess of 10^{14} ohm at 250°C. The symmetrical mounting provided for uniform heat transfer between the electrodes and the surrounding block, and minimized thermal gradients in the samples. The four equivalent sample mounting positions enabled measurements to be made under identical

Table I. Spectrographic analysis of inorganic impurities in Carnauba wax after purificaton by different techniques

Spectrographically determined element	Crude wax,[2] ppm	Filtered wax,[3] ppm	Zone refined top,[4] ppm	Zone refined bottom,[5] ppm	Activated silica,[6] ppm
Mg	7.0	0.4	0.5	0.7	0.2
Al	25	4.0	2.0	3.0	0.25
Na	15	2.0	3.0	4.0	0.2
Si	80	8.0	3.5	5.5	0.75
Ca	3.5	4.0	3.0	3.0	1.25
Ti	2.8	0.2	0.15	0.15	0.03
V	0.1	0.02	0.21	0.01	—
Cr	0.1	0.01	0.01	0.01	0.02
Mn	1.0	0.15	0.06	0.07	0.01
Fe	50	5.0	3.0	4.0	0.4
Ni	0.1	0.04	0.01	—	—
Cu	0.7	0.4	0.15	0.2	0.12
Sr	0.06	0.02	0.02	0.02	—
Sn	0.25	0.1	—	—	—
Ba	0.35	0.08	0.02	0.02	0.01
Pb	0.25	0.1	—	—	—
K	20	—	—	—	—
Zr	0.1	—	—	—	—
Ag	0.05	—	—	—	—
Li	0.75	—	—	—	—
Total impurities	212.1	24.5	15.4	20.7	3.2

[1] Reported by American Spectrographic Laboratories, San Francisco, California.
[2] No. 1 yellow grade Carnauba wax as received from the S. L. Abbot Company, San Francisco, California.
[3] Crude wax[2] filtered twice through Eaton Dikeman No. 617 filter paper at 100°C.
[4] Filtered wax[3] refined by zone melting; 50 passes at 3 in./hr; top portion (mp = 82.5°-83.5°C).
[5] Same as[4], bottom portion (mp = 84°-85°C).
[6] Filtered wax[3] mixed with "Celite" diatomaceous silica and refiltered through Whatman No. 3 paper (mp = 83° ± 0.5°C).

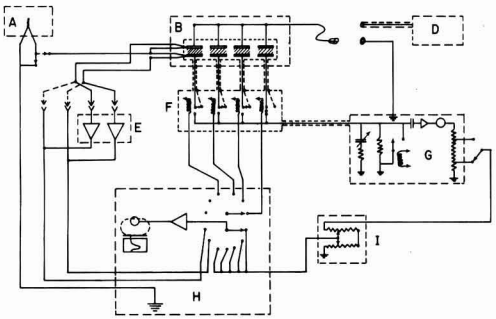

Fig. 1. Schematic diagram of polarization and measurement system. A, constant-temperature bath; B, Blue-M cam-programmed, proportionally controlled oven with sample holder; D, Baird-Atomic Model 319A, 0-5 kv power supply; E, microvolt thermocouple amplifier; F, coaxial relays; G, Cary Model 31 electrometer; H, Honeywell Electronik 10 mv 6-point recorder; I, F & M Model 50 Automatic Attenuator.

thermal conditions on samples with different composition.

The temperature could be controlled between the limits of 25° and 250°C by means of the cam-programmed, proportionally-controlled oven, B (Fig. 1). The temperature usually was increased at a rate of either 0.19° or 0.75°C/min during depolarization.

Samples were polarized and depolarized in the same apparatus. In the case of polarization, the upper electrodes were connected in parallel to the output of a Baird Atomic Model 319A, 0-5 kv power supply, D. The lower electrodes were grounded through a high resistance so that conductivity could be measured with the electrometer, G; guard rings were used on the lower electrodes. The standard polarizing voltage for samples 2 mm in thickness was 1 kv.

The temperature of the block and of one of the upper electrodes usually was measured by a thermocouple circuit during depolarization. (The positions indicated by the dotted lines at locations "a", "b", and "c" in Fig. 1 were used.) The reference temperature of 15°C was provided by a constant temperature bath, A. The thermocouple output without additional amplification drove the recorder, H.

The coaxial relay system, F, connected one sample at a time to the input of the Cary model 31 electrometer, G. Each time a relay was energized, the input was shorted for 2 sec by the Cary 3098150 automatic shorting switch in order to suppress transients. Rigid coaxial line with air insulation was used on all of the input circuits.

The usual measurement procedure involved increasing the temperature to some specific value above ambient and applying 1000v bias for a period of 1-65 hr. The value of conductivity measured at either 14 or 36 hr was recorded. The temperature was reduced to the ambient during a 16-hr period. The samples were shorted through the electrometer for 1 hr and decay currents recorded. Finally, the samples were reheated at a linear rate to a maximum of 76°C and depolarization currents recorded. Typical recorder traces showing the depolarization "glow curves" are shown in Fig. 2. The heterocharge was obtained from the time integral of the depolarization current.

Dependence of Heterocharge on Initial Impurity Content

The heterocharge was determined for Carnauba wax purified by simple filtration, by filtration with activated silica, and by zone refining. Results are shown in Table II.

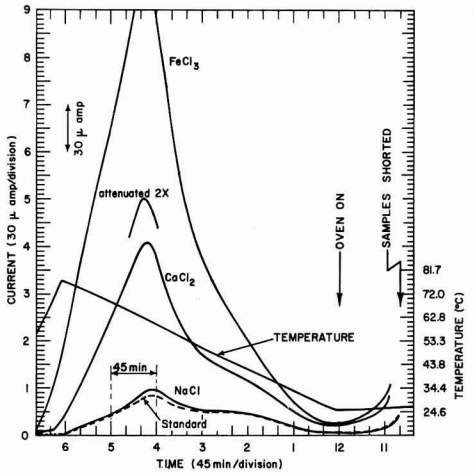

Fig. 2. Typical recorder trace showing the temperature of one electrode and the depolarization current for four samples vs. time. The samples were polarized at 50°C for 5 hr, cooled to 25°C, and shorted as indicated. Original curves are color coded.

It will be noted that although the impurity content was reduced by nearly an order of magnitude, there was no significant change in the heterocharge density.

Modification of Heterocharge by Added Impurities

A different lot of wax was purified with activated silica and reserved for studies on specific added impurities. Solutions of inorganic halides in methanol were sprayed into molten wax to give additive concentrations of about 50 ppm. Sodium and potassium salts formed precipitates in the wax and were removed by the filtration step. Electrets were prepared by polarization for hours at 5 kv/cm and 72°C.

The measured values of heterocharge density are shown in Table III. It will be noted that the heterocharge was doubled by Ca^{+2} and Ce^{+3} additive and was increased fivefold by Fe^{+2} and Fe^{+3} additive. NaCl produced no effect while NaBr increased the heterocharge slightly although analysis for Na showed only 1 ppm.

Dependence of Heterocharge on Polarization Temperature

The effect of the polarization temperature on the ultimate polarization charge was determined for a standard, purified sample of wax and for a selected

Table II. Heterocharge density in purified Carnauba wax

	Charge density, $m\mu$ coul-cm^{-2}	Total impurities, ppm
Filtered—E. D. 617 paper	60-70	24.5
Filtered—activated silica	60	3.2
Zone refined—top	65	15.4
Zone refined—bottom	70	20.7

Table III. Polarization density for Carnauba wax doped with inorganic ions

Compound added	Cation content, ppm	Polarization charge density, $m\mu$ coul-cm^{-2}
None	—	140
NaCl	1	130
NaBr	1	160
$CaCl_2$	50	300
$CeCl_3$	50 (est.)	300 (est. from 50°C data)
$FeCl_2$	50	700
$FeCl_3$	65	700

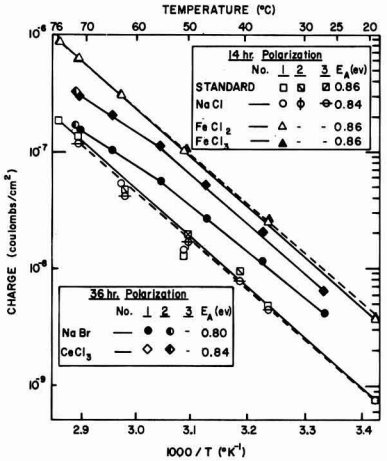

Fig. 3. Specific depolarization charge *vs.* reciprocal polarization temperatures for Carnauba samples doped with inorganic salts. The symbols in column 1 represent values obtained for 2-in. diameter disks banded with 3/32 in. guard rings; in column 2, the values were obtained for 1¾ in. disks; in column 3, the values were interpolated from the data of Fig. 7.

number of doped samples. It was shown by Van Calker and Frohlich (13) that a plot of polarization charge versus reciprocal polarization temperature gave a straight line for mixtures of Carnauba wax and resin. Plots of heterocharge density *vs.* reciprocal temperature are shown in Fig. 3 for doped samples. It will be noted that the lines are all nearly parallel (with the exception of the NaBr sample and the $CeCl_3$ sample above 60°C). Activation energies for polarization were calculated to be 0.86 ev for undoped and Fe-doped samples, and 0.84 ev for NaCl- and $CeCl_3$-doped samples. If the heterocharge were caused by space charge due to the migration of the ionic contaminants, one would expect a wider variation in energies of activation.

In Fig. 4, a similar plot is shown for wax samples treated with $ZnCl_2$-docosanol, and with $ZnCl_2$-docosanol-$FeCl_3$. The docosanol treatment was intended to esterify residual acids and thus increase the probability of precipitating colloidal iron oxide. However, the apparent result was an increase in polarizability in the 40°-60°C temperature region, presumably due to excess free alcohol.

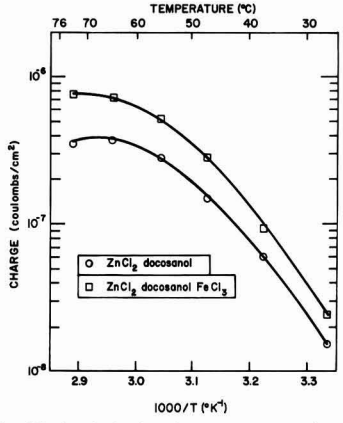

Fig. 4. Specific depolarization charge *vs.* reciprocal temperature for Carnauba samples doped with $ZnCl_2$-docosanol and $ZnCl_2$-docosanol-$FeCl_3$.

Decay Current

At the end of each polarization, the samples were held in short-circuit at 25.3°C for a 1-hr period. During this time the decay current was read on the electrometer and recorded in the usual manner. The time variation of the decay current is shown in Fig. 5. The integral of the decay current taken over the 1-hr period is plotted against the reciprocal of the polarization temperature in Fig. 6. The decay current and its time integral reached maximum values at about 40°C and decreased at higher temperatures. This behavior is rather unusual in view of the steadily increasing value of heterocharge. The decrease in decay current might result either from an increasing surface homocharge or from an increase in the stability of heterocharge.

Polarization Time

It is usually assumed that the polarization charge reaches a saturation value at elevated temperatures

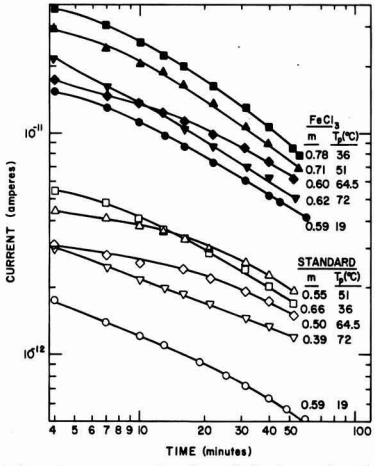

Fig. 5. Decay current *vs.* time for polarized samples of standard and iron-doped wax at 25°C. Polarizing bias was removed at zero time. Tp is the polarizing temperature and m the slope of the final portion of the curve.

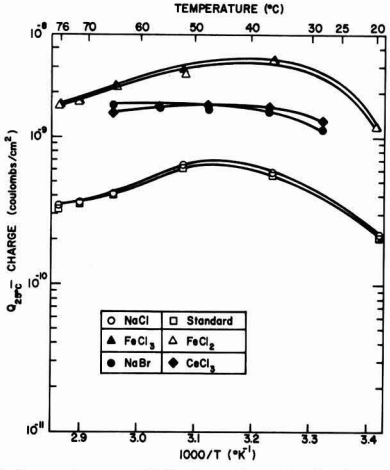

Fig. 6. Decay charge at 25°C, $Q_{25°C}$ (given by the decay current at 25°C integrated for 60 min) *vs.* reciprocal polarizing temperature.

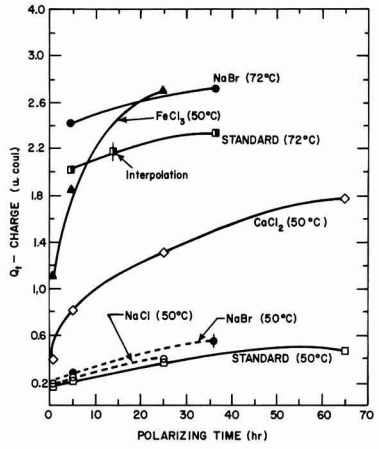

Fig. 7. Depolarization charge, Q_t vs. polarizing time for samples polarized at 50° and 72°C.

after voltage has been maintained for a few hours. In order to verify this assumption and to explore the lower-temperature region, several samples were polarized repeatedly at 50° and at 72°C for different periods of time. The results (Fig. 7) indicate that the polarizing voltage must be maintained for a very long time at 50°C or below in order to attain saturation. However, a temperature-dependent saturation limit appears to exist, and this limit is approached exponentially in time.

Sample Compaction

Carnauba wax is subject to considerable shrinkage when cooled from the melt. It has been postulated that the presence of microscopic voids might lead to interfacial polarization as a result of localized surface conduction. Therefore, we have attempted to alter the degree of compaction by solidifying samples under conditions of both high pressure and vacuum. The heterocharge density for some of these samples is shown in Table IV. It will be noted from the table that the effect of compaction is small; we believe the differences in charge noted in Table IV are within the limits of error for these measurements. The data on vacuum-formed samples are not included because a different batch of wax was involved; indirect evidence, however, has shown no appreciable change in polarization as a result of vacuum-forming.

Depolarization Rate

It is well known that the maximum value of depolarization current increases with the rate of heating; however, it has not been established that the time integral of depolarization current is independent of heating rate. Therefore, depolarization measurements were carried out on several identical samples at two different heating rates. The results (shown in Table V) indicate that the measured charge is independent of heating rate within the limits of 0.19° and 0.75°C/min.

Sample Conductivity

The dependence of electric conductivity on temperature was determined for purified and impurity-doped

Table IV. Polarization density of compacted Carnauba wax

Forming pressure, psi	Charge density, μcoul-cm^{-2}	Sample thickness Before measurement, mm	Sample thickness After measurement, mm
None	0.117	1.83	1.84
10,000	0.093	1.88	1.94
20,000	0.100	1.83	1.89

Table V. Effect of depolarization rate of measured charge

Sample	Measured charge Heating rate 0.19°C-min^{-1}, μcoul	Measured charge Heating rate 0.75°C-min^{-1}, μcoul
Standard	0.20	0.20
NaCl (doped)	0.21	0.20
$CaCl_2$ (doped)	0.82	0.82
$FeCl_3$ (doped)	1.82	1.92

samples of wax. Guard rings were used to prevent surface leakage. The conductivity as a function of reciprocal temperature is shown in Fig. 8 and 9. Values of conductivity were taken after application of bias for periods of 11-36 hr as noted in the figures. The conductivity increased with temperature much more rapidly than did polarization charge (Fig. 3 and 4). The data of Fig. 8 and 9 fail to give straight lines from which activation energies for conduction can be calculated.

Discussion

The studies involving purified samples of wax demonstrated that the original inorganic contaminants have little effect on the internal polarization; the in-

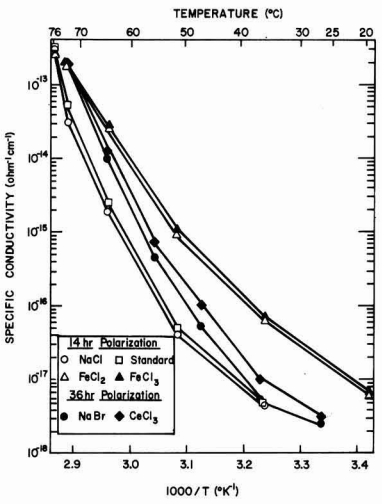

Fig. 8. Specific conductivity vs. reciprocal temperature for standard and doped Carnauba samples.

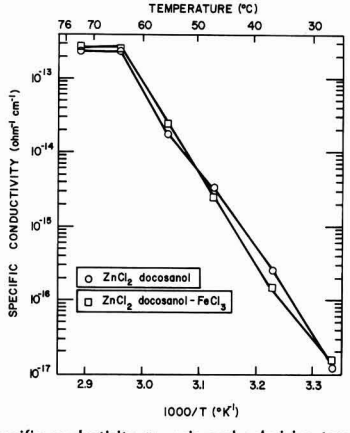

Fig. 9. Specific conductivity vs. reciprocal polarizing temperature for $ZnCl_2$-docosanol and $ZnCl_2$-docosanol-$FeCl_3$ doped Carnauba samples.

ternal polarization or, heterocharge, is a property of the wax itself.

The heterocharge was changed substantially by inorganic additives, but the mechanism of heterocharge formation remains somewhat elusive. The data suggest that free ions are not contributing to the heterocharge since there was no correlation of charge density with valency. For example, Fe^{+2} and Fe^{+3} behave identically and cause a larger increase in polarization than do Ca^{+2} and Ce^{+3}. Also, the conductivities of all samples converge to the same value at high temperature, suggesting a common conduction mechanism characteristic of the wax itself.

The quantity of polarization charge appears to increase exponentially with polarization temperature. It is significant that inorganic additives cause the polarization curves to be displaced to higher values of charge but do not affect the slopes. On the other hand the slopes of the conductivity-temperature curves are much steeper than the slope of the polarization-temperature curves. Also, there is no convergence of the polarization curves at high temperature as there is for the conductivity curves.

In view of the observed exponential dependence of heterocharge density on polarizing temperature, the isothermal decay curves and thermodepolarization "glow" curves were examined for similar exponential dependences. The applicability of luminescence and conductivity glow curve analysis to thermodepolarization curves has been pointed out by the writer (7) and expanded by Bucci *et al.* (14). If depolarization is characterized by a single energy of activation the initial increase of current with temperature should follow a simple exponential law. Also the isothermal, short-circuit, decay current should decrease exponentially with time. The current variations found for Carnauba wax were not exponential in either of these cases. Therefore, although the energy of activation for the thermopolarization process appears to be single valued, no such discrete energy level is associated with depolarization. While a unique physical mechanism for the heterocharge cannot be established as yet, the data are compatible with a distortable double-well model of the type proposed by Fuchs and Von Hipple (15) in connection with dielectric absorption.

Manuscript received Sept. 5, 1967; revised manuscript received Feb. 6, 1968. This paper was presented at the Electrets Symposuim at the Chicago Meeting, Oct. 15-19, as Abstract 128.

Any discussion of this paper will appear in a Discussion Section to be published in the December 1968 JOURNAL.

REFERENCES

1. M. Eguchi, *Phil. Mag.*, **49**, 178 (1925).
2. E. Adams, *J. Franklin Inst.*, **204**, 469 (1927).
3. B. Gross and L. Denard, *Phys. Rev.*, **67**, 253 (1945); B. Gross, *An. Acad. Bras. Cien.*, **20**, 247 (1948); B. Gross, *J. Chem. Phys.*, **17**, 866 (1949).
4. C. Wiseman and G. Feaster, *J. Chem. Phys.*, **26**, 521 (1957).
5. A. Gubkin, *Zhur. Tekh. Fiz.*, **27**, 1954 (1957).
6. B. Gross and R. deMoraes, *J. Chem. Phys.*, **37**, 710 (1962).
7. P. Murphy, S. Costa-Ribeiro, F. Milanez, and R. deMoraes, *J. Chem. Phys.*, **38**, 2400 (1963).
8. M. Perlman and J. L. Meunier, *J. Appl. Phys.*, **36**, 420 (1965).
9. A. Warth, "The Chemistry and Technology of Waxes," Reinhold Publishing Co., New York (1960).
10. K. Murray and R. Schoenfeld, *Australian J. Chem.*, **8**, 424 (1955).
11. T. Callinan and A. Parks, Private communication.
12. H. Frei and G. Groetzinger, *Physits. Z.*, **37**, 720 (1936).
13. J. Van Calker and W. Frohlich, *Ann. der Physik*, **7**, 216 (1959).
14. C. Bucci, R. Fieschi, and G. Guidi, *Phys. Rev.*, **148**, 816 (1966).
15. R. Fuchs and A. von Hippel, *J. Chem. Phys.*, **34**, 2165 (1961).

Ionic Membrane Electrets

Richard A. Wallace*

Polytechnic Institute of Brooklyn, Brooklyn, New York

and Zeljko Urban

University of California, Berkeley, Berkeley, California

ABSTRACT

Heterocharges in the polystyrenesulfonate membrane in its hydrogen, sodium, and silver forms have been measured by means of thermal depolarization. We found that the membrane in sodium form stored the largest amount of electric charges and made for the best ionic membrane electret. Membrane electrets were formed at 60°C in electrical fields of 1.25, 2.5, and 5 kv/cm. In this range the total accumulated charge within the membrane does not depend on the strength of the forming field.

The high dielectric constant of polystyrenesulfonate membranes (1) suggests the possibility that these ionic membranes might be capable of storing large amounts of electric charge. To what extent these electrostatic or internal electric charges can be preserved has not yet been determined. Provided that the charges remain orientated within the membrane after electroformation, then ionic membrane electrets could be prepared. Experiments are now being performed at the Polytechnic to determine the role of the electret effect in water desalination by electrodialysis and in nonthrombogenic bipolymer materials.

In this paper results are presented of measurements of electric charges, formed on the application of d-c fields ranging from 1.25 to 5.0 kv/cm, in sulfonated polymeric membranes. The method of thermal depolarization was used to measure the stored heterocharges released by the membrane electret (2, 3).

Experimental

Sulfonated polymer membranes (AMF, C-60) consisted of approximately 25% by weight of polystyrenesulfonic acid (PSA) supported in a matrix of poly-

* Electrochemical Society Active Member.
This research was sponsored by the Office of Saline Water, United States Department of the Interior.

ethylene. Fixed negative charges within the membrane are carried by sulfonic (SO_3^-) sites along the PSA molecules. These charges are each balanced by positive counter ions, such as H or Na. Each membrane was purified by five batchwise washings with deionized water. Circular strips of membrane, 1.5 in. in diameter and 0.01 in. thick, were cut, silver-coated on both faces, and then vacuum-dried for 24 hr.

Each membrane was clamped between stainless steel electrodes and a d-c electric field applied to the membrane sample, maintained at 60°C. After an arbitrary cut-off time of 4 hr, membrane sample was allowed to cool down to 28°C in the presence of the electroforming field. Membrane charging current and temperature were recorded during electroformation.

Immediately after the forming field was removed, the charged membrane was short-circuited and its discharge current measured at 28°C. This measurement was continued until the current gradually approached zero. After a 24-hr period, the short-circuited membrane was reheated up to 60°C and its discharge current measured again. The variations of this current with time were then recorded.

Results and Discussion

Electroforming of a typical membrane electret by means of a 1.25 kv/cm electric field is illustrated in Fig. 1. In the beginning, the charging current decays as it normally would at room temperature. Later, the trend reverses and the current starts to increase in response to rising temperature. It experiences a peak approximately at the same time as the temperature reaches its maximum value. After that, the current gradually decays, forming a small knee close to the point where the cooling starts. After 350 min, the applied electric field is turned off, the specimen shorted, and its discharge current measured.

Figure 2 shows the discharge current as a function of time at 28°C for various forming field strengths. From this data the stored charge in the cation-exchange membrane is calculated, using the relationship

$$Q = \int_t^\infty J\,(t)\;dt \qquad [1]$$

where Q = charge, coulombs, $J(t)$ = discharge current, amp, and t = time, sec.

According to classical circuit theory, the discharge current of a short-circuited capacitor follows the equation

$$J(t) = I_0\, e^{-t/RC} \qquad [2]$$

where I_0 = discharge current at $t = 0$ and RC = time constant of capacitor (product of resistance and capacitance).

This current, which decays very fast, is present in the case of electret discharge. However, an additional anomalous current appears, slowly decreasing with time. To allow for decay of the classical discharge

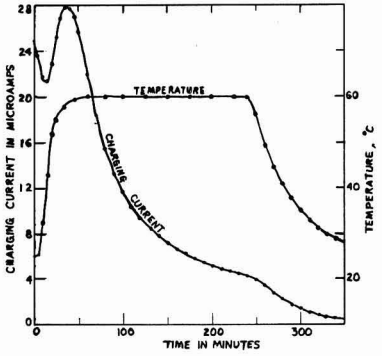

Fig. 1. Electroformation of a PSA membrane electret at 1.25 kv/cm.

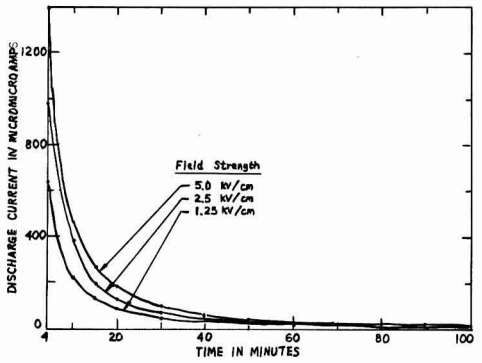

Fig. 2. First discharge at 28°C for PSA membrane electrets formed at various electrical fields.

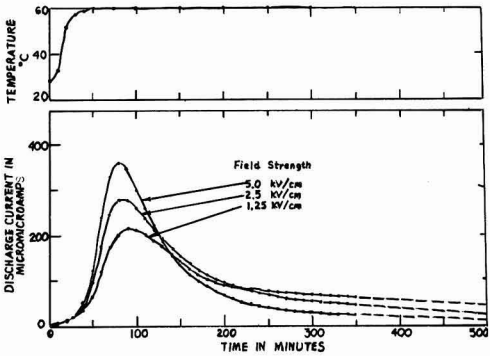

Fig. 3. Second discharge at 60°C of PSA membrane electrets formed at various electrical fields.

current, a 4-min period of discharge time was allowed to pass before the data were recorded. The charges released during the 96-min period, corresponding to the area under the curve, are given in the second column of Table I. Higher forming field yields the higher quantity of released charge during the first discharge period. Similar results were also reported on Carnauba wax electrets (4).

The second discharge was started 24 hr later. Temperature was raised to 60°C, and the discharge current was measured as shown in Fig. 3. The measurements were conducted for 350 min. For the purpose of charge calculations, all the curves are extrapolated to the point where the discharge current reaches zero. The values of released charges were obtained by graphical integration of the curves in Fig. 3, and are listed in the third column of Table I. These charges are up to 9 times larger than the charges released during the first discharge at room temperature.

The total charge is obtained by addition of released charges listed in the second and third columns of Table I and is tabulated in the fourth column of Table I. It can be seen that the total charge essentially does

Table I. Electret properties of the sulfonate membrane in sodium form

Forming field strength, kv/cm	Charge (coulombs × 10^{-6}) First discharge at 28°C	Second discharge at 60°C	Total charge	Position of discharge peak, min	Internal field, v/cm × 10^6
1.25	0.32	2.98	3.30	90	3.27
2.5	0.54	2.86	3.40	85	3.37
5.0	0.70	2.54	3.24	80	3.21

not vary with the change of forming field strength. The lack of dependence of total charge storage on the strength of the forming field indicates that the membrane probably polarized at the lowest forming field used and reached its saturation level at 1.25 kv/cm. However, the position of the peak of current-time curve seems to be dependent on the strength of forming electric field. This dependence, in minutes, is given in the fifth column of Table I.

Reheating shows dramatically how large quantities of residual charge have been left in the membrane after the first discharge. Apparently, charges were locked in and could not be liberated at room temperature during one day of discharge time. As soon as the temperature was raised, they were released. Therefore, the current surge shown in Fig. 3 indicates the liberation of frozen-in charges during the reheating period.

The corresponding internal electric fields produced by these charges have been calculated using the expression

$$E = 1.13 \times 10^{13} \frac{Q}{A} \qquad [3]$$

where E = internal electric field, v/cm, Q = charge, coulombs, and A = area, cm^2.

The calculated values of internal electric fields are given in the last column of Table I. Charge Q in Eq. [3] is the total charge listed in the fourth column of Table I.

In Fig. 4 is shown the 350-min reheating period at 53°C for membrane electrets in three ionic forms: Na, Ag, and H. Charging time was 1.5 hr at a forming field strength 1.25 kv/cm. The membrane electret in sodium form stored the largest amount of charge.

We have recently demonstrated excellent blood compatibility with PSA-incorporated elastomeric and thermoplastic membranes. PSA was also grafted to surfaces of common elastomers; these polysulfonated materials have high electrical resistance (> 10^7 ohm-cm) and make ionic electret materials in solution. Their bulk equilibrium water absorption contents are low and, as a result, are relatively impermeable to

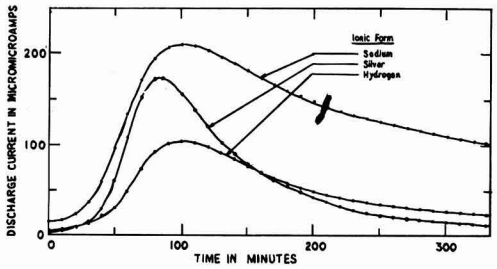

Fig. 4. Discharge at 53°C of PSA membrane electrets in three ionic states.

salt and water in 0.1M NaCl, and in human whole blood.

We deduce that the effects of the matrix on ionic electret phenomena are indirect. The plastic matrix separates the adjacent PSA molecules, reduces the effective dielectric constant and imparts mechanical strength and support to the material. It is suggested that the electret effect and good blood compatibility results are primarily related to the electrochemical properties of the PSA molecule. More detailed data and techniques will be reported in a subsequent article.

Manuscript received Aug. 17, 1967; revised manuscript received Feb. 23, 1968. This paper was presented at the Electrets Symposium at the Chicago Meeting, Oct. 15-19, 1967, as Abstract 129.

Any discussion of this paper will appear in a Discussion Section to be published in the December 1968 JOURNAL.

REFERENCES

1. Z. Urban and R. A. Wallace, *This Journal*, **115**, 276 (1968).
2. S. Wikström, *Arkiv för Fysik*, **7**, 213 (1954).
3. A. I. Froiman and V. M. Fridkin, *Kristallograf.*, **1**, 342 (1956).
4. R. Gerson and J. H. Rohrbaugh, *J. Chem. Phys.*, **23**, 2381 (1955).

On the Origin of an Exponential Vacancy Distribution in Annealed Ta/Ta_2O_5-Structures

K. Lehovec*

Research & Development Laboratories, Sprague Electric Company, North Adams, Massachusetts

ABSTRACT

An attempt is described to explain the exponential vacancy profile in annealed Ta/Ta_2O_5 structures postulated by Smyth *et al.* by a Boltzmann distribution in a constant electric field arising from the emf of the reaction between tantalum and oxygen during the anneal. Implications of this model for the oxygen uptake during the anneal are discussed and compared to experimental data. While the model is able to account for the origin and the attenuation constant of the observed exponential vacancy profile, it involves still unproven assumptions on space charge compensation and electron conduction mechanism.

Smyth and co-workers (1-4) have analyzed capacitance and loss angle measurements of annealed Ta/Ta_2O_5-structures in terms of an exponential conductivity profile at zero d-c bias voltage. The bias voltage dependence of the capacitance was interpreted by means of an exponential oxygen vacancy profile. However, the origin of such a profile has not been clarified.

* Electrochemical Society Active Member.

Defining an attenuation constant K_σ of the conductivity

$$K_\sigma = -\partial \ln \sigma / \partial (x/d) \qquad [1]$$

where x is the distance of a point in the oxide of conductivity σ from the metal, and d is the oxide thickness one obtains (1-4) K_σ-values of the order 50. We noted sometime ago (5) that an exponential conductivity profile could arise from a Boltzmann distribution of

carriers of charge zq in a constant field F, and that the attenuation constant of this Boltzmann factor, $zqFd/kT$, has indeed the same order of magnitude as $K_\sigma \simeq 50$, if $Fd = E$ is taken as the emf of the chemical reaction between tantalum and oxygen. More recent results of Smyth and Shirn (4) suggest that the ionization energy of the oxygen vacancies (which act as donors of electrons) depends on their concentration, and that the attenuation constant of the oxygen vacancy distribution

$$K_s = -\partial \ln N_s/\partial[(x/d)] \qquad [2]$$

is only about 30. The subscript s has been chosen since the vacancy concentration N_s has been obtained (4) by a Schottky plot (6), *i.e.*, from the bias voltage dependence of capacitance at a constant frequency.

The measurements of Smyth and co-workers (1-4) were made on tantalum anodized at various formation voltages and then annealed at elevated temperatures in the range 300°-400°C for periods ranging from 10 min to several hours. During the anneal, no oxide growth occurred. However, there was a weight increase attributed to oxygen uptake of the tantalum metal (1). Anneal time in the investigated range did not have much influence on the room temperature impedance indicating that a quasistationary state was reached within minutes. Most of the measurements were made on anodic films of the thickness range d = 1500-3000Å.

The present paper explores in detail the concept of an exponential vacancy distribution arising from a Boltzmann distribution in a constant field. Its implication on the oxygen uptake during the anneal investigated by Pawel and Campbell (7) and recently by Steidel (8) will also be discussed.

It will be shown that justification of the exponential vacancy profile by a Boltzmann distribution, although enticing at first sight, nevertheless requires a number of ad hoc assumptions, and thus raises problems of its own. However, publication of the present paper, while not leading to a fully convincing model, can be justified by the extensive pertinent experimental work and by the need to investigate critically all consequences of an explanation which appears plausible at first sight.

Origin of an Exponential Distribution of Oxygen Vacancies

During the anneal, oxygen is dissolved in the tantalum metal. This creates oxygen vacancies in the adjacent tantalum oxide. These vacancies move toward the outer oxide surface and generate an oxygen flow from the ambient into the tantalum metal. It is well known that tantalum can dissolve large quantities of oxygen (1, 7, 8). Changes of tantalum resistivity and of its temperature coefficient by oxygen uptake have been demonstrated (8). During anneal an emf of a few tenths of a volt (8, 9) appears across the oxide, the tantalum substrate becoming negative. The fact that the electric properties of annealed Ta/Ta_2O_5-samples, after cooling to room temperature, do not return to the preannealed state indicates a lack of oxygen uptake of the reduced tantalum oxide from the ambient atmosphere at room temperature.

An exponential vacancy distribution would arise under quasiequilibrium conditions from the Boltzmann factor at a constant field, F

$$[V_0^z] = [V_0^z]_{x=0} \exp(-zqFx/kT) \qquad [3]$$

where zq is the charge of the mobile vacancies of concentration $[V_0^z]$.[1] Comparison of [3] with the empirical relation [2] shows that

$$K_S = zqFd/kT \qquad [4]$$

By inserting the values $K_S = 30$ and $kT/q \simeq 60$ mv at the anneal temperature, we obtain $zFd \simeq 1.8$v. Since the oxide thickness d is of the order of 2.10^{-5} cm for most of the samples investigated by Smyth *et al.* (1-4), we are here concerned with an electric field F of the order of 10^5 v/cm. A space independent field implies absence of a significant space charge density, *i.e.*,

$$\int \rho \partial x << \epsilon\epsilon_0 F \qquad [5]$$

the integral extending over the region of constant field. For $F \simeq 10^5$ v/cm, the right side is about 2.10^{-7} C/cm^2 or 10^{12} electron charges per cm^2. This is much smaller than the number of charges derived from the Schottky profile [2]

$$\int_o^d N_s \delta x = N_s^o \, d/K_S \simeq 2 \times 10^{14} \text{ cm}^{-2} \qquad [6]$$

where $N_S^o = 3.10^{20}$ cm^{-3}, $K_S = 30$, and $d \simeq 2 \times 10^{-5}$ cm have been used (4). This leaves us with two possibilities:

(*a*) The concentration of charged vacancies at the anneal temperature is much smaller than N_s, derived from the Schottky profile, perhaps due to partial ionization, or else

(*b*) There exists a mechanism for compensation of the charge of the mobile vacancies at the anneal temperature. The compensating charge must be immobile or else it would assume a Boltzmann distribution of the opposite slope of that of the mobile oxygen vacancies. Such a charge compensation may indeed arise by means of oxygen vacancies occurring in different charged states as will be pointed out in the Appendix.

Implications for the Oxygen Uptake during Anneal

During a quasistationary uptake of oxygen ions *via* a vacancy mechanism, an electron current of equal magnitude flowing from the tantalum outward is necessary for charge compensation. This equality is assured by the establishment of an electric potential of suitable polarity and magnitude. The emf (= difference of the electrochemical potential of electrons at the two boundaries of the oxide divided by charge q) becomes identical to the electrostatic potential if the electron concentration is constant with position, the chemical potential (or "diffusion potential") being then zero. This is the situation we visualize in the Ta_2O_5 during the anneal (or, at least, in the region from which most contributions to the emf arise), for reasons to become clear later. The polarity of the observed emf is such as to generate a field in the oxide driving electrons from the tantalum to the outer oxide, indicating that the electric current is the rate-determining step, at least in a portion of the oxide film. This is in agreement with our previous postulation of a Boltzmann-distribution of oxygen vacancies, which implies quasithermal equilibrium, *i.e.*, the vacancy transport rate is not rate determining. We conclude from the constancy of the electron current i_e through the oxide and from the constancy of the electric field, postulated to explain the exponential vacancy profile, that the electron concentration

$$n = i_e/q\mu_e F \qquad [7]$$

is also a constant, when μ_e is the electron mobility. This justifies the relation

$$F = E/l \qquad [8]$$

between the electric field, the emf E and the width l of the region from which the emf arises and in which the conditions discussed above are realized.

In distinguishing between the oxide thickness d and the region l across which the emf arises, we have taken into account the fact that the exponential vacancy profile has not been established experimentally throughout the entire oxide, and that a Boltzmann distribution of vacancy need not exist across the entire oxide.

[1] A different notation has been used for the vacancy concentration in Eq. [3] at the anneal temperature and the concentration of the Schottky profile, since both are not necessarily identical as will be discussed later.

Within the region of width l, we expect the following inequality between electric (σ_e) and ionic (σ_I) conductivities

$$\sigma_e = nq\mu_e << \sigma_I = [V_0^z] \cdot zq\mu_I \qquad [9]$$

expressing the fact that the electron transport is rate determining. Outside of this region we may well have $\sigma_e > \sigma_I$, and l may then be defined as the position at which

$$\sigma_e = \sigma_I]_{\text{ at } x=l} \qquad [10]$$

Since $\mu_e << \mu_I$, one has there $n << [V_0^z]$. It follows from the Boltzmann distribution [3] that

$$E = kT/zq \ \ln[V_0^z]_{x=0}/[V_0^z]_{x=l} = kT/zq \ \ln \sigma_I(x=0)/\sigma_e(x=l) \qquad [11]$$

where [10] has been used and the ionic mobility μ_I was assumed to be independent of the vacancy concentration.

Comparison with Experimental Data

The importance of electron conduction for the oxygen transfer rate is in agreement with observations by Pawel and Campbell (7) on oxygen uptake of tantalum protected by an anodic oxide film at elevated temperatures. They found that "anodic films exhibiting low leakage currents were more efficient in protecting the metal from oxidation. Local breakdown at a point of weakness may, instead of being self healing, lead to an accelerated deterioration of the remainder of the film." The latter observation is in accordance with our model if lateral electron conduction along the outer oxide surface may occur.

Additional evidence for the electron transfer being the rate-determining step for oxygen flow through part of the oxide is the electromotive force at the anneal temperature (7, 8, 9).

The emf corresponding to the free energy of the reaction $2Ta + 5/2\ O_2 \rightarrow Ta_2O_5$ at 400°C is 1.83v for oxygen-free tantalum and an ambient of 0.2 atm oxygen pressure. The fact that the observed emf (8, 9) is only a fraction of this value can be attributed partially to the outer portion of the oxide film having dominant electronic conduction and partially to oxygen dissolved in tantalum. The end product of the reaction between tantalum and the oxygen ambient at moderate anneal conditions is not tantalum oxide, but oxygen dissolved in tantalum.

Comparing the value $zFd = 1.8$v obtained by [4] from the slope K_S of the observed (4) Schottky profile at room temperature, with the observed (8, 9) emf during the anneal $E = F \cdot l \simeq 0.3$v, we conclude that for $z = 1$: $l/d \simeq 1/6$, and $F \simeq 10^5$ v/cm, while for $z = 2$: $l/d \simeq 1/3$ and $F \simeq 5 \times 10^4$ v/cm.

The Boltzmann factor for $E = 0.3$v and $kT/q = 0.06$v ($T \simeq 400$°C) is $e^{-qE/kT} = 6.7 \times 10^{-3}$ in case that $z = 1$ and $e^{-2qE/kT} = 4.6 \times 10^{-5}$ in case that $z = 2$. Using $N_s^o = 3.10^{20}$ cm^{-3}, we arrive at vacancy concentrations at $x = l$ of 2.10^{18} cm^{-3} and 1.4×10^{16} cm^{-3} for the cases $z = 1$ and $z = 2$, respectively. Since experimental Schottky profiles have been measured which extend to 10^{17} cm^{-3}, we conclude that $z = 2$.

The magnitude of σ_e in that part of the oxide where the Boltzmann distribution of vacancies exists can be estimated by extrapolation to 400°C of data from Fig. 5 or ref. (7). For the film of 1000Å thickness, an oxygen flow of 10^{-11} g-moles/cm^2 min is obtained, which corresponds to 1.2×10^{-7} amp/cm^2 (assuming that $z = 2$). Using a field of 5×10^4 v/cm for the region where [7] is valid, one arrives at $\sigma_e \simeq 2.4 \times 10^{-12}$ ohm^{-1} cm^{-1}.

At room temperature Smyth and Shirn (4) obtain $\mu_e \simeq 1$ cm^2/v sec. Using this value as a rough estimate of the mobility at the anneal temperature, one has $n \simeq 1.5 \times 10^7$ cm^{-3}.

By means of [11], we are able to estimate the vacancy mobility

$$\mu_I \simeq [\sigma_e]_{x=l}/zq[V_0^z]_{x=l} \qquad [12]$$

Using the previously estimated value $[V_0^z]_{x=l} \simeq 1.4 \times 10^{16}$ cm^{-3}, one obtains $\mu_I \simeq 5 \times 10^{-10}$ cm^2/v sec for $z = 2$, which is not unreasonable.

For a nondegenerate electronic semiconductor, the band model provides

$$n = N_c \ \exp[-(\epsilon_c - \epsilon_F)/kT] \qquad [13]$$

where N_c is the density of states (partition sum) for the conduction band and $\epsilon_c - \epsilon_F$ is the energy difference between the bottom of the conduction band ϵ_c and the Fermi level (electrochemical potential per electron) ϵ_F. Provided that ϵ_F does not depend on temperature and neglecting the small temperature dependence of N_c *vs.* that of the exponential term, we obtain an activation energy of $\epsilon_c - \epsilon_F$.

Pawel and Campbell (7) find an activation energy for oxygen uptake of 1.96 ev, while Steidel (8) observed 1.5-1.6 ev. Inserting $n = 1.5 \times 10^7$ cm^{-3}, $\epsilon_c - \epsilon_F = 2.0$ and 1.5 ev, respectively, and $kT/q = 0.06$v into [9], one obtains $N_c = 3.10^{20}$ cm^{-3} and 10^{18} cm^{-3}, respectively; neither value is objectionable.

The magnitude of the ionic conductivity in the outer oxide film can be estimated if we assume that it is of the same order as that of unannealed anodic oxide films. The anodic oxidation rate depends on field as (10-13)

$$i_I = A'(e^{B'F} - e^{-B'F}) \qquad [14]$$

For $B'F << 1$, one obtains

$$\sigma_I = i_I/F = 2\ A'B' \qquad [15]$$

Extrapolating the room temperature values (10-13) of $A' \simeq 5.10^{-19}$ to 6.10^{-21} amp/cm^2 and $B' \simeq 5.10^{-6}$ cm/v to the anneal temperature of 400°C by using the activation energy $U_{A'} = 1.2$ ev (12) for A' and the inverse absolute temperature dependence (12) for B', we obtain $\sigma_I = 10^{-15}$ to 10^{-17} ohm^{-1} cm^{-1}. These values are indeed small compared to $\sigma_e = 2.4 \times 10^{-12}$ ohm^{-1} cm^{-1}. Thus, it is reasonable to expect that oxygen flow in the outer film region, which is in equilibrium with the oxygen ambient, is limited by ionic flow while in the reduced inner film region it is limited by electron transport.

It should be noted that the electron current $i_e = nqF$ as the rate-determining step for oxygen flow could lead to a parabolic growth since $F = E/l$, provided that E and l do not vary with the oxide thickness. Thus, the anneal mechanism here described is not necessarily in disagreement with parabolic growth, which is usually taken as an indication (7) for a growth rate limited by ion diffusion.

Difficulties Encountered by the Present Model

A complete clarification of the anneal mechanism requires knowledge of the oxygen flow mechanism in the outer oxide film region, *i.e.*, $l < x < d$, and of the nature and location of the positive charges which generate the constant electric field in the oxide region $0 < x < l$.

In the case of a simple diffusion current of vacancies through the outer oxide region

$$i_I \simeq \frac{kT}{zq}\mu_I zq[V_0^z]_{x=l}/(d-l) = \sigma_e \frac{kT}{zq}/(d-l) \qquad [16]$$

Since $kT/zq/(d-l) << F$ for $d - l$ of the order of d, it follows that $i_I << i_e = \sigma_e F$, while for quasi-stationary oxygen uptake $i_I = i_e$ is necessary.

It would thus appear that either the field in the outer oxide region is of opposite polarity than that in the inner oxide region, or else the vacancy mobility in the outer oxide region is significantly larger than in the inner region. Arguments for each of these suggestions can be found. Field reversal is not unlikely considering that the rate determining step is electron transport for $0 < x < l$ and vacancy transport for $l <$

$x < d$. A two-layer structure for anodically grown oxide films has been established experimentally by means of tracer studies (14). Some discontinuity in the structure at $x = l$ is thus quite possible if this position marks the interface between the two-layer structure. It is even conceivable that a positive charge layer might form there. However, these assumptions, while possibly correct, have not yet been proven to be so.

Another difficulty of the present model involves the discrepancy between the rather low electron conductivity at the anneal temperature $\sigma_e \simeq 2.4 \times 10^{-12}$ ohm^{-1} cm^{-1} in contrast to the fairly high electron conductivity $\sigma_e \simeq 10^{-7}$ ohm^{-1} cm^{-1} at room temperature in the region adjacent to the tantalum, postulated by ref. (1) to (4). Clearly, this calls for two different conduction mechanisms. Yet both mechanisms must originate from the oxygen vacancies or we lose the relation between vacancy profile established at the anneal and the experimental Schottky profile at room temperature, which formed the starting point of our considerations. It will be shown in the Appendix that space charge neutrality may arise by equal concentrations of $[V'_0]$ and $[V^{\cdot}_0]$ vacancies at the anneal, one of them, $[V^{\cdot}_0]$, being highly mobile. It is reasonable to expect, therefore, that upon cooling, clustering to V^x_{20} complexes takes place.

To provide space charge neutralization, the Fermi level at the anneal temperature is located halfway between the energy levels of the $V^{\cdot}_0$ and V'_0 vacancies. On the other hand, at room temperature, the Fermi level would be determined by the ionization equilibrium of the V^x_{20} complexes and thus might be considerably closer to the conduction band, resulting in a large increase in the electron conductivity.

Perhaps the observed (8, 9) decrease of the emf with decreasing temperature in the lower temperature range can be attributed to the increasing dominance of electronic conduction due to clustering. It might arise also, of course, by the decreased ionic mobility, which shifts the position $x = l$ to smaller values and thus reduces the emf across the region $0 < x < l$.

According to the present hypothesis, the Schottky concentration N_S would be the concentration of ionized clusters $[V^{\cdot}_{20}]$. It is believed that at an applied anodic bias voltage a space charge layer forms adjacent to the tantalum metal by depletion of electrons and complete ionization of the V_{20} clusters. Thus $N_S = [V_{20}]$. If, at the anneal temperature, all clusters are dissociated, then $[V_0] = 2[V_{20}] = 2N_S$. The concentration of mobile doubly charged vacancies, $[V^{\cdot\cdot}_0]$ at the metal boundary would be less, and possibly significantly less, than $[V_0] = 2N_S$. The use of $N_S{}^o = 3.10^{20}$ cm^{-3} for $[V^z_0]_{x=0}$ in Eq. [11] is thus not justified and the distinction between $z = 2$ and $z = 1$ based thereon becomes questionable. Also, the ionic mobility calculated by [13] might be considerably higher than the numerical estimate based on $[V^z_0] \simeq 1.4 \times 10^{16}$ cm^{-3}.

Conclusions

The possible origin of an exponential vacancy distribution in annealed Ta/Ta_2O_5 samples by means of a Boltzmann distribution of vacancies during the anneal was investigated. If this interpretation is correct, oxygen uptake during the anneal is limited by electron transfer rather than ion diffusion, at least in a portion of the oxide film. This view is consistent with the observed appearance of an emf during the anneal and with the rate of oxygen uptake. However, the electron conductivities at the anneal temperature appear much smaller than those at room temperature. The difficulty could be removed by the unproven hypothesis of clustering of vacancies. It is shown in the Appendix that space charge compensation could occur even at large concentrations of vacancies and is consistent with a Boltzmann distribution of mobile vacancies in a constant field.

In summary, a model has been found which leads to a strictly exponential vacancy profile as postulated by Smyth *et al.* The model accounts for the order of magnitude of the attenuation distance. It permits significant conclusions in the mechanism of the anneal process. The model includes, however, several speculative features, which cannot be tested by existing experimental data, thus suggesting further experimental work.

Other models, such as tunneling (15), can also account for the electrical measurements of Smyth *et al.* on annealed Ta/Ta_2O_5. Thus it is conceivable that the Schottky distribution and conductivity profile need not necessarily have the straightforward interpretation (1-4) which was accepted in this paper.

Acknowledgment

The author would like to express his appreciation to D. M. Smyth for making recent experimental results available to him prior to publication and for many stimulating discussions.

Manuscript received Aug. 14, 1967; revised manuscript received *ca.* Dec. 11, 1967.

Any discussion of this paper will appear in a Discussion Section to be published in the December 1968 JOURNAL.

APPENDIX

Space Charge Compensation by Means of Oxygen Vacancies of Different Valency States

Consider the oxygen vacancy species $V^{\cdot}_0$, $V^{\cdot\cdot}_0$, V'_0, and V^x_0 in the notation of Kröger (16). The existence of a single vacancy as either donor or else trap for an electron is well known for the case of F and F^1 centers in alkali-halides. A single vacancy can change its charge by "reaction" with electrons, *e.g.*

$$V^{\cdot}_0 + 2e \rightarrow V'_0 \qquad [A\text{-}1]$$

Several reactions between vacancies and electrons and the corresponding mass action laws are listed in Table I. Also included, are values for the mass action constants in terms of the energy levels involved using customary (16) notation.

Since the concentrations of the various charged vacancy states are in proportion to each other, and, therefore, to the total vacancy concentration, the zero space charge condition for the case of negligible contributions by electrons provides a value for the electron concentration, which does not depend on the vacancy concentration, but only on the mass action constants, which are space independent. A space independent electron concentration was indeed a key feature of our model. For instance, in the case

$$[V^{\cdot}_0] \simeq [V'_0] \qquad [A\text{-}2]$$

one has

$$n = \sqrt{K_2K_3} = N_c\, e^{-\epsilon_c/kT}\, e^{+(\epsilon^x+\epsilon')/2kT} \qquad [A\text{-}3]$$

Comparison to Eq. [13] shows

$$\epsilon_F = (\epsilon' + \epsilon^x)/2 \qquad [A\text{-}4]$$

i.e., the Fermi level lies half-way between the ϵ' and ϵ^x levels, independent of position and vacancy concentration (Fig. 1).

Since the levels ϵ_c, ϵ', and ϵ^x at the oxide-tantalum interface and the Fermi level in the tantalum metal are well defined and independent of each other, the assumption that the levels ϵ' and ϵ^x are an equal distance above and below, respectively, of the Fermi level in the tantalum metal may appear quite arbitrary.

Table I. Electron reactions involving oxygen vacancies and corresponding mass action laws and mass action constants (the energy of electrons in the conduction band and on the V'_0, V^x_0, $V^{\cdot}_0$ levels are designated by ϵ_c, ϵ', ϵ^x and $\epsilon^{\cdot}$, respectively).

Reaction	Mass action law	K_i (i = 1, 2, or 3)
$V^{\cdot}_0 \rightarrow V^{\cdot\cdot}_0 + e$	$[V^{\cdot\cdot}_0] \cdot n = K_1[V^{\cdot}_0]$	$N_c e^{-(\epsilon_c - \epsilon^{\cdot})/kT)}$
$V^x_0 \rightarrow V^{\cdot}_0 + e$	$[V^{\cdot}_0] \cdot n = K_2[V^x_0]$	$N_c e^{-(\epsilon_c - \epsilon^x)/kT)}$
$V'_0 \rightarrow V^x_0 + e$	$[V^x_0] \cdot n = K_3[V'_0]$	$N_c e^{-(\epsilon_c - \epsilon')/kT)}$

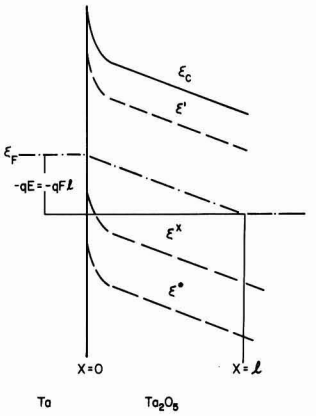

Fig. 1. Hypothetical energy level diagram for the Ta/Ta_2O_5 interface during anneal. ϵ_C is the bottom of the electron conduction band, ϵ' is the energy level for negatively charged oxygen vacancies, i.e., for the third electron at the vacancy; ϵ^x is the level for the second electron at a neutral oxygen vacancy and ϵ^* is the energy for the electron at a positively charged vacancy. Doubly positive charged oxygen vacancies are believed to be mobile and assume a Boltzmann distribution in the region $0 < x < l$, causing the electromotive force $E \simeq Fl$. The emf in the region $x > l$ is just about shorted by dominant electronic conduction. Electron concentration in the region $0 < x < l$ is constant, viz., constancy of $\epsilon_C - \epsilon_F$. A thin space charge layer in the oxide at the metal boundary (indicated schematically by the upward bending of energy levels) adjusts the Fermi level in the metal to the value of $(\epsilon' - \epsilon^x)/2$ in the adjacent portion of the neutral oxide.

However, considering the large concentration of vacancies at the interface, a very thin space charge region should suffice to adjust the levels ϵ' and ϵ^x to positions of equal distance above and below, respectively, of the Fermi level in the adjacent metal. This has been indicated by the upwards bending of the levels in Fig. 1 near the metal interface (assuming a positive space charge).

In order to obtain a Boltzmann distribution of vacancies, we must postulate that only the vacancy species of one sign is mobile. If both positive and negative vacancies were mobile, they would establish two Boltzmann distributions, one decreasing with position and the other increasing with position, while [A-2] requires both species to vary in unison with each other.

A high mobility of positively charged vacancies in contrast to a comparable immobility of negatively charged vacancies can be rationalized as follows: Oxygen vacancies move by jumps of adjacent oxygen ions. A negatively charged vacancy V'_0 repels the adjacent oxygen ions and this suppresses their mobility. The opposite is true for positively charged vacancies and, in particular, of the doubly charged state $V^{\cdot\cdot}_0$. While the V'_0-centers are immobile as an entity, their concentration can still change in proportion to that of the mobile $V^{\cdot\cdot}_0$-centers by the electron transfer reaction

$$V^{\cdot\cdot}_0 + 3e \rightarrow V'_0 \qquad \text{[A-5]}$$

Thus, at a space-independent electron concentration n, the ratios of the concentrations $[V'_0]$, $[V^{\cdot}_0]$ and $[V^{\cdot\cdot}_0]$ are independent of position irrespective of the total concentration $[V^x_0] + [V'_0] + [V^{\cdot}_0] + [V^{\cdot\cdot}_0]$, which assumes a Boltzmann distribution if only the $V^{\cdot\cdot}_0$ species is mobile. In this manner, the mass action relations (Table I), the zero space charge condition[2] [A-2], the Boltzmann distribution of mobile vacancies [3] and the condition of a space independent electron concentration [7] can all be satisfied.

[2] Equation [A-2] assumes that $[V^{\cdot\cdot}_0] \ll [V^{\cdot}_0]$. Similar arguments can be advanced in the case that $[V^{\cdot\cdot}_0]$ contributes measurably to the zero space charge condition.

REFERENCES

1. D. M. Smyth, G. A. Shirn, and T. B. Tripp, *This Journal*, **110**, 1264 (1963).
2. D. M. Smyth and T. B. Tripp, *ibid.*, **110**, 1271 (1963).
3. D. M. Smyth, G. A. Shirn, and T. B. Tripp, *ibid.*, **111**, 1331 (1964).
4. D. M. Smyth and G. A. Shirn, Paper presented at the Dallas Meeting of the Society, May 7-12, 1967, as Abstract 27.
5. K. Lehovec, Paper presented at the Cleveland Meeting of the Society, May 1-5, 1966, as Abstract 28.
6. W. Schottky, *Z. Phys.*, **118**, 539 (1942).
7. R. E. Pawel and J. J. Campbell, *This Journal*, **113**, 1204 (1966).
8. C. A. Steidel, Paper presented at Dallas Meeting of the Society, May 7-12, 1967, as Abstract 39.
9. Yoshioki Ishikawa, Yozo Sasaki, Yasuo Seki, and Shuichi Inowaki, *J. Appl. Phys.*, **34**, 867 (1963).
10. L. Young, *Trans. Faraday Soc.*, **50**, 153 (1954).
11. D. A. Vermilyea, *Acta Met.*, **1**, 282 (1953).
12. R. Dreiner, *This Journal*, **111**, 1350 (1964).
13. P. H. G. Draper and P. W. M. Jacobs, *Trans. Faraday Soc.*, **59**, 2895 (1963).
14. J. J. Randall, Jr., W. J. Bernard, and R. R. Wilkinson, *Electrochim. Acta*, **10**, 183 (1965).
15. K. Lehovec, *This Journal*, **115**, 192 (1968).
16. F. A. Kröger, "Chemistry of Imperfect Crystals," North-Holland Publishing Company, Amsterdam (1964).

Silicon Nitride Thin Films from $SiCl_4$ Plus NH_3: Preparation and Properties

M. J. Grieco,[1] F. L. Worthing, and B. Schwartz*

Bell Telephone Laboratories, Incorporated, Murray Hill, New Jersey

ABSTRACT

Silicon nitride thin films have been deposited on silicon substrates by reacting $SiCl_4$ and NH_3 at 550°-1250°C. The effects of deposition temperature and of $SiCl_4$ and NH_3 concentrations on the deposition rate have been studied. The etch rate of the deposited films is shown to be a function of the deposition temperature. Electrical evaluation has shown the dielectric strength to be independent of contact area and film thickness and the dielectric constant to be in the range seven to eight. Surface charge plus surface state density values range from 7 to 18 x $10^{11}/cm^2$. Nonlinear I-V characteristics of the films have been observed. The deposited films are extremely effective diffusion masks for sodium.

Thin layers of silicon dioxide have found extensive use in the fabrication of semiconductor devices for surface passivation (1), as diffusion masks (2), and as dielectric layers (3). Technological advances and more demanding requirements (4) have led to the need for insulating films with properties superior to those of the oxide. One of the materials currently receiving a great deal of attention as a possible substitute for SiO_2 is silicon nitride. This material has been evaluated for its passivation properties on p-n junctions (5), for its use as a dielectric in a field-effect structure (6), and for its usefulness as a diffusion mask (7, 8), and it has been found to be satisfactory.

From the data in Table I, it is apparent that there are many reactions for forming the nitride that are thermodynamically feasible. However, passing nitrogen or ammonia over solid silicon substrates heated to 1300°C results in extremely thin nitride layers (9), owing to the high efficiency of the material as a diffusion mask. When ammonia is passed over molten silicon, crystals of nitride result, as reported by Kaiser and Thurmond (10), Doo and his co-workers (11) have reported on the deposition of silicon nitride films by the high-temperature reaction of SiH_4 plus NH_3. A number of investigators (12, 13) have made use of various high-field discharge techniques in order to obtain nitride deposition at low temperatures.

This paper will report on deposited nitride thin films obtained by reacting $SiCl_4$ and NH_3 in the presence of silicon substrates heated in the temperature range 550°-1225°C. The kinetics of the deposition process will be discussed and the properties of the deposited films will be described.

Experimental Procedure

Figure 1 is a schematic of the apparatus used for this study; the system was similar to that normally used for silicon epitaxy by the hydrogen reduction of silicon tetrachloride (14). The reaction chamber is shown in Fig. 2; it was an air-cooled, single-walled, 50 mm ID quartz chamber containing a susceptor heated with an externally placed r.f. coil. The susceptor was a high-purity graphite pedestal covered with a quartz sleeve; without the quartz sleeve, NH_3 was adsorbed by the graphite, causing the carbon pedestal to powder and crumble. When a silicon susceptor was used, thick deposits of the nitride formed on the pedestal (the susceptor temperature was normally almost 200°C higher than the substrate temperature), making it necessary to relap the top surface of the suscepter after each run.

Three separate feed lines were used to introduce the reagents into the reaction chamber. In the very early phases of this study, the reagents were mixed together well upstream of the reactor, but it was found that no deposit was formed on the substrate. It was quickly realized that the NH_3 and $SiCl_4$ were reacting immediately on contact, and most of the reaction products were precipitating out of the gas phase. By converting to the system of individually feeding the reagents into the reaction chamber, nitride deposition on the substrate was achieved.

The outlets of the two feed lines inside the reaction chamber were varied from ½ to 4 in. above the silicon substrate. With the outlets of the feed lines close (~1 in.) to the substrate, films of nonuniform thickness were produced. However, with the substrate approximately 3-4 in. below the feed-line outlets, the layer thickness (~3000Å) varied by only about 200Å across a ½ in. square substrate. These last dimensions for the reactor geometry were maintained throughout these experiments.

The silicon substrates were 10 mils thick, p-type, 2-70 ohm-cm, (111) oriented, and chemically polished with an iodine etch (15). Just before the substrates were loaded into the reactor, they were chemically etched for 2 min in 10:1:HNO_3:HF, nitric acid quenched, immersed in concentrated HF for 2 min, and finally rinsed in deionized water. After the substrate was loaded, the entire system was purged with nitrogen, then heat-treated in H_2 at the deposition temperature for 30 min. Deposition was initiated after a second purge with nitrogen. The deposition reaction was carried out using nitrogen as the inert carrier of the silicon tetrachloride vapor. A total flow of 2600 cc/min of gas, composed of approximately 150 cc/min of N_2 + $SiCl_4$ vapor, 50 cc/min of NH_3, and 2400 cc/min of N_2 bypass, was passed through the reactor. The $SiCl_4$ bubbler was maintained at −30°C. The maximum deposition temperature of 1000°C was chosen

Table I. Free energy of over-all reactions*

Reaction	$\Delta G°$ kcal/mol 298°K	1300°K
$3Si + 2N_2 \rightarrow Si_3N_4$	−154.8	−71.4
$3Si + 4NH_3 \rightarrow Si_3N_4 + 6H_2$	−138.8	−165.4
$3Si + 2N_2H_4 \rightarrow Si_3N_4 + 4H_2$	−230.8	−257.8
$3SiCl_4 + 2N_2 + 6H_2 \rightarrow Si_3N_4 + 12HCl$	+15.3	−15.0
$3SiCl_4 + 4NH_3 \rightarrow Si_3N_4 + 12HCl$	+31.3	−109.0
$3SiCl_4 + 2N_2H_4 + 2H_2 \rightarrow Si_3N_4 + 12HCl$	−61.9	−202.6
$3SiH_4 + 2N_2 \rightarrow Si_3N_4 + 6H_2$	−194.4	−179.1
$3SiH_4 + 4NH_3 \rightarrow Si_3N_4 + 12H_2$	−178.4	−283.1
$3SiH_4 + 2N_2H_4 \rightarrow Si_3N_4 + 10H_2$	−270.4	−365.5

* JANAF Thermochemical Tables, Dow Chemical Company.

* Electrochemical Society Active Member.
[1] Present address: IBM Components Division, East Fishkill Facility, Hopewell Junction, New York.

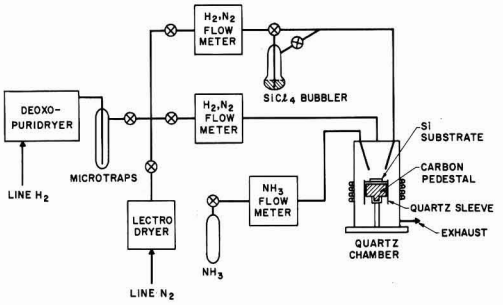

Fig. 1. Schematic diagram of apparatus

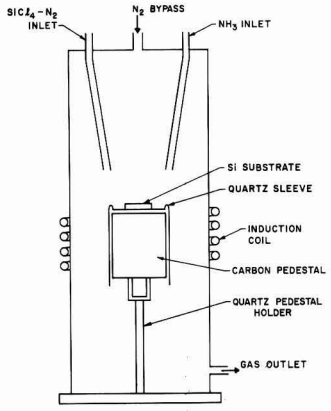

Fig. 2. Quartz reaction chamber

to avoid any substrate conversion; unless it is otherwise stated, this was the deposition temperature used.

The N_2 and H_2 gases were purified by use of a McGraw-Edison Lectrodryer and an Englehard Industries Deoxo Puridryer, respectively. The NH_3 gas (99.99%), obtained from Matheson Company, Inc., was used as received and did not undergo any subsequent purification.

Films in the thickness range 1000-6000Å were generally used for all the measurements made. Film thickness and refractive index of the nitride films were determined by use of variable angle monochromatic fringe observation (VAMFO) (16). In order to use the VAMFO instrument it was necessary to mask a portion of the substrate during deposition or etch a portion of the film down to the substrate to produce a step in the nitride film. Refractive indices measured by VAMFO were in the range of 2.00 ± 0.02.

A Carey spectrophotometer (Model 14) was adapted to measure the thickness of the nitride film (17, 18). The visible and ultraviolet regions were used for the measurement of thickness down to about 1500Å. Measurements of thickness by the spectrophotometer and the VAMFO were in agreement to within 200-300Å, with the spectrophotometer always giving the higher value.

In order to make the necessary electrical measurements, gold dots 5000Å thick and 0.004-0.025 in. in diameter were filament evaporated onto the layers. Back contact to the samples was made by gold plating the silicon substrate.[2]

Dielectric strength tests were made using dc potential applied as a voltage ramp, increasing at a constant rate of 100 v/min. The voltage ramp was generated by use of a motor-driven potentiometer, supplied by a regulated high-voltage power supply. The measurements were made using a Keithley Model 610A electrometer and a Hewlett-Packard Model 425A microammeter; the raw data were displayed on a strip chart recorder fed directly from the microammeter. For most tests, the polarity of the gold dot was negative (silicon positive). For the tests described, dielectric breakdown is defined as occurring at that voltage which is sufficient to produce sudden and irreversible damage to the film, resulting in the permanent loss of its normal insulating properties under the contact being tested.

MIS capacitance measurements were made using a Boonton capacitance bridge, Model 74C-S8, operating at a frequency of 100 kc, with a peak-to-peak signal of approximately 10 mv. The technique used was to start at zero and then apply an increasing negative bias to the gold dot until the maximum desired voltage was reached. The bias was then decreased back to zero and on to the maximum positive bias before it was returned finally to zero. From the capacitance-voltage curves the sum of surface charge plus surface state densities was determined from the flat-band condition, as described by Grove *et al.* (19). Dielectric constant values were also computed from the maximum capacitance values of these curves. In some instances, surface state densities were also obtained from conductance curves, as described by Nicollian and Goetzberger (20).

Tests for charge storage were made as previously described by Yamin and Worthing in their study of silicon dioxide (21, 22).

Sodium drift and diffusion experiments were conducted as previously described by Dalton (7).

Experimental Results of Varying Deposition Conditions

The first part of this study was concerned with the influence of the deposition variables on the kinetics of the process. Figure 3 shows the effect of $SiCl_4$ partial pressure on the deposition rate with constant NH_3 partial pressure. The mol fraction of $SiCl_4$ was varied from 7×10^{-5} to 2×10^{-3} while the NH_3 mol fraction was kept at 4×10^{-2}. The slope of the curve illustrated in Fig. 3 is approximately 0.8.

The effect of changing the NH partial pressure at constant $SiCl_4$ partial pressure was studied. The mol fraction of the NH_3 was varied from 4×10^{-3} to 7×10^{-2} while the mol fraction of the $SiCl_4$ was held at 2×10^{-4}. It appeared that varying the NH_3 concentration had no effect on the deposition rate. However, even at the lowest NH_3 concentration there was still an order of magnitude more ammonia than silicon tetrachloride. A second set of conditions was then

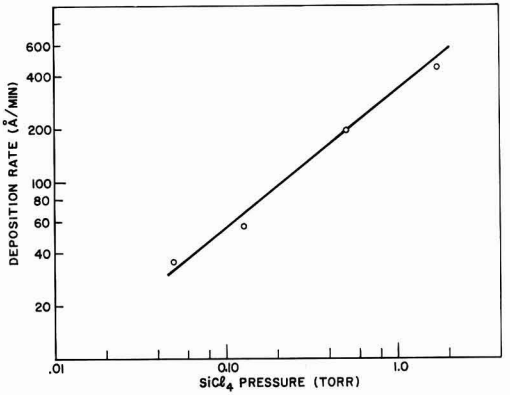

Fig. 3. Effect of $SiCl_4$ partial pressure on deposition rate (at 1000°C and NH_3 partial pressure of 28 Torr).

[2] The plating was accomplished by use of an HF + E55 acid-gold solution (Englehard Industries), followed by 25 msi of alkaline cyanide electroplate gold.

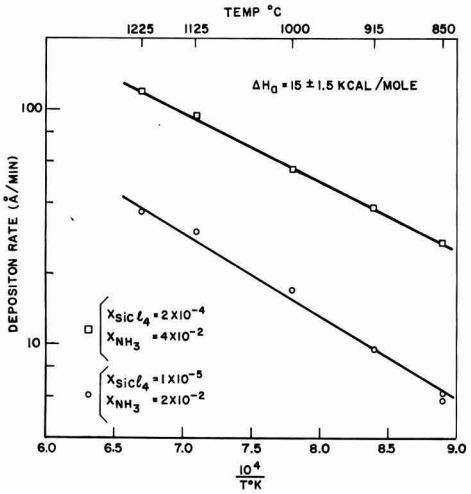

Fig. 4. Temperature dependence of silicon nitride deposition at $2\times10^{-4}:4\times10^{-2}$ and $1\times10^{-5}:2\times10^{-2}$ mol fractions, respectively, of $SiCl_4$: NH_3.

chosen, where the NH_3 mol fraction was varied from 2×10^{-3} to 4×10^{-2} and the $SiCl_4$ mol fraction was maintained at 2×10^{-3}, a factor of 10 higher than in the previous conditions. Again there was no marked effect even when the mol ratio of NH_3 to $SiCl_4$ fell to unity.

The free energy ($\Delta G°$) of the reaction of $SiCl_4$ plus NH_3 to form silicon nitride (see Table I) is negative almost down to room temperature. Figure 4 shows the results of varying the deposition temperature at two different vapor phase concentrations of reagents. The apparent activation energy (ΔH_a) obtained was 15 ± 1.5 kcal/mol.

Silicon nitride films were deposited between 550° and 1225°C with films ranging in thickness from 500Å to 2μ. The 2μ thick layer caused a slight bending of 0.010 in. thick substrates concave upward; under 300X magnification, hairlike cracks were readily visible in this film. However, a film 1.8μ thick deposited on silicon caused no bending of the substrate even though cracks were seen in the film when it was examined under 300X magnification. When this film was exposed to a water-amine-pyrocatechol etching system (23) at 95°C for 30 min, additional hairlike cracks started to appear (see Fig. 5). It was possible to observe the "growth" of these new cracks as etching proceeded. The crack from lower left to center appeared first and then started to get broader before the crack from upper left to lower right appeared. Still later, the crack from center to upper right appeared, and at this point the etching was terminated. The reason for the way these cracks appeared is not known at this time, but one possible explanation might be the relief of strain by preferential stress corrosion of the sample. Films 4000Å thick or less did not show any cracks either before or after exposure to the water-amine-pyrocatechol etching system.

Figure 6 is a plot of the etch rate in concentrated (49%) HF of the samples deposited for the upper curve of Fig. 4. Note that as the deposition temperature decreased the deposition rate decreased but the etch rate of the samples increased.

Optical transmission studies, with a Xenon lamp as a source, were performed on a 4000Å thick silicon nitride film deposited on a sapphire substrate; the effective band gap of the film was found to be 5.6 ± 0.2 ev.

In an attempt to identify the crystal nature and chemical composition of the deposited films, transmission electron diffraction and infrared absorption measurements were made. The electron diffraction patterns obtained on films deposited at all the temperatures studied showed only very diffuse rings, which could not be identified, and which indicated that the films were always amorphous. The infrared spectrum obtained on films deposited at 550° and 1000°C showed the characteristic Si-N band (13) (see Fig. 7). However, it is clearly seen that the films grown at these two temperatures are not identical. This is not surprising in light of the possible mechanisms for the reaction of $SiCl_4$ with NH_3.

Discussion of Deposition Kinetics

The mechanism involved in the deposition of a nitride film from $SiCl_4$ and NH_3 is not understood at this time. Sneed and Brasted (24) indicate that the reactions involved in the formation of silicon nitride are

$$SiCl_4 + 8NH_3 \longrightarrow Si(NH_2)_4 + 4NH_4Cl \quad [1]$$

$$Si(NH_2)_4 \xrightarrow{0°C} SiNH(NH_2)_2 + NH_3 \quad [2]$$

$$SiNH(NH_2)_2 \xrightarrow{100°C} SiN(NH_2) + NH_3 \quad [3]$$

$$2SiN(NH_2) \xrightarrow{900°C} (SiN)_2NH + NH_3 \quad [4]$$

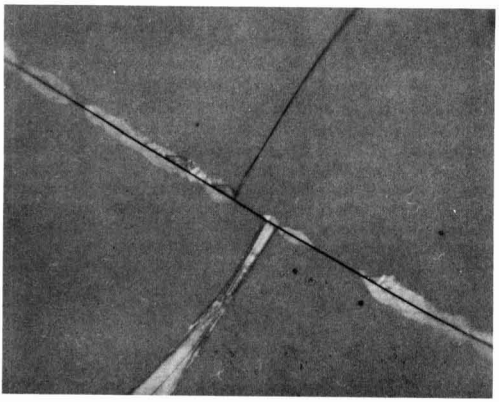

Fig. 5. Photomicrograph of 1.8μ thick film with "cracks" after it has been etched with water-amine-pyrocatechol system. (Magnification *ca.* 200X.)

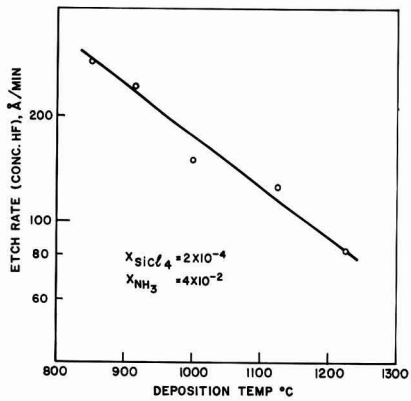

Fig. 6. Etch rate in concentrated HF of silicon nitride films deposited at different temperatures.

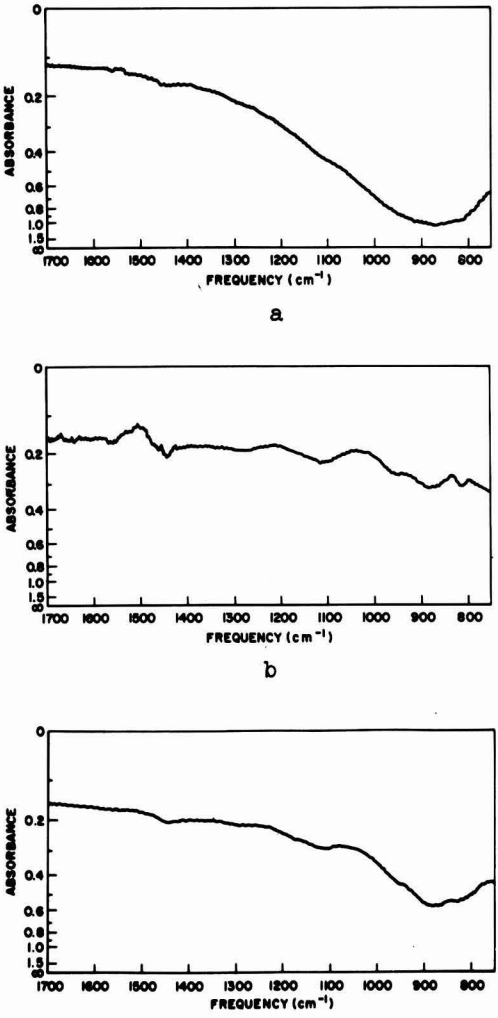

Fig. 7. Infrared analysis spectra: a, spectrum of film deposited at 1000°C; b, silicon substrate blank; c, spectrum of film deposited at 550°C.

$$3(SiN)_2NH \xrightarrow{1200°C} 2Si_3N_4 + NH_3 \quad [5]$$

Billy (9) claims, however, that at room temperature

$$SiCl_4 + 6NH_3 \longrightarrow SiN_2H_2 + 4NH_4Cl \quad [6]$$

which, on continued heating, yields Si_3N_4 by stepwise loss of NH_3 schematically represented by

$$3SiN_2H_2 \xrightarrow{75°C} Si_3N_5H_3 + NH_3 \quad [7]$$

$$Si_3N_5H_3 \xrightarrow{1000°C} Si_3N_4 + NH_3 \quad [8]$$

There is a discrepancy between Billy and Sneed and Brasted about the temperature necessary to obtain the Si_3N_4 form; Billy claims that Si_3N_4 can be achieved at 1000°C, while Sneed and Brasted say that 1200°C is required.

Billy notes that Si_3N_4 can be obtained in the pure form at 550°C by thermally decomposing pure SiN_2H_2, but he also notes that the presence of NH_3 or NH_4Cl will have a strong influence on the decomposition mechanism. We have also seen an influence of NH_4Cl on the deposition kinetics. During our depositions, a white powdery material formed on the upper and lower portions inside of the reactor wall. X-ray analysis showed it to be an impure form of NH_4Cl, possibly containing silicon amine compounds but definitely having no silicon oxide, chloride, nitride, or oxynitride. The reactor wall in the area immediately around the pedestal was clear and uncoated. If three or more depositions were attempted without a cleaning of the reaction chamber, the NH_4Cl built up on the reactor wall would begin to flake off onto the silicon substrate. It was therefore instituted as standard procedure that the reactor tube and pedestal shield be cleaned after every run.

In order that the influence of NH_4Cl might be studied, a series of measurements was performed starting with a clean-walled reactor. Silicon tetrachloride and nitrogen were admitted into the reaction chamber while the substrate temperature was maintained at 1000°C. No visible deposit was obtained on the silicon after 30 min under these conditions. Ammonia was then admitted to the reaction chamber in addition to the silicon tetrachloride plus nitrogen, and both the silicon substrate and the walls were coated. The nitride-coated silicon slice was then removed after the reactor was cooled and purged; the NH_4Cl was not cleaned from the reactor walls. A new silicon slice was then placed in the reaction chamber. Again, after the normal nitrogen purge of the system, only nitrogen and silicon tetrachloride were introduced, and this time a very slow deposition of nitride was observed on the silicon slice. These findings indicate that the material deposited on the walls contributes NH_3 to the ambient.

Another influence of NH_4Cl was observed when the wall of the reaction tube was separately heated with heating tape to 300°-350°C during a deposition. The deposition rate was found to increase by a factor of 5 over that obtained under the equivalent cold-wall conditions.

It is impossible at this time to expound further on the possible reaction mechanism, since no detailed analytical measurements have been made on the film or on the gaseous reaction products.

Results of Electrical Measurements

The dielectric strength was found to range from about 0.5 to 1×10^7 v/cm for all the films tested and to be independent of contact area, film thickness, or conductivity type of the substrate. Samples that were exposed to a water-amine-pyrocatechol etching system at 95°C for 30 min had a negligible pinhole count.[3] This is in agreement with the observed absence of area dependence of breakdown, which might be expected to occur in the presence of defects of the type reported by Lopez (26). Insulating films deposited by other processes have frequently shown a rather strong contact area dependence of dielectric strength.

The absence of a film thickness effect (in the range 1000-6000Å) for the dielectric strength (27) can be explained by the fact that the films were amorphous in structure (28), as was revealed by electron diffraction studies. The dielectric strength was also about the same whether the contact was made positive or negative, although usually the negative polarity was used. Inasmuch as some degree of time dependence of breakdown was found at either polarity, and in view of the rather high current levels sustained prior to breakdown, it appears likely that the true intrinsic value of dielectric strength for these films is somewhat higher than the 1×10^7 v/cm value quoted above. Varying the rate of application of potential by a factor of 10 did not change the breakdown levels.

[3] The water-amine-pyrocatechol etching system has been shown to be capable of delineating pinholes or potential pinholes in silicon nitride films (25).

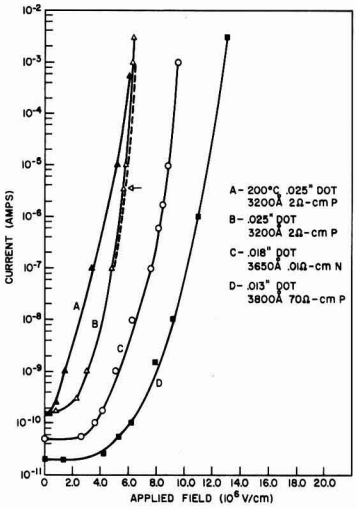

Fig. 8. Curve A, sample M92B—3200Å thick film on a 2 ohm-cm, p-type substrate with a 0.025 in. diameter gold dot and negative polarity on the gold (200°C). Curve B, sample M92B—3200Å thick film on a 2 ohm-cm, p-type substrate with a 0.025 in. diameter gold dot and negative polarity on the gold (room temperature). Curve C, sample M76A—3650Å thick film on a 0.01 ohm-cm, n-type substrate with a 0.018 in. diameter gold dot and negative polarity on the gold (room temperature). Curve D, sample M87A—3800Å thick film on a 70 ohm-cm, p-type substrate with a 0.013 in. diameter gold dot and negative polarity on the gold (room temperature).

In the measurement of dielectric strength, when the applied field reached about 3 x 10^6 v/cm, a rather steep rise in conduction was observed. In Fig. 8 the log of current has been plotted against applied field for several samples; curves B, C, and D show the increase in conduction for three different film samples, all at room temperature, and with negative polarity on the contact dot.[4] The difference in relative levels of these curves at low fields is thought to be due to difference in capacitance. Film thickness for the three samples increases, contact area decreases, and hence capacitance decreases, from left to right. Since potential is being applied by the voltage ramp technique, the current is equal to the charge derivative with respect to time. In other words, the relatively flat portions of the curves observed below a field of about 3 x 10^6 v/cm represent charging current. The conduction phenomena observed at higher fields is probably not related to dielectric failure or thermal breakdown (29) (except possibly in a very small range lying very close to the intrinsic dielectric strength), since it does not cause permanent loss of normal insulating properties of the film. With reference to curve B of Fig. 8, the voltage ramp was stopped when the field reached 5.6 x 10^6 v/cm (arrow), and conduction remained at a level of 3.5 x 10^{-6} amp for 10 min. Thereafter, the voltage ramp was restarted and the conduction curve was retraced about 10 times between 10^{-7} amp and 10^{-3} amp (dashed portion of the curve). Breakdown eventually occurred when the field was increased to 6.4 x 10^6 v/cm; conduction just prior to breakdown was well in excess of 3.0 ma (full scale of our meter). High conduction phenomena in nitride films have also been observed by Doo and Nichols (30) in films obtained from silicon hydride and ammonia and by Hu and Gregor (31) in reactively sputtered nitride films.

In an attempt to learn something of the mechanism of conduction, the sample from which the data for curve B were obtained was heated to 200°C and curve A was obtained. The displacement of the curve to the left at 200°C would seem to rule out impact ionization or avalanche multiplication as the mechanism of conduction; if the latter were responsible one would expect the shift to be in the other direction (32). Tests performed at liquid nitrogen temperature indicate that the high conduction at high fields can be virtually eliminated at low temperature. For one sample tested, with an applied field of 8.3 x 10^6 v/cm, a conduction of 1.2 μa at room temperature decreased to 0.005 na at liquid nitrogen temperature. This would tend to rule out both field emission and impact ionization as mechanisms of conduction. The mechanism tentatively proposed at the present time is deep-trap ionization by field-assisted thermal excitation (Frenkel-Poole effect) (33). The fact that silicon nitride films can show the type of conduction observed here can perhaps be explained by the presence of mechanical strain in the films, as suggested by results obtained with the water-amine-pyrocatechol etching system (see Fig. 5), or by the presence of impurity atoms. It is known that the density of isolated levels or deep traps increases with mechanical strain, with the presence of foreign atoms, and with rise in temperature (34).

The prebreakdown conduction phenomena reported here are not believed to be of the type associated with moisture, since the conduction appears to be only slightly responsive to varying percentages of relative humidity. Furthermore, heating generally causes an increase rather than a decrease in conduction for a given applied potential.

On a good steam-grown oxide on silicon, surface charge densities of 2-4 x 10^{11} charges/cm^2 and surface state densities of about 2 x 10^{11} states/cm^2 are obtained from a combination of conductance and capacitance measurements (19, 20). Figure 9 is the result of an MIS capacitance-voltage sweep made on a double dielectric layer (gold-silicon nitride-silicon dioxide-silicon) where the nitride was deposited on top of 1000Å of steam-grown oxide. Note that the value of 3 x 10^{11}/cm^2 for the sum of surface charge plus surface state density (19) indicates that the deposition of the nitride had no deleterious effects on the surface properties of the already existing Si-SiO_2 interface. For comparison, the normal values of surface charge plus surface state densities obtained when the nitride is deposited on bare silicon at a deposition temperature of 1000°C range from 7-18 x 10^{11}/cm^2 (see Fig. 10). Samples which have low surface charge densities generally also have low surface state densities. Values of surface charge and surface state densities are found to be fairly uniform among different contact dots on the same sample. Figure 11 is a plot for a nitride deposited on bare silicon at 850°C; the value of 16 x 10^{11}/cm^2 for the surface charge plus surface state density is

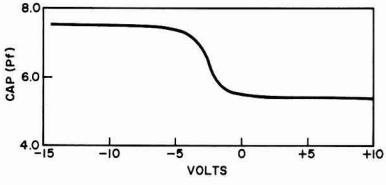

Fig. 9. MIS capacitance curve of a 0.010 in. diameter gold dot on a double dielectric layer (1850Å nitride on 1000Å oxide). The nitride was deposited at 1000°C and the silicon was 1 ohm-cm, p-type. The dielectric constant of the composite layer measures 5.0 and the SC + SS density is 3 x 10^{11}/cm^2.

[4] The negative polarity was originally chosen for this measurement in an attempt to avoid the type of gradual time-dependent breakdown previously reported (29) for atmospheric-pressure, steam-grown SiO_2 films. When a few tests were performed on the nitride with the opposite polarity, results similar to those reported here were obtained.

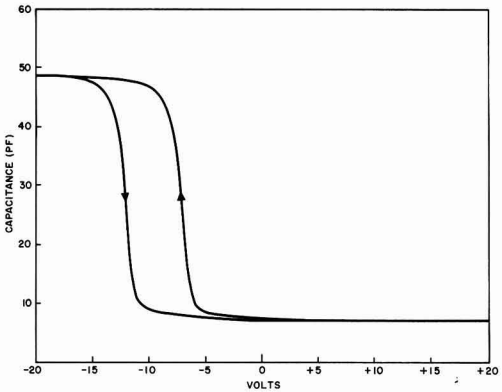

Fig. 10. MIS capacitance curve of a 0.015 in. diameter gold dot on a 1500Å thick nitride layer deposited on 35-40 ohm-cm, p-type silicon at 1000°C. The dielectric constant is 7.3 and the SC + SS density is $17 \times 10^{11}/cm^2$.

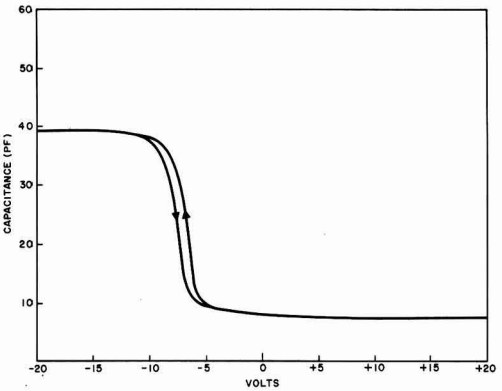

Fig. 11. MIS capacitance curve of a 0.015 in. diameter gold dot on a 1750Å thick nitride deposited on 35-40 ohm-cm, p-type silicon at 850°C. The dielectric constant is 7.1 and the SC + SS density is $16 \times 10^{11}/cm^2$.

comparable with those obtained on films grown at 1000°C.

In Fig. 10 and 11, there are indications of an instability in the passivation capabilities of the nitride as evidenced by the hysteresis loop in the capacitance-voltage plot. Carrier injection from the silicon, with subsequent trapping in the nitride, is probably one of the reasons for this behavior (35). In comparison, the data in Fig. 9 are typical of the stability seen in good oxide passivation of a silicon surface. It is still too early in the development of the nitride deposition work to say that this phenomenon is an intrinsic property of silicon nitride rather than a reflection of the level of technology at this time. It is believed that further development is needed to provide a better understanding of the process variables which influence conditions at the silicon-silicon nitride interface.

The value of dielectric constant, computed from the maximum capacitance values of the MIS capacitance curves, ranged from about seven to eight.

No charge storage of the type ascribed to ion drift in SiO_2 (21, 22) could be found for any of the films tested.

Radioactive sodium drift experiments were carried out at 400°C with +2 to +8v applied to the contact dots for 1 min each. Radiotracer analyses showed that these films provide a barrier to sodium drift under

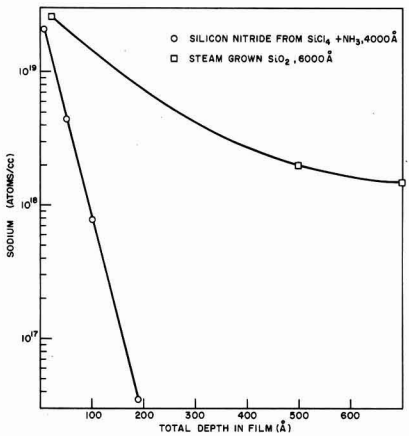

Fig. 12. Thermal diffusion of Na at 600°C into a steam-grown silicon dioxide film and into a silicon nitride film deposited at 1000°C. Courtesy of J. V. Dalton.

the conditions of voltage, time, and temperature described. Incremental etching and counting after drifting showed that all active sodium was removed with <100Å of the film. Tests conducted in the same manner on SiO_2 films have shown that sodium drifts through the film and piles up at the Si-SiO_2 interface (36).

Thermal diffusions of Na were carried out at 600°C for 22 hr on the silicon nitride films. Diffusion profiles of the diffused samples showed that thermal diffusion takes place to a much smaller degree than in atmospheric-pressure steam-grown SiO_2 (Fig. 12). Incremental etching and radiotracer counting of the silicon nitride films after diffusion of the Na^{22}/Na^{23} tracer source showed that all active sodium was removed with <200Å of the film.

Discussion of Electrical Measurements

The panacea for complete surface passivation and control still has not been found. Silicon nitride does provide a better diffusion mask than silicon dioxide against unwanted impurities, but a penalty must be paid in that surface state and surface charge densities are higher with the former material. Generally, this process has yielded numbers for surface charge plus surface state densities of 7-18 x $10^{11}/cm^2$ when the deposition was done at 1000°C. Surface charge plus surface state densities of 10-16 x $10^{11}/cm^2$ were not uncommon when the deposition temperature was dropped to 850°C. It is possible that improvements might result from additional work on the process, but for the present the nitride films seem to have at least one half an order of magnitude more surface charge plus surface state densities than good oxide films. Additionally, the problem of hysteresis effects might also respond to improvements in processing.

Conclusions

It has been demonstrated that a dielectric film can be deposited very easily on a silicon substrate by reacting $SiCl_4 + NH_3$ at elevated temperatures. Infrared spectra of the films and some of their electrical and optical properties have been determined. The use of the films as protective coatings and as diffusion masks is clearly indicated.

Although some of the kinetics of the process have been determined, the mechanism is still far from clear.

Acknowledgment

It is a pleasure to thank J. P. Luongo for the infrared measurements; Miss D. Margel for the electron

diffraction and x-ray analyses; G. P. Carey and P. A. Byrnes for MIS capacitance and conductance measurements; A. Frova for the bandgap measurement; and T. M. Buck, S. M. Sze, and M. J. Rand for many helpful suggestions.

Manuscript received June 23, 1967; revised manuscript received Jan. 22, 1968. This paper was presented at the Philadelphia Meeting, Oct. 9-14, 1966, as Abstract 148.

Any discussion of this paper will appear in a Discussion Section to be published in the December 1968 JOURNAL.

REFERENCES

1. M. M. Atalla, E. Tannenbaum, and E. J. Scheibner, *Bell System Tech. J.*, **38**, 749 (1959).
2. C. J. Frosch and L. Derick, U. S. Pat. 2,802,760; *This Journal*, **104**, 547 (1957).
3. F. P. Heiman and S. R. Hofstein, *Electronics*, **37**, 50 (1964).
4. E. H. Snow, A. S. Grove, B. E. Deal, and C. T. Sah, *J. Appl. Phys.*, **36**, 1664 (1965).
5. Dutch Pat. 6,405,186, November 1964; British Pat. 1,006,803, October 1965.
6. N. C. Tombs, H. A. R. Wegener, R. K. Wheeler, B. T. Kenney, and A. J. Coppola, Digest of Technical Papers, 1966 International Solid State Circuits Conference, **9**, 58 (1966).
7. J. V. Dalton, *This Journal*, **113**, 165C (1966).
8. V. Y. Doo, *IEEE Trans. Electron Devices*, **ED-13**, 561 (1966).
9. M. Billy, *Ann. Chem.*, **4**, 795 (1959).
10. W. Kaiser and C. D. Thurmond, *J. Appl. Phys.*, **30**, 427 (1959).
11. V. Y. Doo, D. R. Nichols, and G. A. Silvey, *This Journal*, **113**, 1279 (1966).
12. H. F. Sterling and R. C. G. Swann, *Solid-State Electronics*, **8**, 653 (1965).
13. S. M. Hu, *This Journal*, **112**, 260C (1965).
14. "Vapor Deposition," C. F. Powell, J. H. Oxley, and J. M. Blocher, Jr., Editors, p. 612, John Wiley & Sons, Inc., New York (1966).
15. P. Wang, *Sylvania Technologist*, **11**, 50 (1958).
16. W. A. Pliskin and E. E. Conrad, *IBM J. Res. Dev.*, **8**, 43 (1964).
17. E. A. Corland and H. Wimpfheimer, *Solid-State Electronics*, **7**, 755 (1964).
18. F. Reizman, *J. Appl. Phys.*, **36**, 3804 (1965).
19. A. S. Grove, B. E. Deal, E. H. Snow, and C. T. Sah, *Solid-State Electronic*, **8**, 145 (1965).
20. E. H. Nicollian and A. Goetzberger, *Bell System Tech. J.*, **46**, 1055 (1967).
21. M. Yamin and F. L. Worthing, *This Journal*, **111**, 62C (1964).
22. M. Yamin, *IEEE Trans. Electron Devices*, **ED-12**, 88 (1965).
23. R. M. Finne and D. L. Klein, *This Journal*, **111**, 63C (1964).
24. M. C. Sneed and R. C. Brasted, "Comprehensive Inorganic Chemistry," Vol. 5, p. 173, D. Van Nostrand Co., New York (1959).
25. F. M. Finne, Private communication.
26. A. D. Lopez, *This Journal*, **113**, 89 (1966).
27. F. Forlani and N. Minnoja, *Physica Status Solidi*, **4**, 311 (1964).
28. K. W. Plessner, *Proc. Phys. Soc.*, **60**, 243 (1948).
29. F. L. Worthing, *This Journal*, **112**, 68C (1965).
30. U. Y. Doo and D. R. Nichols, *ibid.*, **113**, 212C (1966).
31. S. M. Hu and L. V. Gregor, *ibid.*, **113**, 213C (1966).
32. C. R. Crowell and S. M. Sze, *Appl. Phys. Letters*, **9**, 242 (1966).
33. S. M. Sze, *J. Appl. Phys.*, **38**, 2951 (1967).
34. J. J. O'Dwyer, "The Theory of Dielectric Breakdown of Solids," p. 6, Clarendon Press, Oxford (1964).
35. S. M. Hu, D. R. Kerr, and L. V. Gregor, *Appl. Phys. Lett.*, **10**, 97 (1967).
36. T. M. Buck, F. G. Allen, J. V. Dalton, and J. D. Struthers, Paper presented at IEEE Silicon Interface Specialists Conference, Las Vegas, Nev., November 1965.

Phosphors Based on Rare Earth Phosphates Fast Decay Phosphors

R. C. Ropp*

Westinghouse Electric Corporation, Bloomfield, New Jersey

ABSTRACT

Phosphors based on rare earth phosphates and activated by Ce^{+3} can be prepared with efficiencies comparable to the previously known P-16 phosphor as well as having operating maintenance characteristics essentially equivalent to it. In addition, the rare earth phosphate phosphors have decay times nearly three times faster than this commercial material. These new materials may open applications in electronic devices not feasible before.

Decay time of luminescent materials is important in many electronic applications, but has little significance in others. For example, it is not critical in 60-cycle fluorescent lamp operation, but is of major concern for devices such as a flying-spot-scanner since it limits the rapidity of rescan of the device.

Decay time can be classified in two broad categories, exponential and logarithmic, the former being proportional to e^{-t} and the latter to a power function such as t^{-2} (1). Many luminescent materials possess an exponential decay so that it is common to express a time constant as $1/e$ (time to decay to 37% of the original intensity, I_o), or, alternately, time to decay to 10% of I_o. Common decay times range from a few milliseconds (*e.g.*, parity forbidden spin reversal of Mn^{+2}) to several hundred nanoseconds (*e.g.*, allowed dipole transitions). Fast decay phosphors in the nanosecond range have usually involved the Ce^{+3} activator particularly for cathodoluminescent materials. P-16, a widely used phosphor, is a calcium magnesium silicate activated by Ce^{+3} and has a decay time of about 120 nsec. A phosphor with still faster decay time also involved the Ce^{+3} activator and was described by Struck (2). Recently, Blasse and Bril, have also described Ce^{+3} in $Y_3Al_5O_{12}$ (3) as a fast decay material.

In 1941, the emission of Ce^{+3} in 29 different hosts was surveyed by Kroger and Bakker (4). Next followed a survey of ultraviolet emitting phosphors for fluorescent lamp application in 1947 by Clapp and Ginther (5). A fairly comprehensive study of fast decay phosphors for flying spot cathode-ray tubes was made in 1951 by Bril and Klasens (6). The most recent survey covers ultraviolet emission but does not

* Electrochemical Society Active Member.

mention decay time (7). The present paper presents a survey of the rare earth phosphates, activated by Ce^{+3}, with particular reference to decay time and emission properties.

Experimental Methods

Preparation of phosphors.—Phosphors were prepared by precipitating solutions of the appropriate rare earths with a dilute solution of phosphoric acid. Mixtures of the ions were made, including a soluble salt of the activator, before precipitation. An excess of phosphate was maintained at all times by adding the rare earth solutions to the phosphoric acid solution. Because of the method of preparation, no mixing or blending steps were necessary prior to firing to obtain a uniform and homogeneous composition. In general, a hydrated product was obtained, but the degree of hydration was a function of the nature of cations present, concentration of reagents, and temperature employed during the course of precipitation. The materials as produced were then fired to form the phosphor composed of the desired solid solution of phosphates. Firing in air was accomplished in open silica crucibles placed at temperature in a large globar furnace.

Measurements.—Excitation and emission spectra of photoluminescence were obtained with the aid of a commercial spectrofluorimeter (8) which provided a constant energy beam over the range of 20,000-50,000 cm^{-1} (5000-2000Å) and recorded energy corrected spectra directly. Resolution of the instrument varied from a few angstroms in the ultraviolet to about 10Å in the red region of the spectrum. Intensity data were obtained by instrumental integration of the emission bands by means of an integrator directly attached to the recorder.

Most of the cathode-ray intensity data were obtained in a demountable vacuum system consisting of an electron gun and a turntable carrying the phosphor samples, all located in an evacuated glass chamber. The tetrode gun had a tungsten anode and was located about 20 in. from the final anode. Normal operating voltage was about 20 kv with a beam spot size of 5 mm. The phosphors, located in 1.0-cm holes, were viewed one at a time from the bombarded size by means of a first surface 45° plane mirror, a quartz mirror, and a quartz lens. No charging effects from the defocused beam were observed. Decay time was measured in a separate apparatus employing a pulsed electron beam having a rise time of ½ nsec. Emission from the phosphor caused a response in a separate photomultiplier which was displayed on an oscilloscope. Resolution was not limited by the time-constant of the experimental apparatus.

Experimental Results

Both $LaPO_4$ and $GdPO_4$ are monoclinic and possess the monazite structure; YPO_4 is tetragonal and has the xenotime structure (9). Ce^{+3} in each, or any combination of the three compounds, yields both photo- and cathodoluminescence, characteristic of the structure. Shown in Fig. 1 are photoluminescence spectra for phosphors containing 5 g-a/o (gram-atomic per cent) of Ce^{+3} per mol of phosphate. Note that the emission bands peak in the ultraviolet as expected, but that their position is a function of structure and composition. The emission peaks of Ce^{+3} in $GdPO_4$ and $LaPO_4$ are near 3200°, whereas in YPO_4, they are nearer 3500Å.

The excitation bands are more difficult to analyze. It was shown previously (10) that the excitation bands which appear at highest energy in La_2O_3:Gd and Y_2O_3:Gd could be attributed to cationic exciton absorption. A similar explanation was made for $LaPO_4$:Gd and YPO_4:Gd spectra in a prior paper (11) because of identical energy positioning. For YPO_4:Ce and $LaPO_4$:Ce phosphors, the highest energy bands might be caused by absorption due to formation of

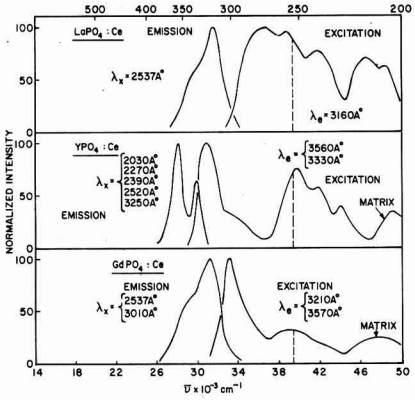

Fig. 1. Photoluminescence of some cerium-activated rare earth phosphates.

exciton states or they may be due to crystal field effects on the $4f^1 \rightarrow 5d^1$ transition of Ce^{+3}. In addition, these bands could also be attributed to upper excited states of Ce^{+3} and might well include such transitions as $4f^1 \rightarrow 6s^1$.

However, in $GdPO_4$:Ce a further solution of the excitation processes can be presented. Excitation in the $4f^7$ levels (transition: $^8S_{7/2} \rightarrow {}^6I_J$) causes both Gd^{+3} and Ce^{+3} emission, the latter from energy transferred from excited Gd^{+3} centers. This can be demonstrated more clearly by considering the effects of Ce^{+3} concentration in $GdPO_4$ (typical spectra are given in Fig. 2). At 0.01 g-a/o of Ce^{+3}, only Gd^{+3} excitation bands are seen as evidenced by the fact that each produces both Gd^{+3} and Ce^{+3} emission. The band at 3105Å is the typical emission found in all Gd^{+3} containing phosphors (*i.e.*, ^6P_J levels). However, at 2.5 g-a/o Ce^{+3}, the Ce^{+3} band at 3000Å produces only typical Ce^{+3} emission, whereas the Gd^{+3} excitation bands at 2740 and 2380Å produce both Gd^{+3} and Ce^{+3} emission. Thus, for the various phosphors shown in Fig. 1, one is led to the conclusion that each excitation band at lowest energy is probably due to Ce^{+3} excitation.

As a photoluminescent material, YPO_4:Ce, the most efficient phosphor, had an integrated output of only 36% of the commercial Ba_3SiO_5:Pb phosphor when excited by 2537Å and measured under identical conditions, as shown in Fig. 3.

Cathode-ray excitation produces spectra nearly identical to those from ultraviolet excitation except that the relative intensities of these phosphors vary somewhat more for the former than for the latter mode of excitation. The intensities shown in Fig. 4 are relative to one another whereas those of Fig. 1 were normalized so that the spectra could be more easily compared. Note that the spectra of YPO_4:Ce and $LaPO_4$:Ce are about equal in output intensity but

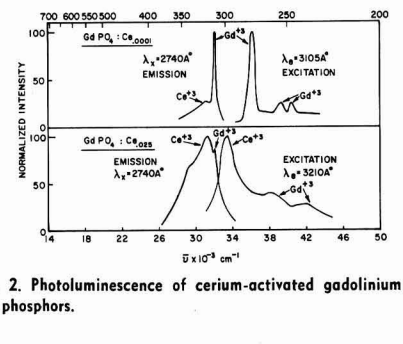

Fig. 2. Photoluminescence of cerium-activated gadolinium phosphate phosphors.

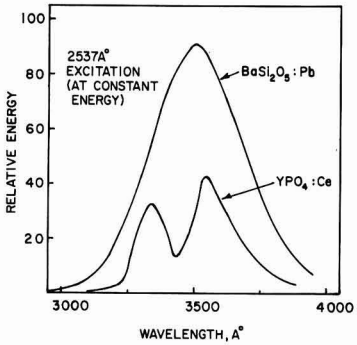

Fig. 3. Radiometric comparison of ultraviolet emitting phosphors

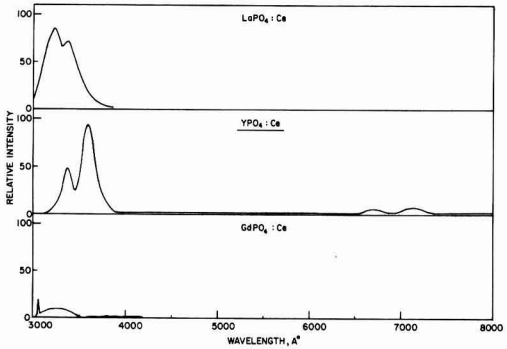

Fig. 4. Cathodoluminescence of Ce^{+3} activated phosphors

that of $GdPO_4$:Ce is much lower. Thus, in a device such as a cathode-ray tube, YPO_4:Ce should be much superior to the others when used in combination with an ordinary glass face-plate whose wavelength cutoff is usually about 3300Å. That this is true is shown in Fig. 5. Figure 5A shows the relative intensity of $LaPO_4$:Ce compared to a standard P-16 phosphor. Figure 5B shows the same phosphor when viewed through a glass face-plate while Fig. 5C shows a YPO_4:Ce phosphor as compared to the same P-16 phosphor, viewed through a similar glass face-plate of a 5-in. cathode-ray tube.

As shown in Fig. 6 for photoluminescence, the optimum activator concentration for the $LaPO_4$ and

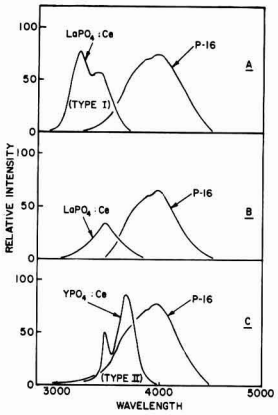

Fig. 5. Relative cathodoluminescence of Ce^{+3} activated rare earth phosphates.

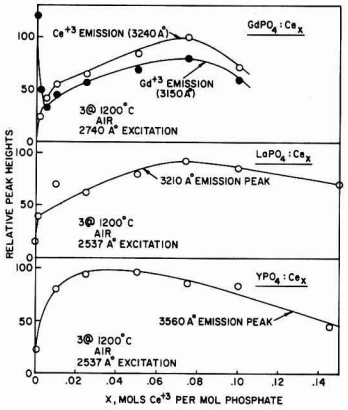

Fig. 6. Optimum activator concentration

$GdPO_4$ compounds is about 7.5 g-a/o Ce^{+3} whereas it is about 5.0 g-a/o in the YPO_4 material. Thus, 6.0 g-a/o Ce^{+3} represents a reasonable average for the three systems.

In the binary Y-Gd system, as shown in Fig. 7, the $GdPO_4$:$Ce_{0.06}$ phosphor has about 10% of the output of the YPO_4:$Ce_{0.06}$ phosphor as measured by comparison of peak heights. In the ternary Y-Gd-La system, as shown in Fig. 8, two types of emission appear, one

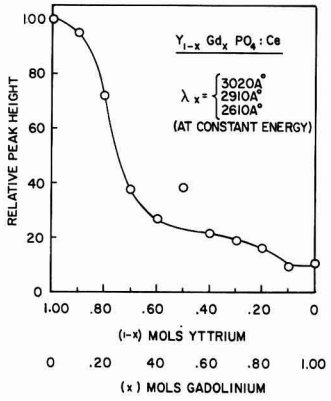

Fig. 7. Relative efficiency of Ce^{+3} activated rare earth phosphates.

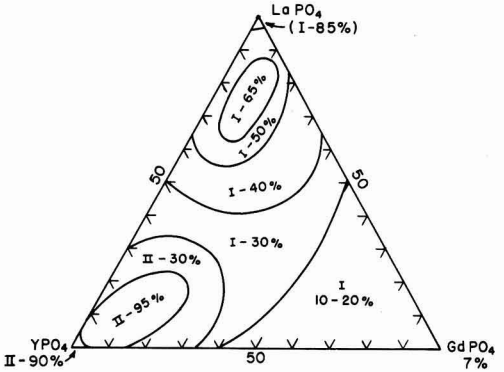

Fig. 8. Luminescent intensity in the ternary system. Emission spectra: type I, $LaPO_4$: Ce; type II, YPO_4 : Ce.

similar to that of $LaPO_4$:Ce and the other to that of YPO_4:Ce. In this system, the relative peak heights of the ternary compositions were compared under constant energy excitation. In this way, a direct comparison of output was obtained even though wavelength positions of the emission bands changed.

It is interesting to find that no more than 10-15% $GdPO_4$ can be tolerated in these systems without adversely affecting the over-all output. The limits of composition, to obtain the best cathodoluminescent phosphor as given in Fig. 8 for the ternary system are:

$$Y_u\,Gd_v\,La_w\,PO_4 : Ce_x$$

$$95\% > u > 60\%$$
$$20\% > v > 0\%$$
$$25\% > w > 0\%$$
$$15\% > x > 2\%$$

At the $Y_{0.80}Gd_{0.10}La_{0.10}PO_4$:$Ce_{0.06}$ composition, the decay time to $1/e$ was found to be 40 nsec, when compared to a standard P-16 phosphor whose decay time was measured to be 114 nsec, as shown in Fig. 9. These results were obtained using a gated oscilloscope with photomultiplier, having a ½ nsec rise time and a 2 nsec pulse width. The decay time of the $LaPO_4$:Ce phosphor was also measured and found to be 32 nsec. Thus, structure does not seem to have a major effect on decay time.

The operating maintenance efficiency of these phosphors was determined to be similar to that of the standard P-16 phosphor, as shown in Fig. 9. A loss of about 50% of the original intensity occurs within 30 min of initial operation under the operating conditions employed for these cathode-ray tubes. This loss

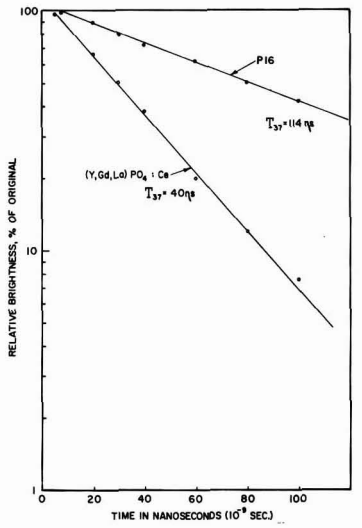

Fig. 9. Comparison of decay time of two phosphors

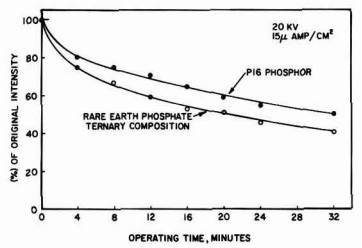

Fig. 10. Comparison of maintenance of efficiency of Ce^{+3} activated phosphors.

indicated is much larger than those encountered under normal operating conditions. Taylor *et al.* (12) have studied various P-16 phosphors and concluded that the poor maintenance of P-16 phosphors in general was due to a surface degradation of the silicate host materials. In view of the results presented herein, it seems more logical that the operating loss is due to a change in the state of the Ce^{+3} activator rather than a change in the host material, particularly since equivalent results were seen and one was a phosphate and the other a silicate.

Discussion

It has been shown that phosphors based on rare earth phosphates, and activated by Ce^{+3}, can be prepared with an output rivaling the P-16 phosphors as well as possessing essentially equivalent operating maintenance characteristics in a cathode-ray tube. In addition, the rare earth phosphate phosphors have decay times nearly three times faster than the best known commercial material P-16.

We can compare the emission properties of these phosphors with those described by Struck (2), who also found fast decay properties for Ce^{+3} in $LaPO_4$ and YPO_4. Struck found identical emission properties for both of these matrices, in contrast to the results presented herein. In Struck's phosphors, the main emission peak occurred close to 3200Å. However, he prepared his materials by solid-state reaction of oxides and phosphates, a method which is certain to produce small amounts of meta and polyphosphates, as has been shown by the extensive and comprehensive work of Thilo (13). In contrast, precipitation from solution produces stoichiometric phosphates and completely different emission properties for YPO_4:Ce. The D_{2d} site symmetry (14) has a major effect on the transition probabilities so that the lower energy emission band contains the greater part of the total emission energy in YPO_4:Ce while in $LaPO_4$:Ce, the opposite is true. Since the site symmetry in $LaPO_4$:Ce is likely to be lower, this leads one to believe that Struck's results could be ascribed to a lower site symmetry in his YPO_4:Ce phosphor, particularly because of the remarkable correspondence of all of his emission bands. One of the probable causes for his results for YPO_4:Ce is nonstoichiometry (*i.e.*, lower symmetry cation site) attendant on the method of preparation employed.

In regard to application, we have found the YPO_4:Ce phosphor to be useful in a one-gun beam-indexing color television tube where the P-16 phosphor cannot be employed because of excessive decay times. In this tube, which is similar to one described previously (15), a mosaic of red-, green-, and blue-emitting-vertical-phosphor-stripes are arranged in a repetitive manner. This screen is aluminized, and a vertical pattern of YPO_4:Ce stripes is superimposed. The ultraviolet emission caused when the electron beam scans past the YPO_4:Ce stripe is picked up by a photomultiplier, and the signal generated is used to modulate the incoming color signals to position the electron beam on the desired color stripe. At the television frequencies employed, a nanosecond decay phosphor is mandatory in order to pinpoint the beam position during each sweep across the screen. The use of the YPO_4:Ce phosphor also obviated the requirement of a quartz window in the tube (and the attendant problems in installing it) in order to pick up the ultraviolet signal. In such a system, we obtained "white" screen brightnesses of 165 ft-L, which is approximately 300% of the current commercial production models.

Acknowledgment

The author is indebted to E. Chen for phosphor preparation, to B. Tartaglio for cathodoluminescent measurements, and Dr. C. K. Lui Wei for x-ray measurements.

Manuscript received Aug. 29, 1967; revised manuscript received Nov. 20, 1967.

Any discussion of this paper will appear in a Discussion Section to be published in the December 1968 JOURNAL.

REFERENCES

1. A. J. Dekker, "Solid-State Physics," Prentice Hall, Englewood, N. J. (1958).
2. C. W. Struck, U. S. Pat. 3,104,226 (May, 1961).
3. G. Blasse and A. Bril, *Appl. Phys. Letters*, **II**, 53 (1967).
4. F. A. Kroger and J. Bakker, *Physica*, **8**, 628 (1941).
5. H. G. Clapp and R. J. Ginther, *J. Opt. Soc. Amer*, **37**, 355 (1947).
6. A. Bril and H. A. Klasens, *Philips Research Repts.*, **7**, 421 (1952).
7. J. W. Gilliland and M. S. Hall, *Electrochem. Techol.*, **4**, 378 (1966).
8. Model 195—Perkin-Elmer Corp., Norwalk, Conn.
9. F. Weigel, V. Scherer, and H. Henschel, *J. Amer. Ceram. Soc.*, **486**, 342 (1965); R. C. L. Mooney, *J. Chem. Phys.*, **16**, 1003 (1948).
10. R. C. Ropp, *This Journal*, **111**, 311 (1964).
11. R. C. Ropp, Papers presented at the Cleveland Meeting of the Society, May 1-6, 1966, as Abstracts 20 and 21.
12. R. C. Taylor, S. A. Ward, and R. E. Rutherford, Jr., *Appl. Phys. Letters*, **6**, 128 (1965).
13. See, for example, E. Thilo, *Angew. Chem.*, **4** 1061 (1965) for a comprehensive review.
14. R. W. G. Wyckoff "Crystal Structures," 2nd ed. vol. 3, p. 15, Interscience Publishers, New York (1965).
15. J. D. Bowker (assigned to RCA), U.S. Pat. 3,164,744, Jan. 5, 1965.

Mixed Valence Europium Phosphors

W. A. McAllister*

Advanced Development Department, Westinghouse Electric Corporation, Bloomfield, New Jersey

ABSTRACT

Replacement of lanthanum in $LaPO_4$:Eu phosphors by barium-lithium pairs ($La_{1-2x}Ba_xEu_xLi_xPO_4$) leads to interesting emission characteristics: (*i*) line emission typical of Eu^{+3} for all ultraviolet excitation but most pronounced at short wavelength; (*ii*) A blue band for excitation wavelengths longer than 266 nm, for certain values of x; (*iii*) a uv band prominent under the same conditions favoring the blue emission. Results of x-ray and microscopic examination indicate a single-phase material. It is concluded that the line emission is due to an Eu^{+3} center which receives energy from the host, the bands to different Eu^{+2} centers.

The characteristic that makes trivalent rare earth ions attractive as activators in phosphor and laser applications, intense emission in a narrow spectral region, is a barrier to gross spectral shifts. Thus, while local site symmetry can alter the ratios of the intensities of the lines, the perceived colors are in the same range, *e.g.*, orange-red for Eu^{+3}, green for Tb^{+3}. Drastic spectral changes are associated with changes in oxidation state of the rare earths. Thus Eu^{+2} typically has band emission peaked at shorter visible wavelengths than the red lines of Eu^{+3}. Coexistence of both species in the same host has not been reported often since the preparative techniques favoring trivalent and divalent europium involve oxidizing and reducing atmospheres, respectively. Jaffe and Banks (1) did include an emission spectrum with both band and line characteristics for hydrogen fired CaO:Eu in a paper on europium activated oxides and sulfides. Similar results, cited herein, were noted when barium-lithium combinations were substituted for lanthanum in $LaPO_4$:Eu-type phosphors using the raw mix formulation $La_{1-2x}Ba_xEu_xLi_xPO_4$. The relative importance of the different emission characteristics, line and band, was found to be a function of europium concentration and excitation energy.

Experimental

Phosphors were prepared by firing raw mixes of Lindsay Chemical (99.9%) La_2O_3, Eu_2O_3, and Mallinckrodt Li_2CO_3, $BaCO_3$, and $NH_4H_2PO_4$ in an atmosphere consisting of nitrogen-2 v/o (volume per cent) hydrogen at 1250°C, using three 1-hr firings with grinding between firings. In the range $x = 0.02$ to 0.20 the products were single phase materials in which emission properties varied with excitation wavelength and the magnitude of x. Details of the emission and excitation spectra were examined at room temperature and with 254, 298, and 312 nm excitation wavelengths using a facility described previously (2). Reflectance characteristics were compared with a $BaSO_4$ standard, in integrating spheres attached to a Cary Model 15 double beam spectrophotometer. X-ray powder diagrams were made using a Philips instrument with Geiger counter detector.

* Electrochemical Society Active Member.

Results

Phosphors with $x = 0.06$ to 0.14 exhibited emission in (*i*) sets of lines in the red with peak intensities at 700, 610, and 595 nm, (*ii*) a blue band peaked at 480 or 420 nm, (*iii*) a uv band centered at 385 nm. The relative importance of these spectral features was a function of exciting wavelength and composition. These relationships are summarized as relative numerical intensities of emission peaks in Table I and, in part, by the emission spectra of Fig. 1. (Where the sets of lines are represented by the envelopes. These were not resolved further, the emphasis here being on

Table I. Relative plaque output of emission peaks for $La_{1-2x}Ba_xEu_xLi_xPO_4$ phosphors

Excitation wavelength, nm	Emission peak wavelength, nm	Relative intensity $x=0.06$	0.10	0.12	0.14
254	385	1	1	14	28
	480	2	1	7	15
	595	250	228	195	174
298	385	1	7	202	220
	420	0	50	0	0
	480	14	12	167	200
	595	34	33	18	15
312	385	1	14	231	260
	420	0	63	0	0
	480	11	17	216	250
	595	2	7	13	19

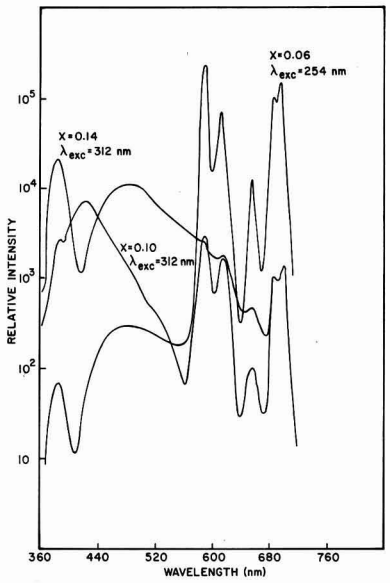

Fig. 1. Emission spectra of $La_{1-2x}Ba_xEu_xLi_xPO_4$ phosphors

the appearance of Eu^{+3} and Eu^{+2} in the same host rather than on the levels within Eu^{+3}.) In the latter presentation, a number of curves were omitted for clarity. Those remaining serve to illustrate the influence of europium concentration and excitation wavelength on emission, it being evident that, in general, high europium concentration and long uv excitation favor the band, and low europium concentration and short wave uv excitation the line, emissions. There is, however, an exception for the peaks under long wave excitation at 312 nm (see Table I), both band and line intensities increasing with concentration although the change is not so pronounced for the latter.

An explanation for this behavior may be found in Fig. 2, the excitation spectrum for emission peaked at 595 nm. This curve strongly resembles a similar one reported for $LaPO_4$:Eu phosphor (3) and consists of a broad band at short uv wavelengths with structure in the region from 300 to 400 nm. One such peak is at about 312 nm where the band emissions of our phosphors were excited most effectively. The result is the small contribution to the line emission noted above. The excitation spectra for the bands were also determined, the findings being summarized in Fig. 3 and the following comments: (*A*) The excitation bands for 385 and 420 nm emission peaks are essentially identical. (*B*) These excitation spectra overlap that of the

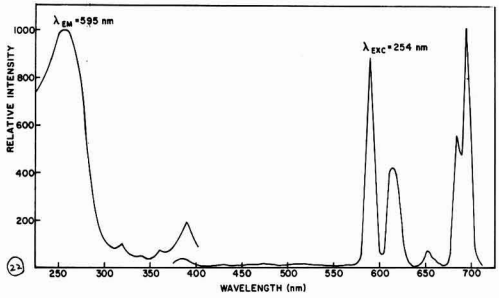

Fig. 2. Excitation spectrum for line emission in $La_{0.72}Ba_{0.14}Eu_{0.14}Li_{0.14}PO_4$ phosphor.

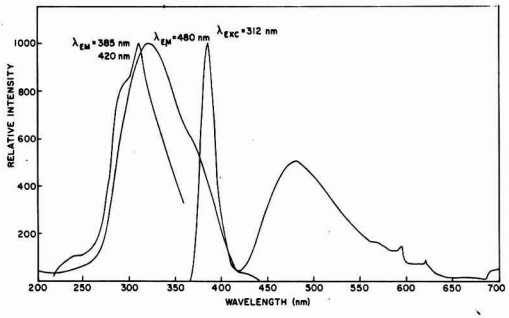

Fig. 3. Excitation spectra for emission bands in $La_{0.72}Ba_{0.14}Eu_{0.14}Li_{0.14}PO_4$ phosphor.

480 nm emission peak and both lie within the wavelength range 200-400 nm in which Eu^{+3} emission is excited. (*C*) The 385 nm emission band overlaps the excitation band for emission peaked at 480 nm, but not for that peaking at 420 nm.

Thus all emissions are present to some extent for incident radiation from 200 to 400 nm and the uv and blue band emissions appear together as a result of overlapping excitation spectra. The reasons for the appearance of a band peaked at 420 nm remained unclear so materials in which either barium or europium was omitted were prepared. In Table II we see that, for samples without europium, there is a new emission centered at 335 nm but only for short wave excitation. (The excitation and emission spectra for this band are shown in Fig. 4.) Band emissions are very weak and line and 385 nm uv peaks are totally absent. Samples without barium also have no uv emission, while the line emission is absent for long wave excitation; the most prominent feature in these formulations is the 420 nm band.

The absorption characteristics were next examined, using reflectance measurements on the powders. The diffuse reflectance curves for phosphors with both barium and europium, in the uv region (Fig. 5) are in general agreement with data for $LaPO_4$:Eu (3). Materials without europium did not absorb well in the short wave region while those without barium absorbed best throughout the entire interval.

Discussion

The line emission in this host is essentially a duplicate of that presented earlier for $LaPO_4$:Eu (3). The major peaks, 595 and 700 nm, are due to the $^5D_0 - {}^7F_1$ magnetic dipole and $^5D_0 - {}^7F_4$ electric dipole transitions, respectively, while 610 nm emission is due to the $^5D_0 - {}^7F_2$ electric dipole transition. The occurrence of these lines, in appreciable intensities, in the both $LaPO_4$ host and our modified material, is interesting. Recent work on crystal structure sensitivity of Eu^{+3} emission (4) associates prominent 610 and 700 nm emission with occupation of sites lacking a center of inversion symmetry ($YAl_3B_4O_{12}$:Eu), strong 595 nm emission in a host (Ba_2GdNbO_6) with a center of inversion. The presence of all three in $LaPO_4$:Eu suggests several different crystallographic sites for the activator.

Table II. Relative plaque output of emission peaks for $La_{1-2x}(Ba \text{ or } Eu)_xLi_xPO_4$ phosphors.

Excitation wavelength, nm	Emission peak wavelength, nm	Relative intensity 0.06 Ba	0.12 Ba	0.06 Eu	0.12 Eu
254	335	155	119	0	0
	420	1	1	24	1
	480	2	1	3	4
	595	0	0	7	2
312	420	1	1	24	6
	480	0	1	4	7

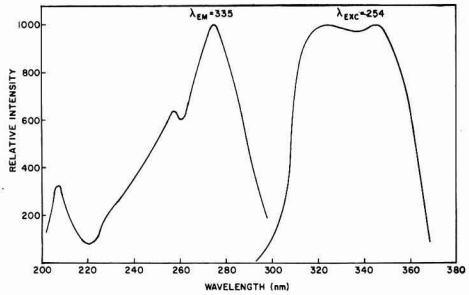

Fig. 4. Excitation and emission of $La_{1-2x}Ba_xLi_xPO_4$ phosphors

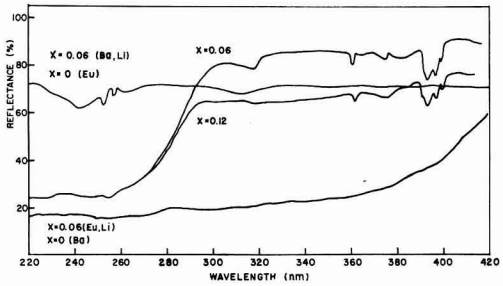

Fig. 5. Diffuse reflectance spectra for $La_{1-2x}Ba_xEu_xLi_xPO_4$ phosphors.

The crystal structures of rare earth phosphates have been reported (5, 6), both hexagonal and monoclinic forms being important. The mineral monazite, the $LaPO_4$:Eu and our barium modification all have the monoclinic structure, with over-all symmetry $P^2/n(C^5_{2h})$. The rare earth in monazite is coordinated to the corners of four different phosphate groups by short (2.46Å) bonds and to two additional tetrahedra by four longer (2.66Å) bonds. Thus the local site has inversion symmetry and the strong 595 nm emission is expected for europium in such sites. The appearance of emission expected for sites lacking inversion symmetry must mean that replacement of lanthanum by europium in $LaPO_4$:Eu produces two types of sites, one having a small deviation from inversion symmetry.

The emission bands noted in $La_{1-2x}Ba_xEu_xLi_xPO_4$ are to be associated with the presence of Eu^{+2}. Such divalent europium emission bands have been reported with peaks at 480 nm in oxides and with various peaks in the range 400-600 nm in halides and silicates (7). This flexibility suggests extension to the near uv as reasonable. Further the excitation peak for the 385 (and 420) nm band is at 310 nm, near the 320 nm absorption peak for Eu^{+2} ($EuCl_2$) in water (8). Interestingly the other broad absorption band found in the same investigation has a maximum at 248 nm so that short wave excitation of the Eu^{+2} centers is possible and (see Fig. 1) observed.

There remains the 420 nm emission band for consideration. Since it has an intensity in samples without barium which can be an appreciable fraction of the value noted in phosphors with both europium and barium, the emission must be due to isolated europium centers. While these are primarily Eu^{+2} centers, the data in Table II show that there is also 595 nm line emission in samples containing europium alone. Increased excitation wavelength and low europium concentration favor the blue band emission. The structure evident in the emission spectra where this band is pronounced (Fig. 1) indicate that it appears in addition to, rather than instead of, the 385 and 480 nm emission. This implies a second phase but none was detected in the x-ray powder patterns or on microscopic examination under long and short wave excitation. Etching with mineral acids also did not disclose a surface phase different from the bulk material. The appearance of this peak at excitation wavelength-concentration combinations for which the line and band features are changing rapidly may signify disordering of the species substituting for host lanthanum.

The uv band emission peaked at 335 nm in $La_{1-2x}Ba_xLi_xPO_4$ phosphors is not evident when europium is also present. The range covered by the band, 310-360 nm, coincides with that in which the other europium band and line emissions are well excited and cannot be isolated when europium is included. Also absorption in europium-containing materials is much better in the range where this host band is excited. The appearance of emission on introduction of Ba-Li pairs does indicate a change in the host favoring absorption in the short wave uv, where phosphates are usually transparent.

While the appearance of Eu^{+2} band emission is most simply explained by the use of slightly reducing atmosphere, the number of such bands demands some qualifying statement. A pertinent observation is the absence of any band emission when strontium or calcium were used for barium in a similar series of phosphors. Since the reduction of europium depends on the availability of an electron the appropriate differences between barium and the other alkaline earths, must be sought. One such comparison, that of orbital radii (9) and energy level, is given below with La^{+3} included. From the standpoint of energy level and radius the barium is the best match for La^{+3}. Further the larger radius of Ba^{+2} permits greater overlap with nearly O^{-2} ions when barium replaces lanthanum and, as barium (and europium) concentration increases the possibility of the Ba-O-Eu configuration does also.

Chemical species	Orbital radius, Å	Orbital
Ba^{+2}	0.87	5p
Sr^{+2}	0.68	4p
Ca^{+2}	0.54	3p
La^{+3}	0.819	5p

Now the spectral properties of europium have been investigated and the importance of charge transfer from the O^{-2} anion of the absorbing group to Eu^{+3} established for both liquids (10) and solids (11). This includes $LaPO_4$:Eu (3) and, in view of the similarity in Eu^{+3} excitation and emission in the two systems, the barium-containing materials we have prepared. This tendency of the oxygen to transfer an electron to europium coupled with the greater overlap of barium with the oxygen may lead to complete transfer, *i.e.*, reduction of Eu^{+3} to Eu^{+2}, in configurations where barium and europium are separated by an oxygen anion. Exchange between cations separated by an anion have been used to correlate bonding with type of magnetic behavior observed (12) and extended to include optical phenomena such as luminescence quenching (13) and efficiency (14) in rare earth activated solids. It is proposed that the appearance of band emission here is due to a similar mechanism.

Acknowledgment

The writer wishes to express his gratitude for the spectral measurements of W. A. Thornton and R. J. Wisnieski and the x-ray diffraction results provided by C. K. Lui Wei.

Manuscript received Sept. 14, 1967; revised manuscript received Dec. 7, 1967. This paper was presented at the Dallas Meeting, May 7-12, 1967, as Abstract 76.

Any discussion of this paper will appear in a Discussion Section to be published in the December 1968 JOURNAL.

REFERENCES

1. P. M. Jaffe and E. Banks, *This Journal*, **102**, 518 (1955).
2. W. A. Thornton, Paper presented at the San Francisco Meeting of the Society, May 10-14, 1965, Extended Abstracts, Abstract 38.
3. W. L. Wanmaker, A. Bril, J. W. ter Vrugt, and J. Broos, *Philips Research Repts.*, **21**, 270 (1966).
4. G. Blasse, A. Bril, and W. C. Nieuwpoort, *J. Phys. Chem. Solids*, **27**, 1587 (1966).
5. R. C. L. Mooney-Slater, *Z. Krist.*, **117**, 371 (1962).
6. R. W. G. Wyckoff, *Crystal Structures*, **III**, 33 (1965).
7. H. G. Jenkins and A. H. McKeag, *This Journal*, **97**, 415 (1950).
8. F. D. S. Butement, *Trans. Faraday Soc.*, **44**, 617 (1948).
9. J. T. Waber and D. T. Cromer, *J. Chem. Phys.*, **42**, 4116 (1965).
10. C. K. Jorgensen, *Mol. Phys.*, **5**, 271 (1962).
11. G. Blasse and A. Bril, *Solid State Commun.*, **4**, 373 (1966).
12. See, for example, J. B. Goodenough, Mol. Designing Mater. Devices *1965*, 42, and references cited therein.
13. L. G. Van Uitert and L. F. Johnson, *J. Chem. Phys.*, **44**, 3514 (1966).
14. G. Blasse, *J. Chem. Phys.*, **45**, 2356 (1966).

Zinc Oxide and Zinc-Cadmium Oxide Phosphors

W. Lehmann*

Westinghouse Research Laboratories, Pittsburgh, Pennsylvania

ABSTRACT

Zinc oxide phosphors may emit in four different bands, the ultraviolet near-edge emission, the common green band (possibly involving sulfur), a yellow-orange band due to selenium, and a red to near infrared band due to ammonia. About 10% of ZnO can be replaced by CdO with a corresponding shift, to lower energies, of the optical absorption edge, of the near-edge emission, and of the green emission. The possibility of an impurity activation due to anion substitution is discussed.

The best known luminescence of zinc oxide consists of a rather broad and structureless band in the green centered at about 2.4-2.45 ev. Partial replacement of ZnO by MgO and resulting shift of the green emission toward blue was reported by Smith(1). We have investigated the influence of a similar partial replacement of ZnO by CdO which does not seem to have been reported before.

Zinc oxide itself may emit in, at least, four different emission bands which are shown in Fig. 1. They are:

(*a*) The near-edge emission, a narrow and somewhat irregularly shaped band in the near-ultraviolet with the peak at about 3.18-3.20 ev at room temperature which is near the optical absorption edge of ZnO (~3.25 ev).

(*b*) The common green emission band whose origin is still a matter of considerable controversy [a discussion of it is given in ref. (2)].

(*c*) A yellow-orange band with the peak at 1.95–2.0 ev which appears in the presence of selenium (3, 4).

(*d*) A red to infrared emission band with the peak at about 1.55 ev which does not seem to have been reported before. We observed this emission in nominally pure ZnO fired in NH_3 at 1000°-1100°C. Similar firings in either H_2 or N_2 are ineffective.

Our work on the influence of a gradual replacement of ZnO by CdO was limited to the first two of these four bands. The phosphors were prepared by firing either ZnO (luminescent grade purity) or intimate mechanical mixtures of ZnO and $CdCO_3$ (reagent grade) under conditions facilitating the one or the other emission band.

The green emission of ZnO is known to require slightly reducing firing conditions (5) and is observed to be enhanced by the presence of traces of sulfur (1, 3, 6). However, and in contrast to ZnO, an addition of a trace of sulfur to (Zn,Cd)O gives only poor results. Apparently, the sulfur reacts mainly with the cadmium and keeps it separate as CdS. Therefore, the (Zn,Cd)O phosphors were fired, without deliberate addition of sulfur, in argon, at about 1100°C. Addition of iodine to facilitate particle growth is permissible and was not observed to have an effect on the emission spectrum which, in every case, consists of a single broad band corresponding to the green band of ZnO with little or no contribution of the near-edge emission.

The preparation conditions used to obtain near-edge emission in (Zn,Cd)O phosphors were those reported for ZnO phosphors (7). This technique completely isolates the near-edge emission with no detectable other emission bands.

Pure CdO ordinarily occurs in the cubic NaCl lattice. It is reported to be soluble in hexagonal ZnO (wurtzite lattice) only up to 4.9% (8). We observed CdO to be soluble in ZnO up to about 10 m/o (molar per cent) as determined by x-ray analysis, by optical reflection spectra, and by luminescence emission spectra. X-ray diffraction spectra of some samples are shown in Fig. 2 where separate lines, corresponding to the NaCl lattice of CdO, are visible at 15%, but not at 10% or below, of CdO added to the ZnO. Higher amounts of added CdO remain undissolved as separate phase which is clearly visible also at the dark body color of the samples. Evaluation of the x-ray spectra permits one to determine mean nearest neighbor dis-

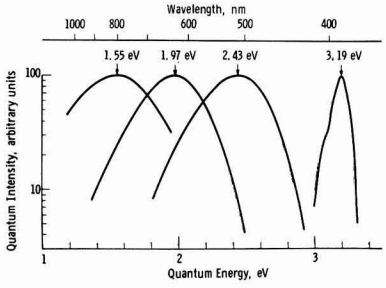

Fig. 1. Four luminescence emission bands observed in ZnO phosphors.

* Electrochemical Society Active Member.

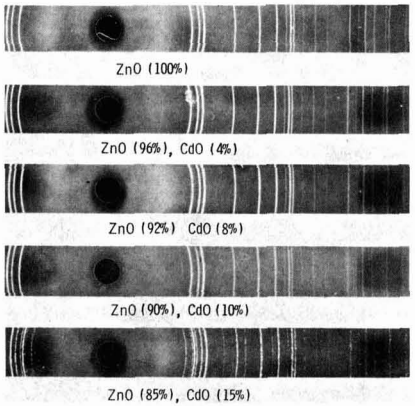

Fig. 2. X-ray diffraction spectra of (Zn,Cd)O

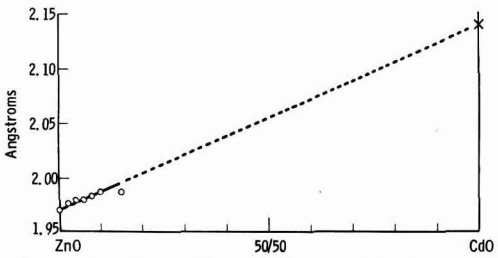

Fig. 3. Next-neighbor distances of hexagonal (Zn,Cd)O; o = measured and x = hypothetical.

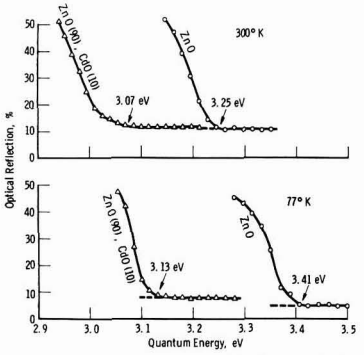

Fig. 4. Optical reflection spectra of ZnO and of ZnO (90%)-CdO (10%).

tances in the lattice. Plotted as a function of the CdO concentration in Fig. 3, they are all, within the accuracy of these measurements, on a straight line connecting the values for ZnO (1.97Å) and the, in reality nonexistent, hexagonal CdO (2.14Å).[1] Hence, Vegard's law is fulfilled at least within the limited range of solubility.

Gradual replacement of ZnO by CdO causes the quantum energy corresponding to the optical absorption edge (or whatever is measured as such under ordinary conditions) to decrease. As a consequence, pure ZnO ordinarily is white, but a solid solution of 90% ZnO-10% CdO is slightly yellow in body color. Some optical reflection spectra demonstrating this shift of the absorption edge are given in Fig. 4.

[1] Determined from the sum of tetrahedrical standard radii, Zn = 1.31Å, Cd = 1.48Å, O = 0.66Å.

The approximate peak position of the near-edge emission as a function of the CdO concentration is shown in Fig. 5 and compared with the corresponding shift of the absorption edge. Both curves are approximately parallel. While the near-edge emission of ZnO is in the near ultraviolet, that of a (Zn,Cd)O phosphor containing 10% of CdO is in the visible violet. Two measured actual emission spectra are given in Fig. 6. Gradual replacement of ZnO by CdO causes also the green ZnO emission to move towards lower quantum energies, *i.e.*, toward yellow (Fig. 7). Measured spectra of ZnO, of a (Zn,Cd)O containing 10% of CdO and, for comparison, of a (Zn,Mg)O phosphor containing 20% of MgO, are shown in Fig. 8.

Conclusions to the origin or luminescence in ZnO phosphors may be drawn from these results. Various models have been proposed in the literature linking either the near-edge emission, or the common green

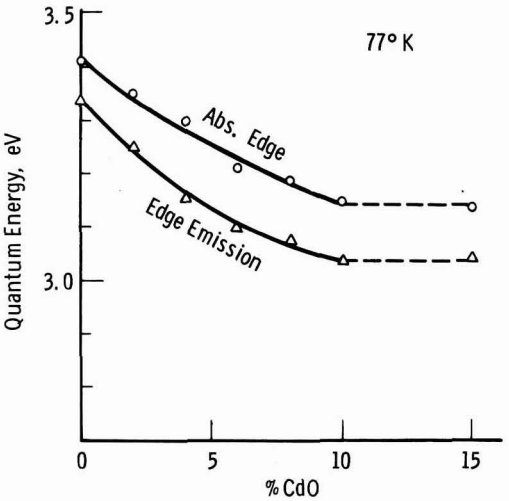

Fig. 5. Optical absorption edge and center of near-edge emission (excited by ultraviolet of 365 nm at 77°K) of (Zn,Cd)O as function of the CdO concentration.

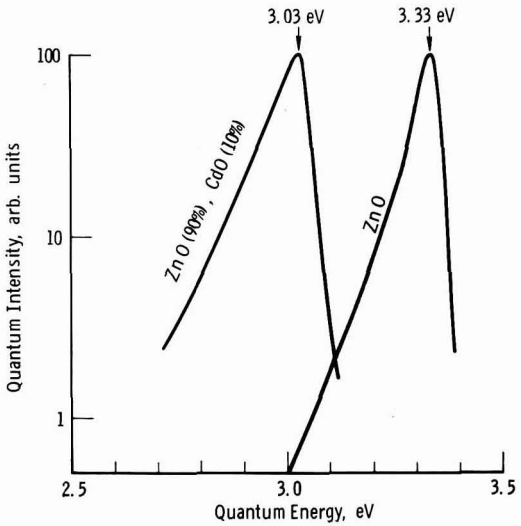

Fig. 6. Near-edge emission spectra of ZnO:Ga and of ZnO (90%)-CdO (10%):Ga excited by utlraviolet of 365, nm at 77°K.

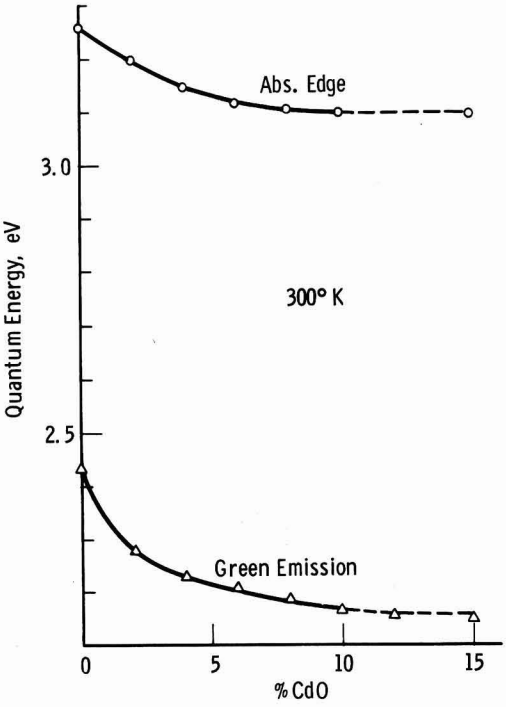

Fig. 7. Optical absorption edge and peak position of the "green" emission (excited by ultraviolet of 365 nm, at room temperature) of (Zn,Cd)O as function of the CdO concentration.

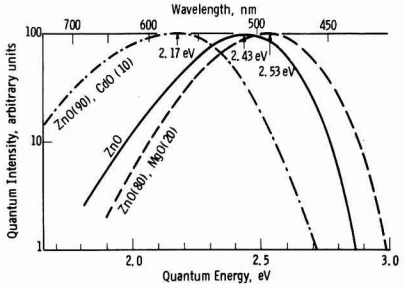

Fig. 8. "Green" emission band spectra of ZnO, of ZnO (90%)-CdO (10%), and of ZnO (80%)-MgO (20%), all excited by ultraviolet of 365 nm at room temperature.

emission, or the yellow-orange emission of ZnO to native lattice defects (*e.g.*, oxygen vacancies) but there seems to be little agreement between the authors. Alternatively, it has been proposed that the green emission band of ZnO might be due to traces of sulfur dissolved in the ZnO lattice (3), and a correlation between the intensity of the green emission and deliberately added sulfur (1, 3, 6) and similar correlations between the yellow-orange emission and deliberately added selenium (3, 4, 6), and between the infrared band and the ammonia atmosphere during firing, undoubtedly do exist. The observation of at least some green emission in ZnO to which no sulfur was intentionally added is not considered to be a sure criterion since sulfur may easily be present in all ordinary "pure" ZnO to start with, or in the carbon black recommended by Leverenz (5), or even in the air, especially of a laboratory. Traces of sulfur in green emitting ZnO are not easily analyzed and may be present only in the ppm range.

The valence band of the predominantly ionic ZnO is mainly determined by the anion, *i.e.*, oxygen. Sulfur and selenium are isoelectronic to oxygen. If they are dissolved in ZnO substituting for oxygen, their effect may be to split states out of the valence band into the forbidden band gap, and particular emission may be due to an electron transition between such state and one of the band edges. Luminescence due to an isoelectronic anion impurity in a II-VI compound, CdS:Te, is known already (9). A similar situation is proposed for the red emission which appears to involve nitrogen and hydrogen (since firing in pure nitrogen, or in pure hydrogen, are ineffective) and which is proposed to be due to N-H pairs. A nitrogen replacing an oxygen atom in ZnO would be an acceptor, an interstitial hydrogen is a donor, consequently, a pair of both would be electrically as neutral as a sulfur or selenium substituting for an oxygen atom.

Gradual replacement of zinc by cadmium shifts the green ZnO emission towards lower energy similar to a corresponding of many emission bands in (Zn,Cd)S phosphors which fairly unambiguously can be understood on the basis of a Schön-Klasens type of recombination (10). Hence, at least the green ZnO emission appears to be due to an electron transition from or near the conduction band edge into a valence state of the sulfur located above the upper edge of the valence band of the ZnO. The same probably holds also for the yellow-orange emission due to selenium and for the infrared emission due to ammonia although corresponding investigations involving a gradual replacement of zinc by cadmium are not yet made. The near-edge emission of ZnO and of (Zn,Cd)O seems to behave differently in some respects, and its mechanism is still too uncertain to be discussed here.

A more practical consideration concerns the availability of ZnO-type phosphors of various emission colors due to gradual replacement of up to 10 m/o of ZnO by CdO. This shifts the extremely fast near-edge emission of n-type doped ZnO (7) out of the near ultraviolet into the visible violet. The energy efficiency of catholuminescence seems to be little affected by this shift, and although it is not too high (estimated: 1-2%), these materials may be useful in applications where high speed of response ($\sim 10^{-9}$ sec or shorter) is imperative. By contrast, the efficiency of catholuminescence of green ZnO ($\sim$ 6-7%) reduces to about 2-3%, at best, as soon as some ZnO is replaced by CdO. This lower efficiency of yellowish (Zn,Cd)O (made without sulfur) compared to green ZnO (made with sulfur) seems to be due to the resistance of sulfur to be dissolved in the material whenever cadmium is present. At the moment, it is not known whether the situation can be improved.

Manuscript received Oct. 20, 1967; revised manuscript received Nov. 15, 1967. This paper was presented at the Dallas Meeting, May 7-12, 1967, as Abstract 28.

Any discussion of this paper will appear in a Discussion Section to be published in the December 1968 JOURNAL.

REFERENCES

1. A. L. Smith, *This Journal*, **99**, 155 (1952).
2. A. Pfahnl, *ibid.*, **109**, 502 (1962).
3. S. M. Thomsen, *J. Chem. Phys.*, **18**, 770 (1950); U. S. Pat. 2,573,817.
4. L. Y. Markowski and N. S. Orshanskaya, *Optics and Spectroscopy*, **9**, 40 (1960).
5. H. W. Leverenz, "An Introduction to Luminescence of Solids," p. 67, New York—London (1950).
6. Confirmed in our laboratory.
7. W. Lehmann, *Solid-State Electronics*, **9**, 1107 (1966).
8. Gmelin's Handb. Anorg. Chem., 8 Edition "Cadmium," p. 431.
9. A. C. Aten and J. H. Haanstra, *Phys. Lett.*, **11**, 97 (1964).
10. W. Lehmann, *This Journal*, **113**, 449, 788 (1966); **114**, 83 (1967).

Doping of Epitaxial Silicon Films

W. H. Shepherd

Fairchild Semiconductor, Research and Development Laboratory, Palo Alto, California

ABSTRACT

The doping of epitaxial silicon layers deposited by the hydrogen reduction of $SiCl_4$ has been studied. The dopants used were phosphorus, arsenic, and antimony introduced as the trichlorides. In each case for fixed dopant to silicon ratios in the gas phase the film resistivity was found to increase with rising temperature and decrease with increasing growth rates. The results are explained by a model which takes into consideration both the transfer and thermodynamic properties of the reactor system. An analysis of the results then leads to values for the activity coefficients for phosphorus, arsenic and antimony in silicon.

In general, control of resistivity in epitaxial silicon films has not presented any serious problems and, as a result, there has been no strong incentive to investigate the mechanisms involved. Only Raichoudhury and Fergusson (1) have attempted an analysis. Wang *et al.* (2) showed that for a constant arsenic/silicon ratio in the gas phase the resistivity of layers deposited by the hydrogen reduction of $SiCl_4$ was sensitive to temperature and to growth rate, but they made no serious attempt to establish the reasons. Nuttall (3) presented similar data for phosphorous and antimony, but again was unable to provide a good explanation for his results. In this paper, a model is proposed which is felt to be of general application. It is tested here for the specific case of layers deposited by the hydrogen reduction of $SiCl_4$ and doped with phosphorus, arsenic, or antimony using trihalide sources of the impurities.

Theory

The resistivity of an epitaxial layer is determined by the relative rates at which silicon and dopant atoms are added to the film. A previous paper (4) considered the processing governing the deposition of silicon by hydrogen reduction of $SiCl_4$ in horizontal reactors. Here it will be assumed that the "deposition" of dopant at the silicon surface can be treated in the same manner. It is in order then to review briefly the silicon deposition process.

Rate of Deposition of Silicon

Figure 1 shows film growth rate plotted logarithmically against $1/T$ °K^{-1} for the small, six-wafer horizontal reactor used in this work. This relationship is typical, qualitatively at least, of most multiwafer reactors using hydrogen reduction of $SiCl_4$. The region at lower temperatures in which the growth rate varies exponentially as $1/T$ °K^{-1} is called the kinetic region since it is thought that at these temperatures the rate-limiting process is the chemical reaction at the silicon surface. As the temperature is raised the chemical reaction rate increases rapidly, the surface concentration of $SiCl_4$ falls, and the concentration gradient of $SiCl_4$ normal to the surface steepens in order to meet the requirements of the faster surface reaction. A point is eventually reached where the surface concentration of $SiCl_4$ is so much smaller than the bulk concentration that a further decrease in its value produces no noticeable increase in the concentration gradient. In this condition $SiCl_4$ is being transferred from the gas stream at the maximum rate possible. It is now the transfer properties of the gas stream which determine the over-all deposition rate, and since these properties vary only slowly with temperature the mass-transfer region is characterized by a very low-temperature sensitivity of growth rate. In Fig. 1 a broken line shows how the growth rate should vary if transport limited throughout the temperature range (4).

In ref. (4) (Eq. 19) a model was developed to describe the deposition process in the mass transfer region. According to this model the rate of deposition, G, is given by an equation of the form

$$G = \Psi_s x_s - A\{(1 + 2\Psi_s x_s)^{1/2} - 1\}^2 \qquad [1]$$

Th first term on the R.H.S. of the equation represents the flux of silicon toward the growing surface as $SiCl_4$ while the second term allows for the fact that silicon is lost from the surface as $SiCl_2$. In Eq. [1] Ψ_s is a gas transfer coefficient for $SiCl_4$ in H_2 and has the same units as those chosen for G, *e.g.*, μ min^{-1}, since x_s is the mole ratio of $SiCl_4$ in the initial, unreacted gas stream and is dimensionless. The parameter A contains both thermodynamic and transfer terms but is essentially temperature independent and a constant for a specific deposition system.

For growth rates less than 1.5μ min^{-1} the second term can be neglected with a resultant error of only a few per cent and even at 2.5μ min^{-1} the error incurred is less than 20%. For simplicity then it will be assumed for the purposes of this paper that the growth rate is given simply by the first term in Eq. [1], and hence is linear in $SiCl_4$ concentration, at least in the mass transfer region.

In the kinetic region the dependence of growth rate on concentration has not been determined. However the rate may be expressed in the form

$$G = f(T, x_s)\Psi_s x_s \qquad [2]$$

where f is a function of temperature and possibly of $SiCl_4$ concentration also. The growth rate *vs.* temperature data of Fig. 1 were obtained at a mole ratio of $SiCl_4$ of 0.0048 and by conducting the experiments in the present work at the same concentration, (actually at a mole ratio of 0.0050), f can be determined empirically as the ratio of the actual growth rate to that expected for a mass transfer controlled process at

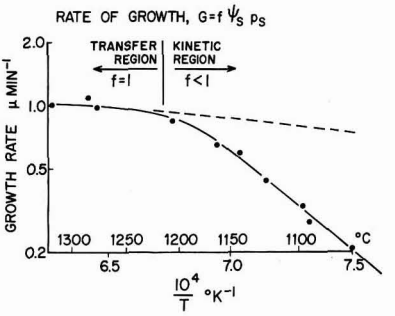

Fig. 1. Temperature dependence of silicon deposition rate for $SiCl_4$ concentration of 0.48 m/o.

the same temperature (*i.e.*, as indicated by the broken line). Actually then, Eq. [2] can be regarded as a general one in which $f = 1$ in the mass transfer region.

Deposition of Dopant

The treatment adopted here parallels that used to develop the model for epitaxial deposition of silicon. That is, it is assumed that the reduction of the dopant compound takes place only at the heated surface, *i.e.*, not in the gas phase or on the reactor walls, that all surface reactions are fast so that rate processes are mass transfer controlled, and that all dopant species at the surface, whether in the silicon or in the adjacent gas phase, are in thermodynamic equilibrium. The assumption that the rate processes are transfer controlled throughout the temperature range employed and that for none of the dopants is there a kinetic region such as observed for silicon is reasonable in view of the ease with which all of the pertinent chlorides are reduced in hydrogen at temperatures well below those of concern in this work. The surface equilibria of concern here are

$$XCl_3 + 3/2\,H_2 \rightleftarrows X(g) + 3HCl$$
$$4X \rightleftarrows 2X_2 \rightleftarrows X_4$$
$$X(ss) \rightleftarrows X(g)$$

where X = P, As, or Sb and X(ss) represents the dopant in solution at the silicon surface. Volume diffusion in the solid will be ignored. Thermodynamic data (5) indicate that for the experimental conditions used the reduction of the compounds, XCl_3, is essentially complete and further that for arsenic and antimony the only gaseous elemental species of interest at the silicon surface are monatomic. For phosphorus, particularly at the lower end of the experimental temperature range, both P and P_2 should be considered, but since the only phosphorus doping data amenable to analysis were taken at the very upper limit of temperature, *i.e.*, 1340°C, it happens that in this case also only the monatomic species need be considered.

The situation then is that dopant compound transfers to the surface where it is completely reduced to monatomic elemental dopant. Some of this dopant is incorporated in the growing silicon film while some remains in the gas phase adjacent to the surface and in equilibrium with its solution in the silicon. Since there is a gradient of elemental dopant out from the surface, loss occurs from the surface to the bulk gas stream. In a steady state, which will be assumed to occur instantaneously, the material balance for dopant at the surface requires that the rate of transfer toward the surface in the form of the halide equals the rate of uptake by the film plus the rate of loss in the elemental form to the gas stream.

The rate of transfer of dopant halide to the surface per square centimeter, assuming a model analogous to that for silicon deposition, is

$$F_D = n\Psi_D x_d \qquad [3]$$

where x_d is the mole ratio of halide in the gas stream, Ψ_D is the transfer coefficient for the halide in hydrogen, and n is an integer denoting the number of atoms of dopant per molecule of halide. Since $n = 1$ for all the halides used, it will be omitted from subsequent equations. With Ψ_D in μ min^{-1} the flux of dopant F_D has the same units.

The rate of transfer of elemental dopant away from the surface F_E (μ min^{-1}) is (ref. 4, Eq. 9)

$$F_E = \Psi_E x_E \qquad [4]$$

where x_E is the mole ratio of element in the gaseous equilibrium region close to the surface and Ψ_E the transfer coefficient for elemental dopant.

The rate of incorporation of dopant in the film, F_I, can be written again in μ min^{-1}, as

$$F_I = GR_s \qquad [5]$$

where R_s is the atom ratio of dopant in the silicon at the silicon-gas interface. Since we have identical numbers of atoms per cubic centimeter for dopant and silicon the film thickness ratio is identical with the atom ratio.

One further relationship is necessary. It has been assumed that equilibrium exists between gaseous and dissolved dopant, and since both are in monatomic dispersion and in general the solutions are dilute so that Henry's law may be applied, the equilibrium can be expressed in the form.

$$x_E = \gamma R_s \qquad [6]$$

In all experiments the ambient pressure was 1 atm so that x_E is equivalent to a partial pressure of gaseous monatomic dopant in atmospheres and if, for the present purposes, unit activity of the dopant is defined as 1 atm pressure of monatomic species then γ is the activity coefficient for the dopant in silicon.

The dopant material balance previously enunciated is otherwise stated as

$$F_D = F_I + F_E$$

Substituting from Eq. [3] through [6] and rearranging gives

$$\alpha = \frac{R_s}{R_G} = \frac{1}{f(1 + \Psi_E\gamma/G)} \frac{\Psi_D}{\Psi_S} \qquad [7]$$

where R_G is x_d/x_s the atom ratio of dopant to silicon in the initial gas stream and α is a distribution coefficient defined in the same manner as that used in conventional crystal growth from a melt. From Eq. [7] it appears that the effects to be investigated are mainly described by the term $(\Psi_E\gamma)/G$ and appear when this term is larger than unity. The behavior of α for different magnitudes of $\Psi_E\gamma/G$ is considered briefly now.

(*a*) If $(\Psi_E\gamma)/G << 1$, Eq. [7] simplifies to

$$\alpha = \frac{1}{f} \cdot \frac{\Psi_D}{\Psi_S} \qquad [8]$$

In the mass transfer region where $f = 1$ the distribution coefficient is simply the ratio of the transfer coefficients for dopant and silicon, and it is not influenced by growth conditions. Further, since the transfer coefficients probably do not differ by much more than a factor of two at the most, it is possible to predict that α should have values in the range 0.5-2.0. In the kinetic range f becomes small and α may increase above this range.

(*b*) At the other extreme when $(\Psi_E\gamma)/G >> 1$, Eq. [7] becomes

$$\alpha = \frac{1}{f} \cdot \frac{G}{\Psi_E\gamma} \cdot \frac{\Psi_D}{\Psi_S} \qquad [9]$$

which, since $G = f\Psi_S x_s$, can be further reduced to

$$\alpha = \frac{\Psi_D}{\Psi_E} \cdot \frac{x_s}{\gamma} \qquad [10]$$

As before Ψ_D/Ψ_E can be expected to be close to unity and to remain constant, but now α is directly proportional to the concentration of $SiCl_4$, x_s, and inversely proportional to the activity coefficient γ and hence is very much affected by growth conditions.

(*c*) The third situation is that in which $\Psi_E\gamma/G \cong 1$. In this case α may tend toward situation (*a*) or (*b*) depending on the exact conditions of growth.

The critical factor determining the magnitude of $\Psi_E\gamma/G$ is γ. Changing dopants will not affect Ψ_E greatly and though, in principle G is infinitely variable, in practice growth rates are normally maintained within a narrow range, *e.g.*, 0.3-1.0 μ/min. The activity coefficient, γ, however, may be varied over several orders of magnitude either as a function of temperature or dopant. Thus if γ is very large, *i.e.*, the dopant evaporates readily from silicon, then the situa-

tion illustrated in (*b*) pertains and the distribution coefficient, α, is sensitive to growth parameters. If γ is small so that the dopant has no tendency to re-evaporate from the silicon, then the situation in (*a*) holds and α is insensitive to growth conditions.

Experimental Details

The experiments were carried out in a small, six-wafer horizontal reactor previously described (4). The arrangement used then was modified by replacing the evaporative $SiCl_4$ source with a liquid feed source. The $SiCl_4$ flow was metered through a Fischer-Porter 1/16-08 size meter. This feed method was employed in order to maintain a constant atom ratio of dopant to silicon in the gas mixture in the simplest manner. The $SiCl_4$ was doped in all cases with the trichloride of the element to be used, *i.e.*, with PCl_3, $AsCl_3$, or $SbCl_3$. First, a master solution was prepared by adding a known volume, approximately 0.5 ml, of the chloride to 1000 ml of undoped $SiCl_4$ (better than 100 ohm-cm n-type) in a fused quartz flask. This was shaken and allowed to stand for 24 hr to ensure mixing. The solutions doped with arsenic and antimony were then chemically analyzed and found to be within 20% of the expected concentrations. In the case of the phosphorus master solution, analysis was considered to be too inexact to be worthwhile. The master solutions were diluted further in the same manner to produce the final mixtures. The atom ratios of dopant to silicon used were: phosphorus 1.1×10^{-6}; arsenic 1.2×10^{-6}; antimony 8.8×10^{-6}.

Epitaxial layer resistivities were determined from V/I and groove and stain measurements on 15-20μ thick deposits grown on boron doped substrates of approximately 1 ohm-cm p-type. Quoted resistivities and growth rates were averaged from measurements on three wafers. Temperatures were measured optically and corrected by amounts varying from 140°C at the highest temperature used to 100°C at the lowest.

Results

General discussion.—Figure 2 shows the influence of deposition temperature on layer resistivity. All experiments were conducted at a constant $SiCl_4$ concentration of 0.5 m/o (mole per cent) ($\cong 1.0\mu$ min^{-1} at 1250°C) rather than a constant growth rate, since this was experimentally simpler to control. Phosphorus exhibits virtually no change, antimony, a very marked increase in resistivity with rising temperature, while arsenic is intermediate in behavior. In Fig. 3, the distribution coefficients calculated from the resistivity data are plotted *vs.* deposition temperature. The most notable feature is the very low value of α for antimony doping. Reference to the theoretical discussion of Eq. [7] through [10] indicates that for antimony in silicon γ is large and is the predominant factor in α, for phosphorus γ is small, while for arsenic γ has an intermediate value.

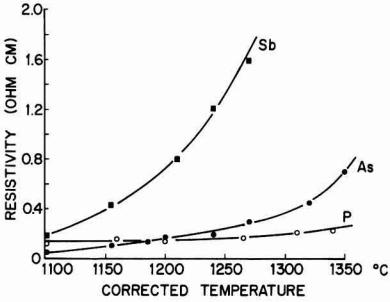

Fig. 2. Temperature dependence of epitaxial layer resistivity for $SiCl_4$ concentration = 0.5 m/o (= 1μ min^{-1} at 1250°C).

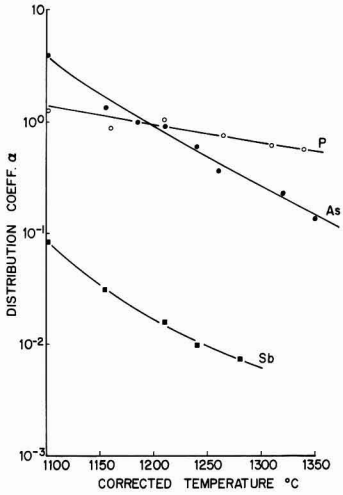

Fig. 3. Temperature dependence of α for P, As, and Sb. $SiCl_4$ concentration 0.5 m/o (= 1μ min^{-1} at 1250°C).

Figure 4 presents data on the influence of film growth rate on layer resistivity at temperatures in the mass transfer region. For the phosphorus study, a higher than normal temperature had to be employed to obtain readily observable effects. The distribution coefficients calculated from these data are plotted as a function of growth rate in Fig. 5. The results are consistent with those obtained from the temperature dependence of α on the basis of the proposed doping mechanism. Thus, from Eq. [8] if γ is small, α should tend to a limiting value, probably in the range 0.5-2.0 at high growth rates. This is observed for phosphorus. If γ is large, α becomes small and directly proportional to growth rate. The data for antimony satisfy these conditions. For arsenic, the data appear to show a slight curvature, but insufficient to be conclusive and indicate no close approach to a limiting value.

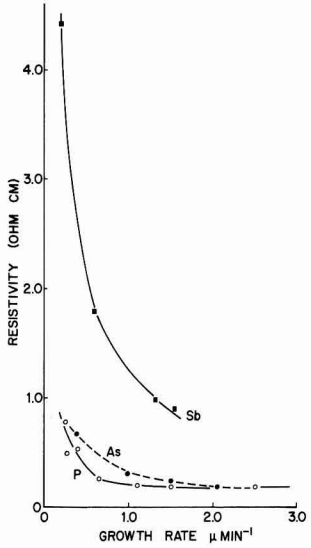

Fig. 4. Growth rate dependence of epitaxial layer resistivity for P(1340°C), As(1240°C), and Sb (1270°C).

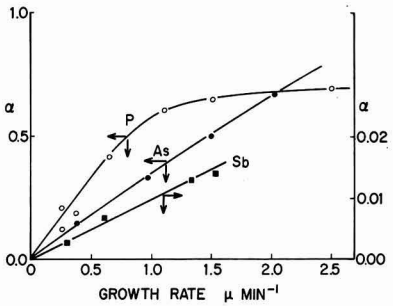

Fig. 5. Growth rate dependence of α for P(1340°C), As(1240°C), and Sb(1270°C).

Calculation of activity coefficients.—Equation [7] can be rearranged to give

$$\gamma = \frac{\Psi_D}{\Psi_E}\left(\frac{1}{\alpha} - \frac{\Psi_S}{\Psi_D}\cdot f\right) x_s \qquad [11]$$

This is a convenient form to employ for analysis of the α *vs.* temperature data which were obtained for a constant x_s. The terms in this equation can be evaluated except for Ψ_E which cannot be separated from γ using any of the present measurements.

For antimony, $\alpha < 10^{-1}$ at all temperatures investigated, and γ may be approximated from the simplified relationship

$$\gamma = \frac{\Psi_D}{\Psi_E}\cdot\frac{x_s}{\alpha} \qquad [12]$$

For phosphorus and arsenic, it is necessary to evaluate the term $(\Psi_S/\Psi_D)\cdot f$.

The value of f can be obtained from Fig. 1 as previously indicated and for phosphorus (Ψ_S/Ψ_D) can be determined from the high growth rate limit of α in Fig. 5. However, for phosphorus, the term $1/\alpha - \Psi_S/\Psi_D \cdot f$ is very much smaller than $1/\alpha$ or $\Psi_S/\Psi_D \cdot f$ and the present data are insufficiently accurate to permit a worthwhile analysis except at the highest temperatures used.

For arsenic, Ψ_S/Ψ_D cannot be obtained from Fig. 5 since no rate limit of α is observed. However, Eq. [7] may be written in the form

$$\frac{1}{\alpha} = \gamma\cdot\frac{\Psi_E}{\Psi_D}\cdot f\,\Psi_S\cdot\frac{1}{G} + \frac{\Psi_S}{\Psi_D}\cdot f \qquad [13]$$

Hence, a plot of α^{-1} *vs.* G^{-1} should be linear with an intercept on the α^{-1} axis equal to (Ψ_S/Ψ_D) ($f = 1$ in the mass transfer region). Such a plot is shown in Fig. 6 from which a value of $(\Psi_S/\Psi_D) \approx 0.4$ is measured. This would give the high-growth-rate limit for α, if it could be achieved, as 2.5 which is reasonable.

Activity coefficients, or at least values of $(\Psi_E/\Psi_D)\cdot\gamma$, can be obtained also from Fig. 5, for the temperature used. As the growth rate tends to zero, α in all cases is given by Eq. [10] so that

$$\frac{d\alpha}{dx_S} = \frac{\Psi_D}{\Psi_E}\cdot\frac{1}{\gamma} \qquad [14]$$

But in the mass transfer range $G = \Psi_S x_S$ hence

$$\gamma\cdot\frac{\Psi_E}{\Psi_D} = \left(\Psi_S\frac{d\alpha}{dG}\right)^{-1} \qquad [15]$$

where $\Psi_S \approx 230\mu$ min^{-1} (4). Using Eq. [15] a value of $(\Psi_E/\Psi_D)\cdot\gamma$ was calculated for phosphorus at 1340°C, and using Eq. [11] and [12] similar calculations were made for arsenic and antimony over a range of temperatures. The results are plotted in Fig. 7 as $(\gamma\,\Psi_E/\Psi_D)$ *vs.* $1/T$ K°$^{-1}$. We may reasonably make the assumption $\Psi_E/\Psi_D = 1$, and as for other ratios of gaseous transfer coefficients the uncertainty introduced should not exceed a factor of 2-3.

The phosphorus data points represented by open squares are calculated from the diffusion data of Coupland, (6), which related surface concentration to pressure of phosphorus vapor and hence can be analyzed to give γ. The data are in surprisingly good agreement with the single point (open circle) obtained in this work.

The data for arsenic and antimony plot linearly in Fig. 7 as they should if they represent activities, and all data are in the expected relative order, *i.e.*, $\gamma_{Sb} > \gamma_{As} > \gamma_P$ (7).

Although the experiments have been performed using only the chlorides of the doping elements, the proposed doping model, if correct, shows that essentially the same results will be obtained regardless of the compounds used, *e.g.*, hydrides. This is substantiated by the work of Wang *et al.* (2) for AsH_3 and will still be true if the compound is unstable enough to decompose on the reactor walls so that the dopant passes through in elemental form. This may not be so obvious but an analysis similar to that presented above shows it to be so. Minor differences will result because of different transfer coefficients for various doping compounds but the basic characteristics are determined by the activity coefficient of the dopant which is not dependent on the doping compound employed.

Acknowledgments

The author is indebted to J. Ruiz for the experimentation and to many colleagues for helpful discussions.

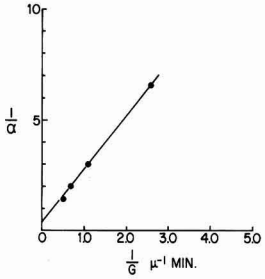

Fig. 6. Plot of $1/\alpha$ vs. $1/G$ for As doping at 1240°C

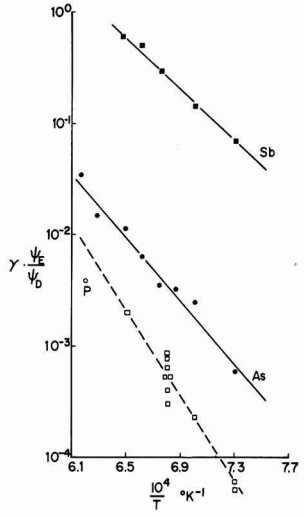

Fig. 7. Arrhenius plot of γ for P, As, and Sb in silicon (assuming $\Psi_E/\Psi_D = 1$).

Manuscript received July 27, 1967; revised manuscript received *ca.* Dec. 5, 1967. This paper was presented at the Philadelphia Meeting, Oct. 9-14, 1966, as Abstract 192.

Any discussion of this paper will appear in a Discussion Section to be published in the December 1968 JOURNAL

REFERENCES

1. P. Raichoudhury and R. R. Fergusson, Paper presented at the Cleveland Meeting of the Society, May 1-6, 1966, as Abstract 37.
2. P. Wang, U. S. G. Res. Rep, Ad 601343 April 1964.
3. R. Nuttall, *This Journal*, **111**, 317 (1964).
4. W. H. Shepherd, *This Journal*, **112**, 988 (1965).
5. (a) JANAF Thermochemical Data Tables, Compiled by Dow Chemical Co.; (b) Thermodynamic Properties of the Elements, Stull and Sinke, Advances in Chemistry Series No. 8 (1956).
6. M. J. Coupland, *Proc. Phys. Soc.*, **73** (4), 577 (1959).
7. S. E. Bradshaw and A. I. Mlavsky, *J. Electronics*, **2**, 134 (1956).

Effects of Back-Melting on the Dislocation Density in Single Crystals: GaSb

R. S. Mroczkowski,[1] A. F. Witt,* and H.C. Gatos*

Department of Metallurgy and, Center for Materials Science and Engineering, Massachusetts Institute of Technology, Cambridge, Massachusettts

ABSTRACT

A pronounced reduction in dislocation density was observed in gallium antimonide single crystals after partial back-melting and controlled resolidification. The distribution of dislocations in the parent crystals and regrown sections was studied by etch-pit counting and x-ray topography (Lang method). The observed reduction in dislocation density was explained in terms of the dislocation distribution in the parent crystal and the geometry and thermal conditions of the back-melting process.

A back-melting process has been employed recently for studying the formation of heterojunctions and mixed single crystals of different III-V compounds (1, 2). Since the geometry of the resolidification process and the associated thermal conditions differ from those encountered in Czochralski and other crystal growth techniques it was decided to study the influence of these contrasting growth conditions on the crystalline perfection of the regrown material. Accordingly, single crystal wafers of gallium antimonide were partially melted and regrown with the unmelted rest of the original wafer acting as substrate. These types of conditions are similar to those encountered in the traveling solvent method (3). This paper reports some interesting results concerning density and distribution of dislocations in regrown single crystal wafers.

Experimental Procedure

Gallium antimonide wafers (1.5 x 2 x 3 mm) with their large faces of (110), (211), and (111) orientation, were chemically etched in a modified CP-4 etchant ($5HNO_3$ conc.; $3CH_3COOH$; 3HF 48%) and placed between two carbon strip heaters (6 x 1 x 70 mm at a horizontal separation of 10 mm) with independent power supplies. The heaters were installed in a glass chamber in which the back-melting experiments were conducted in a hydrogen atmosphere of about 10 mm Hg overpressure. The back-melting and resolidification processes were observed through an externally mounted binocular microscope with a long working distance objective. During the back-melting experiments the upper carbon strip was first heated to about 1200°C. The resulting temperature gradient between the heated strip and the nonheated lower strip (on which the gallium antimonide was placed) just initiated back-melting of the wafer. By means of a controlled current through the lower strip the temperature gradient between the strips could be adjusted in such a way that the location of the solid-melt interface could be kept in any desired position and could also be moved at controlled rates. In this way any portion of the gallium antimonide wafer could be melted. After the appropriate region was melted, controlled resolidification was initiated by reversing the melting procedure, *i.e.*, the current through the lower strip was reduced at a rate appropriate for the desired resolidification rate; the actual regrowth rates varied between 1 and 10 in./hr. It was observed that within this range the structural characteristics of the regrown material were independent of the actual growth rate.

The density and distribution of dislocations in the parent crystal and the regrown sections were investigated by etch-pit counting and by x-ray topography employing the Lang technique (4). Etch-pit counting was carried out in a plane normal to the regrowth axis after the wafer was mechanically polished with 0.03μ alumina and etched with the above mentioned modified CP-4. The etch-pit distribution was examined by light microscopy under the appropriate magnification. X-ray topography was performed using a Lang camera and an x-ray microfocus unit. Standard Lang transmission geometry was employed. In all instances Ag, K-α radiation was used and the images recorded on nuclear emulsions.

Results

In a series of experiments gallium antimonide wafers were subjected to back-melting and regrowth with the solid-melt interface normal to the <211> direction. Since the semiconductor melt under the given experimental conditions is only subjected to gravity and surface tension it always assumes the shape of a distorted spherical segment. Because of volume expansion during solidification the regrown single crystals assume a dome-like shape. The regrown wafers were mounted in plastic, polished to expose a (111) plane, and finally etched to reveal dislocations and other defects.

Figure 1 is a photomicrograph of an etched single crystal in which the upper part has been regrown. The lowest position of the crystal-melt interface during the back-melt process can readily be recognized as a curved remelt line which sharply delineates areas

* Electrochemical Society Active Member.
[1] Present address: RCA Research Laboratories, Somerville, New Jersey.

of high and rather low dislocation densities. Etch-pit counting revealed a varying dislocation density ranging from 10^3 to 10^4 dislocations per square centimeter in the parent crystal below the remelt line and a dislocation density of close to zero in the adjacent regrown section above the remelt line. Not shown in Fig. 1 is the uppermost part of the regrown crystal in which the dislocation density is very high (due to very rapid solidification), exceeding that of the parent crystal. Since the detection of dislocations in the form of etch-pits requires that individual dislocations intersect the surface under consideration, the absence of dislocation etch-pits in the regrown section could not be considered as indicating complete absence of dislocations.

A (220) x-ray topograph of a regrown crystal of the above series of experiments is shown in Fig. 2. In this topograph the regrown section can be readily differentiated from the parent crystal by the drastic change in dislocation density. However, the dislocation density in the upper part is not as low as appears in Fig. 1. Most of the dislocations in the regrown section are observed to run nearly parallel to the regrowth axis and do not intersect the (111) plane on which the etch-pit count was performed.

The relationship between the dislocations in the parent gallium antimonide and the regrown crystals was further investigated by successively regrowing the same wafer in two perpendicular directions, as indicated in Fig. 3. In the first stage of this experiment the section left of the remelt line A (Fig. 3a) was regrown. The wafer was subsequently ground flat on one side, rotated on the heating strip and again remelted perpendicular to the original remelt direction, thus producing the remelt line B (Fig. 3a) on the regrown wafer. A topograph of such a twice regrown single crystal is shown in Fig. 3b. In region I, the unmelted parent crystal, the dislocation density is very high. Regions II and III which were both regrown only once exhibit the previously discussed reduction in dislocation density. Region IV which was twice regrown in different directions shows that the second regrowth process led to a further reduction in the density of dislocations. The very high dislocation density observed in the upper part of Fig. 3b is the result of turbulent, rapid growth which is always observed in the final stages of the resolidification process.

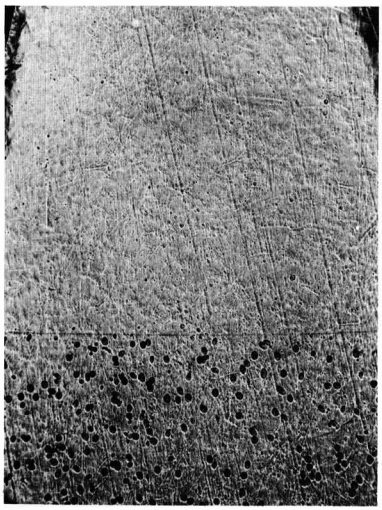

Fig. 1. Dislocations in parent crystal and regrown section of a gallium antimonide wafer. The curved remelt line separating the two regions is clearly visible. The (111) plane shown is normal to the regrowth axis. Magnification *ca.* 105X.

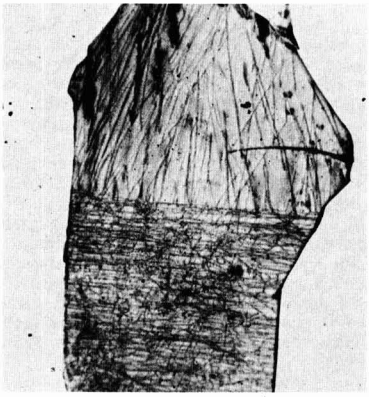

Fig. 2. X-ray topograph of partially regrown gallium antimonide wafer. The regrown region exhibits a marked decrease in the dislocation density; Ag, Kα radiation; (220) reflection. Magnification *ca.* 20X.

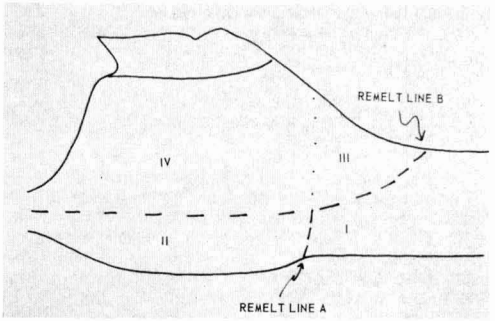

Fig. 3a. Schematic diagram of a twice regrown gallium antimonide wafer corresponding to x-ray topograph of Fig. 3b. A and B are the remelt lines resulting from the first and second back-melting experiments respectively. Region I represents the original parent crystal; region II was once regrown during the first back-melt experiment, region III was once regrown during the second back-melt experiment. Region IV was regrown twice in different directions.

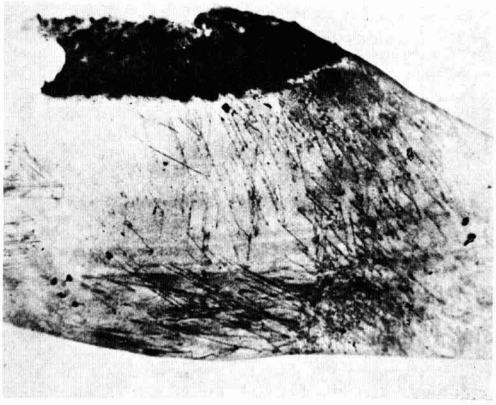

Fig. 3b. X-ray topograph of twice regrown gallium antimonide wafer (corresponding schematic is shown in Fig. 3a). Note the very low dislocation density in the twice regrown section (area IV in Fig. 3a) Ag, Kα radiation; (220) reflection. Magnification *ca.* 25X.

Fig. 4. X-ray topograph of a gallium antimonide wafer exhibiting a high density of dislocations. Two sets of dislocations can be observed. One set of rather long dislocations appears aligned along the <111> growth direction, the other consists of a network of dislocation loops. Ag, Kα radiation (220) reflection. Magnification *ca.* 40X.

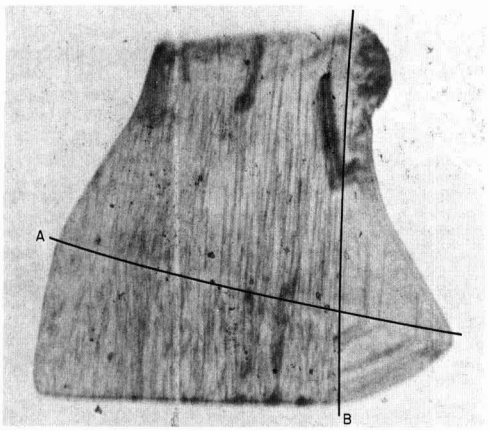

Fig. 5. X-ray topograph of a twice remelted gallium antimonide wafer of low dislocation density. Back-melting in the direction of the original growth axis (remelt line A) resulted in a material exhibiting essentially the original dislocation density. The second remelt experiment (from right to left) normal to the original growth axis (remelt line B) led to a noticeable reduction in dislocation density. Ag, Kα radiation, (220) reflection. Magnification *ca.* 25X.

Discussion

In crystals grown from the melt two types of dislocations are usually observed. The dislocations of the one type propagate from the seed and are generally long and straight. In the second type belong dislocations which are introduced by thermal stresses encountered in crystal growth systems. These latter dislocations assume complex shapes [tangles (5)] and frequently appear as loops or partial loops. They can readily be differentiated from the long and rather straight dislocations previously discussed. The density of dislocations (ρ) caused by thermal stress, has been related to the deviation from the average thermal gradient (6), $\delta\nabla T$ in the growth system as follows

$$\rho = \frac{1}{a}\alpha\delta\nabla T$$

where a is the lattice constant and $\alpha = da/adT$ the coefficient of thermal expansion.

While the exact origin of individual dislocations cannot be determined unambiguously because of their complex movement under different stresses, some pertinent observations can be made. Figure 4 is a topograph of a poor quality gallium antimonide single crystal exhibiting a very high dislocation density. Many of the dislocations are straight and aligned along the <111> growth direction. On the other hand, a large number of randomly oriented complex shaped dislocations can be observed which are apparently due to the presence of thermal and solidification stresses. The observed reduction of the dislocation density in partially regrown single crystal wafers is attributed to two factors. First all dislocations which originate and terminate within the region subjected to back-melting are eliminated and are not regenerated during the resolidification process. Second, the small size of the wafer and the absence of constraints on the solid-liquid system result in resolidification under significantly reduced thermal and mechanical stress (compared to the conditions in Czochralski pulling systems) and are responsible for the absence of stress induced dislocations. The dislocation density in the regrown region is determined by the propagation of dislocations present in the parent crystal with a component along the regrowth direction. Apparently the orientation of the propagated dislocations is largely dependent on their orientation in the parent crystal. In this regard the experiment illustrated in Fig. 5 is of particular interest. Here regrowth along the original growth axis did not noticeably reduce the dislocation density whereas regrowth normal to the growth direction of the parent crystal resulted in substantial reduction in dislocation density.

The type of solidification discussed here under the virtual absence of thermal stresses could prove most useful for the detailed study of dislocation elimination and propagation.

Acknowledgment

This work was supported by the Advanced Research Projects Agency under Contract SD-90.

Manuscript received Oct. 23, 1967; revised manuscript received *ca.* Dec. 3, 1967.

Any discussion of this paper will appear in a Discussion Section to be published in the December 1968 JOURNAL.

REFERENCES

1. D. E. Hinkley, R. H. Rediker, and M. C. Lavine, *Appl. Phys. Letters*, **5**, 110 (1964).
2. R. S. Mroczkowski, M. C. Lavine, and H. C. Gatos, *Trans. AIME*, **233**, 456 (1965).
3. W. G. Pfann, *ibid.*, **203**, 961 (1955); A. I. Mlavski and M. Weinstein, *J. Appl. Phys.*, **34** [9], 2885 (1963).
4. A. R. Lang, *Acta Met.*, **5**, 358 (1957).
5. A. E. Jenkinson and A. R. Lang, "Imperfections in Crystals," p. 471, Interscience Publisher, Inc., New York (1962).
6. J. Friedel, "Dislocations," p. 205, Addison-Wesley Press (1964).

Diffusion from a Plane, Finite Source into a Second Phase with Special Reference to Oxide-Film Diffusion Sources on Silicon

A. E. Owen[1] and P. F. Schmidt*[2]

Westinghouse Research and Development Center, Pittsburgh, Pennsylvania

ABSTRACT

A model is set up for the diffusion from a source of finite thickness into an adjacent second phase of semi-infinite extent. With the principal assumption of no diffusion in or out of the system, a solution is obtained for the diffusion profile in the second phase. It is also assumed that the diffusion coefficients are independent of concentration, but segregation at the interphase boundary is taken into account and so also, to a first approximation, is the possibility of precipitation or reaction at the interface. The model predicts a change in the profile from an ERFC to Gaussian shape depending on whether the diffusion length in the source is much less than or much greater than its thickness, *i.e.*, as the diffusion time increases.

The theoretical predictions of the model are compared to tracer diffusion results from phosphorus doped anodic oxide sources on silicon. These experiments were carried out with unprotected (no undoped SiO_2 film covering the source) oxide sources in a sealed quartz tube. Thus the phosphorus initially lost by out-diffusion could not escape from the system altogether, and it is shown that these conditions approximated the boundary condition of no out diffusion. The diffusion results obtained in this way are in agreement with the model.

In recent years interest has grown in the use of doped oxide films as diffusion sources for device fabrication in semiconductors (1-6). These sources can be deposited by a variety of means, such as anodization, pyrolytic decomposition, or reactive sputtering, and offer the advantages of control of the dopant concentration and of low deposition temperatures which do not alter pre-existing diffusion profiles in the semiconductor substrate. Anodic oxidation also provides very accurate control of the oxide thickness and the possibility of depositing the diffusion source only in the windows of a diffusion mark. Electrophoretic deposition of doped oxides (7) is interesting from the materials point of view since it is practically unlimited in its scope as to substrates or dopants. The present paper solves the diffusion equations for the two-phase system: very thin oxide source/semi-infinite substrate, subject to the idealized assumptions of no loss of dopant to the ambient by out-diffusion and of concentration independent diffusion coefficients. Segregation coefficients at the oxide/semiconductor interface, as well as precipitation or compound formation at this interface, however, are taken into account.

The concentration dependence of phosphorus[3] diffusivity in silicon is well known (8-10), and could be taken into consideration in the calculations; very little, however, is known about the strong concentration dependence of phosphorus diffusivity in phosphosilicate glass and in phosphorus doped SiO_2 (11). In the present paper the diffusion coefficients are regarded as concentration independent. This assumption may not be as severe a limitation on the usefulness of the theory as it might appear at first glance, precisely because of the very strong concentration dependence of diffusivity in the oxide. The diffusivity is relatively high in the phosphosilicate composition range (20) but drops sharply just outside this range to very small values of diffusivity in pure SiO_2. Probably very little phosphorus is supplied by the oxide source to the silicon substrate after the diffusivity in the oxide has become strongly concentration dependent due to the beginning of depletion of the source; from this point on the amount and profile of phosphorus already in the silicon will determine the further development of the profile in the silicon. The strong concentration dependence of diffusivity in the oxide will thus show up mostly as a reduced effective concentration of dopant originally contained in the oxide source.

While the theory proposed is still only an approximation, it is a step closer to being exact than existing theories since it does not treat the oxide source as an infinitely thin plane source. For very short diffusion times, as long as the oxide source is not yet being depleted, it will act like an infinite source, and the resulting profile in the substrate will be a complementary error function (ERFC); for long diffusion times, it may be regarded as an infinitely thin plane source. The effect of the diffusion parameters (oxide thickness, ratio of diffusivities in oxide and substrate, segregation coefficient, and compound or precipitate formation) on the shape of the diffusion profile as a function of time forms the main body of this discussion. It is easy to show that the important parameter, which governs the transition from ERFC to Gaussian is the diffusion length for the impurity in the oxide, *i.e.*, $\sqrt{D_1 t}$ (where D_1 is the diffusion coefficient for the impurity in the oxide, and t is the diffusion time).

Model and Solution of the Diffusion Equations

To regard the anodic oxide film as equivalent to a plane source is to assume that the impurity can diffuse across the oxide in times short compared with the diffusion time. The validity of such an assumption would obviously depend on the relationship between the diffusion coefficient in the oxide, oxide thickness, and diffusion time. Such an approximation is not expected to be appropriate in all circumstances therefore, and in any more general analysis it is necessary to consider a two-phase system taking into account the properties of the oxide film. The model adopted is shown schematically in Fig. 1, in which phase 1 represents the oxide and phase 2 the silicon. The oxide has a thickness l (measured negatively from zero), a concentration-independent diffusion coefficient D_1

* Electrochemical Society Active Member.
[1] Present address: Department of Electrical Engineering, University of Edinburgh, Scotland.
[2] Present address: Bell Telephone Laboratories, Inc., Allentown, Pennsylvania.
[3] The experimental work included in this paper deals exclusively with phosphorus; in principle, the theory applies to the diffusion of any other dopant as well.

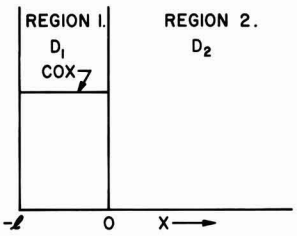

Fig. 1. Theoretical model for the anodic oxide diffusion source. Region 1 represents oxide with uniform initial concentration of phosphorus C_{ox} and diffusion coefficient D_1. Region 2 represents silicon with zero initial concentration of phosphorus and diffusion coefficient D_2.

for the impurity and an initial uniform[4] concentration of impurity C_{ox}. The silicon extends from zero to infinity, has a zero initial impurity concentration and a concentration-independent diffusion coefficient for impurity D_2. The diffusion equations for the system of Fig. 1 are therefore
in region 1

$$\frac{\partial^2 C_1}{\partial x^2} - \frac{1}{D_1}\frac{\partial C_1}{\partial t} = 0 \qquad [1]$$

in region 2

$$\frac{\partial^2 C_2}{\partial x^2} - \frac{1}{D_2}\frac{\partial C_2}{\partial t} = 0 \qquad [2]$$

and these have to be solved simultaneously with the initial conditions

$$C_1 = C_{ox}; -l < x < 0, \quad t = 0 \qquad [3]$$

$$C_2 = 0; \; x > 0, \qquad t = 0 \qquad [4]$$

The boundary conditions have been chosen as follows
At

$$x = -l, \frac{dC_1}{dx} = 0 \qquad [5]$$

At

$$x = 0, D_1\frac{dC_1}{dx} = D_2\frac{dC_2}{dx} \qquad [6]$$

and

$$C_1 = mC_2 \qquad [7]$$

At

$$x = \infty \quad C_2 = 0 \qquad [8]$$

Boundary conditions [6], [7], and [8] are straightforward and physically reasonable. Condition [6] simply expresses the continuity of flux and [7] the segregation of impurity at the interface, with a segregation coefficient m. Boundary condition [5], however, which requires that there is no flow of impurity from the oxide to the ambient or *vice versa* requires particular consideration. At first sight this would seem to be an unrealistic condition, but there are indications that it is a fair approximation under the conditions of the experiments described in ref. (1), in which unprotected (*cf.* below) oxide sources were used in conjunction with sealed quartz diffusion tubes of small volume; in the case of protected oxide sources [see ref. (2)], boundary condition (5) holds almost exactly. Evidence for these points will be mentioned below.

Surprisingly, a complete solution of the diffusion problem set out in Fig. 1 and Eq. [1] to [8] does not appear to have been given before. Carslaw and Jaeger (12) quote ref. (13) for the temperature at the interface of a hot magmatic intrusion into a cold rock (*i.e.*, a parameter corresponding to the concentration C_0 at the silicon-oxide interface) but solutions corresponding to concentration profiles are not available. It should be remarked in passing, therefore, that although the model used here is only an approximation for the oxide film diffusion source situation, it does provide an exact solution (subject to concentration-independent coefficients) to the problem of diffusion from a source sandwiched between two semi-infinite media of a second phase, *i.e.*, two of the models drawn in Fig. 1 placed back-to-back.

Using the Laplace transformation (12) the simultaneous partial differential Eq. [1] and [2] have been solved for the concentration in the phase 2, C_2, subject to the initial conditions [3] and [4] and the boundary conditions [5] to [8]. The solution is

$$C_2 = \frac{C_{ox}}{2}\frac{(1-\alpha)}{m}\left[\sum_0^\infty (-1)^n \alpha^n \operatorname{erfc}\frac{(2Rln + x)}{2\sqrt{D_2 t}} - \sum_0^\infty (-1)^n \alpha^n \operatorname{erfc}\frac{(n+1)\,2Rl + x}{2\sqrt{D_2 t}}\right] \qquad [9]$$

in which C_{ox}, D_2, l, and m have already been defined, t is the diffusion time, and x is the depth at which the concentration is C_2. The parameters R and α are given by

$$R = \sqrt{(D_2/D_1)} \qquad [10]$$

and

$$\alpha = \frac{(R/m) - 1}{(R/m) + 1} \qquad [11]$$

For the purpose of computation Eq. [9] has been expressed in terms of dimensionless parameters

$$\frac{C_2}{C_{ox}}m = \frac{(1-\alpha)}{2}\left[\sum_0^\infty (-1)^n \alpha^n \operatorname{erfc}\frac{[2(R/m)n + x/\mathrm{lm}]}{2\sqrt{D_2 t}/ml} - \sum_0^\infty (-1)^n \alpha^n \operatorname{erfc}\frac{[2\,(R/m)\,(n+1) + x/lm]}{2\sqrt{D_2 t}/ml}\right] \qquad [12]$$

Equation [12] has been programmed and the concentration (C_2/C_{ox}) m computed as a function of distance (x/lm) for various values of time $(\sqrt{D_2 t}/ml)$ and the parameter (R/m). The diffusion Eq. [12] has the important property that the concentration profile in the phase 2 changes shape from ERFC to Gaussian according to the relationship between the time parameter $(\sqrt{D_2 t}/ml)$ and the parameter (R/m). For instance, for a given (R/m) the profile changes from ERFC to Gaussian as the diffusion time increases and, conversely, for a constant time $(\sqrt{D_2 t}/ml)$ the profile changes from Gaussian to ERFC as (R/m) increases. In actual practice it is to be expected, of course, that (R/m) remains constant while the diffusion time is varied, but for convenience in illustration the change in shape of the profile is shown in Fig. 2 for a constant $(\sqrt{D_2 t}/ml) = 5$ with (R/M) varying. Also plotted in Fig. 2 are points corresponding to true Gaussian and ERFC curves, and it will be noticed that the profile of Eq. [12] is approximately intermediate between Gaussian and ERFC when

$$\frac{\sqrt{D_2 t}}{ml} = \frac{R}{m} \qquad [13]$$

Substituting for R $(= \sqrt{D_2/D_1})$ and rearranging gives the set of conditions: if

$$\sqrt{D_1 t} < l, \text{ profile tends to ERFC} \qquad [14a]$$

$$\sqrt{D_1 t} \approx l, \text{ profile is intermediate} \qquad [14b]$$

$$\sqrt{D_1 t} > 1, \text{ profile tends to Gaussian} \qquad [14c]$$

Thus the shape of the profile in the phase 2 depends, in fact, only on the diffusion time and the characteris-

[4] It is shown in ref. (1) that the initial distribution of phosphorus in an anodically grown oxide is, in fact, practically uniform.

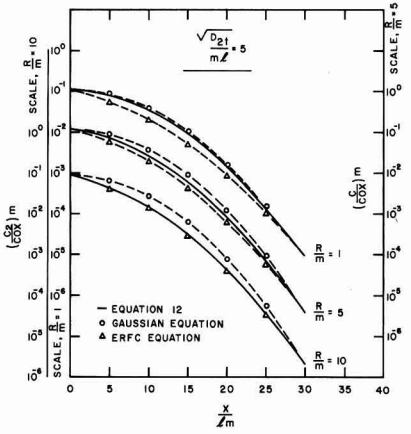

Fig. 2. Illustrating the change from Gaussian to ERFC form of the profile predicted by Eq. [12] as R/m varies at constant time, $(\sqrt{D_2t}/ml) = 5$.

tics of phase 1 (the oxide). When the diffusion length of impurity in the oxide, $\sqrt{D_1t}$, is much less than the thickness of the oxide l the oxide tends to behave as an infinite source (ERFC), but when the diffusion length is much greater than the thickness of the oxide, it tends to behave as an infinitely thin plane source (Gaussian). Physically these conditions are perfectly reasonable and could have been anticipated from the remarks made at the beginning of this section. Another way of looking at this is to regard the "effective" thickness of the oxide as depending upon time and, through the diffusion coefficient, on temperature.

In device fabrication the impurity surface concentration in the silicon, C_o, is an important parameter, and this has been plotted in a reduced form in Fig. 3. The surface concentration expressed as $[(C_o/C_{ox})m]$ is given as a function of time, $(\sqrt{D_2t}/ml)$, for various values of the parameter (R/m). The surface concentration can be written analytically by putting $(x/lm) = 0$ in Eq. [12] and simplifying, leading to

$$\frac{C_o}{C_{ox}} M = \frac{(1-\alpha)^2}{2} \sum_{n=1}^{\infty} (-\alpha)^{n-1} \operatorname{erf} \frac{nl}{\sqrt{D_1t}} \qquad [15]$$

This equation shows that the time variation of the surface concentration depends only on the diffusion time and the characteristics of the oxide. At a given value of (R/m) the surface concentration is independent of time for very small values of time; in this region the oxide will behave as an infinite source. As the time parameter $(\sqrt{D_2t}/ml)$ approaches (R/m) the surface concentration begins to decrease slowly at first and then more rapidly when $(\sqrt{D_2t}/ml) = (R/m)$. When $(\sqrt{D_2t}/ml) >> (R/m)$ the surface concentration decreases linearly with the inverse of $(\sqrt{D_2t}/ml)$, and in this region the oxide behaves as an infinitely thin plane source. Note also that in this region the surface concentration depends only slightly on (R/m) whereas in the ERFC region it depends strongly on (R/m).

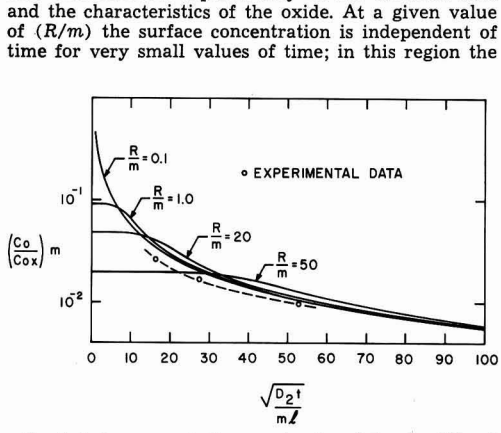

Fig. 3. Surface concentration as a function of time for different values of R/m according to Eq. [12]. Also shown for comparison are some experimental points.

The bulk of the work reported in ref. (1), 2), and (14) is concerned with the use of phosphorus-doped anodic oxide films as diffusion source. In early diffusion experiments with P-32 labeled phosphorus, sectioning of the silicon after diffusion revealed the presence of a sharp spike of phosphorus within the first 1-2,000Å of the silicon surface. The material in this spike was subsequently identified as silicon phosphide precipitates by Schmidt and Stickler (15), who also give some examples of the diffusion profile in the Si. Later work (16) showed that precipitates of SiP forming during the initial stages of diffusion on silicon surfaces of any orientation (17, 18) tend to become especially large on (110) surfaces and do not disappear even at long diffusion times; the phosphorus incorporated into these precipitates is lost for the diffusion process. Since the silicon bars, on which experimental work reported here was carried out, had their large surfaces (110) oriented, the SiP precipitates must have formed readily, and this fact presumably accounts for the shift to lower concentrations of the phosphorus diffusion profile observed in the early tracer runs (*cf.* Fig. 3).

Irrespective of the mechanism by which precipitates or compounds are formed at the interface, their formation results in a certain fraction of the phosphorus flux crossing the oxide/silicon interface being retained at the interface. If such a process takes place, the boundary condition [6] for flux continuity across the oxide/silicon interface must be modified; assuming that the fraction K of flux retained at the interface is a constant, this boundary condition becomes

$$D_1 \frac{dC_1}{dx} + K\, D_1 \frac{dC_1}{dx}\bigg|_{x=0} = D_2 \frac{dC_2}{dx} \qquad [16]$$

Solving the same equations with the boundary condition [16] in place of [6] again leads to Eq. [12] but now the parameter α is given by

$$\alpha = \frac{(R/m) - (1-K)}{(R/m) + (1-K)} \qquad [17]$$

Thus, when K is zero (no spike formation) Eq. [12] is unchanged as it obviously should be; when $K = 1$ (all the phosphorus retained at the interface) $\alpha = 1$ and $C_2 = 0$, *i.e.*, there is no diffusion into the silicon, again as expected. The effect of K in Fig. 3 is to make (R/m) appear larger than it would otherwise be in the absence of spike formation, *i.e.*, to lower the curves and reduce their slope slightly.

Discussion: Relevance to Anodic Oxide Diffusion Sources

The theoretical work described herein was initiated during the early stages of development of doped anodic oxide sources (1), when nondoped anodic oxide films, grown on top of the doped source[5] as a protection against out-diffusion, were not yet available. Subsequently it was found that these protective oxide covers, a few hundred angstroms thick, act as complete barriers to out-diffusion into the ambient for any time-temperature diffusion conditions of practical interest (2). This masking ability is, of course, a consequence of the very strong concentration dependence

[5] The anodic formation of nondoped oxide on top of a doped oxide is possible because the anodization of silicon proceeds by cation migration (1).

of phosphorus diffusivity in pure SiO_2. In the heavily doped source, on the other hand, the phosphorus diffusivity is relatively high, so that most of the phosphorus has diffused into the silicon before the protective oxide cover is penetrated by phosphorus diffusing outward.

Oxide diffusion sources with protective oxide covers thus come very close to the boundary condition [5] of no diffusion across the oxide/ambient interface; the amount of phosphorus diffusing into the pure SiO_2 cover is negligible compared to the amount diffusing into the Si substrate. Unfortunately, the experimental work described in ref. (2) was oriented toward process development, and the diffusion times chosen were either not short enough to demonstrate the transition from an ERFC to a Gaussian profile, or not long enough to show the predicted deviation of junction depth from a square-root of time dependence at long diffusion times. This became clear only after conclusion and evaluation of the tracer results; while the results obtained in [2] are not at variance with the theory proposed here, they could not be used to prove the correctness of the theory.

The only tracer work in which very short and very long diffusion times were used are the early tracer runs, made with unprotected oxide sources in sealed small quartz tubes. In these experiments there was an initial very fast loss of phosphorus from the outer surface of the oxide; however, this phosphorus could not escape from the sealed system, and for longer diffusion times there actually occurred some reabsorption of phosphorus from the gas phase by the oxide. The amount of phosphorus reabsorbed was, however, small compared to that left in the system oxide + silicon after the initial fast out-diffusion, and for practical purposes the assumption of "no out-diffusion" appears to be valid after the first 5-10 min of heat-treatment, as will be discussed in more detail below.

It should be noted that the experimental results are quoted only to show that they are not in disagreement with the proposed theory; they are not assumed to prove its validity. Specifically, it should also be noted that the results quoted are not representative of the potential usefulness of doped oxide sources; for practical applications, the reader is referred to ref. (1-6).

Evidence for the approximate validity of boundary condition [5] in the experimental work (unprotected oxide sources about 1500Å thick; doping level in the oxide up to $4x10^{21}$/cc; argon filled quartz tubes; diffusion temperatures of typically 1175°C) is then given in Fig. 4 where the amount of phosphorus (in atoms/cm²) in the silicon, that which remains in the oxide, and the total in oxide plus silicon, is plotted as a function of the square-root of time at 1175°C. The data of Fig. 4 were obtained from experiments using P-32 as a tracer. Note that the vertical ordinate has been compressed and should, on this scale, extend to three or four times the height shown. These data show that during the very early stages of diffusion there is an extremely rapid loss of phosphorus from the oxide. At times still short compared with the experimental diffusion times, this out-diffusion apparently ceases, however, and eventually there is actually an increase in total phosphorus with time, *i.e.*, there is some in-diffusion. The increase at longer diffusion times, however, is relatively small. The assumption of no out-diffusion implicit in boundary condition (5) therefore appears to be experimentally justifiable at least for comparatively long diffusion times. Support for this was provided by another experiment made under similar conditions in which the phosphorus in the silicon and oxide was measured for diffusion times between 5 and 90 min (in increments of 5 min), and it was found that after the first 5-10 min the total amount of phosphorus in oxide plus silicon became practically constant, *i.e.*, a condition equivalent to Eq. [5].[6] Yet further supporting evidence is to be found in the phosphorus profiles in the oxide, determined after diffusion, by etching oxide away in a step-wise fashion, and counting the radioactive P-32 removed. Three such profiles are shown in Fig. 5; in each case the oxide was grown by the method of ref. (1), to a thickness of 1450Å and was found to have a phosphorus concentration before diffusion of $2.2\text{-}2.5x10^{21}$ atoms/cm³. The original phosphorus concentration is shown by the horizontal lines in Fig. 5. Figures 5(a), 5(b), and 5(c) correspond to diffusion times of 1.5, 5, and 15.9 hr at 1175°C in an argon-filled sealed quartz tube. The data of Fig. 5 are not very accurate, due to some nonuniformity in the local dissolution rate of the oxide, and the profile has deliberately been drawn in horizontal at the outer surface to conform with boundary condition [5], but at least they fairly conclusively indicate a situation corresponding to no out-diffusion. The effective concentration of phosphorus in the oxide, C_{ox} will, of course, be less than that initially present. According to the data of Fig. 4 about 80% of the original phosphorus is lost from the oxide-silicon system and consequently in the samples of Fig. 5, for instance, C_{ox} would be approximately $5x10^{20}$ atoms of phosphorus cm^{-3}, as indicated.

The fact that the phosphorus concentration at the outer surface of the oxide remained high for all diffusion times is undoubtedly due to the sealed tube operation; it would not have remained high in an open flow system. Diffusion of phosphorus into the dense quartz of the tube walls is very slow, so that out-

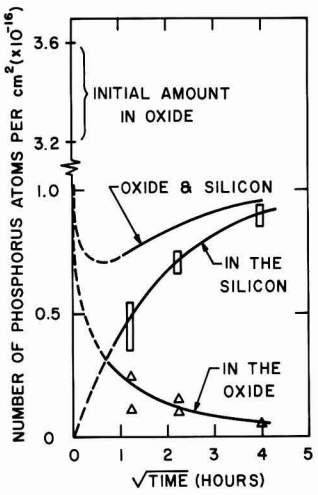

Fig. 4. Amount of phosphorus found in the silicon, the amount remaining in the oxide, and the total in oxide and silicon as a function of diffusion time.

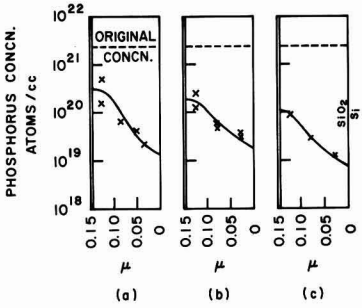

Fig. 5. Phosphorus profiles in oxide after diffusion: (a) 1½ hr at 1175°C; (b) 5 hr at 1175°C; (c) 15 9/10 hr at 1175°C.

[6] The authors are indebted to their colleague, T. W. O'Keefe, for carrying out these measurements.

diffusion will have practically stopped as soon as saturation of the gas phase and internal tube surfaces with P_2O_5 occurred. Eventually some of the phosphorus pentoxide on tube walls and in the gas phase becomes available for back-in-diffusion as the concentration in the oxide source drops due to diffusion into the Si substrate.

Note that the diffusion must be carried out in an inert ambient: diffusion in air would lead to the formation of new oxide at the SiO_2/Si interface, and to a much more complicated situation.

It is not quite clear which factor is mostly responsible for the approximate constancy of the total amount of phosphorus in oxide plus silicon after the first 5-10 min of heat-treatment. It may be due to a relatively slow transport of phosphorus across the outer oxide surface due to a shallow diffusion gradient, but it is also possible that the outer surface of the oxide underwent a drastic structural change during the initial stage of rapid out-diffusion of phosphorus, and that the diffusivity of phosphorus in this surface layer became strongly different from its initial value.

An assessment of Eq. [12] can be obtained from a comparison of predicted junction depths and surface concentrations with those obtained experimentally. The samples of Fig. 5, for instance, were prepared on 2 ohm-cm p-type material, and gave the junction depths plotted on a reduced scale, as a function of time, in Fig. 6. In obtaining this figure the diffusion coefficient of phosphorus in silicon at 1175°C was taken to be 10^{-12} cm^2/sec (19), oxide thickness l = 1450Å, and m was taken as 0.3. (In six samples m was found experimentally to vary between 0.2 and 0.4 with a mean of approximately 0.3). From the data of Irvin (20) the base concentration of 2 ohm-cm p-type silicon is $7.00\text{x}10^{15}$ atoms/cc and thus, at the junction, the dimensionless concentration parameter of Eq. [12] has a value

$$\frac{C_B}{C_{ox}} m \approx 4\text{x}10^{-6}$$

where C_{ox} has been given the effective value for the samples of Fig. 5 (*i.e.*, $5\text{x}10^{20}$ atoms/cc) and C_B is the concentration at the junction. Predicted values for the junction depth were then obtained graphically by plotting $(C/C_{ox})m$ *vs.* the reduced depth x/lm for various values of the time parameter $\sqrt{D_2t}/ml$ at particular values of (R/m), and reading off the depth corresponding to the above reduced concentration. Theoretical curves obtained in this way for (R/m) equal to 10 and 20 are also drawn in Fig. 6, and the experimental points fall roughly between these two curves. Two features of Fig. 6 should be noted in passing. First, the theoretical curves begin to deviate from the linear dependence on square-root of time and at longer diffusion times this deviation becomes even more marked. And second, for (R/m) values in this range the junction depth-time relationship is not very sensitive to (R/m).

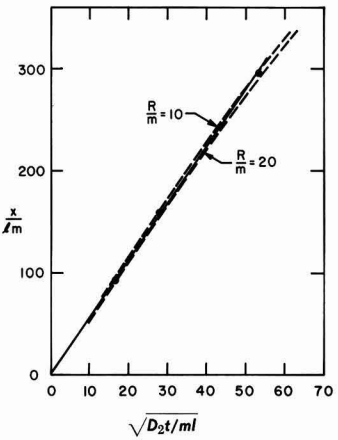

Fig. 6. Junction depths as a function of time in terms of the parameters of Eq. [12]. Comparison with the predictions of Eq. [12] with (R/m) = 10 and 20 and base concentration corresponding to (C/C_{ox}) m $\approx 4\text{x}10^{-6}$.

Now according to Sah, Sello, and Tremere (21) R is very nearly 3 at temperatures of 1100° and 1150°, but for an unspecified amount of phosphorus in the oxide. A value of R = 3 at 1175°C would, therefore, seem reasonable and hence, using the value of m = 0.3, quoted above

$$R/m = 10$$

The experimental points plotted in Fig. 6 suggest that (R/m) is a little larger than this, say about 15, but the nature of the comparison is such that this discrepancy is hardly significant, and the experimental data can be considered consistent with the model. Thurston, Tsai, and Kang (11) report, however, that R is rather sensitive to the amount of phosphorus in the oxide and also possibly, depending on the actual concentration, on temperature. In the present experiments the oxide contained about 5 w/o (weight per cent) of phosphorus and from the data of Thurston *et al.* a value in the region of 5 would be appropriate for R at 1175°C, whence

$$R/m \approx 16$$

This agrees rather well with the experimental results of this paper although it must be pointed out that according to ref. (11) much larger values of R, and hence R/m, are possible. Thus, the value of (R/m) = 10 would seem to represent a lower limiting value, and without knowing precisely what is the appropriate concentration of phosphorus in the oxide a more definite estimate cannot be made.

The experimental surface concentrations for the same samples are plotted, again in dimensionless form, in Fig. 3. As anticipated earlier, these samples, like those of ref. (15), showed a "spike" in the phosphorus concentration at the surface; this spike was neglected in arriving at the measured surface concentrations plotted in Fig. 3. The experimental points show about the right time dependence for a value of (R/m) in the range 10 to 20 implied by the results of Fig. 6 and tentatively suggested by the data discussed above. In magnitude, however, the points are somewhat lower than expected. The reasons for this are almost certainly connected with the formation of the spike for, as already shown, the removal of a fraction of the flux at the interface would have the effect of lowering the theoretical curves of Fig. 3. Qualitatively such an adjustment would bring the experimental points into better agreement with the predictions.

Finally, it should be pointed out that the trend of the experimental results presented in Fig. 3 and 6 lead one to expect that the concentration profiles in the silicon should be nearly Gaussian, especially at the longer diffusion times. As was mentioned early in this paper this is not unexpected, and the profile shape resulting from anodic oxide diffusion sources is examined in ref. (14).

Conclusions

The solution of the two-phase diffusion problem given in this paper, exact where the diffusion coefficients are independent of concentration and out-diffusion can be neglected, may be approximately applicable to the more complex practical situation for diffusion from doped (anodic) oxides on silicon. For the samples discussed in this paper, nonprotected oxide sources diffused in a sealed tube at 1175°C, there appears to be an intermediate range of diffusion time (*i.e.*, 1½ hr to perhaps 15 or 16 hr) in which the assumption of no-flow across the oxide-ambient interface is reasonably justified. Under these conditions sat-

isfactory agreement is found between the predictions of the model and measured parameters such as the junction depth. In the particular samples studied here the concentration profile in the silicon is expected to be nearly Gaussian, especially at the longer diffusion times. A Gaussian profile is not always to be expected, however, and the theoretical model shows that the important quantity is the diffusion length $\sqrt{D_1 t}$, in the oxide. When the diffusion length is small compared with the thickness of the oxide (*i.e.*, short diffusion times) an ERFC profile will result.

Acknowledgments

This work was carried out while the authors were members of the Westinghouse Research Laboratories, Pittsburgh; they are indebted to the company for providing facilities, and to several of their former colleagues for cooperation and assistance during all phases of the work. Particular thanks are due to Miss Freedman and Mr. Heath of the Mathematics Department for programming and computing the diffusion equation. Dr. O'Keefe was responsible for the out-diffusion experiment mentioned in the text and Mr. Roney assisted with the other experiments.

Manuscript received Aug. 30, 1967; revised manuscript received *ca.* Dec. 12, 1967.

Any discussion of this paper will appear in a Discussion Section to be published in the December 1968 JOURNAL.

REFERENCES

1. P. F. Schmidt and A. E. Owen, *This Journal*, **111**, 682 (1964).
2. P. F. Schmidt, T. W. O'Keefe, J. Oroshnik, and A. E. Owen, *ibid.*, **112**, 800 (1965).
3. H. Becke, D. Flatley, W. Kern, and D. Stolnitz, *Trans. Metallurg. Soc. AIME*, **230**, 307 (1964).
4. H. Kunz, D. Clerc, and D. Jahn, *Brown Bovery Rev.*, **53**, 34 (1966).
5. J. Scott and J. Olmstead, *RCA Rev.*, **26**, 357 (1965).
6. W. V. Münch, *IBM J. Res. Dev.*, **10**, 438 (1966); *Solid State Electronics*, **9**, 619 (1966).
7. Westinghouse Electric Corp., Research Lab., ASTIA Report 473801, dated November 1965.
8. E. T. Handelman, *Solid State Electronics*, **2**, 123 (1961).
9. S. Maekawa, *J. Phys. Soc. Japan*, **17**, 1592 (1962).
10. J. J. Chang, *IEEE Trans. Electron Devices*, **ED-10**, 357 (1963).
11. M. O. Thurston, J. C. C. Tsai, and K. D. Kang, ASTIA Report AD 261 201 (1961).
12. H. C. Carslaw and J. C. Jaeger, Conduction of Heat in Solids, 2nd Edition, p. 236 (OUP).
13. T. S. Lovering, *Bull. Geol. Soc. Amer.*, **47**, 87 (1936).
14. T. W. O'Keefe and P. F. Schmidt, To be published.
15. P. F. Schmidt and R. Stickler, *This Journal*, **111**, 1188 (1964).
16. T. W. O'Keefe, P. F. Schmidt, and R. Stickler, *ibid.*, **112**, 878 (1965).
17. E. Kooi, *ibid.*, **111**, 1383 (1964).
18. H. Garski, Z. Naturforschg., **22a**, 6 (1967).
19. C. S. Fuller and J. A. Ditzenberger, *J. Appl. Phys.*, **27**, 544 (1956).
20. I. Fränz, H. Langheinrich, and K. H. Löcherer, *Telefunken-Z.*, **37**, 194 (1964).
21. J. C. Irvin, *Bell Syst. Tech. J.*, **41**, 387 (1962).
22. C. T. Sah, H. Sello, and D. A. Tremere, *J. Phys. Chem. Solids*, **11**, 288 (1959).

The Close-Spaced Growth of Degenerate P-Type GaAs, GaP, and $Ga(As_x, P_{1-x})$ by $ZnCl_2$ Transport for Tunnel Diodes

P-A. Hoss,*[1] L. A. Murray, and J. J. Rivera[2]

Electronic Components and Devices, Radio Corporation of America, Somerville, New Jersey

ABSTRACT

A close-spaced growth system is described in which zinc chloride is used as both the transport agent and the doping source to grow GaAs, GaP, and $Ga(As_x, P_{1-x})$ epitaxial layers on GaAs substrates. Uniform transport and doping is obtained by situating resistively heated molten zinc chloride on both sides of the inductively heated close-space furnace. Degenerate GaAs layers with areas of 10 cm^2, thicknesses of 1 mm, and reproducible doping levels of 5×10^{19} cm^{-3} were used to produce up to 1600-amp tunnel diodes.

In the development of high current tunnel diodes uniformly doped wafers of degenerate GaAs 8-12 cm^2 in area are needed. Melt grown crystals do not show sufficient reproducibility of doping or adequate uniformity in these dimensions. The close-spaced growth of epitaxial GaAs has been discussed by a number of authors (1-5). Using H_2O or HCl as the transport agent this method has produced rapid growth rates (circa 1 mm/hr). A close-spaced inductive furnace (6) has the ability to accept the 10 cm^2 undoped GaAs substrates for epitaxial growth. In these systems doping was achieved by incorporation of n-type dopants such as Se, S, and Te in the source material. Our attempts to grow p-type GaAs using zinc in this manner resulted in n-type layers and loss of the "volatile" zinc to the hydrogen ambient. This paper discusses a new open-tube method of uniformly introducing zinc chloride vapor into the close-spaced furnace for the p-type epitaxial growth of GaAs, GaP, and their alloys on undoped GaAs substrates, and the use of grown GaAs and $Ga(As_{0.8}P_{0.2})$ in making tunnel diodes.

* Electrochemical Society Active Member.
[1] Present address: TRW Electronics, 14520 Aviation Boulevard, Lawndale, California, 90260.
[2] Present address: Burroughs Corporation, Plainfield, New Jersey.

Apparatus

The apparatus used is shown diagrammatically in Fig. 1. The close-spaced radio frequency induction furnace (6) is composed of two series-connected, flat-wound copper coils geometrically parallel, as shown. These are powered by a 10 kw generator either at 450 kc, or at 3 Mc. The coils couple to a pair of carbon susceptors placed in a quartz reaction tube of 4.3 x 1.3 cm^2 cross section. The susceptors heat the source and substrate, which are themselves separated by 1 mm thick molybdenum spacers. The required source-substrate temperature difference is obtained by mechanically moving the pair of RF coils vertically toward or away from the pair of susceptors. Temperatures are monitored by means of electrically isolated molybdenum sheathed thermocouples imbedded in the susceptors. One thermocouple electronically main-

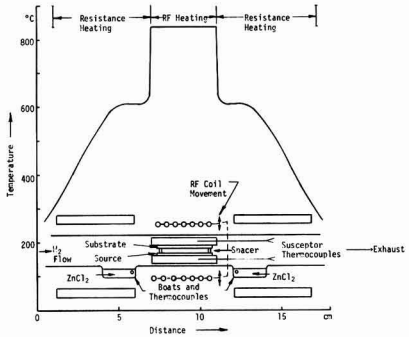

Fig. 1. Close space RF furnace with resistively heated side furnaces and temperature profile at start of growth.

tains the substrate susceptor to within 1°C of the growth temperature by controlling the RF generator with a differential amplifier, magnetic amplifier and saturable reactor series. At low hydrogen flows the source susceptor tracks to within 2°C of the temperature required. At each end, the rectangular quartz tube is depressed 1 cm to form 4 cm x 2 cm boats to contain the zinc chloride. Into the side of each boat a thin tube is fused so that its tip is surrounded by the liquid zinc chloride at operating temperatures. The tubes accept thermocouples which electronically control the cylindrical resistance furnace around each boat to within 4°C of its desired temperature. All furnaces can be reproducibly located such that the temperature gradient along the tube is maintained from run to run. Uniformity of the susceptors to within 2°C is periodically checked with a pyrometer. The temperature profile shown in Fig. 1 was obtained by inserting a molybdenum sheathed thermocouple from each end and profiling the running furnaces with the susceptors at equal temperature in nitrogen, but without the source and substrate present. The sharp temperature change in the region between the susceptor and the ambient nitrogen is probably due in part to heat conduction along the 60 mil OD molybdenum sheath. The sheath is grounded, eliminating RF pickup in the thermocouple circuits as checked by rapid turn off and on of the RF generator at operating power. Furthermore, molybdenum appears inert to the reaction atmosphere.

Procedure

The GaAs substrates are melt grown, undoped, and angle-cut 2-3°C off the (111) plane to give up to 10 cm^2 in area. Growth takes place on the chemically polished $(\bar{1}\bar{1}\bar{1})$ plane. The back (111) side has been previously coated with SiO_2 from the thermal decomposition of ethyl orthosilicate to reduce decomposition of the backs during the growth of 1 mm layers.

The GaAs and GaP sources were single-crystal or polycrystalline undoped wafers 1-2 mm thick. The $Ga(As_x, P_{1-x})$ sources were wafers of pressed and sintered mixtures of pure GaAs and GaP powders. X-ray diffraction from copper radiation is used to measure the alloy composition with change in d-spacing. The (111) plane was used for sintered powders and the (444) plane for single crystals.

Zinc chloride has been shown capable of transporting GaAs (8) in a closed-tube system and the effectiveness of zinc as a p-dopant for GaAs is known. Zinc chloride was found well suited for close-spaced transport when treated to reduce its moisture content. CP zinc chloride, as purchased, is stored at 140°C under mechanical vacuum of 30-50μ. It is loaded while still warm, and just prior to the run the zinc chloride and susceptors-substrate-source assembly are held at 300°C in flowing hydrogen for 5 min. This bakeout virtually eliminates hillocks on the epitaxial layers, possibly caused by gallium oxide inclusions.

After bakeout the hydrogen flow is adjusted to 10-30 cm^3/min through the 4.3 x 1.3 cm^2 rectangular tube cross section of which 2.4 cm^2 is occupied by the susceptors-source-substrate cross section. The GaAs source is then heated to 840°C with GaAs substrate 10°-20° higher to etch off some of the substrate. Simultaneously the zinc chloride is heated to approximately 430°C. After etching the temperature is inverted, with the source held at 840° and the substrate at 800°C. For the growth of $Ga(As_x, P_{1-x})$ with $0 < x \leq 1$ the source is held at 950° and the substrate at 910°C.

Experimental Results

The growth rates and resistivity of GaAs and GaP grown by close-spaced transport depend on the temperature of the zinc chloride, the hydrogen flow, the source and substrate temperatures, and the spacing between them. The system has been operated at no hydrogen flow, but the flow range of 10-30 cc/min resulted in a reduction of hillocks on the surface. At these low hydrogen flows the zinc chloride still achieves near saturation, based on growth rate and doping level comparisons with no flow. The GaAs substrate temperature of 800°C for GaAs growth and 910°C for GaP and phosphide-arsenide alloys were found high enough to give satisfactory growth with no tendency to polycrystallinity. The source temperature 40° higher was picked to achieve growth rates in the range of 100 μ/hr under the condition of growth for thick layers for tunnel diodes. While not studied in detail, the growth rate can be halved to doubled by reducing or increasing the temperature of the source, with little effect on this high doping level. The observed change in growth rate of GaAs with change in the zinc chloride temperature is shown in Fig. 2. Thickness was measured by a micrometer before and after the run. A 5000Å silicon dioxide layer deposited from the thermal decomposition of ethylorthosilicate eliminates back etching of the substrate during growth and the thicknesses measured agree well with measurements between the top of the layer and the substrate where the spacers had prevented growth. The observed change in doping level with changes in zinc chloride temperature was also studied for GaAs, as seen in Fig. 3.

Carrier concentrations are determined by the plasma resonance technique (7). This method gives zinc concentrations in GaAs reproducible to about 3% by IR reflectance in the 2 x 10^{19} to 9 x 10^{19} carriers/cm^3 range. Since the plasma resonance measurement covers a circle about 4 mm in diameter, this method is also used to measure the doping uniformity of layers. An

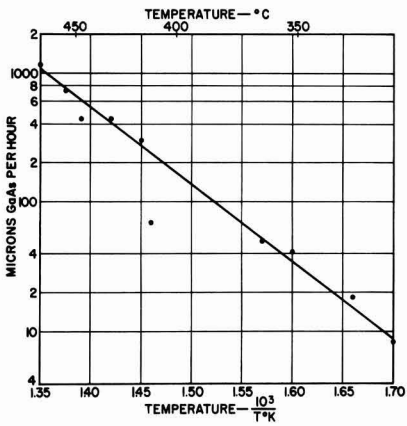

Fig. 2. GaAs growth rate as a function of zinc chloride temperature

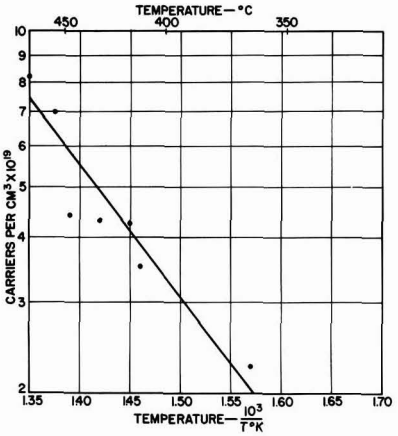

Fig. 3. GaAs doping level as a function of zinc chloride temperature

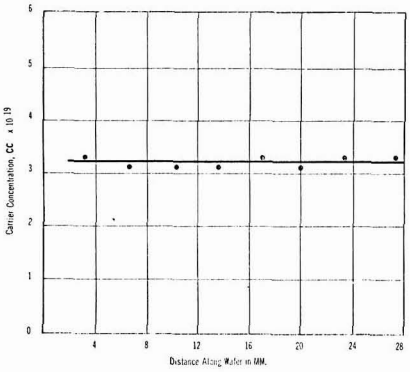

Fig. 4. Doping variation across a large area GaAs grown layer

example of the high degree of doping uniformity obtainable is shown in Fig. 4, as measured along a 28 mm line of a 32 x 22 mm wafer. The run-to-run reproducibility of zinc doping GaAs was checked out on 19 consecutive runs with temperature and flow settings unchanged. The minimum wavelengths as read by plasma resonance and the equivalent carrier concentrations are shown in Table I. The average is 5.5 x 10^{19} carriers/cm³ and the average deviation 13%. The Hall mobilities of the GaAs layers varied from 40 to 50 cm²/v-sec in the zinc concentration of 3 to 5 x

Table I. Minimum wavelengths as read by plasma resonance and equivalent carrier concentrations

Run	λ Min in microns	N × 10^{19} carriers/cm³
1	5.7	4.2
2	5.4	5.1
3	5.3	5.5
4	5.3	5.5
5	5.3	5.5
6	5.3	5.5
7	5.4	5.1
8	5.5	4.7
9	5.2	5.9
10	5.6	4.5
11	5.5	4.7
12	5.0	6.9
13	5.1	6.5
14	5.2	5.9
15	5.8	3.9
16	5.2	5.9
17	5.2	5.9
18	5.8	3.9
19	5.2	5.9

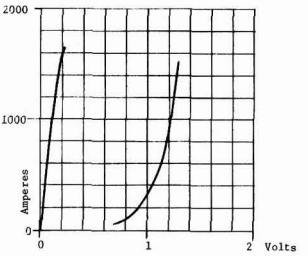

Fig. 5. Current-voltage plot of a high current GaAs tunnel diode 200 amp/division, 0.2 v/division.

10^{19} carriers/cm³. The Hall mobility of a zinc doped $Ga(As_{0.8}P_{0.2})$ sample was 30 cm²/v-sec.

Tunnel Diode Fabrication

Epitaxial layers 0.6 to 1.0 mm thick with concentrations of 5 to 6 x 10^{19} carriers/cm³ were used to fabricate tunnel diodes. A contact is placed on the top grown $(\bar{1}\bar{1}\bar{1})$ surface by lapping it flat, coating with sintered gold, nickel plating the gold, and evaporating another sintered gold layer. The wafer is then reversed and the original GaAs substrate, on the (111) side, lapped off and the wafer polished to a final thickness of 0.4-0.5 mm. A tin-lead dot about 6 cm² in area is then alloyed into the (111) surface to form the junction and top contact. The diode is then soldered to its package with Au-Ga-Zn alloy and tested. Figure 5 shows the current voltage trace of such a tunnel diode. Electrical characteristics are as follows: I_P = 1640 amp; V_P = 0.21v; V_F = 1.3v; I_V = 60 amp; V_V = 0.64v.

Smaller tunnel diodes were similarly fabricated from $Ga(As_{0.8}P_{0.2})$ wafers. I_P/I_V ratios up to 30:1 were achieved.

Discussion

The authors' previous experience has shown the need for low carrier gas flows if uniformity of growth is to be maintained in close-spaced transport and the reactants kept between the source of substrate. For tunnel diodes where a high doping level is also required, the use of a zinc chloride source on each side allows for low flows without sacrificing doping uniformity. Since the growth rate and doping level were found reproducibly dependent on the zinc chloride temperature, the temperature of the liquid zinc chloride must control the partial pressure of the zinc chloride in the high-temperature region of the furnace. The growth rate can be adjusted independently by means of the source and substrate temperatures.

Acknowledgments

The authors are indebted to P. D. Gardner, P. M. Britt, and Mrs. E. M. Strouse for fabricating and measuring the tunnel diodes and for valuable suggestions and discussions. They also thank R. D. Miller, J. S. Doyle, and A. G. Salerno for their assistance during this program.

The authors gratefully acknowledge the support of the Air Force Aeropropulsion Laboratory, Research and Technology Division, Air Force System Command, USAF.

Manuscript received Oct. 8, 1965; revised manuscript received *ca.* Dec. 11, 1967. This paper was presented in part at the Washington Meeting, Oct. 11-15, 1964, as Abstract 161.

Any discussion of this paper will appear in a Discussion Section to be published in the December 1968 JOURNAL.

REFERENCES

1. F. H. Nicoll, *This Journal*, **110**, 1165 (1963).
2. E. Sirtl, *J. Phys. Chem. Solids*, **24**, 1285 (1963).
3. P. H. Robinson, *RCA Rev.*, **24**, 574 (1963).
4. G. E. Gottlieb and J. F. Corboy, *RCA Rev.*, **24**, 585 (1963).

5. H. Flicker, B. Goldstein, and P-A. Hoss, *J. Appl. Phys.*, **35**, 2959 (1964).
6. P-A. Hoss and L. A. Murray, Paper presented at the Washington Meeting of the Society, Oct. 11-15, 1964, Extended Abstract 161.
7. L. A. Murray, J. J. Rivera, and P-A. Hoss, *J. Appl. Phys.*, **37** 4743 (1966).
8. N. Holonyak, D. C. Jillson, and S. F. Bevacqua, "Metallurgy of Semiconductor Materials," Metallurgical Society Conference V. 15, p. 49, John Wiley & Sons, Inc., New York (1962).

The Effects of Growth Rate on the Thermoelectric Properties of Bi_2Te_3-Sb_2Te_3-Sb_2Se_3 Pseudoternary Alloys

W. M. Yim and E. V. Fitzke

RCA Laboratories, Princeton, New Jersey

ABSTRACT

The effects of growth rate on the thermoelectric properties of n- and p-type Bi_2Te_3-Sb_2Te_3-Sb_2Se_3 pseudoternary alloys have been investigated and correlated with microstructures. The results show that higher values of the figure of merit (Z) are invariably associated with lower growth rates and hence greater homogeneity. For both n- and p-type alloys, the improvement in Z was as large as 50% when the growth rate was reduced from about 6 to 0.6 cm/hr. However, the growth-rate dependence of individual thermoelectric parameters was not the same for both alloys. For the n-type alloy, which is a single-phase alloy, slow growth rates resulted in an increase in the Seebeck coefficient, and a decrease both in the lattice thermal conductivity and electrical resistivity. For the p-type alloy, the variations with growth rate in the Seebeck coefficient and, to a lesser extent, in the lattice thermal conductivity were similar to those for the n-type alloy. However, its electrical resistivity increased with decreasing growth rates, and this was shown to be associated with the presence of a Te-rich second phase in the p-type alloy. Consistent with this interpretation are the results of an annealing study of these alloys.

The figure of merit of a thermoelectric material is often lowered by the presence of compositional and microstructural inhomogeneities in the material (1). These inhomogeneities are, in large part, related to growth conditions used for the material's preparation. Although the importance of optimum growth condition is generally recognized, only a few detailed studies (2) have been made in the past to elucidate the role of growth variables on the thermoelectric properties.

In this paper, we shall present the results obtained in a study of the effects of various growth rates on the thermoelectric properties of n- and p-type Bi_2Te_3-Sb_2Te_3-Sb_2Se_3 pseudoternary alloys (3) grown by the Bridgman technique. The presentation of the results will include the metallographic observation of microstructures, and the dependence on growth rate of the Seebeck coefficient, electrical resistivity, and thermal conductivity at room temperature. Included also in this paper are the results of the effects of annealing at 390°C on the room temperature thermoelectric properties of these alloys.

It will be shown that lower growth rates result in better homogeneity and higher figures of merit for both n- and p-type alloys. However, the growth-rate dependence of their individual thermoelectric parameters is not the same, and this difference will be related to the difference in the microstructure of n- and p-type alloys, in particular, to the presence of a second phase in the latter alloy. These results will be corroborated by the annealing study.

Experimental Procedure

An n-type composition $(Bi_2Te_3)_{75}(Sb_2Te_3)_{20}(Sb_2Se_3)_5$ doped with 0.16 w/o (weight per cent) SbI_3, and a p-type composition $(Sb_2Te_3)_{70}(Bi_2Te_3)_{25}(Sb_2Se_3)_5$ containing 2 w/o excess Te were used for the present study.[1]

In the preparation of the alloys, high-purity (99.999%) component elements were used, and these were obtained from the American Smelting and Refining Company. The alloys were grown by a vertical Bridgman method with freezing rates ranging from 0.24 to 7.6 cm/hr but under a constant temperature gradient of ~ 25°C/cm in the melt near the freezing interface. The resulting ingots, 0.7 cm in diameter and 18 cm long, consisted of coarse grains, whose cleavage characteristics suggested a preferred orientation with their (111) cleavage planes generally aligned with the long axis of the ingots, and this was particularly true for slowly grown ingots.

The metallographic observation of microstructure was made on sections cut perpendicular to the long axis of the ingots. The etchant used for the n-type material was 20% HNO_3 in H_2O, and that for the p-type material was 1 HNO_3-2 HCl-2 saturated $K_2S_2O_8$ in H_2O.

The measurements of electrical resistivity ρ, Seebeck coefficient Q, and thermal conductivity κ were made on short cylinders, 0.7 cm diameter and about 0.7 cm long. The electrical or temperature gradient was applied in the direction of the axis of the cylinder, which was the growth direction of the ingot and, as a result of the preferred growth, this direction coincided approximately with a direction perpendicular to the [111] trigonal axis of the crystallites. The mea-

Key words: thermoelectric alloys; Bi_2Te_3-Sb_2Te_3-Sb_2Se_3 alloys; microstructures; thermoelectric properties; effects of growth rate; effects of annealing.

[1] All compositions are in mole per cent unless otherwise specified, and they represent starting compositions. It should be noted that the above compositions do not correspond to the alloys of the highest figures of merit found in the pseudoternary system. The best n-type alloy is SbI_3-doped $(Bi_2Te_3)_{90}(Sb_2Te_3)_5(Sb_2Se_3)_5$, and the best p-type alloy is excess Te-doped $(Sb_2Te_3)_{72}(Bi_2Te_3)_{25}(Sb_2Se_3)_3$, having room temperature figures of merit 3.2×10^{-3} and 3.4×10^{-3} deg^{-1}, respectively (3). Nevertheless, the results presented in this paper are representative of n-type materials in the Bi_2Te_3-rich end and p-type materials in the Sb_2Te_3-rich region of the pseudoternary alloys.

surement techniques have been given in detail in previous papers (3, 4). The measurements of these individual thermoelectric parameters provided a direct determination of the materials figure of merit, $Z = Q^2/\kappa \cdot \rho$.

A selected group of n- and p-type specimens was annealed in a partial pressure of Ar at 390°C for a duration as long as 1000 hr. The annealing temperature chosen was, as will be shown later, slightly lower than the melting point of a second phase present in the p-type material. The thermoelectric properties of each specimen were measured at room temperature before and after the annealing treatment. In addition, room temperature Hall coefficients were measured on a few representative slow-grown samples to study the effect of annealing on the carrier concentration and mobility. Hall specimens were prepared by cleaving the bulk material, and had typical dimensions of 7x2x0.3 mm. The direction of magnetic field was perpendicular to, and the current was parallel to, the cleavage plane.

In all measurements, specimens were taken from approximately the same location of ingots, ~ 6 cm from the first portion to freeze.

Effects of Growth Rate

Microstructure.—The compound semiconductors Bi_2Te_3, Sb_2Te_3, and Sb_2Se_3 form pseudoternary solid-solution alloys over a wide range of compositions except in the neighborhood of large Sb_2Se_3 concentrations (5). The phase diagrams of Bi_2Te_3-Sb_2Te_3 (6) and Bi_2Te_3-Sb_2Se_3 (7) show that the equilibrium distribution coefficient of Sb_2Te_3 in Bi_2Te_3 and that of Sb_2Se_3 in Bi_2Te_3 are nearly equal to unity. Therefore, the present materials, when undoped, are pseudoternary alloys of approximately uniform compositions along the length of ingots. For the n-type alloy used in the present study, the amount of SbI_3 added was within its solubility limit of about 0.2 w/o in the Bi_2Te_3-rich pseudoternary alloys; hence, the present n-type alloy is a single-phase material. The distribution of the dopant appeared generally uniform, as inferred from a straight resistance-scan trace along the ingot except for the first and last 2-cm portions to freeze. For the present p-type alloy, the Te addition exceeded the solubility limit of about 0.2 w/o and therefore the p-type alloy is a two-phase material. Although the equilibrium distribution coefficient of Te in the Sb_2Te_3-rich pseudoternary alloys is less than one, the distribution of second phase was fairly uniform along the ingot except again near the first and last portions to freeze.

In Fig. 1, microstructures of fast-grown, n- and p-type alloys (a and c) are compared with those of slow-grown alloys (b and d). It is clearly seen that at the slow growth rates one obtains an improvement in the microstructural homogeneity.

(*N-type alloy.*)—The n-type alloy, when slowly grown (~ 0.6 cm/hr), is a homogeneous material of large grain size, as evident from typical cleavage cracks running obliquely through the middle of Fig. 1(b). These cracks were introduced during polishing in one grain, and the dark area at the top of the photomicrograph is a portion of another grain. By contrast, the fast-grown (~ 4 cm/hr) n-type alloy consists of a lamellar structure, as shown in Fig. 1(a). These are probably the regions of severely varying composition, but are to be distinguished from second phase such as that present in the p-type alloy [Fig. 1(c) and 1(d)].

The lamellar structure is probably associated with constitutional supercooling (8). During growth of multicomponent alloys under a constant temperature gradient, unless the growth rate is sufficiently slow, constitutional supercooling would occur with ensuing compositional segregation. This appears to be the case for the fast-grown n-type alloy shown in Fig. 1(a). By using a slow growth rate, the constitutional supercooling was avoided, as in Fig. 1(b). The effect on microstructure of different temperature gradients with a constant growth rate was not investigated. However, the effect of increasing the temperature gradient would be, as is well known (8), essentially similar to that of lowering the growth rate.

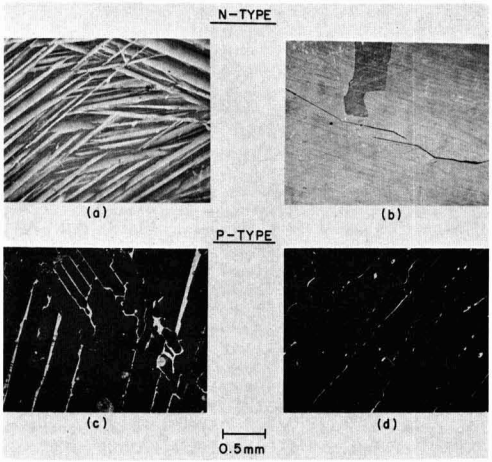

Fig. 1. Growth rate (*R*) dependence of microstructures on n-type SbI_3-doped $(Bi_2Te_3)_{75}$ $(Sb_2Te_3)_{20}$ $(Sb_2Se_3)_5$ and p-type excess Te-doped $(Sb_2Te_3)_{70}(Bi_2Te_3)_{25}(Sb_2Se_3)_5$ alloys: (a) fast-grown n-type, R = 3.8 cm/hr, $Z = 1.4 \times 10^{-3}$ deg^{-1}; (b) slow-grown n-type, R = 0.57 cm/hr, $Z = 2.1 \times 10^{-3}$ deg^{-1}; (c) fast-grown p-type, R = 7.6 cm/hr, $Z = 2.2 \times 10^{-3}$ deg^{-1}, and (d) slow-grown p-type, R = 0.64 cm/hr, $Z = 3.1 \times 10^{-3}$ deg^{-1}. All taken on ingot cross sections.

(*P-type alloy*).—The p-type alloy is, as stated above, a two-phase material consisting of a pseudoternary Sb_2Te_3-Bi_2Te_3-Sb_2Se_3 solid-solution matrix and a second phase, which appears as lamellae on an etched cross section. An electron-probe analysis showed that the second phase was composed of approximately 90 a/o (atomic per cent) Te with small amounts of Bi, Sb, and Se. The melting point of this second phase was found by DTA to be about 415°C, as compared with ~ 450°C for pure Te. From these observations, it appears that the second phase is a eutectic rich in Te. It is interesting in this connection to note that the second phase, whether it resulted from the excess addition of Te or Se, melted at about the same temperature. This shows that in both cases the second phase is similar in composition, indicating that Se preferentially enters into solid solution, and rejects from it the Te-rich second phase (3, 4).

There is a marked difference in the microstructure, especially in the second phase, between fast- and slow-grown p-type alloys. At a growth rate of about 8 cm/hr, the second phase appears as thick lamellae along cleavage planes and grain boundaries, as in Fig. 1(c). At a much lower growth rate of 0.6 cm/hr, the second phase precipitates as thin discontinuous lamellae dispersed in the matrix, as in Fig. 1(d).

Thermoelectric properties.—The growth-rate dependence of the thermoelectric properties at 300°K of n- and p-type pseudoternary alloys is shown in Fig. 2(a) (Seebeck coefficient Q), 2(b) (electrical resistivity ρ), 2(c) (measured total thermal conductivity κ_{total}, and lattice thermal conductivity κ_{ph}), and 2(d) (figure of merit Z). The lattice thermal conductivity was obtained from the measured total thermal conductivity by using the relation, $\kappa_{total} = \kappa_{el} + \kappa_{ph}$ where κ_{el} is the electronic thermal conductivity and no ambipolar contribution was assumed. The electronic contribution was calculated from the Wiedemann-Franz relation,

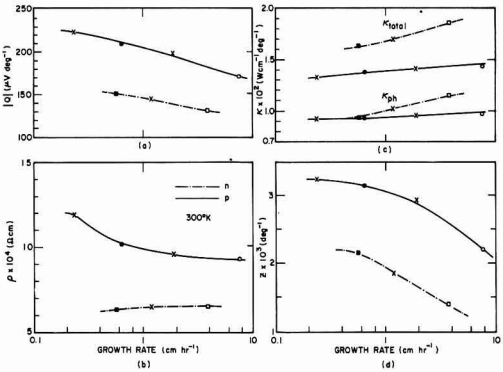

Fig. 2. Growth-rate dependence of thermoelectric properties at 300°K of n-type SbI$_3$-doped $(Bi_2Te_3)_{75}(Sb_2Te_3)_{20}(Sb_2Se_3)_5$ and p-type excess Te-doped $(Sb_2Te_3)_{70}(Sb_2Te_3)_{25}(Sb_2Se_3)_5$ alloys: (a) The Seebeck coefficient (Q), (b) electrical resistivity (ρ), (c) total thermal conductivity (κ_{total}) and lattice thermal conductivity (κ_{ph}); and (d) figure of merit (Z).

for which the Lorentz number corresponded to the simple case of acoustical lattice scattering and non-degeneracy, $2(k/e)^2$, where k is the Boltzmann constant and e is the electronic charge.

For both the n- and p-type alloys, Q increases, and κ_{total} and κ_{ph} decrease, with decreasing growth rate R. The variations in ρ with R are, however, not the same for both materials: ρ of the n-type decreases, while that of the p-type alloy increases, with decreasing R.

In general, in a given material where doping impurities are fully ionized, one would expect the electrical resistivity to decrease as the material becomes more homogeneous. The change in ρ of the n-type alloy [Fig. 2(b)] shows this to be the case, since a greater inhomogeneity is associated with a slower growth rate, as shown by the microstructure in Fig. 1(b). However, the observed change in ρ of the p-type alloy cannot be explained on the basis of homogeneity alone.

It has been shown (3) that Te acts as a donor in the p-type alloy, and therefore the Te atoms in solid solution would raise the electrical resistivity of the p-type matrix by compensation. However, it is not the resistivity of the matrix that alone is responsible for the ρ of the bulk. A single-phase p-type alloy having the same major composition as the present one, when doped with a maximum soluble amount of Te of about 0.2 w/o, showed only a slight increase in ρ to 7.5×10^{-4} ohm-cm from the undoped value of 6.5×10^{-4} ohm-cm. With further additions of Te, the second phase started to precipitate, but the bulk ρ increased regularly with corresponding increase in Q up to an onset of the intrinsic conduction. Thus, the Te-rich second phase was essential in controlling the resistivity of the p-type alloy.[2]

The second phase at slow growth rates appears as thin, discontinuous lamellae [Fig. 1(d)] as contrasted to thick, continuous lamellae [Fig. 1(c)] at fast growth rates. While no simple explanation is available, it may be that the higher ρ for the slowly grown p-type alloy is due to the discontinuous nature of the second phase, in addition to a larger Te concentation in the matrix because of more time available for the solution of Te atoms. This is corroborated by annealing results, the discussion of which will follow shortly.

The present result on the growth-rate dependence of ρ of the p-type alloy is in disagreement with the result of Cosgrove *et al.* (2), who reported that the resistivity of a p-type material decreased with decreasing growth rate. The composition of their p-type alloy was $BiSbTe_3$ doped with 0.56 w/o Se or, in the pseudoternary notation, the material corresponded approximately to a solid solution of $(Bi_2Te_3)_{50}(Sb_2Te_3)_{48}(Sb_2Se_3)_2$ containing 1 w/o excess Te, most of which would appear as a second phase. Because of this difference in the alloy composition, a direct comparison of the previous and the present results is difficult to make.

Cosgrove *et al.* (2) did not report the presence of a second phase, but they did detect n-type regions in the p-type matrix by thermal probing. It is possible that the n-type regions were of a similar nature to the Te-rich second phase, although in the present work the relatively small dimensions of the second phase rendered the thermal-probe technique unsuccessful.

The increase in Q for the p-type alloy with decreasing R is to be expected [Fig. 2(a)], since in an extrinsic semiconductor the Seebeck coefficient is approximately proportional to $\ln\rho$. Thus, the increase in Q for the p-type alloy can be accounted for by the corresponding increase in ρ. For the n-type alloy, the observed variation in Q with R is contrary to what one would expect from the change in ρ. It was first pointed out by Airapetiants (1) that compositional inhomogeneities can substantially reduce the Seebeck coefficient and, at the same time, increase the thermal conductivity of a thermoelectric material by "circulating currents." As a consequence, the inhomogeneities lead to a lower figure of merit for the material. The increase in Q of the n-type alloy, in spite of a decrease in ρ, may be ascribed to an improvement in the material's homogeneity with decreasing growth rate.

The measured total thermal conductivity, as well as the lattice thermal conductivity, decreased with decreasing growth rate, as shown in Fig. 2(c). For the n-type alloy, the κ_{ph} decreased by about 20% when R was reduced from 4 to 0.6 cm/hr. By comparison, the κ_{ph} of the p-type alloy decreased only 5% on reducing R from 8 to 0.6 cm/hr.

Circulating currents tend to enhance heat transport; hence, a material containing second phase may exhibit a higher thermal conductivity than a similar material without the second phase. However, there is an additional effect on heat transport of the second phase, which tends to decrease the thermal conductivity. In a two-phase material, the possibility exists that submicroscopic precipitates or crystalline defects, such as arrays of dislocations present at the phase boundaries, may cause significantly the scattering of phonons. Thus, the phonon scattering by these defects would modify the extent of increase in the thermal conductivity arising from circulating currents. Since the present two-phase p-type alloy is already imperfect, even when prepared under most ideal conditions [for instance, a dislocation density of $10^{10} \sim 10^{11}$ cm^{-2} (2) would be required to maintain lattice registry between the second phase and matrix], variations in the growth rate would not drastically alter the defect density. The fact that the κ_{ph} of the p-type alloy is nearly independent of R suggests this may be the case. Therefore, it appears that the contribution of the circulating currents is relatively small for the present materials, especially for the p-type alloy, over the range of growth rates used. The changes in κ_{ph} for the present case are in no way as large (by a factor of two) as those reported by Cosgrove *et al.* (2) for p-type $BiSbTe_3$ doped with Se.

The changes in Q, ρ, and κ with different growth rates are reflected in the figures of merit, as seen in Fig. 2(d). The figures of merit of the n- and p-type alloys were significantly improved by using slow growth rates: the resulting improvement in Z for both materials is more than 50%. The factors contributing the most to this improvement are the increase in Q and the reduction in κ_{ph} for the n-type, and the increase in Q^2/ρ for the p-type alloy. The results shown in Fig. 2(d) demonstrate clearly the important role of optimum growth conditions in achieving high figures of merit.

[2] The increase in ρ with increasing excess Te addition may alternatively be explained by the assumption that the second phase depletes the matrix of Bi and Sb (acceptors), and thus causes a decrease in the hole concentration in the material.

Effects of Annealing

The changes in the room temperature thermoelectric properties of annealed specimens are shown in Fig. 3(a) (Q), 3(b) (ρ), 3(c) (κ_{total} and κ_{ph}), and 3(d) (Z). It is interesting to note that the rate of the changes is generally greater during the first 10-hr than longer-time annealing. As in Fig. 2, the broken curves are for n-type and the full curves are for p-type alloys. For ease of reference, the same symbol for each individual data point was used in Fig. 3 as in Fig. 2. For example, a full circle at zero annealing time in Fig. 3 corresponds to the same p-type alloy grown at 0.6 cm/hr shown by the full circle in Fig. 2. Also included in Fig. 3 (open triangles) are the annealing data of slow-grown, single-phase, undoped, p-type alloy having the same major composition as the Te-doped alloy.

For fast-grown n-type alloy, Q increased while ρ and κ_{ph} decreased; thus, Z increased with annealing in a manner similar to the effects of decreasing the growth rate. Although no apparent change in microstructure was observed, this improvement must be related to a partial homogenization of segregated structures. As might be expected, the slowly grown n-type alloy showed essentially no change upon annealing in its thermoelectric properties.

For Te-doped p-type material, annealing resulted in an increase in Q and ρ, while κ_{ph} remained unchanged for both the fast- and slow-grown alloys; hence, there was a slight improvement in Z. These changes in the thermoelectric properties are again reminiscent of the effects of lowering the growth rate.

Since the single-phase, undoped, p-type alloy showed essentially the same properties before and after the annealing, the increase in Q and ρ of the Te-doped alloy must have resulted from the presence of the Te-rich second phase in the doped alloy. It is most probable that on annealing some re-solution of Te takes place, which causes a decrease in the hole concentration and results in an increase in ρ and Q. The metallographic examination, however, revealed no change in the microstructure after annealing. This is reasonable in view of the following simple argument.

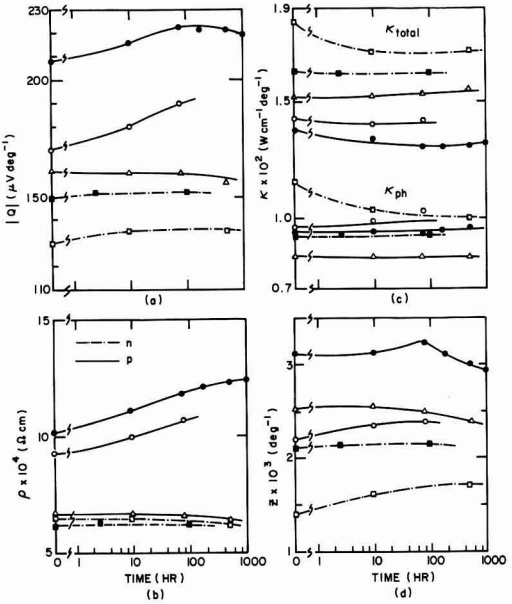

Fig. 3. Variations in thermoelectric properties at 300°K of n-type SbI_3-doped $(Bi_2Te_3)_{75}(Sb_2Te_3)_{20}(Sb_2Se_3)_5$; p-type undoped, and excess Te-doped $(Sb_2Te_3)_{70}(Bi_2Te_3)_{25}(Sb_2Se_3)_5$ with annealing time: (a) the Seebeck coefficient (Q); (b) electrical resistivity (ρ); (c) total thermal conductivity (κ_{total}) and lattice thermal conductivity (κ_{ph}), and (d) figure of merit (Z). (○) excess Te-doped p-type, R = 7.6 cm/hr; (●) excess Te-doped p-type, R = 0.64 cm/hr; (△) undoped p-type, R = 0.64 cm/hr; (□) SbI_3-doped n-type, R = 3.8 cm/hr; and (■) SbI_3-doped n-type, R = 0.57 cm/hr.

Table I. Effect of annealing on room temperature carrier concentration and mobility

	Anneal. time, hr	Carrier conc., 10^{19}/cm³	Mobility, cm²/v · sec
p-type	0	2.3	271
	73	1.9	280
n-type	0	7.0	143
	100	6.8	149

p-type: doped with 2 w/o excess Te, grown at 0.64 cm/hr; n-type: doped with 0.16 w/o SbI_3, grown at 0.57 cm/hr.

If one assumes that each Te atom acts as a singly ionized donor, and that the hole mobility is independent of annealing, then one can calculate the change in the hole concentration corresponding to the change in ρ. The number of Te atoms that must dissolve in order to effect the experimentally observed ρ change, was calculated to be negligibly small as compared with that present in the second phase. Thus, one would not expect to see any change in the structure metallographically. The same conclusion was also arrived at from the calculation of the change in Q on annealing, with the assumption that Q is inversely proportional to logarithm of the carrier concentration. A slight decrease in Q and Z for the slow-grown p-type alloy beyond 100-hr annealing may be due to evaporation of Te from the specimen, as evidenced sometimes from a thin, shiny film deposit on the inside wall of quartz ampoule.

In a material such as the present p-type alloy, it is difficult to obtain reproducible Hall data because of the presence of second phase. Nevertheless, the data shown in Table I[3] indicate that the changes with annealing in Q and ρ of slowly grown p-type alloy were due mostly to a change in the carrier concentration, resulting presumably from the Te re-solution. For slowly grown n-type alloy, the Hall data show that there was essentially no change in the carrier concentration, nor in the mobility.

Conclusions

The effects of various growth rates on the thermoelectric properties of n- and p-type Bi_2Te_3-Sb_2Te_3-Sb_2Se_3 pseudoternary alloys have been investigated and correlated with microstructures. The results show that higher values of the figure of merit are invariably associated with lower growth rates and hence greater homogeneity. For both n- and p-type alloys, the improvement in the figure of merit was as large as 50% when the growth rate was reduced from about 6 to 0.6 cm/hr. However, the growth rate dependence of individual thermoelectric parameters was not the same for both alloys.

For the n-type alloy, which is a single-phase material, slow growth rates resulted in an increase in the Seebeck coefficient, and a decrease both in the lattice thermal conductivity and electrical resistivity. These changes are what one would expect from an improvement in the material's homogeneity with decreasing growth rate, since the deleterious effects of circulating currents would diminish as material's homogeneity improves. For the p-type alloy, which is a two-phase material, the variations with growth rate in the Seebeck coefficient and, to a lesser extent, in the lattice thermal conductivity were similar to those in the n-

[3] The carrier concentration was calculated with the assumption of simple spherical band structure, and the mobility reported here is the Hall mobility, $R_H \cdot \sigma$, where R_H is the Hall coefficient and σ is the electrical conductivity.

type alloy. However, slow growth rates resulted in an increase in its electrical resistivity. The resistivity increase in the p-type alloy was interpreted on the basis of Te re-solution from the Te-rich second phase present in the alloy. Consistent with this interpretation are the results of an annealing study of these alloys. The annealing effects, while less pronounced, were essentially similar to those brought about by variations in the growth rate.

Acknowledgments

The authors are grateful to E. J. Stofko and T. V. Pruss for their valuable contributions in materials preparation and thermoelectric measurements. Constructive comments by F. D. Rosi during the course of this work are gratefully acknowledged.

Manuscript received Dec. 5, 1967.

Any discussion of this paper will appear in a Discussion Section to be published in the December 1968 JOURNAL.

REFERENCES

1. S. V. Airapetiants, *Soviet Phys.—Tech. Phys.*, **2**, 429 (1957); S. V. Airapetiants and M. S. Bresler, *ibid.*, **3**, 1778 (1958).
2. G. J. Cosgrove, J. P. McHugh, and W. A. Tiller, *J. Appl. Phys.*, **32**, 621 (1961); R. W. Ure, Jr., *ibid.*, **33**, 2290 (1962).
3. W. M. Yim, E. V. Fitzke, and F. D. Rosi, *J. Materials Sci.*, **1**, 52 (1966).
4. F. D. Rosi, B. Abeles, and R. V. Jensen, *J. Phys. Chem. Solids*, **10**, 191 (1959).
5. I. Teramoto and S. Takayanagi, *J. Phys. Chem. Solids*, **19**, 124 (1961).
6. M. J. Smith, R. J. Knight, and C. W. Spencer, *J. Appl. Phys.*, **33**, 2186 (1962).
7. V. G. Kuznetsov and K. K. Palkina, *Russ. J. Inorg. Chem.*, **8**, 624 (1963); also, A. Matsumura, Private communication.
8. See, for example, B. Chalmers, "Principle of Solidification," John Wiley & Sons, Inc., New York, (1964).

Technical Note

Eu^{+2} Activation in Some Alkaline Earth Strontium Phosphate Compounds

M. V. Hoffman*

Lighting Research Laboratory, General Electric Company, Cleveland, Ohio

The fluorescence of divalent europium has received increased attention recently, and a number of phosphors emitting in the blue or ultraviolet region have been described. The efficiency and the narrow spectral distribution of Eu^{+2}-activated phosphors make them attractive for use in reprographic and black light applications and for ultraviolet emission in cathode-ray tubes. Nazarova (1) found cathodoluminescence in $Sr_3(PO_4)_2$, α and β $Sr_2P_2O_7$ and $Sr(PO_3)_2$, all with Eu^{+2} activation. In another group of strontium compounds, Gorbacheva (2) found that Eu^{+2} did not enter the β $(Sr,Mg)_3(PO_4)_2$ structure completely unless very strong reducing conditions were used, and this gave yellow emission. She also found blue emission with Eu^{+2} in $SrMg_2(PO_4)_2$. More recently, Wanmaker and ter Vrugt (3) have reported that divalent europium responds efficiently to ultraviolet excitation in alkaline earth pyrophosphates and showed that the strontium compounds were the most efficient. They described $Sr_2P_2O_7$:Eu and $Sr_{0.8}Mg_{1.2}P_2O_7$:Eu and showed that they are efficient phosphors with narrow emission bands.

As pointed out by Wanmaker and ter Vrugt, the Sr compounds are suitable potential host lattices for Eu^{+2} activation because of the similarity of ionic radii (Sr^{+2} 1.13Å, Eu^{+2} 1.17Å). In addition to a site for Eu^{+2} substitution, the host lattice should have chemical stability in the nonoxidizing atmospheres required to place Eu in the site as a divalent cation and also the absence of a site or structure which will hold Eu in its preferred trivalent state.

A group of compounds which illustrate these requirements are found in the ternary systems SrO-MgO-P_2O_5 and SrO-ZnO-P_2O_5, and these were examined with Eu^{+2} activation. The orthophosphate joins of these systems have been described previously by Sarver, Hoffman, and Hummel (4). The compounds on these joins are the true ternary orthophosphates, $SrMg_2(PO_4)_2$ and $SrZn_2(PO_4)_2$, and the stabilized high-temperature forms, or β form of $Sr_3(PO_4)_2$, which are found only in the ternary region. These systems also contain the compounds $SrMgP_2O_7$, $Mg_3Sr_2P_4O_{15}$, and $SrZnP_2O_7$. The compatibility triangles are shown in Fig. 1 and 2. No solid solutions were found except in the β orthophosphate regions.

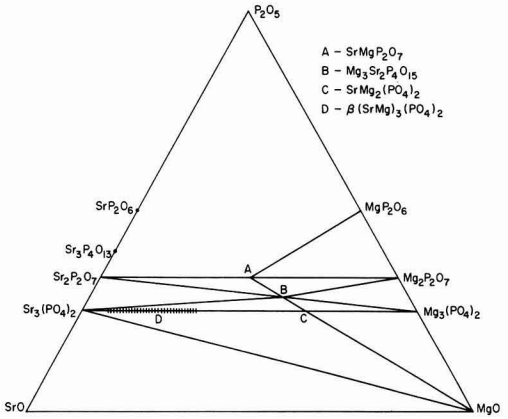

Fig. 1. Compatibility triangles in part of SrO-MgO-P_2O_5 system

* Electrochemical Society Active Member.

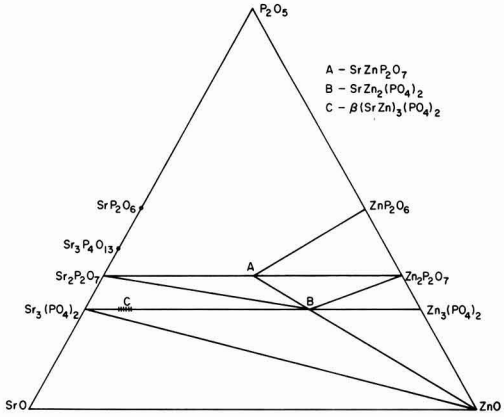

Fig. 2. Compatibility triangles in part of SrO-ZnO-P_2O_5 system

The x-ray diffraction data for these compounds are shown in the Appendix.

Phosphor Preparation

The starting materials used in these experiments were $SrHPO_4$, $SrCO_3$, $MgNH_4PO_4 \cdot H_2O$, $MgCO_3$, ZnO, $(NH_4)_2HPO_4$, and Eu_2O_3, all of purity normally used in phosphor manufacture. The europium was used either as the oxide or coprecipitated with the strontium compounds. The materials were mixed dry and fired in air at temperatures of from 900° to 1100°C, depending on the composition used. Samples containing a large amount of $(NH_4)_2HPO_4$ were fired initially at 550°C for several hours, milled, and then refired at a higher temperature. The final firing was in a flowing nonoxidizing atmosphere, usually a mixture of less than 1% H_2 in N_2. Other atmospheres such as mixture of CO and CO_2 can also be used satisfactorily.

Measurements

The identifications of these compounds and their determination when present as minor, second phases in the various phosphor preparations were made by x-ray diffraction, using the General Electric XRD-5 with CuK_α radiation. The emission spectra were obtained with a corrected, direct recording spectrometer with a grating monochromator (5). The excitation response between 120 and 300 nm was determined with a vacuum monochromator and is relative to sodium salicylate. The reflectance spectra in this region were determined on the same instrument and are relative to CaF_2. This standard is used because it has a higher reflectivity in the ultraviolet than MgO and also is more stable with time. The method used to measure the excitation and reflectance below 300 nm has been described by Johnson (6).

The reflectance measurements in the visible and near ultraviolet regions were made on a Cary 14 spectrophotometer and are also relative to CaF_2. In the Cary 14, monochromatic light is directed on to the sample, and the photocell detects all wavelengths coming from the sample; *i.e.*, reflected light of the incident wavelength and also any fluorescence emitted by the sample, if it is excited by the incident light. The instrument is modified to measure reflectance of materials fluorescing in the visible by the insertion of a Corning 7-54 filter between the sample and the detector when measuring in the ultraviolet region. Fuorescence in the ultraviolet is transmitted by the 7-54 filter and is recorded as a rise in the reflectance curve at the exciting wavelengths. The Cary 14 is extremely sensitive in this region and can be used to detect weak ultraviolet fluorescence. With phosphors as efficient as those reported here, the interference of the fluorescence is too large to obtain meaningful reflectance

Table I. Summary of fluorescence spectra

Compound	Emission peak 254 nm excitation nm	Half width nm	Relative peak height
$SrMgP_2O_7$:0.02Eu	393	26	100
$\alpha Sr_3(PO_4)_2$:0.01Eu	405	43	60
$\alpha Sr_2P_2O_7$:0.18Eu	415	40	47
$Sr_3P_4O_{13}$:0.02Eu	415	60	20
$SrMg_2(PO_4)_2$:0.02Eu	410	47	18
$Mg_3Sr_2P_4O_{15}$:0.02Eu	440	—	5

curves below 400 nm. The instrument, as modified by the insertion of the 7-54 filter, was used to determine the presence or absence of ultraviolet fluorescence, and to give a qualitative measure of the excitation.

Results

The incorporation of Eu^{+2} is possible in all of the strontium compounds in these systems, resulting in strong absorption bands in the ultraviolet region. The emission and excitation spectra are dependent on the composition and structure of the host lattice. Table I summarizes the fluorescence spectra found for the more efficient phosphors in these systems.

Of the orthophosphate compounds, only $\alpha Sr_3(PO_4)_2$:Eu^{+2} is efficient. Nazarova (1) reported an emission peak at 425 nm under cathode-ray excitation. We measured the emission at 405 nm under 254 nm excitation. The $SrMg_2(PO_4)_2$ compound is much less efficient, peaks at 410 nm, and is excited by radiation below 260 nm. The spectral distribution curves of these two phosphors are shown in Fig. 3. The compound, $Mg_3Sr_2P_4O_{15}$, is the least efficient and peaks at 440 nm, with the major excitation below 250 nm.

The $SrZn_2(PO_4)_2$ and $SrZnP_2O_7$ compounds are strongly absorbing with Eu^{+2} present, but have no visible or ultraviolet fluorescence. The reflectance curves show no evidence of ultraviolet emission under any excitation, Fig. 4. Measuring the reflectance and excitation of $SrZn_2(PO_4)_2$:Eu between 140 and 300 nm with the vacuum monochromator also showed no emission and 75-85% absorption in this region.

The substitution of Eu in the $\beta(SrMg)_3(PO_4)_2$ compound gave both blue and red emission from the two valence states of Eu and showed Eu^{+3} absorption lines, even when fired in an atmosphere of 5% H_2 in N_2.

The β structure is stabilized by the incorporation of a divalent cation such as Mg, Ca, Zn, or Cd in the orthophosphate stoichiometry (4) and should be expected to accept Eu^{+2} without difficulty in the Sr site. The β structure, however, can also be stabilized by a trivalent cation, such as Al^{+3}, and this stoichiometry falls on the $Sr_3(PO_4)_2$-$AlPO_4$ join, resulting in a de-

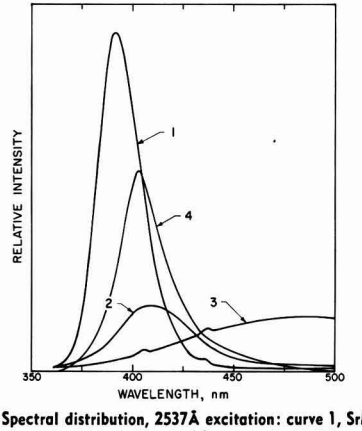

Fig. 3. Spectral distribution, 2537Å excitation: curve 1, $SrMgP_2O_7$:$02Eu^{+2}$; curve 2, $SrMg_2(PO_4)_2$:Eu^{+2}; curve 3, $MgWO_4$; curve 4, $\alpha Sr_3(PO_4)_2$:01Eu.

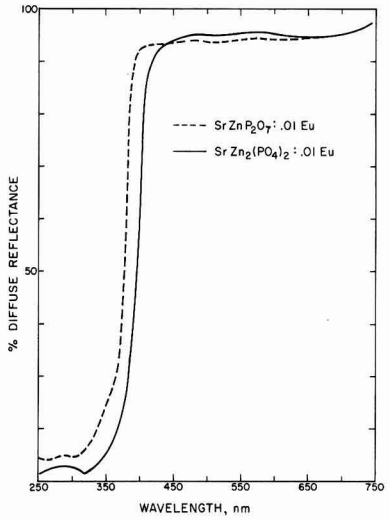

Fig. 4. Diffuse reflectance curves, $SrZnP_2O_7$:01Eu^{+2} and $SrZn_2(PO_4)_2$:01Eu^{+2}.

fect structure (7). The substitution of YPO_4 also forms a compound with an x-ray diffraction pattern very similar to Al-stabilized β $Sr_3(PO_4)_2$ and may also be the β form. The presence of both blue and red fluorescence suggests that Eu has substituted for Sr^{+2} and is also present as Eu^{+3}, plus a cation vacancy. Both types of substitution may be present in the same structure, but more likely, the presence of Eu^{+3} has moved the composition into a two-phase region of β $(Sr,Mg)_3(PO_4)_2$ and a β-type structure stabilized with Eu^{+3}.

The ternary pyrophosphate $SrMgP_2O_7$ is the most efficient phosphor found in these systems, as shown in Table I. The compatibility relationships show that this compound does not accept $Mg_2P_2O_7$ or $Sr_2P_2O_7$ in solid solution, *i.e.*, compositions on the join on either side of $SrMgP_2O_7$ will be two-phase material. The luminescent data and the x-ray diffraction pattern given in ref. (3) for the composition $Sr_{0.8}Mg_{1.2}P_2O_7$:Eu reflect the presence of more than one phase. The inclusion of $Mg_2P_2O_7$ with $SrMgP_2O_7$ has no effect on the Eu^{+2} emission other than a decrease of the measured intensity due to dilution with an inert material. Composition high in $Sr_2P_2O_7$, however, affect the emission and absorption much more strongly than the relative intensities of the two phosphors would indicate. $\alpha Sr_2P_2O_7$ accepts considerable $Eu_2P_2O_7$ in solid solution and reaches its peak fluorescence intensity at compositions between $Sr_{1.9}Eu_{0.1}P_2O_7$ and $Sr_{1.8}Eu_{0.2}P_2O_7$, or about five to ten times the amount found to be optimum in other Eu^{+2}- activated phosphors. When mixtures containing $Sr_2P_2O_7$ and $SrMgP_2O_7$ are prepared with Eu^{+2}, $Sr_2P_2O_7$ preferentially accepts the activator, and the emission of $Sr_2P_2O_7$:Eu^{+2} at 415 nm is present in much greater proportion than the compound itself.

The peak fluorescence intensity in the ternary pyrophosphate is found between the composition $Sr_{0.99}Eu_{0.01}MgP_2O_7$ and $Sr_{0.90}Eu_{0.10}MgP_2O_7$, with almost constant intensity between $Sr_{0.99}Eu_{0.01}MgP_2O_7$ and $Sr_{0.95}Eu_{0.05}MgP_2O_7$. This phosphor peaks at 393 nm under long and short ultraviolet and under cathode-ray excitation. The reflectance curve from the Cary 14 shows considerable emission under 360 nm excitation and strong fluorescence below 325 nm. The true excitation and reflectance curves in the region from 140 to 300 nm are shown in Fig. 5.

The response to excitation between 120 and 300 nm was compared to sodium salicylate, which is constant between the region of 230 to 330 nm, and has a quantum yield of 64% (8, 9). From this comparison, $SrMgP_2O_7$:Eu is almost constant over the range 220-300 nm and has a quantum yield of 90-95%.

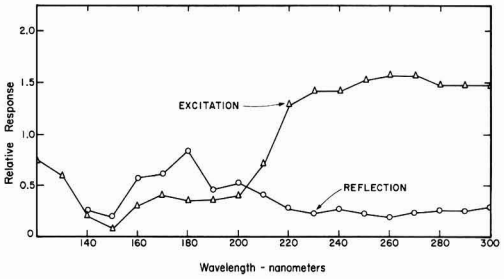

Fig. 5. $SrMgP_2O_7$:02Eu phosphor: △ excitation relative to NaC_7H_5O = 1; ○ reflectance relative to CaF_2 = 1.

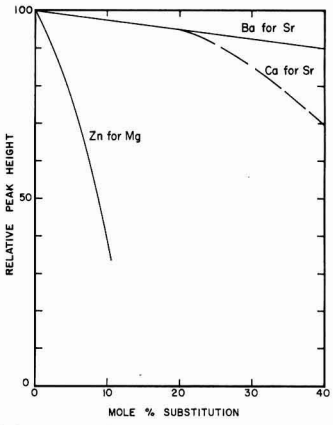

Fig. 6. Relative intensity of 393 nm peak for cation substitution in $SrMgP_2O_7$:02Eu^{+2}.

Cation Substitution

$SrMgP_2O_7$ has two sites for cation substitutions, and a wide range of solid solutions are possible. Complete solid solution is probably between $SrMgP_2O_7$ and $BaMgP_2O_7$ and between $SrMgP_2O_7$ and $SrZnP_2O_7$. Partial substitution of Ca for Sr can be made although the analogous compound $CaMgP_2O_7$ does not exist. The effect on the Eu^{+2} emission was measured for substitutions of these cations, and the changes in peak height of the 393 nm emission are shown in Fig. 6. At least 20 mole % of Ba can be substituted without an appreciable change in the peak intensity. With 40% substitution, the brightness is decreased only about 10%, but the compound with complete substitution, $BaMgP_2O_7$:Eu, emits at 400 nm, with about 10% of the efficiency of the $SrMgP_2O_7$ analogue. With the substitution of Ca^{+2}, a smaller cation, the intensity is decreased and the emission peak is shifted to longer wavelengths (Fig. 7). Substitutions of 10% Zn for Mg changed the absorption edge of the lattice to 390 nm, and the intensity of the emission decreased by about 50%.

Acknowledgments

The author would like to thank Dr. R. L. Brown, T. E. Lusk and B. Walsh for the emission and excitation data. The samples were prepared and measured by R. P. Kattler.

Manuscript received Nov. 30, 1967; revised manuscript received *ca.* Jan. 29, 1968. This paper was presented at the Boston Meeting, May 5-9, 1968, as Abstract 59.

Any discussion of this paper will appear in a Discussion Section to be published in the December 1968 JOURNAL.

APPENDIX

X-Ray Diffraction Patterns, CuK$_\alpha$ *Radiation*

$SrMgP_2O_7$			$Mg_3Sr_2P_4O_{15}$			$SrZnP_2O_7$		
2θ	d	I	2θ	d	I	2θ	d	I
12.7	6.99	26	12.4	7.13	4	12.75	6.93	23
13.9	6.37	54	15.1	5.86	5	13.7	6.46	9
17.6	5.04	10	15.5	5.71	7	13.85	6.39	18
18.1	4.90	6	15.7	5.64	13	19.90	4.46	9
19.9	4.46	6	19.5	4.55	4	21.80	4.07	18
21.0	4.23	14	20.1	4.47	3	22.80	3.90	3
21.4	4.15	17	21.5	4.13	2	23.60	3.77	4
22.5	3.95	16	23.55	3.77	57	25.80	3.45	7
23.5	3.79	14	24.9	3.57	2	26.80	3.32	100
24.4	3.65	45	25.9	3.44	2	27.40	3.25	67
25.6	3.48	10	26.6	3.35	23	28.34	3.15	25
26.8	3.33	100	27.7	3.22	53	29.00	3.08	63
27.2	3.28	70	29.45	3.03	63	30.20	2.96	46
28.2	3.16	70	30.3	2.95	11	30.90	2.89	42
29.2	3.06	70	32.0	2.79	100	33.50	2.67	24
30.1	2.97	36	32.85	2.73	28	33.70	2.66	28
30.8	2.90	66	34.4	2.61	11	34.60	2.59	30
33.1	2.70	46	35.4	2.53	12	35.50	2.53	12
33.8	2.65	60	37.8	2.38	17	36.20	2.48	2
34.5	2.60	37	38.7	2.33	14	36.95	2.43	12
35.6	2.52	20	39.0	2.31	7	39.20	2.30	16
39.4	2.29	46	39.6	2.27	6	39.60	2.27	16
41.0	2.20	30	41.0	2.20	15	40.50	2.22	4
41.8	2.16	7	41.7	2.16	4	41.08	2.19	18
43.6	2.08	13	42.9	2.11	23	41.62	2.17	11
44.2	2.05	64	44.7	2.03	3	44.08	2.05	44
45.7	1.99	30	46.3	1.96	3	44.07	2.03	9
46.1	1.97	24	46.9	1.94	5	45.96	1.97	37
			47.4	1.92	3	47.0	1.93	7
			48.35	1.88	29			
			49.0	1.86	3			
			49.3	1.85	6			
			50.1	1.82	16			
			50.8	1.80	29			

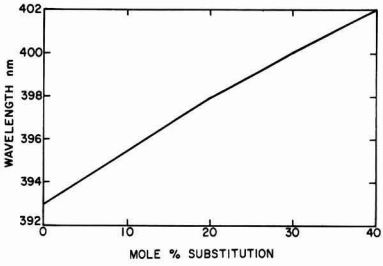

Fig. 7. Shift of peak position with Ca substitution for Sr in $SrMgP_2O_7$:02Eu^{+2}.

REFERENCES

1. V. P. Nazarova, *Bull. Acad. Sci. USSR, Phys. Ser.*, **25,** 323 (1961).
2. N. A. Gorbacheva, *ibid.*, **30,** (1966).
3. W. L. Wanmaker and J. W. ter Vrugt, *Philips Research Repts.*, **22,** 355 (1967).
4. J. F. Sarver, M. V. Hoffman, and F. A. Hummel, *This Journal*, **108,** 1103 (1961).
5. R. L. Brown, *Illum. Eng.*, **61,** 230 (1966).
6. P. D. Johnson, *J. Opt. Soc. Amer.*, **51,** 1235 (1961).
7. Ref. (4) and unpublished work, J. F. Sarver and M. V. Hoffman.
8. N. Kristianpoller and R. A. Knapp, *Appl. Optics*, **3,** 915 (1964).
9. N. Kristianpoller, *J. Opt. Soc. Amer.*, **54,** 1285 (1964).

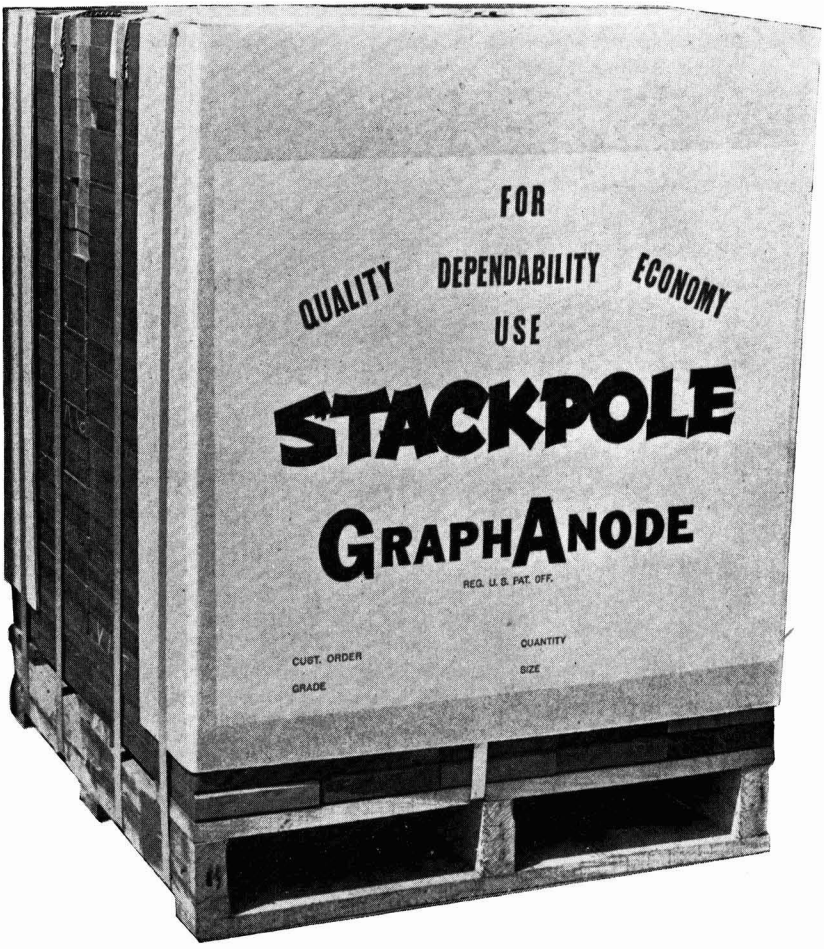

GET A LOAD OF THIS

If you're looking for improved performance, greater productivity, and reduced operating costs, investigate the savings of Stackpole GraphAnodes®. Rigid manufacturing controls assure material uniformity and permit proper cell alignment that makes for even wear and longer life. Whatever your anode needs, Stackpole GraphAnodes® can help you cut costs. Try a load. Write or call: Stackpole Carbon Company, Carbon Division, St. Marys, Pennsylvania 15857. Phone: 814-781-8463. TWX: 510-693-4511.

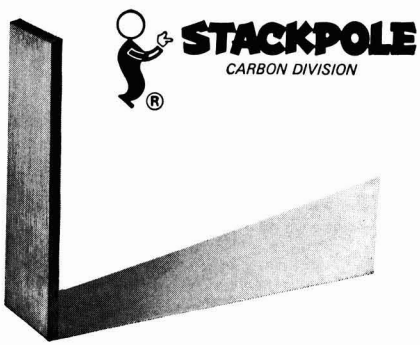

ELECTROCHEMICAL SOCIETY

NEWS AND REVIEWS — MAY 1968

The Early History of the Electrodeposition and Separation of Particles

Myron Robinson

Research-Cottrell, Incorporated, Bound Brook, New Jersey

ABSTRACT

The existence of electrostatic forces of attraction had been known to classical antiquity, but the first reported observations in the electrostatics of airborne particles date from about 1600. Closely associated with studies of smoke and other fine suspended particles in an electric field was the discovery of the man-made corona discharge after 1670. A review is presented of the contributions of the very early investigators of electrodeposition, electroseparation, and the high-voltage discharge, among whom are some of the foremost names in the history of science: Gilbert, Boyle, Newton, Coulomb, and Faraday.

Electrostatic dust precipitation, liquid spraying, mineral separation, xerography, and other widespread applications of the electrodeposition and separation of particles are, for the most part, developments of the twentieth century. But as is commonly the case in the history of science, the essential phenomena had been demonstrated in principle long before an advancing technology provided the ancillary equipment required for effective commercial utilization.

The following survey briefly reviews the older historical background of the subject, from the earliest times to 1907, the year marking the first successful commercial application of electrostatic precipitation.

The Beginnings of Particle Electrostatics and the Discovery of the Corona Discharge

Thales of Miletus, one of the seven wise men of Greece and founder of the school whence Socrates came, is commonly mentioned as the discoverer of electrostatic attraction. This claim, particularly frequent in textbooks on electrostatics, is not, however, well documented by the literary remains available to us. No writings of Thales have survived, and it is to Diogenes Laertius, the third century biographer of the philosophers, that we are indebted for information on Thales' electrical "researches." In this connection, Diogenes notes simply that ". . . Aristotle and Hippias [Greek sophist, fifth century B.C.] say that he [Thales] attributed souls also to lifeless things, forming his conjecture from the nature of the magnet, and of amber" (1). Aristotle, on the other hand, speaks only of the animation of the magnet as an opinion that originated with Thales, and even of this he is not altogether certain: "Thales, too, apparently judging from the anecdotes related of him, conceived soul as a cause of motion, if it be true that he affirmed the loadstone to possess soul, because it attracts iron" (2).

Since the two foregoing quotations comprise the known evidence linking Thales to the discovery of electrostatic attraction, the association of Thales with amber may well have been an invention of Diogenes 800 years after the alleged event. That this could have been so is not strange, for the early writers closely associated electric and magnetic phenomena, often speaking of electricity as a kind of magnetism, and considering magnetic action the general case of attractive mechanism. As late as 1600, for example, William Gilbert, the "Galileo of magnetism," still preserved this already old tradition by having in his "De Magnete" (Fig. 1) a chapter entitled "On the Magnetic Coition," of which the first segment was subtitled "On the Attraction of Amber" (3).

It is clear, in any case, that the existence of electrostatic forces of attraction had been known to classical antiquity, for the observation that a rubbed amber attracts straws, dried leaves, and other light bodies ostensibly in the same way a magnet attracts iron is variously credited to Theophrastus (ca. 300 B. C.), Pliny (first century), and Solinus (third century), as well as other ancients, Greek and Roman (4). But owing to the deficiency of scientific method and to the absorbing interests of practical life, repeated accounts of electrostatic attraction from the earliest times to the advent of Gilbert, revealed little in the way of novelty either in observation or interpretation. Indeed, it remained for Gilbert to observe specifically that electrostatic forces could deflect particulate matter from an aerosol. Discussing the attractive power of amber, sulfur, diamond, and other "electricks" (i.e., dielectrics) "when stimulated by friction," Gilbert reported that such materials would "entice smoke sent out by an extinguished light" (3). ("Electric" for-

REVIEW SECTION

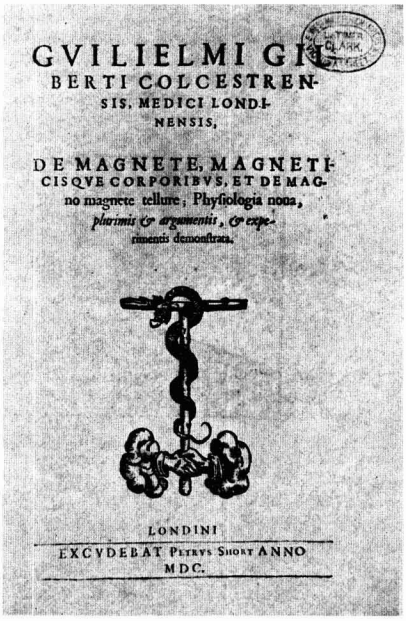
GVILIELMI GI
BERTI COLCESTREN-
SIS, MEDICI LONDI-
NENSIS,
DE MAGNETE, MAGNETI-
CISQVE CORPORIBVS, ET DE MAG-
no magnete tellure; Physiologia noua,
plurimis & argumentis, & experimentis demonstrata.
LONDINI
EXCVDEBAT PETRVS SHORT ANNO
MDC.

Fig. 1. Title page of *De Magnete*. The text reads: "William Gilbert of Colchester, Physician of London, On the Magnet, Magnetic Bodies Also, and on the great magnet the earth; a new Physiology, demonstrated by many arguments & experiments. London, 1600."

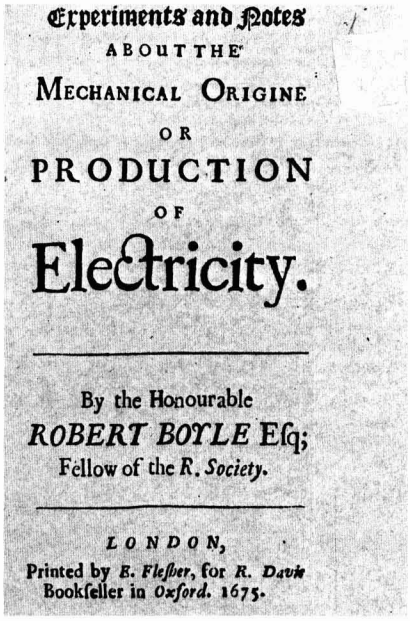
Experiments and Notes
ABOUT THE
MECHANICAL ORIGINE
OR
PRODUCTION
OF
Electricity.
By the Honourable
ROBERT BOYLE Esq;
Fellow of the R. Society.
LONDON,
Printed by E. Flesher, for R. Davis
Bookseller in Oxford. 1675.

Fig. 2. Title page of Boyle's book treating his electrical researches. The term "mechanical" refers to the frictional origin of electricity. This was the first printed book on electricity to appear in English.

merly designated a nonconductor. The term originated with Gilbert who applied it to substances capable of receiving a charge by rubbing. "Nonelectric" referred to a conductor.)

Three quarters of a century later the experiment was repeated by the Irish natural philosopher Robert Boyle (Fig. 2): "For having well-lighted a Wax-taper, which I preferred to a common Candle to avoid the stink of the snuff, I blew out the flame; and when the smoak ascended in a slender stream, held, at a convenient distance from it, an excited piece of Amber or a chafed Diamond, which would manifestly make the ascending smoak deviate from its former line, and turn aside, to beat, as it were, against the Electric, which, if it were vigorous would act at a considerable distance . . . " (5).

In both foregoing examples, the smoke was attracted to the dielectric either by virtue of a charge acquired by the particles in the incomplete combustion process, or as a result of the polarization of the electrically neutral particles in the nonuniform electric field surrounding the dielectric. Since a corona discharge was not used to impart a net charge to the particles, neither instance can be regarded as a true forerunner of electrostatic precipitation or liquid spraying in the conventional present-day sense. Nevertheless, Boyle may not have missed the mark by much. As Joseph Priestly informs us in his celebrated history of electricity, "Mr. Boyle got a glimpse, as we may say, of the electric light: for he found that a curious diamond . . . brought from Italy, gave light in the dark when it was rubbed against any kind of stuff; and . . . it became electrical" (6).

Together with his predecessors, Boyle noted the ability of amber to draw "not onely Sand and Mineral Powders, but Filings of Steel and Copper, and beaten Gold it self." He supported the contention, first put forth by Gilbert, that magnets attract iron whereas amber "draws indifferently all bodies whatsoever" (6). There was at this early time, however, no mention of the possibility of electrostatic mineral separation, or any suggestion that particles of unlike physical characteristics might behave differently in the presence of amber.

Production of a substantial man-made corona could not have antedated the development of the high-voltage generating machine. A frictional machine consisting of a sulfur sphere mounted on a crankshaft was described in 1672 by Otto von Guericke, better known for his invention of the vacuum pump and Magdeburg hemispheres. The sulfur sphere was charged by rubbing the hand against it while it was rotated in a wooden frame (Fig. 3). Using this apparatus, von Guericke made the important discovery of the effectiveness of pointed conductors in attracting charged bodies. He noted further that the rubbed globe glowed in the dark and that when it was brought

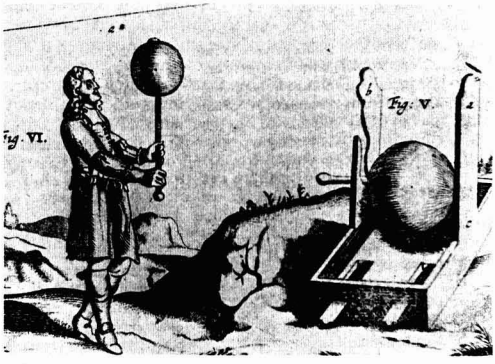

Fig. 3. Von Guericke's frictional electrostatic machine is on the right. On the left, the burgomeister is demonstrating how a feather *a*, first charged by contact with the sphere, may be made to move about in the air as he chose. This is probably the earliest example of achieving the directed motion of a particle under the action of an electric field (7).

to the ear "roaring and crashings" were heard in it (7).

The experiments of Boyle and von Guericke were made about the same time, neither deriving advantage from the labors of the other. Their observations seem to be the earliest recorded of the corona discharge.

Von Guericke's frictional machine and subsequent improvements on it were to accelerate the progress of electrical science, but the more primitive charging methods lingered tenaciously. In 1709, Francis Hauksbee, curator of instruments for the Royal Society of London, reported that he had experienced a weak sensation of pressure, presumably the electric wind, by holding a charged tube close to his face (Fig. 4). Hauksbee's announcement of his discovery throws interesting light on the state of electrical knowledge and experimental technique at the time. "Having procured a Tube, or hollow Cylinder, of fine Flint Glass," he wrote, "about one Inch diameter, and thirty in length; I rubb'd it pretty vigorously with paper in my hand until it had acquired some Degree of Heat . . . When the Tube became hottest by the strongest Attrition, the Force of the [electrical] Effluvia was render'd manifest to . . . [the] Sense . . . of feeling. They . . . were plainly to be felt upon the Face or any other tender part, if the rubb'd Tube were held near it. And they seemed to make very nearly such sort of stroaks upon the Skin, as a number of fine limber Hairs pushing against it might be suppos'd to do. This vigorous Action of the Effluvia put me upon an attempt, to find in what manner such a motion was propagated, and in what figure or sort of track it went along. For which end I held the rubb'd Tube near the Flame of a Candle, Smoke, Dust and surfaces of Liquids; but without any manner of success."

Hauksbee's efforts to employ smoke-tracer and similar techniques to follow the flow pattern of the electric wind failed. In fact, he gives the impression that the drag force of the wind was so weak and the electric attractive force on the smoke particles and other substances so strong that the particles and liquid moved against the air current to deposit on the tube. In Hauksbee's view this deposition confined the electric effluvia within the tube and thereby suppressed the wind: "For the small parts of Dust and Powders, the streams of Liquids, the oleaginous Fumes of Flame, and the like sort of parts of Smoke it self, immediately adher'd to the surface of the Tube, and so kept in the Effluvia: which therefore requir'd the assistance of a fresh Attrition to open their passage and give them vent again" (8).

Once again, the principle of the modern electrostatic sprayer or precipitator, the charging of particles to the same polarity as that of the discharge electrode and their subsequent repulsion from that electrode, was yet to be clearly demonstrated. It is possible, though, that a step in the right direction had already been taken by the savants of the Academy del Cimento of Tuscany, contemporaries of Boyle and von Guericke (Fig. 5). To these gentlemen "we are indebted for several observations on the subject of electricity," among them a report of 1667 that a stream of smoke rising near a piece of rubbed amber would in part "bend . . . and be arrested by the *Amber* and in part, as if reflected from a *Glass* . . . mount upwards." The attracted portion, "as the *Amber* cools, rises in *smoak* again, and vanishes"(9). The latter statement may be the first recognition of a frequent problem in commercial electrostatic precipitation, the failure of particles of low resistivity to adhere to a collecting electrode. The twin columns suggest the smoke is of mixed charge, particles of opposite sign being drawn off in different directions.

The splitting of a column of smoke in an electric field, a phenomenon vaguely reminiscent of the important Stark and Zeeman discoveries of a later period, has since been noted time and again in the literature. As late as 1839 Faraday regarded this experiment worthy of mention in his "Experimental Researches:" "If a smoking wax taper be held . . . towards a charged prime conductor . . . two currents will [often] form, . . . one . . . passing to the conductor, and the other . . . outwards, and from the conductor . . ."(10) (A prime conductor is a high-capacity, corona-free conductor for storing charge generated by an electrostatic machine. See Fig. 6.)

Shortly after Hauksbee, Isaac Newton performed a similar corona experiment. "The electric Vapour," he wrote, ". . . excited by the friction of the . . . [Sphere] against the Hand will . . . be put into such an agitation as to emit Light . . . and in pushing out of the . . . [Sphere] will sometimes push against the Finger so as to be felt"(11). No mention is made,

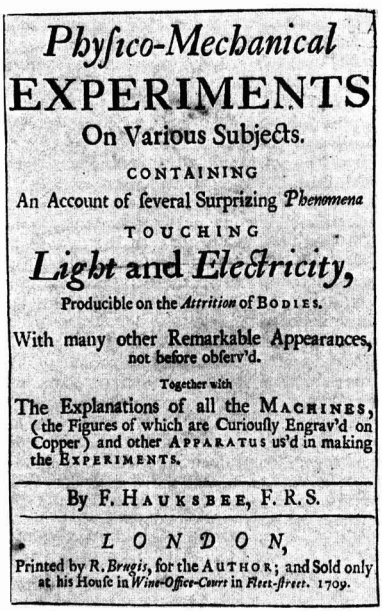

Physico-Mechanical
EXPERIMENTS
On Various Subjects.
CONTAINING
An Account of several Surprizing *Phenomena*
TOUCHING
Light and *Electricity*,
Producible on the *Attrition* of BODIES.
With many other Remarkable Appearances, not before observ'd.
Together with
The Explanations of all the MACHINES, (the Figures of which are Curiously Engrav'd on Copper) and other APPARATUS us'd in making the EXPERIMENTS.
By F. HAUKSBEE, F. R. S.
LONDON,
Printed by R. *Brugis*, for the AUTHOR; and Sold only at his House in *Wine-Office-Court* in *Fleet-street*. 1709.

Fig. 4. Hauksbee's title page. The *Light* referred to is that emitted in an electrical discharge.

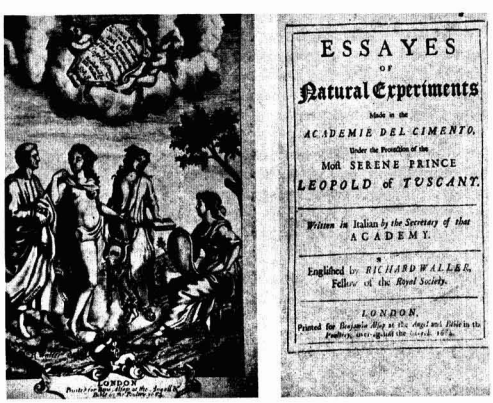

ESSAYES
OF
Natural Experiments
Made in the
ACADEMIE DEL CIMENTO,
Under the Protection of the
Most SERENE PRINCE
LEOPOLD of TUSCANY.
Written in Italian by the Secretary of that ACADEMY.
Englished by RICHARD WALLER, Fellow of the Royal Society.
LONDON,

Fig. 5. English translation, authorized by the Royal Society of London, of "Saggi di naturali esperienzi" which orignally appeared in Florence in 1667. The frontispiece illustrates the timelessness and universality of science: The personified Academy del Cimento is handing a copy of the Essayes to the seated Royal Society while Aristotle and the goddess of nature look on.

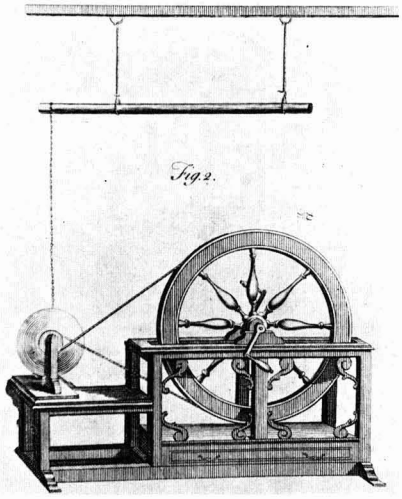

Fig. 6. A frictional electrostatic machine *circa* 1767 (16). The glass sphere at the left replaces von Guericke's sulfur ball. A fine chain dragging against the sphere transfers charge from the surface of the latter to the suspended prime conductor.

however, of the action of the "electric Vapour" on aerosols.

In 1746, the French philosopher Jean Antoine Nollet revealed his findings that electrified points displayed "brushes of light" (12). A year later, Benjamin Franklin revealed in a letter to his friend Peter Collinson of the Royal Society, "the wonderful effect of pointed bodies, both in drawing off and throwing off the electrical fire"(13). Nollet's and Franklin's observations were largely a rediscovery of a phenomenon noted earlier by von Guericke and long since forgotten. But this time, the corona discharge was to be established as a favorite subject of experimental study among the electrical investigators of the day. (The term "corona," with reference to a gaseous discharge, is of comparatively recent origin, commonly appearing in the literature only after 1900.)

In 1771, the Italian electrician-astronomer, Giambatista Becarria, succeeded where Hauksbee had not. "The movements that the electric wind can excite," he noted, ". . . repel the hot smoke of a candle just blown out, and if you present a strongly electrified point to the flame of a candle . . . the flame will . . . be repelled by the wind." Becarria thus seems to have been the first to bring about the repulsion of suspended particles from a high-voltage electrode by means of a corona discharge. However, he was concerned with observing the flow patterns of the electric wind issuing from a point and was apparently unaware that Coulombic forces as well as aerodynamic drag played a direct role in the repulsion of the particles. "It is false," Becarria asserted with but partial accuracy, "that it be the outflowing electrical matter that itself directly thrusts away the smoke, blows out the candle or . . . constitutes the electric wind, an opinion in which I see some people firmly persist"(14).

Experiments with a candle are not as straightforward as they may seem. Analysis is complicated by the ionized structure of the flame: the tip and mantle are positively charged whereas the core exhibits a surplus negative charge. Consequently, a candle flame may be subjected to conflicting electrostatic and aerodynamic forces in the presence of a point discharge.

Electrical Characteristics of Gasborne Particles

The electrical conductivity of dust and smoke particles, today a matter of chief importance in electrodepositional devices, particularly precipitators and conductance separators, was early an object of scientific inquiry. In 1746 the English physician William Watson, "the most distinguished name in this period in the history of electricity," reported to the Royal Society that a charge is acquired by an insulated conductor placed in a column of smoke rising out of an electrified vessel of burning turpentine. The doctor's experimental set-up was quaintly animate: holding vessel or conductor at each end of the bizarre transmission line was an "electrified man" suitably isolated from ground. Watson concluded, with some surprise, "here we find the smoke of an originally-electric a conductor of Electricity"(15).

Nine years later, the subject was again brought to the attention of the Royal Society with an account of a modification of the foregoing experiment, but now yielding a contrary result. "Mr. Henry Eeles of Lismore in Ireland . . . electrified a piece of down, suspended in the middle of a long silk string, and made steam and smoke of several kinds pass . . . through it, and observed that its electricity was not in the least diminished, as he thought it would have been, if the vapour had been non electric, and consequently had taken away with it part of the electric matter with which the down was loaded"(16).

Eeles flatly concluded that "exhalations of all kinds are electrical [*i.e.*, nonconducting]." Further clarification on this score awaited the Anglo-Italian electrical researcher Tiberius Cavallo. Repeating the smoke-attraction experiment, but using a charged metal sphere in place of his forerunners' rubbed dielectric, Cavallo wrote, in 1777, "the smoak . . . will be attracted by the electrified body and . . . form a kind of atmosphere about it. This atmosphere will remain for a few seconds . . . and gradually vanish, . . . diffus[ing] . . . itself into space." No previous performer of this now popular demonstration had offered an adequate explanation of the mechanism involved. Cavallo's views, on the other hand, are remarkably up to date and go so far as to reveal an appreciation of the concept of charging time constant: "The smoak is attracted by the electrified body . . . for the same reason that other bodies are attracted by it . . . It . . . is not immediately repelled, because it is a bad Conductor, and acquires Electricity very slowly; but having acquired a sufficient quantity . . . , it begins to quit the electrified body, and ascending into the air, extends itself into a large space, in consequence of the repulsion existing between its own electrified particles"(17).

Elsewhere Cavallo proceeded to obtain a semi-quantitative measurement of aerosol conductivity. Suspending a cork-ball electrometer over the prime conductor of an electrostatic machine, he noted that the balls did not diverge. But putting "upon the prime conductor a wax-taper just blown out, so that its smoke may ascend to the electrometer . . . the balls . . . will immediately separate a little . . . which shows that smoke is a Conductor in a small degree" (18). (An electrometer is an instrument consisting of two cork balls suspended from a common point by insulating threads. Like charges on the balls cause them to diverge. See Fig. 7.)

A few decades later Michael Faraday could speak of "the power of particles of dust to carry off electricity in cases of high tension" as being "well known,"(19) and cautions that high-voltage apparatus "be perfectly free from *dust* or small loose particles, for these very rapidly lower the charge and interfere on occasions when their presence and action would hardly be expected"(20).

The Dust Controversy and Gaseous Conductivity

The problem of the electrification of dust, without specific reference to intentional electrodeposition, played a curious role in the history of gaseous electronics. Coulomb, who in 1785 investigated the loss of electricity from a charged body suspended by in-

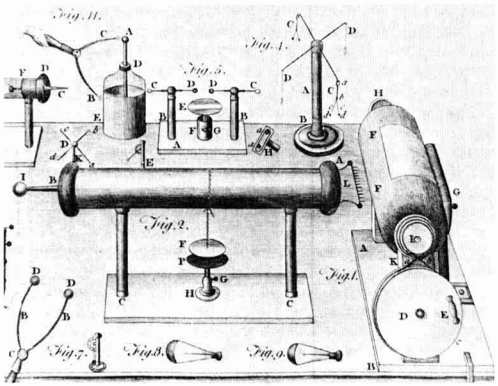

Fig. 7. Illustrations of Cavallo's apparatus (17). In the electrostatic machine, Fig. 1, the earlier manually rubbed glass sphere has been replaced by a cylinder F rubbed by a silk cushion G stuffed with hair. Charge is drawn off onto the prime conductor, Fig. 2, by means of the corona points L. Fig. 4 C shows a cork-ball electrometer.

sulating strings, thought that after allowing for leakage along the supports, some lost charge still remained to be accounted for by a convective discharge through the air (21). Convective discharge or electrical convection were the terms applied to the passage of electricity from one place to another by the motion of charge-bearing particles of ordinarily uncharged matter, *e.g.*, gas molecules, dust, *etc.* Coulomb supposed that air particles in contact with a charged body acquired an electrical charge of the same sign as the body and that the particles were then repelled by the body. Accordingly, molecules of air could be charged with electricity, much like bits of metal.

Here and there an occasional question was raised regarding the validity of this charging theory. Faraday, though voicing some reservations, went along with the prevailing belief. Kinnersley and Franklin had objected more strongly. As Priestly tells us, "Mr. Kinnersley of Philadelphia, in a letter dated March 1761, informs his friend and correspondent Dr. Franklin, then in England, that he could not electrify anything by means of steam from electrified boiling water; from whence he concluded that, contrary to what had been supposed by himself and his friend, steam was so far from rising electrified that it left its share of common electricity behind" (16, 22).

In time, however, experimental data accumulated which seemed to be explicable only on the hypothesis that molecules of gases or vapors resisted electrification. Warburg in 1872, supported by Nahrwold in 1887, adduced compelling evidence that the loss of charge from an isolated electrified body could be accounted for by the presence of dust in the ambient air (23, 24). These researchers held that it was the dust and not the air striking the charged body that was responsible for carrying off the electricity. In this newer view the dust did not even have to be present in the original air. It might, it was believed, be given off by the charged conductors under investigation. Thus, Lenard and Wolf demonstrated in 1889 that when ultraviolet light fell on a negatively electrified platinum surface, a steam jet in the neighborhood of the surface showed by its change of color that the vapor had been condensed (25). Lenard and Wolf attributed the condensation of the jet to dust or metallic vapor emitted from the illuminated surface, the dust producing condensation by forming nuclei around which the water droplets coalesced. The experimenters were, of course, observing the photoemission of electrons from the metallic surface by means of a primitive cloud chamber. But being unaware of the existence of electrons or gaseous ions and supposing that dust was indispensible to droplet condensation, Lenard and Wolf were led to conclude that the metal was disintegrating under the action of the light, the metallic vapor carrying off the negative electricity and leaving behind the positive. The belief that air molecules could not be charged was further supported by the experimental results of Blake in 1882 and Sohncke in 1888 (26, 27). These studies seemed to show that not only is there no electricity produced by the evaporation of an unelectrified liquid, but also that the vapor rising from an electrified liquid does not carry a charge. It was natural enough to argue that if molecules of vapor are capable of receiving a charge under any circumstances, they should be expected to do so in this case.

Lord Kelvin and Magnus MacLean further observed in 1894, "That air can be electrified either positively or negatively is obvious from the fact that an isolated spherule of pure water, electrified either positively or negatively, can be wholly evaporated in the air . . . This demonstrates an affirmative answer to the question, can a molecule of gas be charged with electricity? It shows that the experiments referred to as pointing to the opposite conclusion are to be explained otherwise" (28). Despite this, F. Braun could write as late as 1896, "The question of whether a gas can be electrified is answered mostly in the negative, at least among German investigators. All phenomena indicating the possibility of electrification can be explained by the presence of dust particles that might have been contained in the gas from the outset or else introduced during the process of electrification" (29). It was not long, however, before the last vestige of doubt on this score was eliminated. X-rays were discovered in 1895. Almost immediately J. J. Thomson, at the head of a brilliant group of young scientists at the Cavendish Laboratory of Cambridge, undertook to answer the question of how dust-free gases are made conductive by the new radiation. It was quickly found that gas rendered conducting this way lost all its conductivity when filtered through glass wool or traversed by a current-producing electric field. The conclusion was inevitable that gaseous conductivity was due to the presence of electrified particles. These particles were called ions by analogy with the term coined by Faraday in 1834 with reference to the charge carriers of electrolytic solutions (30).

Practical Electrodeposition

Credit for the earliest electrodepositional device comprising both a corona discharge electrode and a particle-collecting surface belongs to a German teacher of mathematics, M. Hohlfeld. Having observed in thunderstorms that increased rainfall usually followed closely after lightning discharges, Hohlfeld speculated in 1820 that electric discharges simulated in the laboratory might produce a corresponding effect. Filling a bottle with smoke from burning paper, he "corked the bottle, passing through the cork a wire . . . extending to within three inches of the bottom of the bottle. The . . . [wire] was connected to . . . [an electrostatic machine] so that the electricity was silently transferred into the bottle and brought in contact with the smoke . . . With the passing of the first spark the smoke vanished, the water from the smoke appearing on the bottom of the bottle" (31).

Hohlfeld evidently thought that a spark discharge was required to achieve his purpose because he was trying to simulate thunder. That a (relatively) silent corona would accomplish the same result was reported 30 years later by C. F. Guitard, unaware that any attention had previously been drawn to the subject. In his words: "It . . . struck me, that if I brought a wire from an electrifying machine into . . . [a glass] cylinder [filled with tobacco smoke] the air would immediately become charged with electricity, which would cause each portion of smoke to fly to the

sides of the cylinder . . . The [experimental] effect produced was perfectly magical; the slightest turn of a small electrifying machine produced immediate condensation. It was astonishing to see how small a quantity of electricity produced a most powerful effect" (32).

Experimental studies of the behavior of aerosols in electric fields, with or without a corona discharge, are seen to have been pursued sporadically and largely independently by workers in several countries from 1600 on into the 19th Century. But not until 1883 do we find the proposal put forth (by Oliver Lodge, professor of physics at University College, Liverpool) that the charging and precipitation of dust in a corona might offer an effective means of suppressing atmospheric contamination (33). In 1870, John Tyndall, the British physicist whose name brings to mind the well-known light-scattering effect, had noted that a dust-free space formed over a hot body in strongly illuminated dusty air. Further study of this phenomenon, which is now known to be a consequence of differential molecular bombardment (radiometry), was undertaken by Oliver Lodge. Professor Lodge's lecture demonstrator, J. A. Clark, hypothesized that air streaming over a hot surface might become electrified by friction, and that from air so charged, dust could somehow be expelled. To test this supposition, a rod mounted in a smoke-filled box was raised to a few thousand volts. With the appearance of corona "a very violent and remarkable effect was noticed; the . . . [clear region] widened enormously and tumultuously and the whole box was rapidly cleared of smoke" (34). Electrical precipitation had once again been brought to light.

In a letter to *Nature* in 1883 in which he announced Clark's discovery, Lodge, unlike his predecessors, went on to suggest several practical ideas. "It is somewhat surprising," he noted, "considering the perfection to which electrostatic machines have been brought that they have not received any practical application. The electrical clearing of the air of smoke rooms, or of tunnels, is perhaps not an impractical notion. The close relationship between fogs, epidemics, &c., and the suspension of solid particles in the air, suggests the use of electrical means for sanitation and for weather improvement" (33).

Lodge's first thoughts centered on treatment of the already polluted atmosphere rather than on the true offender, the actual sources of pollution. A proposal that this latter approach might offer the solution to a vexing problem was made by Alfred Walker, a lead smelter who, with Lodge's advice, promptly undertook the construction of a full-sized precipitator at his furnaces in Bagillt in Wales (35, 36). Here, Lodge recalled years later, clouds of lead oxide fume had been escaping into the air "to the damage of the neighboring agriculture. But the method of producing high-tension electricity in those days was rather primitive, and by no means of an engineering character. [The 50-kv, 0.3-ma Wimshurst machines which had then only recently been developed, and of which much was expected, proved to be less than satisfactory for the application at hand.] Moreover, the difficulties of insulation were not properly appreciated. . . . It is doubtful if any real electrification was communicated to the flues, along which the hot, flaming, and smoky gases were rushing at a considerable pace from the smelting furnaces: so that the first attempt at practical application was unsuccessful, and . . . was discontinued" (37).

There is some question as to whether Walker would have succeeded in any case. Modern experience has shown that the highly resistive, finely divided, lead oxide fume is one of the most troublesome of aerosols to precipitate.

Lodge was not dismayed by the disappointing outcome of Walker's attempt. Over the ensuing years, with his son, he carried forward his researches. But despite his many large-scale experiments leading to various improvements (*e.g.*, introduction of the transformer and tube rectifier and development of suitable high-voltage insulators), the technical breakthrough on which the birth of a new industry hinged was to be made elsewhere.

The widespread publicity attendant on the investigations of Lodge and his associates stimulated activity by others. Over the next two decades, in addition to Walker's patents in half a dozen countries, additional patents and an occasional publication served to keep alive interest in the "electrical condensation" of smoke. It remained ultimately for Frederick Cottrell, professor of physical chemistry at the University of California, to bring to fruition the process of electrostatic precipitation that now bears his name. Avenues of technical communication open to Cottrell at the turn of the century were so far from adequate that not until he constructed his first commercial precipitator did he become aware of Lodge's work antedating his own by some 20 years. Cottrell himself appears to have had no clear-cut recollection of how the idea of precipitation came to him. Nevertheless, he fully acknowledged Lodge's priority and characteristically minimized his own considerable contribution (38). Writing in 1914 of his introduction to the subject, Cottrell had this to say: "Some eight years ago, while studying various methods for the removal of acid mists in the contact sulphuric process . . . the author had occasion to [independently] repeat the early experiments of Lodge and became convinced of the possibility of developing them into commercial realities. The subsequent work may fairly be considered as the reduction to engineering practice as regards equipment and construction of the fundamental process long since laid open to us by the splendid pioneer work of Lodge, a feat vastly easier to-day than at the time of Lodge and Walker's original attempt" (39).

In 1907, following impressive laboratory demonstrations, Cottrell set out "to duplicate these experiments on a scale some two hundred-fold larger. This was carried out . . . at the E. I. duPont de Nemours Powder Co. at Pinole, on San Francisco Bay, where the contact gases from one of their . . . sulphuric acid units were employed" (39). The operation was an unqualified success.

Epilogue

Practical electrostatic precipitation on a commercial scale had been born. In a much broader sense, though, the accumulated effort of the preceding two millenia and more now heralded an era in which particulate electrodeposition and separation were to find commonplace and diverse application. The subsequent explosive industrial expansion of fine particle electrostatics calls to mind Lodge's prophetic words before the Royal Dublin Society in 1884: "Whether anything comes of it [electrodeposition] practically or not, it is an instructive example of how the smallest and most unpromising beginnings may, if only followed up long enough, lead to suggestions for large practical application. When we began the investigation into the dust-free spaces found above warm bodies we were not only without expectation, but without hope or idea of any sort, that anything practical was likely to come of it . . . [And so] it may happen that the yet unapplied and unfruitful results evoke a sneer, and the question . . . ["What good is it?"] the only answer to which question seems to be: No one is wise enough to tell beforehand what gigantic developments may not spring from the most insignificant fact" (40).

Developments in recent decades in the application of particle electrostatics have indeed been impressive: among typical electrodepositional or separating devices may be numbered mineral and foodstuff separators, electrostatic flock coaters and particle orientors, electrostatic painting, coating, and printing devices, gas and liquid filters, and still others. But

these achievements of the more recent past comprise a story of their own, one that is told, under appropriate headings, in other papers of this series.

Acknowledgments

The author is indebted to George A. Carkhuff whose careful photographic work under adverse conditions provided the illustrations for this paper, and to the Institute of Electrical and Electronic Engineers and the American Institute of Physics in whose publications portions of this history have previously appeared.

Manuscript received Nov. 28, 1967. This paper was presented at the Chicago Meeting, October 15-19, 1967 as Abstract 144.

REFERENCES

1. Diogenes Laertius, "The Lives and Opinions of Eminent Philosophers," p. 15, Transl. C. D. Yonge, George Bell and Sons, London (1895).
2. Aristotle, "De Anima," Book I, Chap. 2, p. 17, Transl. R. D. Hicks, Hakkert, Amsterdam (1965).
3. W. Gilbert, "De Magnete," London, 1600. Engl. Transl. "William Gilbert of Colchester . . . on the Magnet," p. 46ff, The Gilbert Club, London (1900).
4. "Photii Bibliotheca," Rothomagi, folio, col. 1040-1, cod. 242, 1653, cited by P. F. Mottelay, "Bibliographical History of Electricity and Magnetism," p. 7, Charles Griffin and Co., Ltd., London (1922).
5. R. Boyle, "Experiments and Notes About the Mechanical Origine or Production of Electricity," pp. 13-4, London (1675).
6. J. B. Secondat de Montesquieu, "Histoire de l'électricité," p. 141 (1746). Cited by ref. (16) *op. cit.*, 5th ed., p. 6 (1794).
7. O. von Guericke, "Experimenta nova magdeburgica," pp. 147-50 and figures, Amsterdam (1672).
8. F. Hauksbee, "Physico-Mechanical Measurements on Various Subjects," pp. 46-7, London (1709).
9. "Saggi di naturali esperienze," Academia del Cimento, Florence, 1667. Engl. Transl. R. Waller, "Essayes of Natural Experiments Made in the Academie del Cimento," pp. 128-132, London (1684).
10. M. Faraday, "Experimental Researches in Electricity," London, Vol. 1, 1839, par. 1602.
11. J. Newton, "Opticks," 2nd ed., pp. 315-6, London, (1718).
12. J. A. Nollet, "Essai sur l'électricité des corps," Paris, 1746.
13. A. H. Smith, "Writings of Benjamin Franklin," New York, Vol. 2, p. 303 (1905).
14. G. Becarria, "Elettricismo artificiale," Turin, 1772, par. 781, 783.
15. W. Watson, *Trans. Roy. Soc. London*, **10**, 296 (1746).
16. J. Priestly, "History and Present State of Electricity," 1st ed., pp. 214-216 and figures, London (1767).
17. T. Cavallo, "A Complete Treatise of Electricity in Theory and Practice," pp. 309-10, plate I, London (1777).
18. Ref. (17), *op. cit.*, 4th ed., Vol. 1, p. 321 (1795).
19. Ref. (10), *op. cit.*, par. 1569.
20. *Ibid*, par 1201.
21. C. A. de Coulomb, "*Memoires de l'Academie des Sciences*," p. 612, Paris (1785).
22. E. Kinnersley, *Phil. Trans. Roy. Soc. London*, **53**, 84, (1763).
23. E. Warburg, *Ann. Physik*, **145**, 578 (1872).
24. R. Nahrwold, *ibid.*, **32**, 1 (1887).
25. P. Lenard and M. Wolf, *ibid.*, **37**, 443 (1889).
26. L. J. Blake, *ibid.*, **145**, 578 (1872).
27. L. Sohncke, *ibid.*, **34**, 925 (1888).
28. Lord Kelvin and M. MacLean, *Proc. Roy. Soc. London*, **56**, 84 (1894).
29. F. Braun, *Ann. Physik*, **59**, 688 (1896).
30. J. J. Thomson and E. Rutherford, *Phil. Mag.*, **42**, 392 (1896).
31. M. Hohlfeld, *Archiv Gesamte Naturlehre*, **2**, 205 (1824).
32. C. F. Guitard, *Mechanics Magazine*, **53**, 346 (1850).
33. O. J. Lodge, *Nature*, **28**, 297 (1883).
34. O. J. Lodge, *J. Soc. Chem. Ind.*, **5**, 572 (1886).
35. A. O. Walker, Great Britain, Pat. 11,120, Aug. 9, 1884.
36. A. O. Walker, *Engineering*, **39**, 627 (1885).
37. O. J. Lodge, "Electrical Precipitation," pp. 21-40, Oxford University Press, London (1925).
38. F. Cameron "Cottrell, Samaritan of Science," Doubleday, New York (1952).
39. F. G. Cottrell, "Problems in Smoke, Fume and Dust Abatement," Publication 2307, Government Printing Office, Washington, D. C., 1914.
40. O. J. Lodge, *Nature*, **29**, 610 (1884).

SECTION NEWS

Boston Section

The Boston Section held its second meeting of the 1967-1968 season at the Ledgemont Laboratory of the Kennecott Copper Corp., Lexington, Mass., on November 14, 1967.

Mr. Ralph B. Soper was presented with a Past-Chairman's pin in appreciation of his services in that office during 1966-1967.

The speaker for the evening was Ivor E. Campbell, Vice-President of The Electrochemical Society, who spoke on "Vapor Deposition, Past, Present, and Future." Dr. Campbell reviewed the development of vapor deposition processes, their present commercial status, and opportunities for further utilization. The relative advantages of chemical and physical vapor deposition were discussed as well as the relationship of these processes to other coating processes.

R. G. Donald,
Secretary

Cleveland Section

During the year 1967-1968 the Cleveland Section, as usual, has had a wonderful year of programs arranged by Program Chairman R. J. Brodd. Dinner meetings are held monthly on the second Tuesdays from September to June except in October and May when the National Meetings of the Society are in session.

The principle speakers and titles for meetings are as follows:

September—"Current Distribution on and in Porous Electrodes," R. J. Brodd, Union Carbide.

November—"Edison plus TEFLON–Application of New Material to Electrochemical Cells," G. Frysinger, U. S. Army Electronic-Command.

December—"A Chemical View of Semiconductors," D. Trivich, Wayne State University.

January—"Conduction and Electroluminescence in Oxide Films," T. W. Hickmott, I.B.M. Corp.

February—"Electrochemistry and Reactive Intermediates in Electrosynthesis in Nonaqueous Solvents," M. E. Peover, National Physical Lab., Teddington, England.

March—"The Influence of Adsorption on Electrode Reactions at the dropping Mercury Electrode," J. Kuta, Heyrovsky Polarographic Institute, Czechoslovakia.

April—"Between Science and Art—Recent Research in Nonaqueous Solvents and Electrochemical Calorimetry," R. T. Foley, American University.

The June meeting will be "Ladies Night" with a subject of general interest.

It has been a custom of the Cleveland Section to have a short after dinner talk at each meeting. The subjects for the year are of great variety, ranging from "Recent Advance on CdS Thin Film Cell," by W. Bower, "Comments on the World-Wide Chlorine Industry," L. E. Vaaler, "Some Recent Developments in Electroplating," K. Willson, to "Society Affairs," by Vice-President N. Corey Cahoon.

T. S. Lee,
Secretary

Detroit Section

The annual joint dinner meeting of the Detroit Section and the National Association of Corrosion Engineers was

held on February 15, 1968 at the Engineering Society of Detroit. The speaker for the evening was Julius J. Harwood, Manager, Metallurgy Department, Ford Motor Co. Scientific Laboratory, who spoke on "The Reaction and Interaction of Research and Technology."

Mr. Harwood pointed out in his presentation that the coupling of science to technology and the interaction of research and engineering are issues receiving serious attention on the national research scene. The conversion of research to technology, i.e., the process of innovative, like any other chemical reaction, can be viewed in terms of "thermodynamic driving forces" and kinetic factors operating in a fluctuating, dynamic environment. The factors underlying the relation of research to technology and the innovation process were analyzed in the particular context of basic research in an industrial organization, including the role of research, criteria for evaluation of the productivity of basic research, "catalytic" and environmental factors, the role of management etc.

The findings of a series of case histories of successful research-technology transfers were used to illustrate these considerations.

E. A. Romanowski,
Second Vice-Chairman

Midland Section

On February 20, 1968 the Midland Section of the Society held a meeting in the Research Auditorium of the Dow Chemical Co. in Midland. Prior to the meeting a dinner in honor of the speaker was held at the Hickory House in Midland.

The speaker was Stanford R. Ovshinsky of Energy Conversion Devices, Inc., who spoke on "Amorphous Semiconductor Devices." This is a very controversial subject since the electronic properties of amorphous materials, notably certain glasses, are still not well understood. Mr. Ovshinsky verbally described several devices based on this concept; the "Ovonic" threshold switch and the "Ovonic" memory switch. Both of these switches employ thin films, deposited by a variety of means, of chalcogenide glasses. These glasses are compounds of selenium, tellurium, silicon, oxygen, and sulfur with some "crystallinity inhibitors" such as arsenic. Purity of materials is said to be noncritical and easily controlled. Unlike conventional solid state devices that operate only with direct current, these new amorphous devices are inherently symmetrical and can be employed in a-c circuits.

At present these switches are being studied for some military applications as well as a limited number of civilian applications. Audience discussion was enthusiastic and lengthy.

John A. Van Westenburg,
Secretary-Treasurer

National Capital Area Section

On March 7, 1968 the National Capital Area Section met at the American University, Washington, D. C., to hear N. Corey Cahoon, Vice-President of The Electrochemical Society, who spoke on current and proposed affairs in the National Society. Dr. Cahoon also spoke on "New Developments in Batteries," and also described a typical cell and its electrode reactions. He discussed the new method used to measure the electrode voltages and cell capacities.

Frank X. McCawley,
Secretary

Ontario-Quebec Section

On February 16, 1968 an all-day symposium on Interfacial Electrochemistry and Corrosion was held at Atomic Energy of Canada Ltd., Sheridan Park, Ontario. The location proved to be ideal as Atomic Energy's research center is located in a research community some 17 miles west of Toronto. Sheridan Park was initially inspired by the Ontario Research Foundation and construction of a campus-like development for the establishment of industrial sponsored facilities devoted purely to research and development began in 1963. At present 9 organizations have their individual research centers located in Sheridan Park.

The following papers were presented:

"Double Layer Theory and Electrode Kinetics," J. N. Butler, Tyco Laboratories, Inc.

"Electrochemistry of the Mercury-Electrolyte Interface," R. G. Barradas, University of Toronto

"The Anodic Behavior of Iron," Morris Cohen, National Research Council

"The Mechanisms of Corrosion of Aluminum," M. J. Pryor, Olin Mathieson Chemical Corp.

"Corrosion and Inhibition of Zinc," M. M. Wright, Cominco Research Laboratories

The program was followed by a tour of the research facilities of the International Nickel Co. of Canada.

Plans are at present being made for the Spring Meeting which will be held at the Windsor Hotel in Montreal on April 5, 1968. The annual business meeting of the Section will also be held at this time.

The following papers will be presented:

"Technology and Use of Mercury Cells in North America," W. C. Gardiner, Olin Mathieson Chemical Corp.

Experimental Design and Process Optimization," A. Mular, Queen's University

"A Review of Latest Work by the Mines Branch in Smelting in Combined Shaft and Electric Furnaces," G. E. Viens, Dept. of Energy, Mines, and Resources.

A paper explaining some practical designing considerations of submerged arc furnaces will be presented by Z. B. Wowk, Metals & Carbon, Union Carbide Canada, Ltd.

The luncheon speaker will be R. A. Fortier, Industrial Relations Manager, Aluminum Co. of Canada Ltd., who will speak on the important aspects of the human problems arising in the rapidly changing industrial enterprise.

C. B. Camplong,
Secretary-Treasurer

PEOPLE

Wilbur W. Kirk has been appointed manager of the Harbor Island Corrosion Laboratory, International Nickel Co., Inc., Wrightsville Beach, N.C.

Prior to his new appointment he had been supervisor of the marine corrosion section at the Harbor Island works. He joined the company in 1962 as an engineer at Harbor Island. Before this, Mr. Kirk was an engineer in the Core Engineering Department at Bettis Atomic Power Laboratory in Pittsburgh, Pa.

Frederick P. Kober has been appointed to the newly-created position of assistant director of research at Yardney Electric Corp., New York, N.Y.

Prior to joining Yardney Electric, Dr. Kober was associated for four years with General Telephone & Electronics Laboratories, Bayside, N.Y., where he was section head in Basic Electrochemistry.

Thomas P. May will transfer to the New York office of the International Nickel Co., New York, N. Y., as assistant to the product development manager. Dr. May has been manager of the company's Harbor Island Corrosion Laboratory at Wrightsville Beach, N.C.

Mr. May transfers to the New York office after having been manager of the company's Harbor Island Corrosion Laboratory since 1957. He was appointed technical manager of the laboratory in 1954. Dr. May joined the International Nickel organization in 1947 as a member of the corrosion engineering section of the Development and Research Department in New York.

Eugene Y. Weissman joined Globe-Union, Inc., in Milwaukee as manager of the Electrochemistry Branch, Corporate Applied Research Center.

NEW MEMBERS

It is a pleasure to announce the following new members of The Electrochemical Society as recommended by the Admissions Committee and approved by the Board of Directors in March 1968.

Active Members

Fasolino, L. G., Wellesley, Mass.
Gynn, G. E., Fort Wayne, Ind.
Kraus, Herbert, Richardson, Texas
Manz, R. C., Morristown, N. J.
McDonald, G. D., Milwaukee, Wis.
Russell, J. L., New York, N. Y.
Sard, Richard, Elizabeth, N. J.
Schlaikjer, C. R., Cambridge, Mass.
Smith, A. G., Livonia, Mich.
Stevenson, Archibald, Selma, Ala.
Winhler, J. H., Hollywood, Calif.

Associate Member

Simon, R. H., Wickliffe, Ohio

Student Member

Zelouf, Shbmo, University Park, Pa.

OBITUARIES

Ralph Brown

Ralph Brown, consultant, Pratt & Whitney Aircraft, South Windsor, Conn., died on December 12, 1967. He was 32 years old.

Dr. Brown received his B.S. degree (Chemical Engineering) from Massasetts Institute of Technology in 1957. He was awarded the Ph.D. degree (Chemical Engineering) from the University of Michigan in 1960.

Dr. Brown, an author and co-author of several papers appearing in Society publications, was a member of the Society since 1962.

Marcello Stefano Pirani

Marcello Stefano Pirani, Emeritus Member of The Electrochemical Society, died on January 11, 1968.

Dr. Pirani was a holder of the Gauss Medal and the Federal Cross of Merit, a fellow of the Royal Society of Arts, London, and member and honorary member of numerous learned societies in Germany, England, and America.

NEWS ITEMS

19th CITCE Meeting

The 19th Meeting of CITCE will be held in Detroit, Mich., from September 22-27, 1968. Symposia will be held on (1) "Electrocrystallization," (2) "Adsorption on Electrodes," and (3) "New Instrumental Methods in Electrochemistry." In addition, there will be sessions of the Sections of CITCE.

The preliminary program for the Symposia is:

Electrocrystallization
Organized by J. O'M. Bockris

"Theory of Electrodeposition of Alloys," K. M. Gorbunova
"Growth and Structure of Metals Obtained by Electrocrystallization," M. Froment
"The Theory of Crystal Growth Examined by Potentiostatic Transients," R. Thirsk
"Electrolytic Phase and Growth of Perfect Crystal Faces," E. Budevski
"The Relationship Between Electrocrystallization Process, Crystal Defects, and Surface Steps," L. H. Jenkins
"The Electrocrystallization of Metals: A General Survey," J. O'M. Bockris

Adsorption on Electrodes
Organized by P. Delahay

"Adsorption of Ions and Atoms on Platinum Metals," A. N. Frumkin
"The Demonstration of Adsorbed Intermediates and the Determination of Reaction Mechanisms by Pulse Electrolysis," M. Fleischmann
"Adsorption and Diffusion of Hydrogen Through Noble Metals," E. Gileadi
"An Investigation of the Oxygen Overvoltage on Pt-Rh Alloy Electrodes," J. P. Hoare
"The Electrical Double Layer in Non-Aqueous Solutions," R. Payne
"Metal Ion Adsorption at Solid Electrodes," E. Schmidt

New Instrumental Methods in Electrochemistry
Organized by P. J. Elving

"Optical Methods for Investigating the Electrode-Solution Interphase," W. N. Hansen
"Electrical Methods for Investigating the Electrode-Solution Interphase," H. Bauer
"Use of Radioactive Isotopics Tracer Technique in Electrochemical Research," N. A. Balashova
"Rotating Disk and Ring-Disk Techniques," A. C. Riddiford

Papers to be presented in the meetings of the Sections will be in the areas of electrochemical thermodynamics, electrochemical kinetics, experimental methods in electrochemistry, electrochemistry of high temperatures, corrosion, and batteries.

Attendance is by preregistration only. The registration fees are $15.00 for members and $20.00 for nonmembers. The deadline for receipt of completed registration forms is July 1, 1968.

Registration forms may be obtained from: Dr. Seward E. Beacom, Electrochemistry Department, Research Laboratories, General Motors Corp., 12 Mile and Mound Roads, Warren, Mich. 48090.

Third International Symposium on Passivity

Dr. Henry Leidheiser, Chairman of the Corrosion Division of The Electrochemical Society, announces that the Third International Symposium on Passivity of Metals is scheduled to be held in Cambridge, England, July 6-10, 1970. Dr. T. P. Hoar of the Metallurgy Department at the University of Cambridge is in charge of local arrangements. The Committee representing

The Electrochemical Society consists of Morris Cohen, Michael Pryor, Henry Leidheiser, and H. H. Uhlig. Further details concerning the program, registration, presentation of papers and their eventual publication will be announced later.

The First International Symposium on Passivity was held at Schloss Heiligenberg near Darmstadt, West Germany, in September 1957. The Symposium was organized by Professor Ulrich Franck, now of the Technische Universität Aachen, and the late Dr. K. Bonhoeffer of the Max Planck Institut für Physikalische Chemie in Gottingen. Papers presented at this Symposium were published in a special issue of the "Ziet. f. Elektrochemie," Vol. 62, pp. 619-827 (1958).

The second symposium was held at the University of Toronto in September 1962. Dr. Morris Cohen of the National Research Council in Ottawa was in charge of local arrangements. Papers presented at this symposium were published in a special issue of the JOURNAL OF THE ELECTROCHEMICAL SOCIETY, Vol. 110, pp. 596-708 (1963). Both the first and second symposia were sponsored by The Electrochemical Society, the Deutsche Bunsengesellschaft, and the Faraday Society. The second symposium was sponsored in addition by the American Society for Testing and Materials. The Board of Directors of the Society at its meeting on January 5, 1968 voted to sponsor, as before, the third symposium.

It is expected that the third symposium, like the first two, will attract the participation of many scientists from all major countries of the world. The subject is one which has particular importance to the science underlying modern corrosion resistant alloys, corrosion inhibitors called passivators, and new techniques for corrosion control such as anodic protection.

Crystal Syntheses

Springer-Verlag announces the initiation of a new serial volume entitled "Crystal Syntheses" to be edited by Dr. R. A. Laudise, Bell Telephone Laboratories, Inc., Murray Hill, N. J., assisted by an International Editorial Advisory Board. "Crystal Syntheses" will be patterned after "Inorganic Syntheses" and "Organic Syntheses" and will publish straightforward procedures in recipe format for the growth of single crystals. Where possible, the procedures will be checked in a second laboratory before publication.

The following are members of the Editorial Board:

W. Bardsley
F. R. Charvat
F. Hubbard Horn*
R. Kern
R. A. Lefever
Rudolf Nitsche
A. Rabenau
T. B. Reed
Rustum Roy
M. Schieber
J. H. Wernick
E. A. D. White

Further information concerning "Crystal Syntheses" and instructions for the preparation of manuscripts may be obtained from the editor Dr. R. A. Laudise, Head, Crystal Chemistry Research Department, Bell Telephone Laboratories, Inc., Murray Hill, N.J. 07974, U.S.A.

* Electrochemical Society Active Member.

Intensive Short Courses

The Saul Gordon Associates Center for Professional Advancement, Hopatcong, N. J., will conduct the following short courses:

August 12-26—Luminescence Techniques Workshop
August 19-23—Electroanalytical Techniques Workshop

During September and December short courses will be given on:

Laser Techniques
Microencapsulation Techniques

For information and application forms write Saul Gordon Associates Center for Professional Advancement, P. O. Box 66, Hopatcong, N. J. 07843.

Second Integrated Circuits Engineering Courses

The Second Annual Integrated Circuits Engineering Summer Institute will be conducted at the University of Arizona, Tucson, Ariz. It is jointly sponsored by the Electrical Engineering Department through its Solid State Engineering Laboratory and the Division of Continuing Education.

The two-week sessions will consist of intensive and comprehensive design and fabrication experiences based on lectures prepared by the staff of the Solid State Engineering Laboratory. The emphasis will be on the fundamentals of monolithic integrated circuit design and fabrication. In addition to the fabrication of actual circuits, device theory will be reviewed and engineering design compromises will be considered.

Sessions will be held as follows:

Session I—June 3-14, 1968
Session II—June 17-28, 1968
Session III—July 8-19, 1968

For additional information, contact Dr. Roy H. Mattson, Director of the Institute and Head of Electrical Engineering Department, University of Arizona, Tucson, Ariz. 85721.

Polytechnic Short Course

The Polytechnic Institute of Brooklyn is planning to offer a three-week intensive course in basic electronics and instrumentation techniques from July 20 and August 10, 1968. The course is designed for engineers, physical and biological scientists, and science educators who must use instruments in their work.

For additional information, contact Kenneth R. Jolls, Assistant Professor

(Continued on p. 142C)

THREE NEW MEETING SYMPOSIUM VOLUMES

The Electrochemical Society, Inc.
30 East 42nd St.
New York, N. Y. 10017

Return after 5 days postage guaranteed

Name _____

Address _____

City _____

State _____ Zip Code _____

Country _____

( ) copies of
Optical Properties of Dielectric Films

do not cut

Payment must accompany order. We regret that purchase orders without remittance cannot be accepted, acknowledged or invoiced. Make sure your name and address appear both below and on the shipping label adjacent.

"Optical Properties of Dielectric Films"
U. S. $9.00 (15 papers, Spring 1968)

Please send (no. of copies)_____

Payment enclosed_____U. S. $_____

Name _____

Address _____

City _____ State _____

Zip Code _____ Country _____

PLEASE RETURN THIS CARD WITH YOUR PAYMENT TO:

THE ELECTROCHEMICAL SOCIETY, INC.,
30 East 42nd St., New York, N. Y. 10017

The Electrochemical Society, Inc.
30 East 42nd St.
New York, N. Y. 10017

Return after 5 days postage guaranteed

Name _____

Address _____

City _____

State _____ Zip Code _____

Country _____

( ) copies of
Electron and Ion Beam Science
and Technology

do not cut

Payment must accompany order. We regret that purchase orders without remittance cannot be accepted, acknowledged or invoiced. Make sure your name and address appear both below and on the shipping label adjacent.

"Electron and Ion Beam Science and Technology"
U. S. $21.00 (63 papers, Spring 1968)

Please send (no. of copies)_____

Payment enclosed_____U. S. $_____

Name _____

Address _____

City _____ State _____

Zip Code _____ Country _____

PLEASE RETURN THIS CARD WITH YOUR PAYMENT TO:

THE ELECTROCHEMICAL SOCIETY, INC.,
30 East 42nd St., New York, N. Y. 10017

The Electrochemical Society, Inc.
30 East 42nd St.
New York, N. Y. 10017

Return after 5 days postage guaranteed

Name _____

Address _____

City _____

State _____ Zip Code _____

Country _____

( ) copies of
Dielectrophoretic and
Electrophoretic Deposition

do not cut

Payment must accompany order. We regret that purchase orders without remittance cannot be accepted, acknowledged or invoiced. Make sure your name and address appear both below and on the shipping label adjacent.

"Dielectrophoretic and Electrophoretic Deposition"
U. S. $9.00 (13 papers, Fall 1967)

Please send (no. of copies)_____

Payment enclosed_____U. S. $_____

Name _____

Address _____

City _____ State _____

Zip Code _____ Country _____

PLEASE RETURN THIS CARD WITH YOUR PAYMENT TO:

THE ELECTROCHEMICAL SOCIETY, INC.,
30 East 42nd St., New York, N. Y. 10017

News Items continued

of Chemical Engineering, Polytechnic Institute of Brooklyn, 333 Jay St., Brooklyn, N. Y. 11201.

Metal Finishing Conference

The 7th International Metal Finishing Conference and 36th Meeting of the European Federation for Corrosion will be held at Hanover, Germany from Sunday May 5th to Thursday May 9, 1968. Technical Sessions will start Monday May 6, in the Stadthalle.

Conference languages are English, French, and German. All papers and discussion will be translated simultaneously.

Papers being presented by ECS Members are:

"Chemical Vapor Deposition of Rhenium," A. Brenner
"Nickel Addition Agents, Corrosion Inhibitors, and Catalysis," A. H. DuRose
"Plastic Coatings via Dry Powder Formulations," D. R. Savage
"The Effect of Inadequate Cleaning on the Plating Process," H. B. Linford
"Corrosion Protection Studies with Copper—Multiple Nickel-Micro-Porous Chromium Plate," R. J. Clauss and R. W. Klein
"Hydrogen Absorption by Steel during Cleaning," G. T. Sink
"Analytical Investigations of Defective Electroplated Parts as Related to Basic Metal Surface Conditions," T. H. Briggs and R. W. Steinmetz
"AES-Research," W. Blum

BOOK REVIEW

"Corrosion Engineering," by M. G. Fontana and N. D. Greene. Published by McGraw-Hill Book Co., New York 1967. 391 pages; $12.50.

This is a good book for the engineer—for the one actively engaged in the field for it brings together the topic in a coherent manner listing of materials data and references and for the beginning entrant into the field for it succinctly and pragmatically details the problems and parameters involved.

As a textbook, I would hesitate to use it for it covers too much of the practical and little of the theoretical in detail. It has no problems listings and contains far too many details for teaching. In many ways it is almost a reference book. For teaching purposes I would propose that the authors consider breaking the text into two volumes, one theoretical with amplification of many of their points and the second volume, a practical and reference work.

This book should be must reading for the materials engineer and in fact for any engineer or designer who utilizes construction materials. The book's intent is such that it should enable the working engineer to make a choice of the proper material of construction once he defines the parameters of use. For the individual who is thinking of entering corrosion research, it is an excellent starting point.

Julius Klerer
The Cooper Union

NEW BOOK

"The Thermal Properties of Transition Metal Ammine Complexes," by W. W. Wendlandt and J. P. Smith. Published by American Elsevier Publishing Co., New York, 1967. 255 pages; $17.00.

A detailed and practical reference treatise on the thermal dissociation of metal-ammine complexes outlining the thermoanalytical techniques utilized with a thorough discussion of the complexes of cobalt, chromium, copper, nickel, cadimum and zinc, plus platinum, palladium, and some other less well known types.

FROM PUBLISHERS

"Research on Improved II-VI Crystals," Report AD-660 874,* 61 pages; $3.00
"Semiconducting Thin Films: An Annotated Bibliography, 1956-1966," Report AD-655 100,* 291 pages; $3.00

* Order from the Clearinghouse, U. S. Department of Commerce, Springfield, Va. 22151.

POSITION AVAILABLE

Please address replies to the box number shown c/o The Electrochemical Society, Inc., 30 East 42 St., New York, N. Y. 10017.

Electrochemist—experienced experimentalist with excellent theoretical background to investigate electrical conductivity phenomena, both electronic and ionic, of oxide films and ionic solids. Reply Box B-36.

Future Meetings of The Electrochemical Society

May 5-9, 1968
Boston, Mass.
Statler Hilton Hotel
October 6-11, 1968
Montreal, Canada
Queen Elizabeth Hotel
May 4-9, 1969
New York City
Commodore Hotel
October 5-10, 1969
Detroit, Mich.
Statler Hilton Hotel
(also Sheraton Cadillac)
May 10-15, 1970
Los Angeles, Calif.
Statler Hotel (also Biltmore Hotel)
October 4-9, 1970
To be announced
May 9-14, 1971
Washington, D. C.
Sheraton Park Hotel
October 3-8, 1971
Cleveland, Ohio
Sheraton Cleveland Hotel
May 7-12, 1972
Houston, Texas
Shamrock Hilton
October 8-13, 1972
Atlantic City, N. J.
Chalfonte Haddon Hall
May 12-18, 1973
Chicago, Ill.
Sheraton Chicago
October 7-12, 1973
Boston, Mass.
Sheraton Boston
May 5-10, 1974
San Francisco, Calif.
Sheraton Palace
October 13-18, 1974
New York City
Commodore Hotel
May 11-16, 1975
Toronto, Canada
The Royal York
October 5-10, 1975
Dallas, Texas
Sheraton Dallas

ATTENTION, MEMBERS AND SUBSCRIBERS

Whenever you write to The Electrochemical Society about your membership or subscription, please include your Magazine address label to ensure prompt service.

ATTACH LABEL HERE

Change of Address

To change your address, please give us five weeks' advance notice. Place magazine address label here. Print your NEW address below. If you have any question about your subscription or membership, place your magazine label here and clip this form to your letter.

Mail to the Circulation Department, The Electrochemical Society, Inc., 30 East 42 St., New York, N. Y., 10017.

name

address

city state zip code

The Electrochemical Society

INSTRUCTIONS TO AUTHORS OF PAPERS

(Revised as of 6/1/67)

Journal of the Electrochemical Society is the fundamental research journal serving the interdisciplinary interests of chemistry, physics, electronics, biology, medicine, and engineering as they pertain to electrochemistry and to electrochemical phenomena. Written for the research scientist in industry, government, the independent laboratory and the university, it publishes contributed Technical Papers, Technical Notes and Brief Communications describing current basic research of original character, and is edited in two sections: 1) ***Electrochemical Science*** including such areas as batteries, fuel cells, corrosion and corrosion mechanisms, electrothermics and metallurgy, electrodeposition, electroorganic reactions and phenomena, and allied work of theoretical electrochemical nature. 2) ***Solid State Science*** including such areas as dielectrics and insulation, electrothermics and metallurgy, semiconductors, luminescence and related solid state investigations.

Electrochemical Technology is the journal of applied electrochemistry written for the application-oriented researcher, consultant, R & D engineer, product designer and production engineer whose responsibility lies in such areas as: batteries and fuel cells, corrosion and its control, dielectrics and insulation, electrodeposition and plating, electrothermics and metallurgy, electroorganic synthesis, industrial electrolysis and the process aspects of semiconductors and related solid state products. It publishes original contributed Technical Papers, Technical Notes and Brief Communications describing current application of electrochemistry and electrochemical phenomena to products and systems. Its Feature Section also publishes original contributed reviews pertinent to electrochemical interests.

GENERAL

Manuscripts must be submitted in triplicate to expedite review. They should be typewritten, double-spaced, with 2½-4 cm (1½ in.) margins.

Titles should be brief, followed by the author's name and professional connection. Authors should be as brief as is consistent with clarity and should omit introductory or explanatory material which may be regarded as familiar to specialists in the particular field. Proprietary and trade names should be generally avoided; if used with discretion, they should be capitalized to protect the owners' rights.

Authors are encouraged to suggest qualified reviewers for their manuscripts, the Editor reserving the right of final choice. It is helpful if the author tells which ECS **Division** would be most interested in his paper.

Present Society policy permits manuscript review in several weeks. Manuscripts returned to the author for revision should be resubmitted promptly to allow publication in five months or less from date of original receipt.

TYPES OF ARTICLES

Fundamental Technical Articles must describe original research of basic nature and must have adequate scientific depth. **Applied Technical Articles** may deal with any practical aspect of the fields of interest to the Society, **e.g.**, plant design or operation, production and control methods, economics. Articles of wide diversity of interest are acceptable, but subjects primarily covered in other specialized journals (**e.g.**, analytical or nuclear chemistry) are not considered appropriate. An **Abstract** should state the scope of the paper and summarize fully its results and contents. Suitable headings and subheadings should be included, but sections should not be numbered. Articles in recent issues should be consulted for current style.

Technical Notes are used for reporting briefer research, developmental work, process technology, new or improved devices, materials, techniques, or processes which do not involve more extensive basic scientific study. No abstract is required.

Brief Communications are used only to report new information of scientific or technological importance which warrants rapid dissemination. They need not necessarily reflect a complete research project; interim reports are acceptable. Length should be a nominal 700 words, with up to two illustrations. No abstract is required. Publishing time is normally less than three months.

EQUATIONS

Mathematical Equations should be written on a single line if possible, and parentheses, brackets, the solidus (/), negative exponents, etc., may be used freely for this purpose. Authors are urged to consult Chapter VI of the "Style Manual" of the American Institute of Physics (available for $1.00 at American Institute of Physics, 335 East 45 Street, New York, N. Y. 10017) and to follow the patterns described there.

SYMBOLS

Authors are encouraged to use symbols extensively. These should be defined in a list at the end of the paper, with units given. For example:

$a, b \ldots$ = empirical constants of Brown equation
f_i = fugacity of pure ith component, atm
D_v = volume diffusion coefficient, cm^2/sec

KEY WORDS

Authors are responsible for supplying a list of key words, to facilitate information retrieval. Generic terms generally are to be avoided. Key words acceptable to **Chemical Abstracts** are also generally acceptable in Society publications. List key words in the margin of the first page of the manuscript.

ABBREVIATIONS UNITS

The AIP "Style Manual" referred to here gives a suitable list of common **Abbreviations.** Units usually will be abbreviated without periods throughout the text, as sec, min, hr, cm, mm, etc. **Metric Units** should be used throughout, unless English units are clearly more appropriate in the area of discussion.

POTENTIAL SIGNS

Electrode Potentials: Authors are urged to state and make use of the polarity of test electrodes with respect to the reference electrode used, **i.e.,** Zn is normally negative, Cu normally positive with respect to the standard hydrogen electrode. The sign for the emf of a cell should conform to the free energy change of the chemical reaction as written or implied, in accordance with the definition $\Delta G = nFE$. These suggestions agree with the IUPAC conventions adopted in 1953.

REFERENCES

Literature References should be listed on a separate sheet at the end of the paper in the order in which they are cited in the text. Authors' initials must be given, and the style and abbreviations adopted by **Chemical Abstracts** should be used. Any recent issue of Society journals may be consulted. Literature cited should be readily available; consequently personal communications, Department of Defense (DOD), and Office of Technical Services (OTS) citations should be minimized. When references are not readily accessible, **Chemical Abstracts** citation numbers must be supplied.

PUBLICATION CHARGE

A charge of $40 per printed page is made for publication of technical material in Society journals. A 10% reduction is allowed if at least one author of an article is an ECS member or an employee of a Patron or Sustaining Member firm. However, acceptance of a manuscript is in no way dependent on such payment, and the charge may be waived in individual cases.

ILLUSTRATIONS

Photographs should be used sparingly, must be glossy prints, and should be mailed with protection against folding. **Micrographs** should have a labeled length unit drawn or pasted on the picture. On both, label "top" where any uncertainty might arise. **Captions** for figures (including photographs) must be included on a separate sheet. Figure numbers must **not** appear in the body of the figure; they will be removed if they do. **Numerical Data** should not be duplicated in tables and figures.

Drawings and **Graphs** ordinarily will be reduced to 8.3 cm (3¼ in.) column width, and after such reduction should have lettering no less than 0.15 cm high. Lettering must be of letter-guide quality. India ink on tracing cloth or paper is preferred, but India ink on coordinate paper with blue ruling is acceptable. Line weight 2 is used for borders and zero lines. When several curves are shown, each may be numbered and described in the caption. Lettering shown is approximately ⅛ in. In plotting current or potential as ordinate, increasing negative values should go down. The sample graph shown conforms to suggestions of the United States of America Standards Institute (USA Report Y15.1-1959).

SAMPLE CURVE DRAWING FOR REDUCTION TO $\frac{1}{2}$ SIZE

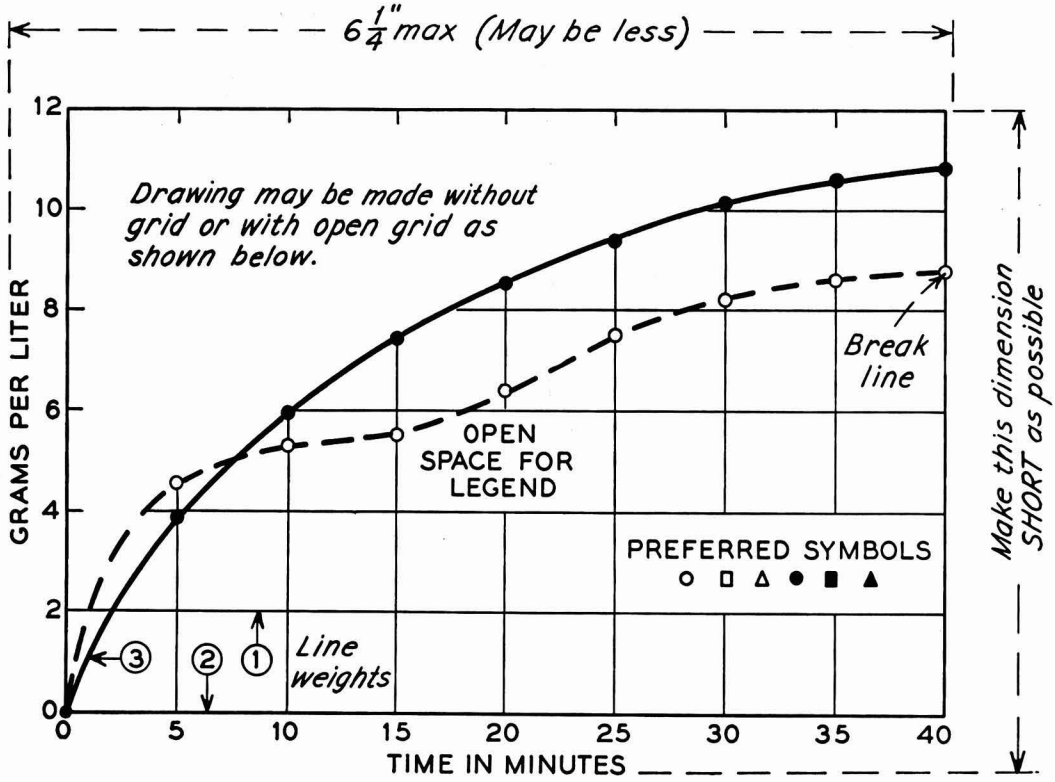

Call for Papers
134th National Meeting
Montreal, October 6-11, 1968

Divisions which have scheduled sessions are listed overleaf, along with symposium topics.

1. Symposium Papers.

Authors desiring to contribute papers to a symposium listed overleaf should check first with the symposium chairman to ascertain appropriateness of the topic.

2. General Session Papers.

Each of the several Society Divisions which meets in Montreal can plan a general session. If your paper does not fit readily into a planned symposium, you should specify "General Session."

3. To Submit a Meeting Paper.

Each author who submits a paper for presentation at a Society National Meeting should do three things:

A—Determine whether the meeting paper is to be submitted to a Society journal for publication. If so, see below for details.

B—No later than May 15, 1968, submit three copies, on the form printed overleaf, of a 75-word abstract of the paper to be delivered. You may use a facsimile of the form if necessary. These abstracts are required for publication in the printed program of the meeting.

C—No later than July 1, 1968, submit three copies of an extended abstract of your paper. See below for details. No deadline extension is possible.

Send all material to The Electrochemical Society, Inc., 30 East 42 St., New York, N. Y. 10017.

4. Meeting Paper Acceptance.

Notification of acceptance for meeting presentation, along with scheduled time, will be mailed to authors with general instructions no earlier than two months before the meeting. Those authors who require more prompt notification are requested to submit with their abstracts a self-addressed postal card with full author-title listing on the reverse.

5. Extended Abstract Book Publication.

Division programs will be the subject of an extended abstract volume in a manner prescribed by the Society Board of Directors. The volume is published by photo offset directly from typewritten copy submitted by the author. Therefore, special care should be given to the following typing instructions to insure legibility.

A—Abstracts are to be from 500-1000 words in length (two pages single-spaced) and are to contain to whatever extent practical all significant experimental data to be presented during oral delivery.

B—Please send original and two copies of the abstract typed single-spaced. Use white bond paper, size 8½ x 11 inches, with 1¼ margins on all sides. Typing guide forms are available from Symposium Session Chairman and from National Headquarters.

C—Title of paper should be in capital letters. Author(s) name and affiliation should be typed immediately below. It is not necessary in the heading or body to designate paper as "Extended Abstract" or to quote the divisional symposium involved.

D—Submit all copy, including figures, symbols and corrections, in black ink. No handwritten corrections, please. Submit graphs on onion skin without grids, or on graph paper specifically designed for offset reproduction; strip-on tape is acceptable.

E—Paste figures within typing dimensions indicated, with lettering no smaller than ⅛ inch. Submit only the important illustrations. Avoid use of half-tones except where absolutely necessary. Type captions no wider than figure dimensions and paste in proper place in the abstract. Place figure caption at bottom of figure. Place table title at top of table.

F—Mail to The Electrochemical Society. Inc., unfolded.

G—Please note that the extraordinarily low price of the extended abstract volume is made possible only through your strict adherence to these instructions. Any deviation threatens this low cost.

6. Manuscript Publication in a Society Journal.

Presentation of a paper at a Society National Meeting incurs no obligation to publish. However, all meeting papers upon presentation become the property of The Electrochemical Society, Inc., and should be submitted as promptly as possible in full manuscript form in order to be considered for publication in a Society publication. The Society "Instructions to Authors," are available from National Headquarters, set forth manuscript style and format.

Montreal Meeting Symposia Plans—Fall 1968

Battery Division Symposia Plans

The program for the Fall Meeting in Montreal, October 6-11, 1968 in addition to a general session will include the regular biennial symposium on Fuel Cells and a special symposium on Silver-Zinc Batteries.

Fuel Cells

Papers are solicited from those active in research and development on fuel cells of all types. Contributions ranging from fundamental aspects of electrode behavior and electrocatalytic phenomena to performance of fuel cells and fuel cell batteries in relation to design are desired. Questions and suggestions concerning the program should be addressed to the Program Chairman, R. R. Witherspoon, General Motors Research Laboratories, Warren, Mich. 48090.

Silver-Zinc Batteries

A symposium consisting completely of invited papers and reviews thereof will be held as a separate session lasting approximately four and one-half days. The symposium, cosponsored by the Air Force Aero Propulsion Laboratory, will feature papers on the history, electrode chemistry and electrochemistry, thermodynamics, mass transport, materials and manufacturing techniques, separators, and specifications, applications and performance of silver-zinc batteries. After editing, the contents of the symposium will be published as a hard-bound book which will bring together for the first time under one cover the science and technology of this high-energy electrochemical battery. This is not a closed meeting; attendance by all will be welcome.

Chairman for this symposium is J. J. Lander, Delco-Remy, Division of General Motors, Anderson, Ind. 46011.

Corrosion Division Symposia Plans

Three symposia in addition to general sessions are planned for the Fall 1968 Meeting of the Corrosion Division in Montreal.

Corrosion of Multilayer Deposits

Corrosion of Multilayer Deposits will be held jointly with the Electrodeposition Division. Chairmen for this symposium are: Karl Willson, Harshaw Chemical Co., 1945 E. 97 St., Cleveland, Ohio 44106 and E. J. Seyb, Jr., M&T Chemicals Inc., 1700 East Nine Mile Rd., Detroit, Mich. 48220.

See listing under **Corrosion and Electrodeposition Symposium Plans.**

Corrosion in Desalination

Corrosion in Desalination will be chaired by M. J. Pryor, Olin Matheson Chemical Corp., Metals Research Division, 275 Winchester Ave., New Haven, Conn. 06511.

No later than May 15, 1968, submit three copies, on the form overleaf, of a 75-word abstract of the paper to be delivered. No later than July 1, 1968, submit three copies of an extended abstract, 500-1000 words. Send all material to The Electrochemical Society, Inc., 30 E. 42 St., New York, N. Y. 10017

Corrosion of Architectural Materials

Corrosion of Architectural Materials will be chaired by Henry Leidheiser, Jr., Center for Surface and Coatings Research, Lehigh University, Bethlehem, Pa. 18015.

Those desiring to present papers at these symposia are requested to communicate directly with the symposium chairman. Several sessions of general papers will also be included.

The Corrosion Division will also institute on a trial basis a short session devoted to research results of newsworthy interest. Presentation time will be limited to 5 minutes and an abstract must be available at the meeting for posting. Permission to appear on the program must be obtained from the Chairman of the Division at the meeting. No advance permission is required.

Corrosion and Electrodeposition Divisions Symposium Plans

Corrosion of Multilayer Deposits

The Corrosion and Electrodeposition Divisions have scheduled a joint symposium on Corrosion of Multilayer Deposits for the Fall 1968 Meeting in Montreal.

This symposium will include reports on systems including at least one applied metallic deposit (vapor, electroless or electrolytic). Subsequent or concurrent layers may be metallic or nonmetallic. Papers are particularly solicited on chromium-chromium oxide on steel, conversion and organic coatings over metal layers as well as multilayer metal coatings over metallic or plastic substrates.

Inquiries and suggestions should be addressed to either of the Symposium Chairmen: E. J. Seyb, M&T Chemicals Inc., 1700 East Nine Mile Rd., Detroit, Mich. 48220 or K. S. Willson, Harshaw Chemical Co., 1945 East 97 St., Cleveland, Ohio 44106.

Dielectrics and Insulation Divisions of Symposium Plans

Deposited Thin Film Dielectric Materials

A symposium on Deposited Thin Film Dielectric Materials is scheduled for the Fall 1968 Meeting in Montreal.

There will be a number of invited papers; contributed papers are also being solicited.

Categories of subject matter being actively considered for the symposium include: (a) studies on the electrical and mechanical properties of deposited thin film dielectrics; (b) new techniques for the deposition of thin film dielectrics; (c) properties and applications of thin film dielectrics.

This symposium is particularly directed to the new sputtering technology, new means of evaporative deposition, and recent advances in vapor deposition techniques for preparation of dielectric thin films.

Suggestions and questions are welcome, and should be directed to the Chairman of the Symposium. F. Vratny, Bell Telephone Laboratories, Inc., Murray Hill, N. J., is Chairman.

Ferroelectrics

A symposium on Ferroelectric Materials is scheduled. The following topic areas are being actively considered for the sessions: (a) growth and characterization of ferroelectric crystals, (b) phenomenological and theoretical treatments of ferroelectricity, (c) dielectric properties of single crystals, polycrystal and composite materials, (d) domain structure and polarization reversal, (e) optical and electro-optic properties, and (f) device applications of ferroelectric materials.

There will be a number of invited speakers; contributed papers are also being solicited. Suggestions and questions concerning this symposium are welcome, and should be directed to the Chairman, Leslie E. Cross, Materials Research Laboratory, The Pennsylvania State University, University Park, Pa. 16802.

Electronics Division Symposia Plans

Semiconductor General Sessions

The Fall Meeting program for the Electronics Division will include Semiconductor General Sessions. H. F. John, Westinghouse Research and Development Center, Churchill Road, Pittsburgh, Pa. 15235 is Chairman.

Electrical Contacts to Semiconductors

The Electronics Division is sponsoring

a special symposium on Electrical Contacts to Semiconductors to be held at the Fall 1968 Meeting in Montreal. The fundamentals of the physics, chemistry, and metallurgy of ohmic contacts will be explored, and advances of technological importance will be discussed. The program is to include both contributed papers and invited speakers. Papers are being solicited on such topics as: theory of ohmic contacts, techniques of ohmic contact fabrication, evaluation of contact properties, modes of contact failure, composite contacts, special property contacts (e.g. optical transparency, thermal conductivity).

Any questions or suggestions should be addressed to the Symposium Chairman, Bertram Schwartz, Bell Telephone Laboratories, Inc., Murray Hill, N. J. 07974.

Photosensitive Materials for Electronic Applications

This symposium will cover the properties and uses of photosensitive materials in the electronics industry. Topics which will be considered for the program include xerography, photochromism, novel photographic techniques, photochemistry (e.g. photoresists), vidicons, storage phosphors etc. Papers on the above or closely related topics are solicited.

Questions concerning this symposium should be addressed to the Symposium Chairman, Erik M. Pell, Manager, Physics Research Laboratory, Xerox Corp., 800 Phillips Rd. Webster, N. Y. 14580.

Electrothermics and Metallurgy Division Symposium Plans

Preparation and Purification of Ultra-Pure Metals

A symposium on Preparation and Purification of Ultra-Pure Metals in addition to general sessions will be held at the Fall 1968 Meeting in Montreal. This symposium forms the first of a series planned by the Division to deal with materials of particular interest to Society members.

Papers are solicited from those active in research and development of these metals. Invited key-note speakers will survey theory and methods for preparation, purification, and determination of residual elements in ultra-pure metals.

Sessions will encompass contributions on preparation by electrochemical deposition, electron beam melting and volatilization; purification by zone refining, electrochemical and vaporization methods, determination of residual elements by micro-chemical techniques, and influence of residual elements on chemical and physical properties.

Inquiries and suggestions should be directed to either of the cochairmen: W. C. Cooper, Noranda Research Centre, 240 Hymus Blvd., Pointe Claire, Quebec, Canada or W. W. Smeltzer, Department of Metallurgy and Materials Science, McMaster University, Hamilton, Ont., Canada.

75-Word Abstract Form—Montreal Meeting October 6-11, 1968

Mail no later than May 15, 1968 to The Electrochemical Society, Inc., 30 East 42 St., New York, N. Y. 10017

Abstract No. .....
(do not write in this space)

.....
(Title of paper)

.....

.....
(Author) (Underline name of author presenting paper)

.....
(Business Affiliation)

.....
(Address)

(Type your abstract in this space—double space with two carbon copies on plain white paper.)

Division and Symposium .....

Do you require any audiovisual equipment? ☐ 35 mm (2x2 in.) slide projector; ☐ 3¼ x 4 in. slide projector; ☐ other (specify) _____.

Is a full length paper on this work to be submitted for Society publication? ☐ Yes ☐ No

Papers presented before a national technical meeting become the property of the Society and may not be published elsewhere without written permission of the Society.

For Office Use

Extended Abstract rec'd: ..... requested: .....

Sent to: .....

75-word Abstract sent to: ..... date: .....

SUSTAINING MEMBERS (CONTINUED)

Fairchild Semiconductor Corp.,
Palo Alto, Calif.

FMC Corp.,
Inorganic Chemicals Div.,
Buffalo, N. Y.
Inorganic Chemicals Div.,
South Charleston, W. Va.

Foote Mineral Co.,
Exton, Pa.

Ford Motor Co.,
Dearborn, Mich.

General Motors Corp.,
Allison Div., Indianapolis, Ind.
Delco-Remy Div., Anderson, Ind.
Research Laboratories Div., Warren, Mich.

General Telephone & Electronics Laboratories, Inc., Bayside, N. Y.

Globe-Union, Inc.,
Milwaukee, Wis.

B. F. Goodrich Chemical Co.,
Cleveland, Ohio

Gould-National Batteries, Inc.,
Minneapolis, Minn.

Great Lakes Carbon Corp.,
New York, N. Y.

Harshaw Chemical Co.,
Cleveland, Ohio (2 memberships)

Hercules Inc.,
Hercules Research Center,
Technical Information Div.,
Wilmington, Del.

Hill Cross Co., Inc.,
West New York, N. J.

Honam Electric Industrial Co.,
Kwangju City, Korea

Honeywell, Inc.,
Minneapolis, Minn.

Hooker Chemical Corp.,
Niagara Falls, N. Y. (2 memberships)

HP Associates,
Palo Alto, Calif.

Hughes Research Laboratories, Div. of Hughes Aircraft Co., Malibu, Calif.

International Business Machines Corp.,
New York, N. Y.

International Minerals & Chemical Corp.,
Skokie, Ill.

International Resistance Co.,
Philadelphia, Pa.

ITT Federal Laboratories, Div. of International Telephone & Telegraph Corp.,
Nutley, N. J.

Jones & Laughlin Steel Corp.,
Pittsburgh, Pa.

K. W. Battery Co.,
Skokie, Ill.

Kaiser Aluminum & Chemical Corp.,
Div. of Metallurgical Research,
Spokane, Wash.

Kawecki Chemical Co.,
Boyertown, Pa.

Kennecott Copper Corp.,
New York, N. Y.

Leesona Moos Laboratories, Div. of Leesona Corp., Great Neck, N. Y.

Arthur D. Little, Inc.,
Cambridge, Mass.

Lockheed Aircraft Corp.,
Missiles & Space Div.,
Sunnyvale, Calif.

Mallinckrodt Chemical Works,
St. Louis, Mo.

P. R. Mallory & Co.,
Indianapolis, Ind.

Melpar, Inc.,
Falls Church, Va.

Mobil Oil Corp.,
Dallas, Texas

Molybdenum Corporation of America,
New York, N. Y.

Monsanto Chemical Co.,
St. Louis, Mo.

M&T Chemicals Inc.,
Detroit, Mich.

Nalco Chemical Co.,
Chicago, Ill.

National Cash Register Co.,
Dayton, Ohio

National Lead Co.,
New York, N. Y.

National Steel Corp.,
Weirton, W. Va.

North American Aviation, Inc.,
El Segundo, Calif.

Northern Electric Co.,
Montreal, Que., Canada

Norton Research Corp.,
Cambridge, Mass.

Owens-Illinois Glass Co.,
Toledo, Ohio

Pennsalt Chemicals Corp.,
Philadelphia, Pa.

Phelps Dodge Refining Corp.,
Maspeth, N. Y.

Philips Laboratories, Inc.,
Briarcliff Manor, N. Y.

Pittsburgh Plate Glass Co.,
Chemical Div.,
Pittsburgh, Pa.

Potash Co. of America,
Carlsbad, N. Mex.

Radio Corp. of America
Electronic Components and Devices,
Lancaster, Pa.

Republic Foil Inc.,
Danbury, Conn.

Reynolds Metals Co.,
Richmond, Va.

Shawinigan Chemicals Ltd.,
Montreal, Que., Canada

Sonotone Corp.,
Elmsford, N. Y.

Sprague Electric Co.,
North Adams, Mass.

Stackpole Carbon Co.,
St. Marys, Pa.

The Standard Oil Company of Ohio,
Cleveland, Ohio

Stauffer Chemical Co.,
Dobbs Ferry, N. Y.

Syncro Corp.,
Oxford, Mich.

Texas Instruments, Inc.,
Dallas, Texas
Metals and Controls Corp.,
Attleboro, Mass.

3M Company,
St. Paul, Minn.

Titanium Metals Corp. of America,
Henderson, Nev.

Tyco Laboratories, Inc.,
Waltham, Mass.

Udylite Corp.,
Detroit, Mich. (4 memberships)

United States Steel Corp.,
Pittsburgh, Pa.

Upjohn Co.,
Kalamazoo, Mich.

Varian Associates,
Palo Alto, Calif.

Western Electric Co., Inc.,
Chicago, Ill.

Wyandotte Chemicals Corp.,
Wyandotte, Mich.

Yardney Electric Corp.,
New York, N. Y.

THE ELECTROCHEMICAL SOCIETY PATRON MEMBERS

Aluminum Co. of Canada, Ltd., Montreal, Que., Canada

Dow Chemical Co.
Chemicals Dept., Midland, Mich.
Metals Dept., Midland, Mich.

General Electric Co.
Capacitor Dept., Hudson Falls, N. Y.
Chemical Laboratory, Knolls Atomic Power Laboratory, Schenectady, N. Y.
Chemical Systems and Processes Laboratory, Research and Development Center, Schenectady, N. Y. (3 memberships)
Direct Energy Conversion Operation, West Lynn, Mass.
Lamp Div., Cleveland, Ohio
Materials & Processes Laboratory, Large Steam Turbine-Generator Dept., Schenectady, N. Y.

The International Nickel Co., Inc., New York, N. Y.

Olin Mathieson Chemical Corp.
Chemicals Div., Research Dept., New Haven, Conn.

Union Carbide Corp.
Divisions:
Carbon Products Div., New York, N. Y.
Consumer Products Div., New York, N. Y.

Westinghouse Electric Corp.
Electronic Tube Div., Elmira, N. Y.
Lamp Div., Bloomfield, N. J.
Molecular Electronics Div., Elkridge, Md.
Semiconductor Div., Youngwood, Pa.
Research Laboratories, Pittsburgh, Pa.

THE ELECTROCHEMICAL SOCIETY SUSTAINING MEMBERS

Airco Speer Electrodes and Anodes, St. Marys, Pa.

Allen-Bradley Co., Milwaukee, Wis.

Allied Chemical Corp., General Chemical Div., Morristown, N. J.

Aluminum Co. of America, New Kensington, Pa.

American Metal Climax, Inc., New York, N. Y.

American Potash & Chemical Corp., Los Angeles, Calif.

American Smelting and Refining Co., South Plainfield, N. J.

American Zinc Co., St. Louis, Mo.

American Zinc Co. of Illinois, East St. Louis, Ill.

The M. Ames Chemical Works, Inc., Glens Falls, N. Y.

Ampex Corp., Redwood City, Calif.

Armco Steel Corp., Middletown, Ohio

Beckman Instruments, Inc. Fullerton, Calif.

Bell Telephone Laboratories, Inc., New York, N. Y. (2 memberships)

Bethlehem Steel Corp., Bethlehem, Pa. (2 memberships)

Boeing Co., Seattle, Wash.

Burndy Corp., Norwalk, Conn.

Canadian Industries Ltd., Montreal, Que., Canada

Carborundum Co., Niagara Falls, N. Y.

Chrysler Corp., Detroit, Mich.

Clevite Corp. Burgess Battery Div., Freeport, Ill. (2 memberships)

Cominco Ltd., Trail, B. C., Canada (2 memberships)

Cyclops Corp., Universal-Cyclops Specialty Steel Div., Bridgeville, Pa.

Diamond Alkali Co., Painesville, Ohio

Wilbur B. Driver Co., Newark, N. J.

E. I. du Pont de Nemours & Co., Inc., Wilmington, Del.

Eagle-Picher Industries, Inc., Electronics Div., Joplin, Mo.

Eastman Kodak Co., Rochester, N. Y.

Eltra Corp. Prestolite Div., Toledo, Ohio C&D Batteries, Conshohocken, Pa.

Engelhard Industries, Inc., Newark, N. J.

The Eppley Laboratory, Inc., Newport, R. I.

ESB Inc., Philadelphia, Pa. (2 memberships)

Esso Research and Engineering Co., Engineering Technology Div., Florham Park, N. J.

Exmet Corp., Bridgeport, Conn.